SKYLAB'S

Astronomy and Space Sciences

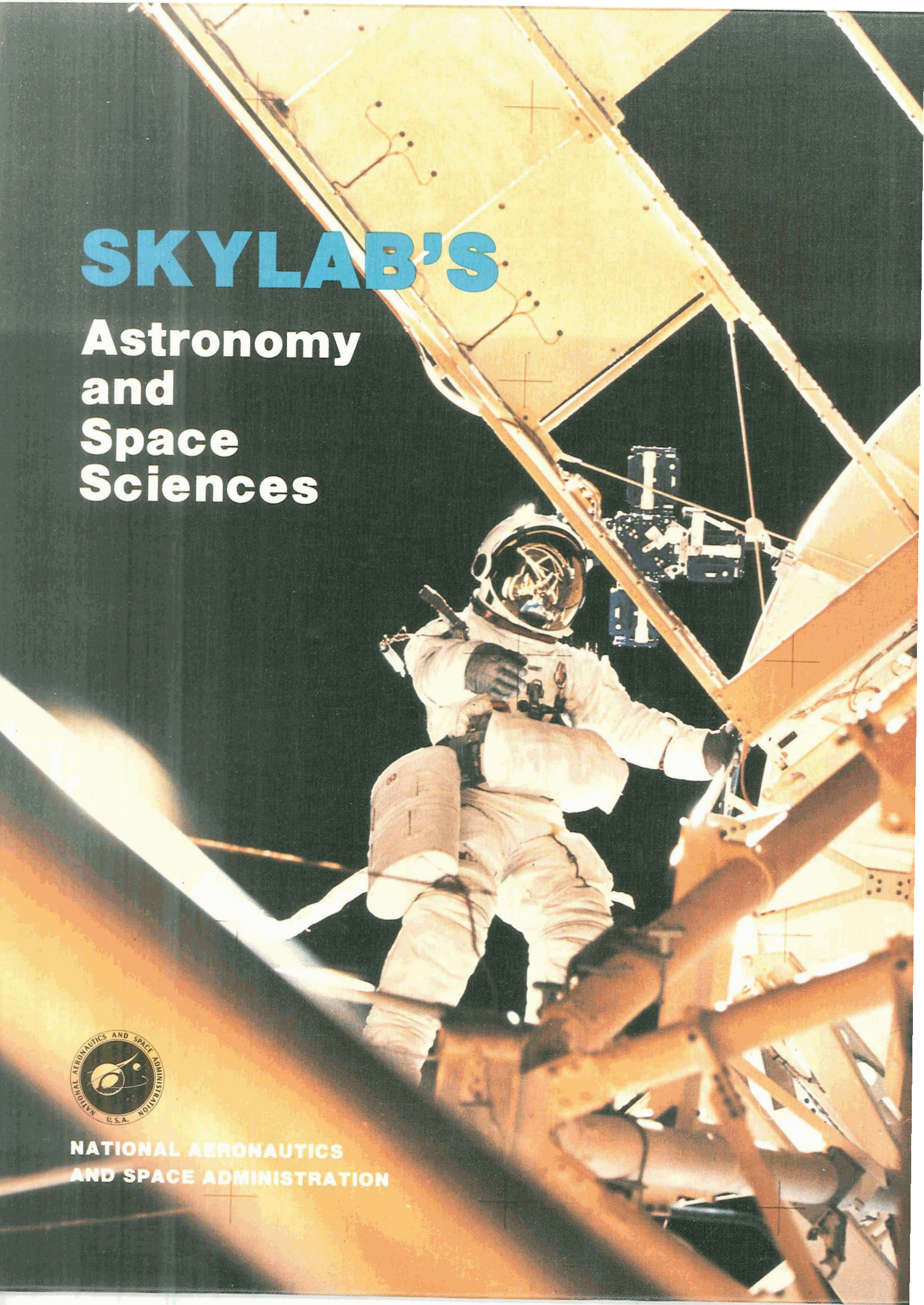

NATIONAL AERONAUTICS AND SPACE ADMINISTRATION

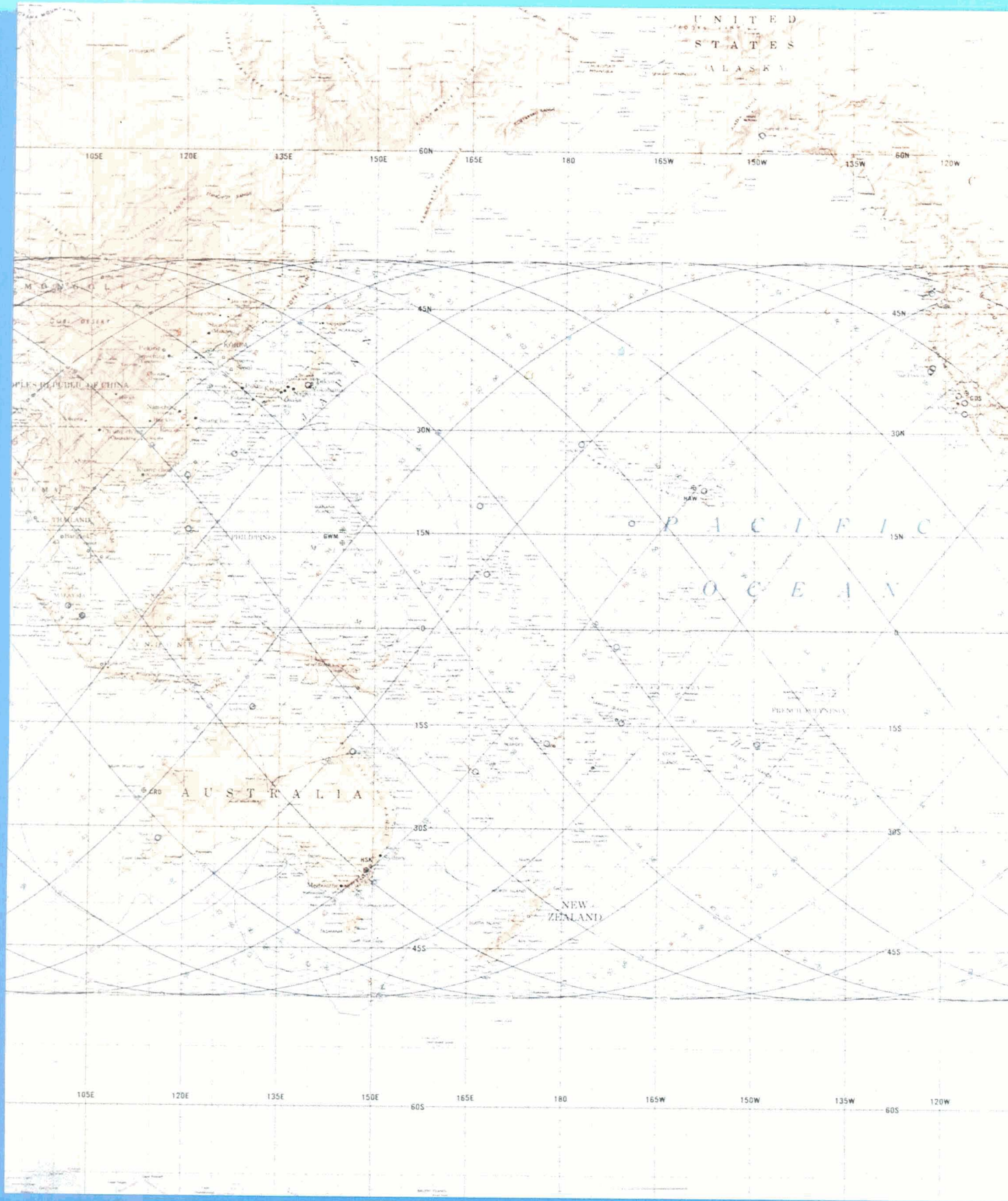
UNITED
STATES
ALASKA
MONGOLIA
GOBI DESERT
PEOPLE'S REPUBLIC OF CHINA
KOREA
THAILAND
PHILIPPINES
MALAYSIA
INDONESIA
PACIFIC
OCEAN
FRENCH POLYNESIA
AUSTRALIA
NEW
ZEALAND
GWM
HAW
CRO
HSK
105E
120E
135E
150E
165E
180
165W
150W
135W
120W
60N
45N
30N
15N
0
15S
30S
45S
60S

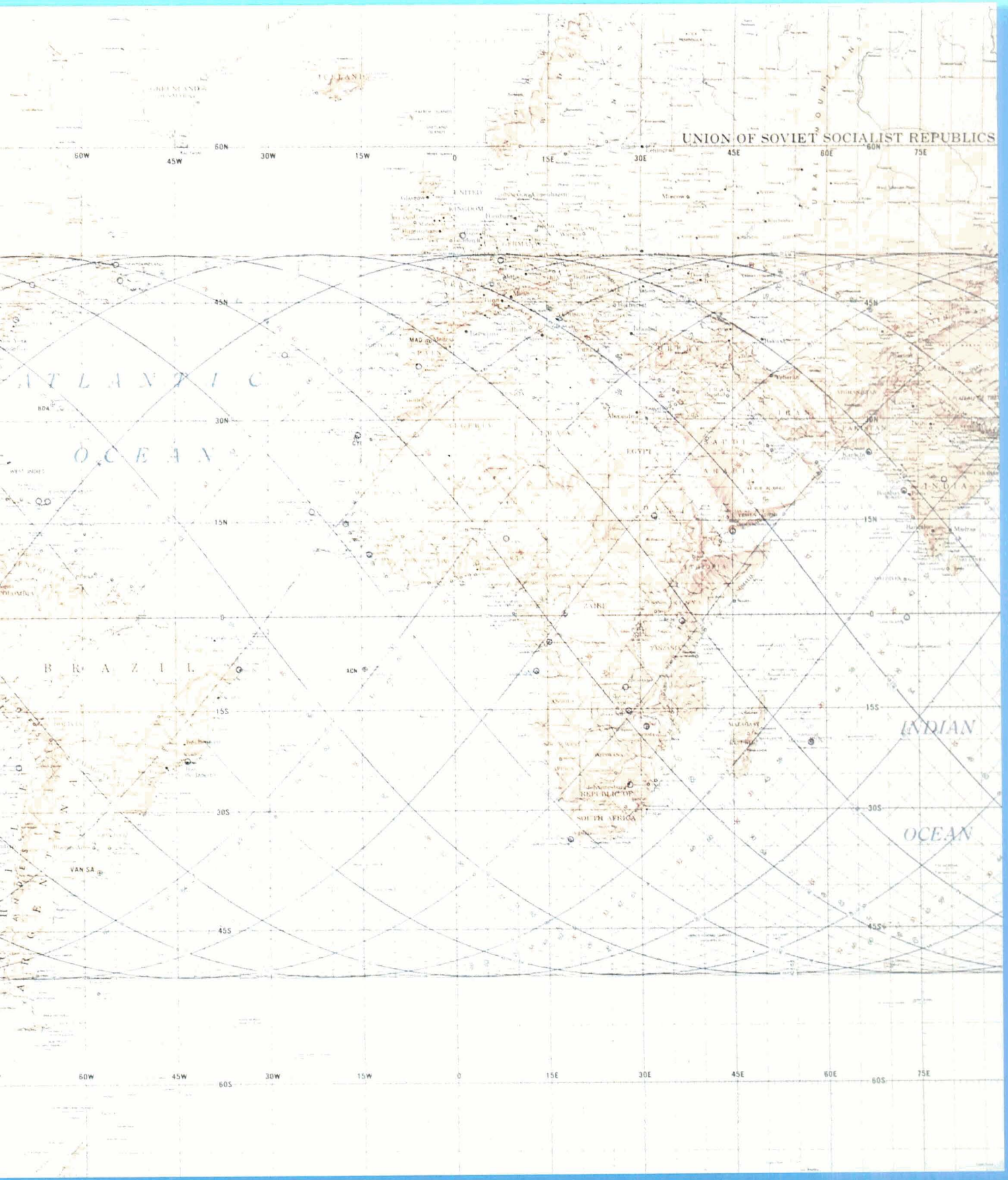
UNION OF SOVIET SOCIALIST REPUBLICS
ATLANTIC
OCEAN
INDIAN
OCEAN
BRAZIL
EGYPT
INDIA
SOUTH AFRICA
REPUBLIC OF
60W
45W
30W
15W
0
15E
30E
45E
60E
75E
60N
45N
30N
15N
15S
30S
45S
60S

Skylab's Astronomy and Space Sciences

NASA SP-404

Skylab's

Scientific and Technical Information Branch
NATIONAL AERONAUTICS AND SPACE ADMINISTRATION
Washington, D.C.
1979

Astronomy and Space Sciences

Edited by
Charles A. Lundquist

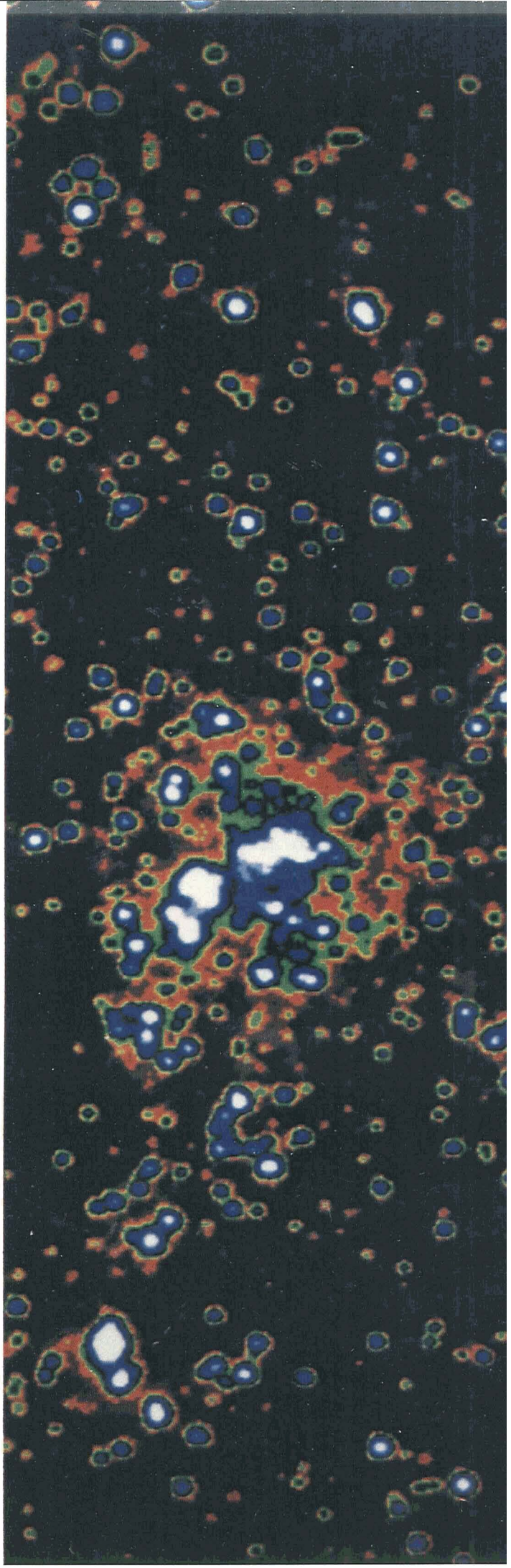

Library of Congress Cataloging in Publication Data

United States. George C. Marshall Space Flight Center,
Huntsville, Ala.
Skylab's astronomy and space sciences.

(NASA SP ; 404)
Includes index.
Supt. of Docs. no.: NAS 1.21:404
1. Astronomy. 2. Atmosphere. 3. Skylab Project,
I. Lundquist, Charles A. II. Title. III. Series: United
States. National Aeronautics and Space Administration.
NASA SP ; 404.
QB4.U47 1978 520 78-606051

For sale by the Superintendent of Documents
U.S. Government Printing Office, Washington, D.C. 20402

Stock No. 033-000-00767-1

PREFACE

In addition to the large, and to some extent better known, instrument groups onboard Skylab, there were also a sizable number of relatively small instruments serving a variety of scientific disciplines. These instruments were small, not in terms of their scientific importance, but in terms of their individual demands on the resources of Skylab. Some of them explored various areas of space science and astronomy, and the results are summarized in this volume.

In the area of far-ultraviolet astronomy, data obtained by one instrument on Skylab increased by a factor of 10 the number of stars with well-resolved spectra between 1400 and 2000 Å, and indicated the need for some revision in the classification of hot stars. The search for "superheavy" cosmic rays was once again unsuccessful, no elements with atomic number greater than 110 having been found. Evidence was found of a "soft auroral zone" at an altitude of 100 km, between the aurora at 120 km and the airglow at 80 km. Comet Kohoutek provided a particular flurry of activity during the last Skylab mission—the astronauts participated in the large coordinated effort to observe it. In the ultraviolet region of Kohoutek's spectrum, the known OH and CN emission lines at 3100 and 3900 Å, respectively, were again observed, but no other lines were seen. Photographs from one of the 35-mm Skylab cameras provided a tie between ground-based observations and the Apollo Telescope Mount coronagraph observations of the comet. Kohoutek results, however, were not spectacular because it turned out that Kohoutek was only a modest comet.

As in many areas of science, most of the specific results will be of particular interest to the principal investigators and their colleagues, but the total Skylab science program should have far-reaching significance for a much larger audience. One of the special characteristics of Skylab was its ability to provide a platform for a large number of physically small and relatively simple experiments that could never have obtained a solo ride on a satellite. Its multidisciplinary character allowed the Skylab mission to serve a very broad science constituency—ranging from observations of cosmic rays to the growth of semiconductor crystals. The multidisciplinary science payload also permitted very full utilization of the space laboratory. A satellite devoted solely to solar astronomy can observe the Sun during only roughly two-thirds of each orbit. The same is true of a satellite devoted solely to Earth observations, etc.

On the other hand, the multidisciplinary nature of Skylab greatly increased its complexity and required frequent compromises between totally nonequivalent science goals. The issue of whether to obtain a medical run or to make an Earth observation pass during a given time period is never resolved in a truly satisfactory manner.

The length of the Skylab missions and, most importantly, the presence of man onboard allowed us unprecedented flexibility in modifying both observing plans and procedures. Ironically, our flexibility in replanning was probably helped by the problem experienced during Skylab's launch, which immediately necessitated a large replanning effort and very quickly accustomed us to the idea of short-term replanning. During the missions, the scheduling of the major blocks of time for each day was accomplished 24 to 36 hours ahead of time. For Earth observation passes, the lead time for some details was occasionally reduced to approximately 6 hours, and, in cases of solar activity, observing programs were modified in real time. Because of the "revisit" capability, we were able to respond to the arrival of Comet Kohoutek by sending up the electrographic camera after the Skylab itself had been launched. Although an electrographic camera of very similar design had previously flown on Apollo 16, it is still worth noting that the total time for preparing and planning the Skylab electrographic camera experiment, including camera modifications, was less than 6 months. Because of its flexibility, Skylab functioned very much like an "ordinary" laboratory here on Earth.

It is to be hoped that, having learned how to provide a laboratory with responsive accommodations and a flexible operating climate, we will be able to build successfully on the Skylab experience and achieve an even more flexible and productive environment for research as we enter the Space Shuttle era.

ROBERT A. PARKER
Skylab Program Scientist
Lyndon B. Johnson Space Center

CONTENTS

Chapter 1	Introduction to Skylab	1
Chapter 2	Stellar and Galactic Astronomy	7
Chapter 3	Interplanetary Dust	27
Chapter 4	Observations of Comet Kohoutek	43
Chapter 5	Energetic Particles	65
Chapter 6	The Earth's Atmosphere	79
Chapter 7	Orbital Environment	93
Appendix	Skylab's Astronomy and Space Science Experiments	116
Editor's Note		118
Index		119

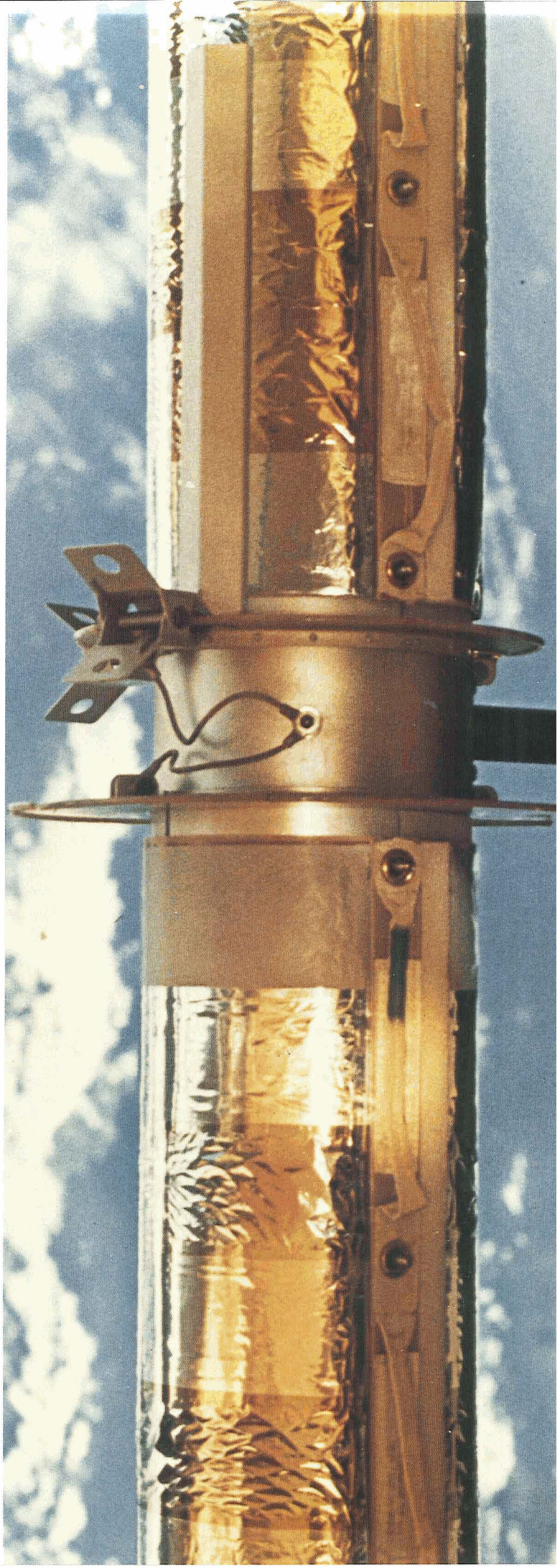

1
Introduction to Skylab

Skylab, a versatile scientific and engineering laboratory (fig. 1-1), was launched into Earth orbit on May 14, 1973, on a Saturn V rocket. Three crews of three men each subsequently visited the space station during extended missions for a total of 171 days of manned occupancy. A Saturn IB rocket launched each three-man crew in an Apollo spacecraft that was also the reentry vehicle. The manned missions lasted 28, 59, and 84 days (fig. 1-2). During the flight out of the Earth's atmosphere, Skylab's micrometeoroid and heat shield was unexpectedly torn off. A specially built parasol to shield the space station was therefore sent up with the first crew, whose launch was consequently delayed until May 25, 1973. The second crew was launched on July 28, and the third on November 16. The last mission was originally planned for 56 days, but because the

Figure 1-1.—The Skylab space station.

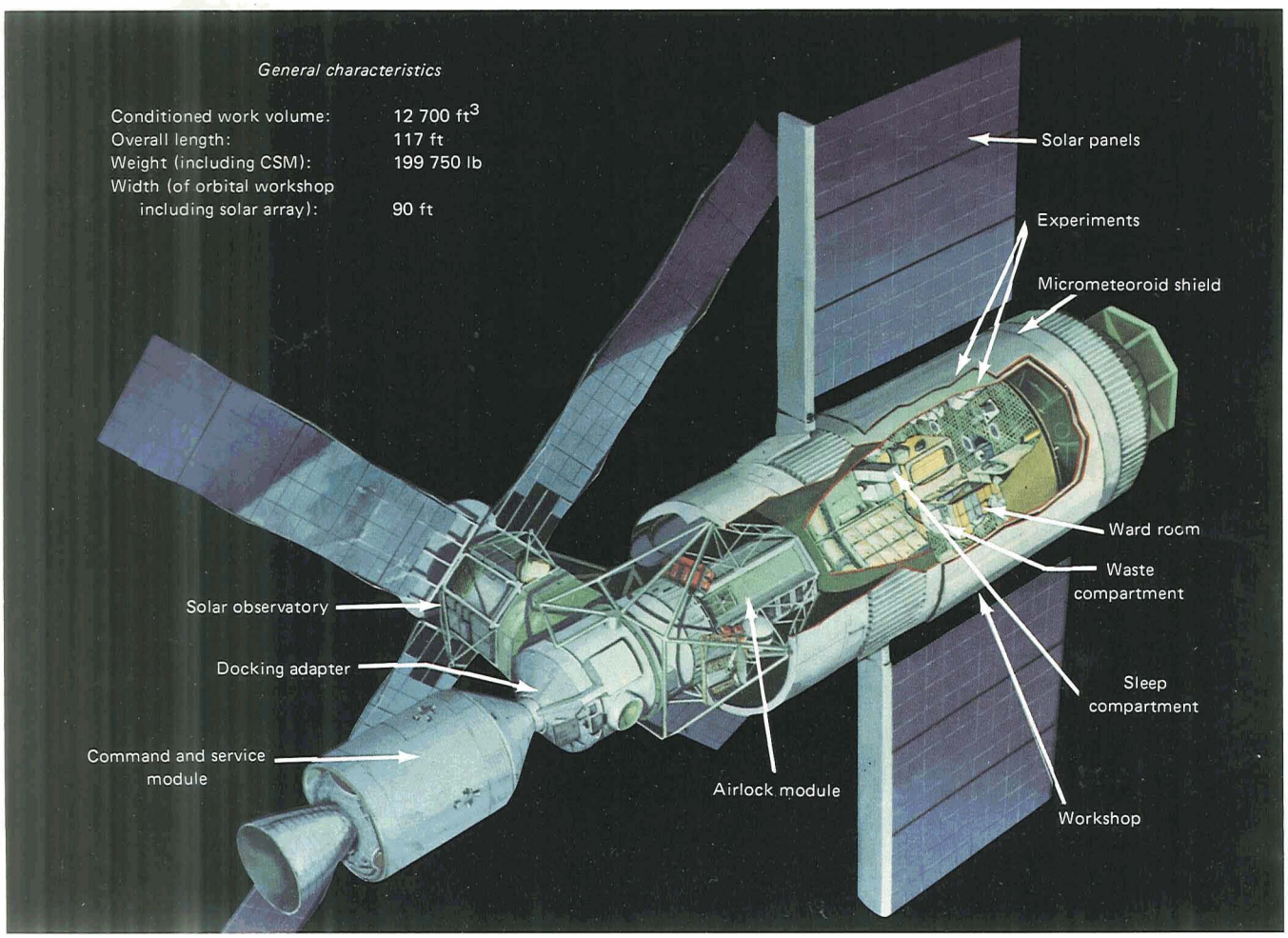

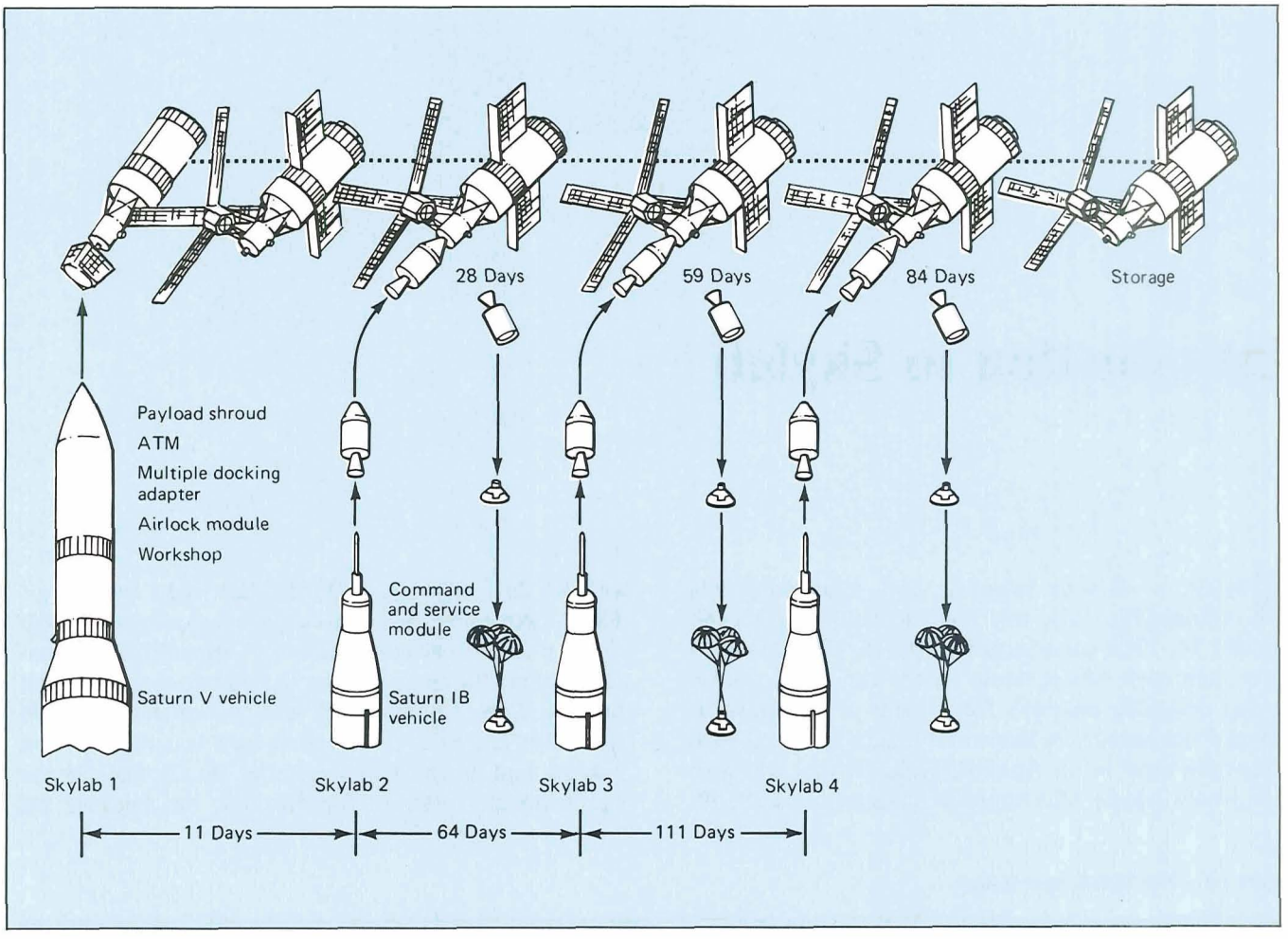

Figure 1-2.—Skylab mission sequence.

overall performance had been very successful, the final mission was extended by 28 days, the entire length of the first mission. The third crew splashed down on February 8, 1974.

Circling 50° north and south of the Equator at an altitude of 435 km, Skylab orbited the Earth every 93 min and completed some 3900 orbits from launch to the end of the third manned mission. The zone containing the spacecraft's track includes 75 percent of the Earth's surface, 80 percent of its developed land, and 90 percent of its population.

An extensive tracking network kept radio and television contact between ground controllers and the Skylab crews. During some orbits (fig. 1-3) contact was maintained almost continuously (track A); during others, there were periods of up to 90 min without contact with the crew (track B).

ASTRONOMY AND SPACE SCIENCE

Radiant energy at some wavelengths passes through the Earth's atmosphere and reaches the ground. At other wavelengths, the atmosphere is opaque, and the only way to make astronomical observations at these wavelengths is to lift the instrument above the Earth's atmosphere. Skylab made observations in two such wavelength bands, the ultraviolet and the X-ray.

The astronomy experiments included measurements of the ultraviolet brightness and spectral lines of stars and galaxies. Galactic X-ray sources were observed with an instrument attached to the third stage of the Saturn V rocket, which briefly orbited behind and below Skylab. Measurements were also made at visible wavelengths of low-light phenomena such as the zodiacal light (light scattered from dust in the solar system). These measurements are difficult to make from the ground

because of interference from airglow in the atmosphere, even on clear nights when viewing conditions are optimal.

Above the Earth's atmosphere, it is possible to see regions near the Sun without the interference of scattered light. Only during an eclipse of the Sun can these regions be seen from the Earth's surface. By artificially eclipsing the Sun, Skylab cameras photographed Comet Kohoutek near the Sun when it could not be detected by Earth-based cameras. The astronauts were also able to observe and sketch the comet at this time. In addition, Skylab provided an excellent vantage point for studying the upper atmospheric airglow, the aurorae, and the ozone layers.

The atmosphere shields the Earth from cosmic ray particles, which are high-energy atomic nuclei traveling through space at speeds near that of light. When they collide with the atmosphere, they cause showers of secondary particles. These showers can be studied by instruments in balloon flights and sounding rockets, but the analysis of significant numbers of the primary cosmic ray particles, especially the rarer ones, requires long-duration observations above the atmosphere. Skylab experiments were able to record tracks of these cosmic rays.

Near the northern and southern extremes of its orbit, Skylab passed through portions of the Van Allen belts and through a portion of the South Atlantic anomaly, off the coast of South America. The latter is a region of the radiation belts that dips toward the surface because Earth's magnetic axis is displaced from the planet's center. The charged particles trapped in the belts were measured from Skylab at high latitudes as well as in the South Atlantic anomaly.

Other studies made by Skylab included observations of neutrons, micrometeoroids, and materials emanating from the space station itself. The neutrons inside the Skylab vehicle came mainly from the interaction of Van Allen belt protons with Skylab's structural materials. Special detection devices were used to measure neutrons, to gather micrometeoroid particles, and to measure contamination from the space station itself.

Figure 1-3.—Skylab ground trace and tracking stations.

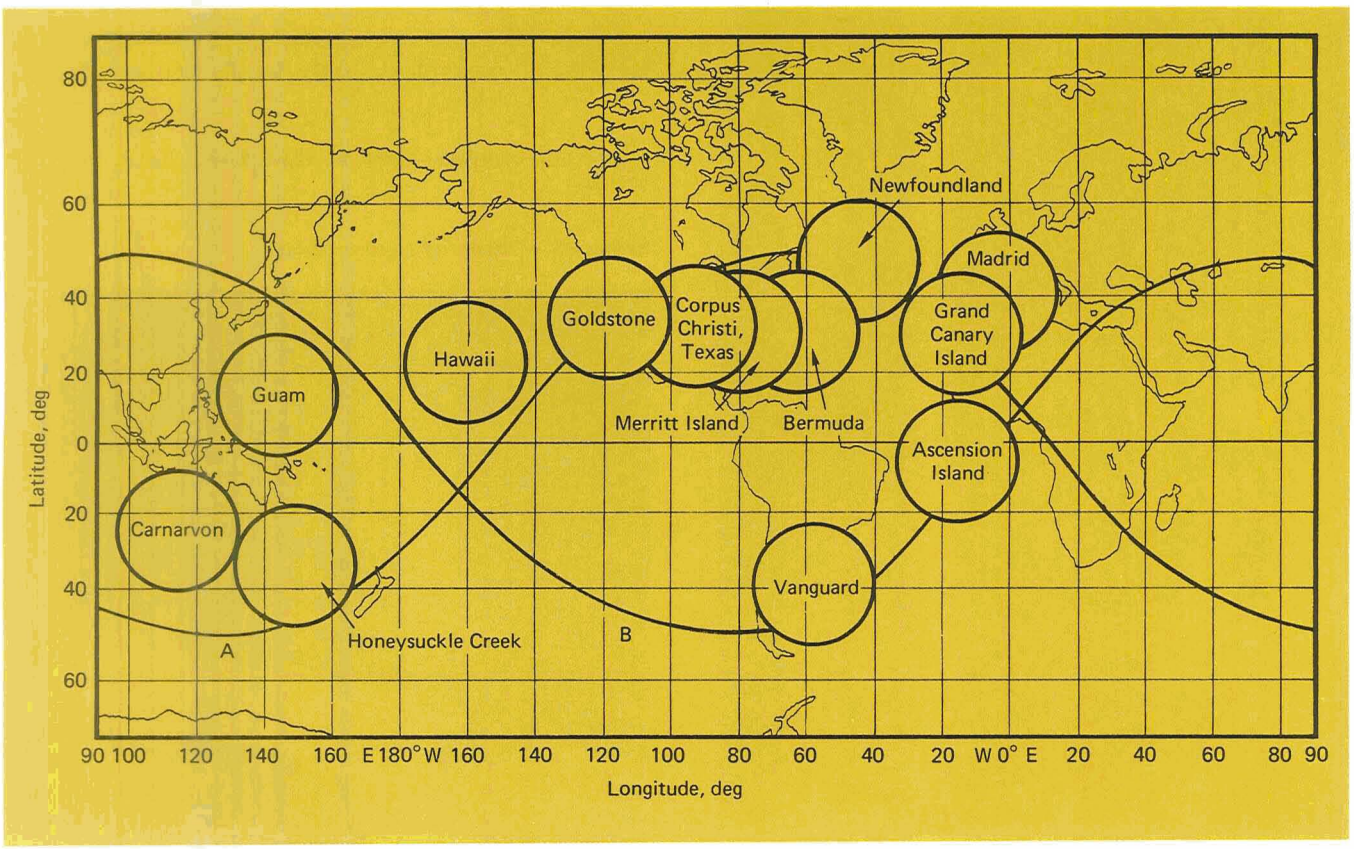

Skylab's Special Accommodations for Astronomy and Space Science

Several Skylab experiments viewed the sky in the all-important ultraviolet wavelengths. Since this region of the electromagnetic spectrum is absorbed by optical glasses, the windows and lenses for these experiments were fabricated of quartz and certain metal fluorides, which transmit ultraviolet light.

Two small airlocks were installed through Skylab's workshop wall, one on the side facing the Sun and one pointed in the opposite direction. They provided direct access to space and eliminated the need to depressurize the workshop. Each instrument using an airlock was first sealed to the inner port of the airlock, which was then evacuated and the outer port opened to space. When instruments were not occupying an airlock, a quartz window for specialized photography or a metal plate was installed.

In the weightlessness of free flight, man can handle heavy pieces of equipment with ease. Owen K. Garriott of the second crew had no trouble maneuvering the large Earth-terrain camera with three fingers, as shown in figure 1-4. The small airlock that was used for the Earth-terrain camera and other instruments is on the wall at the left of Garriott's right hand.

Figure 1-5 shows the exterior of the Sun-facing airlock; the photograph was taken by the first Skylab crew

Figure 1-4.—Astronaut Owen K. Garriott with the Earth terrain camera.

Figure 1-5.—Exterior of the solar airlock.

before docking. The blistered appearance of the workshop was due to the loss of the micrometeoroid and heat shield, which caused bonding material to be irradiated by the Sun for several days. The parasol flown up with the first crew was deployed through this airlock. The workshop cooled down, but the airlock was blocked from further use in scientific experiments. Some instruments that would have used it were redesigned for spacewalks during later visits; others were used in the remaining (antisolar) airlock.

The antisolar airlock is shown in figure 1-6 from the inside of the workshop with a window installed and the outer door closed. The vacuum hose, wrapped around the airlock, was used for equipment depressurization. Film canisters, for example, were evacuated before they were stored in film vaults. The airlock was used sequentially for several instruments. Scheduling to obtain optimal data and to take advantage of targets of opportunity, such as Comet Kohoutek, was a continuing challenge to the Skylab astronauts and the ground planning teams, especially with the solar airlock occupied by the parasol.

A mirror with ultraviolet-reflecting surfaces was used in the ultraviolet stellar astronomy experiment (fig. 1-7) and with other instruments. It was mounted in the antisolar airlock and extended beyond the spacecraft wall where it could be tilted $\pm 15°$ and rotated through 360° to scan the sky. Because of this maneuverability, instruments pointed at the mirror from inside Skylab could view a selected target on the celestial sphere without having to move the entire space station.

The flat mirror was elliptical and measured 19 by 38 cm. Its reflective surface had an aluminum coating with a thin magnesium fluoride overcoating. In figure 1-7, the ultraviolet stellar astronomy experiment's optical canister and film canister are attached to the mirror mechanism.

The airlock, vacuum hose, maneuverable mirror, and other multiple-use equipment provided a flexibility used repeatedly throughout the Skylab mission. Their adaptability allowed rescheduling experiments displaced by the emergency use of the solar-facing airlock and accommodated unanticipated comet observations.

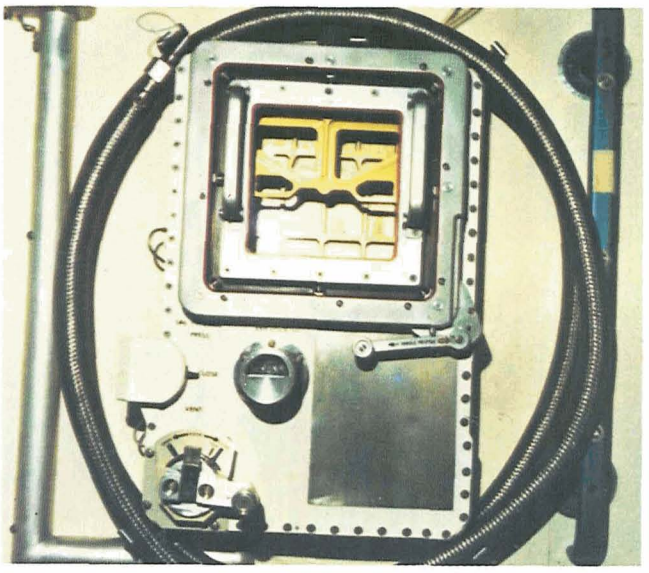

Figure 1-6.—Inside the antisolar airlock.

Figure 1-7.—Ultraviolet stellar astronomy instrument with the tilting and rotating mirror used for several experiments.

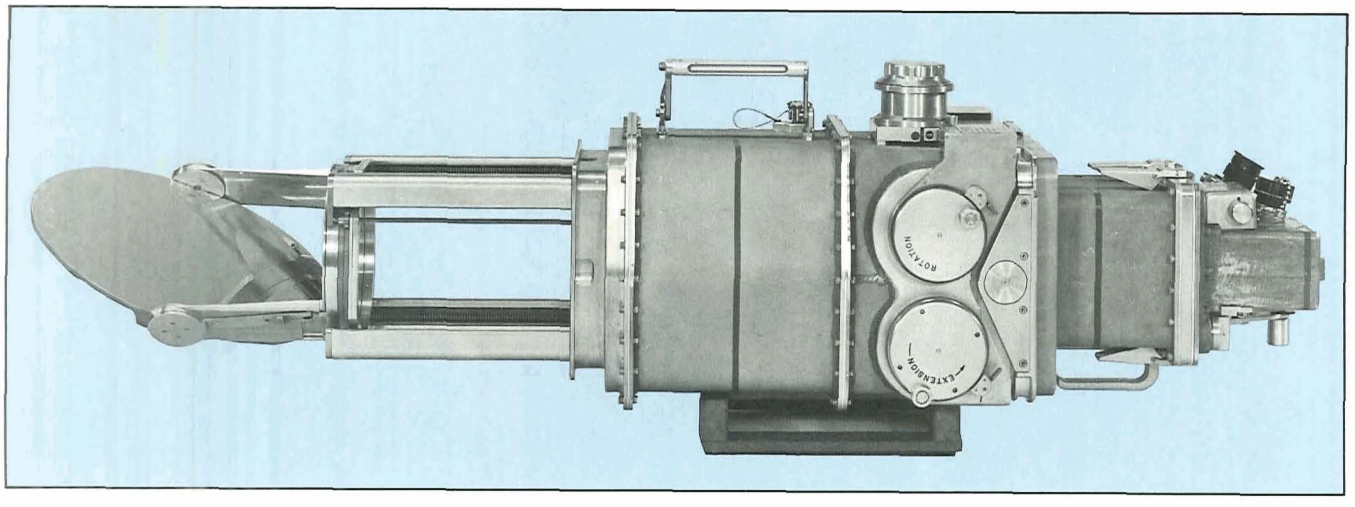

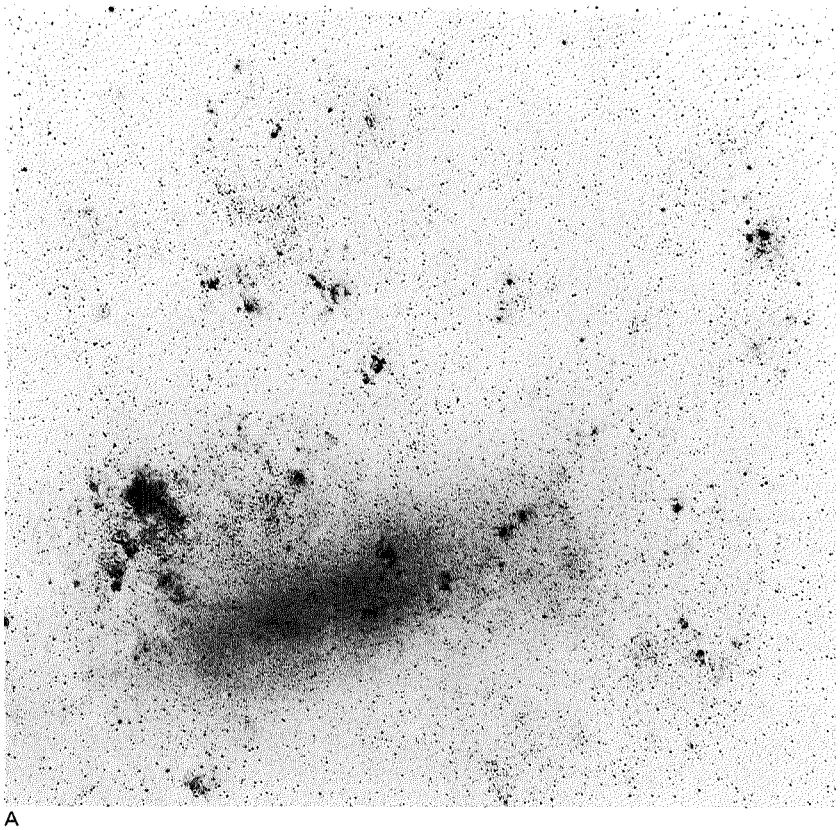

A

B

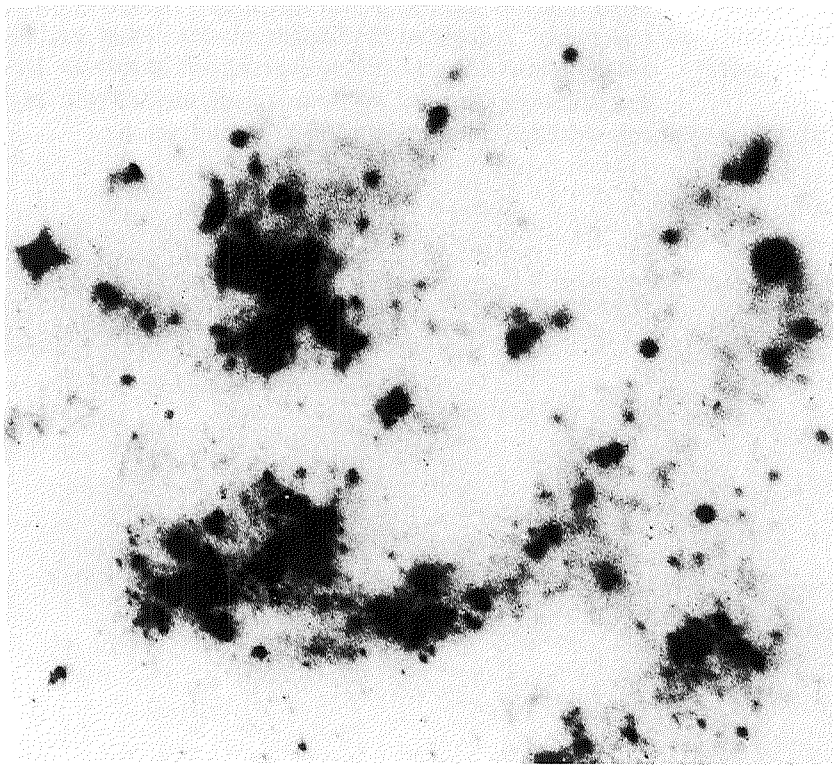

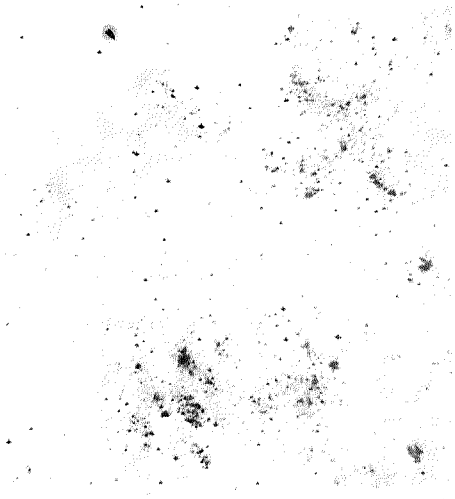

C

Figure 2-1.—Large Magellanic Clouds. (A) In red light from the ground; (B) in far-ultraviolet from the Moon (Apollo 16 mission); (C) in ultraviolet by the Skylab stellar astronomy experiment; (D) in ultraviolet taken by the ultraviolet panorama camera on Skylab.

D

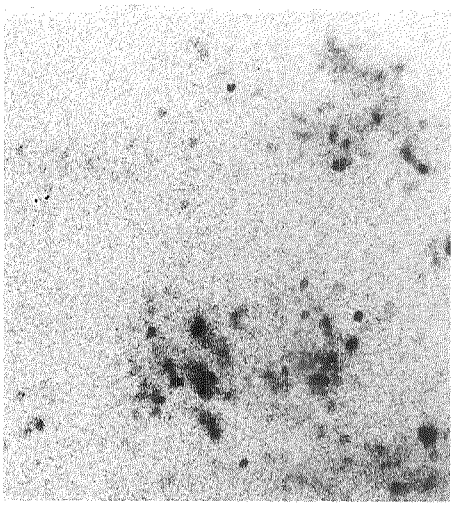

2
Stellar and Galactic Astronomy

Astronomy was limited to observations in the narrow band of visible wavelengths until a few decades ago. Investigations in other parts of the electromagnetic spectrum began in the 1930s with radio astronomy and have since been extended to cover almost the whole spectrum.

The greatest single obstacle to ground-based observations is the atmosphere. The ozone, oxygen, and nitrogen molecules of the Earth's upper atmosphere almost completely absorb ultraviolet radiation and prevent any Earth-based astronomy at wavelengths shorter than about 3000 Å. Various vehicles have been used to transport instruments beyond the atmosphere's interference. Balloons, aircraft, sounding rockets, and unmanned satellites have provided large amounts of new information. These observations, however, were incomplete in the far-ultraviolet to soft-X-ray region and were confined to bright objects. The Skylab experiments were designed for additional observations at these wavelengths and for the observation of faint objects.

SKYLAB'S ULTRAVIOLET EXPERIMENTS

Figure 2-1 illustrates the different information that can be obtained from photographs in different wavelength bands. It shows the Large Magellanic Clouds in red light from Earth, in the far ultraviolet from the Moon's surface, and in the ultraviolet from Skylab.

Importance of the Ultraviolet Region

The ultraviolet region of the spectrum is of special importance to astrophysics. The strongest emissions of the two most abundant elements in the universe, hydrogen and helium, lie in the ultraviolet, as do the strongest emissions of other important elements, such as carbon, nitrogen, and oxygen and their ions. (An ion is an atom that has lost one or more electrons. A neutral carbon atom is designated by C I; a carbon atom with one electron missing is C II, etc.)

Figure 2-2.—Astronaut Alan Bean operating the ultraviolet stellar astronomy experiment (S019) in the orbital workshop.

Stars are classified by spectral class according to a system of letters (table 2-I), each letter class being further subdivided from zero to 10. The youngest, hottest, and most massive stars, of the spectral classes O and B, emit most of their radiation in the ultraviolet; for example, a B star emits 80 percent of its total radiation at wavelengths shorter than 3000 Å. Although their visible radiation gives some information on the nature of the hot stars and was used for the conventional classification of stars, ultraviolet data are essential for calculating their total rate of energy loss and their lifespan.

Table 2-I.—Spectral Classification of Stars

Class	Temperature range, K	Spectral lines in visible light
O	30 000–50 000	Ionized helium
B	10 000–30 000	Neutral helium Strong hydrogen
A	7500–10 000	Very strong hydrogen
F	6500–7500	Strong hydrogen Ionized calcium Weak metal lines
G	5000–6000	Weak hydrogen Many metal lines
K	3500–5000	Many metal lines
M	2000–3500	Molecular spectra, especially TiO, Many metal lines

Observations in the ultraviolet have recently revealed that many of these stars are blowing away their outer layers. This reaction not only affects their evolution but also replenishes and modifies the interstellar gas and dust from which new stars will be formed.

Ultraviolet Stellar Astronomy Experiment (S019)

The S019 ultraviolet stellar astronomy experiment was designed by astronaut Karl S. Henize while an astronomer at Northwestern University to survey the ultraviolet spectra of a much larger number of stars than had been possible in earlier similar programs. It was able to reach somewhat dimmer stars than could the Orbiting Astronomical Observatories launched in the 1960s and early 1970s, and therefore could contribute a broader statistical base for the interpretation of these spectra.

The experiment was operated during all three Skylab missions and photographed spectra in a total of 188 star fields. These fields cover an area in the sky of approximately 3660 square degrees and include roughly 24 percent of a 30°-wide band centered on Gould's belt, a band around the sky in which the brighter stars concentrate. Nearly 1600 stars photographed by Skylab have measurable brightnesses at wavelengths of 2000 Å or less. Of these, 400 show useful data at 1500 Å or less, and about 170 show easily measurable absorption lines. Before Skylab, only about 30 spectra below 1500 Å had been obtained, with sounding rockets.

Instrumentation

The S019 ultraviolet stellar astronomy experiment used a 15-cm-aperture telescope converted into an objective-prism spectrograph by placing a prism of calcium fluoride in front of it. Such a system has the advantage of being able to obtain the spectra of several stars (all the bright stars in a 4° by 5° field of view) in a single exposure, whereas a conventional slit spectrograph photographs only one star at a time.

Since the objective-prism spectrograph operated from the antisolar scientific airlock, an articulated-mirror system was extended through the airlock and then rotated and tilted in order to view any desired part of the sky. This mirror system was also used in other astronomical experiments operated through the airlock. Figure 2-2 shows the equipment being operated by astronaut Alan Bean. The operation was entirely manual. The astronauts pointed the mirror, verified (during the first exposures of each observing session) the mirror pointing by observing stars in a finding telescope, advanced the film, opened and closed the shutter, and timed the exposures.

Operating Modes

The calcium fluoride prism disperses starlight into a spectrum. Since the fine spectral lines in such narrow

Figure 2-3.—Ultraviolet spectra in the 1500-Å region taken with the objective-prism spectrograph in the widened-spectrum mode.

spectra tend to be obscured by the graininess of the photographic film, most of the spectra were also widened to 0.6 mm in the direction perpendicular to the dispersion by slowly tilting the rear end of the mirror canister (to which the spectrograph was attached) during each exposure. This widened-spectrum mode (fig. 2-3) showed improved detail in the spectra and was able to produce spectra in the 1500-Å region of BO stars as faint as visual magnitude 6.5 (barely visible to the naked eye).

It was possible to obtain spectra from even fainter stars in the same exposure time if the spectra were not widened. Even though the unwidened-spectrum mode yielded less spectral detail (fig. 2-4), it was used in a large fraction of the fields to record fainter stars.

A no-prism mode was also used. The prism was removed from the spectrograph, and lateral chromatic aberration, which would normally be considered a defect in the optical system, was used to produce very low resolution spectra. The ultraviolet image of each star was closer to the center of the plate than was its visible-light image, thus producing images elongated radially outward from the center of the plate (fig. 2-5). Although the no-prism mode produced only very crude spectra, it had the advantage of showing the spectral distribution of energy in much fainter stars than could the other two modes. This mode was used mainly to observe the distribution of very hot faint stars in galaxies relatively close to the Milky Way.

Figures 2-3, 2-4, and 2-5 show spectra taken in each mode in the region of M8, a cluster of hot stars enveloped in a glowing cloud of gas and dust from which the stars may have been formed.

Character of the Widened Spectra

Figure 2-6 is a negative print of a typical star field in the southern constellation Carina and illustrates the information available in the widened spectra. A wavelength scale in angstrom units is shown above the star Alpha Carinae on the right. Several other stars are marked with their catalog number, visual magnitude, and spectral type.

In Alpha Carinae, the absorption lines of ionized carbon (C II) at 1335 Å and ionized silicon (Si IV) at 1394 and 1403 Å are visible; in Iota Carinae (upper right), a line caused by magnesium ions (Mg II) at 2800 Å and a cut-off caused by the blending together of several ionized iron (Fe II) lines at 2416 Å are seen.

These two stars illustrate how the relative amount of ultraviolet radiation depends on the surface temperature of the star. Although Iota Carinae (surface temperature

Figure 2-4.—Ultraviolet spectra of faint stars taken with the objective-prism spectrograph in the unwidened-spectrum mode.

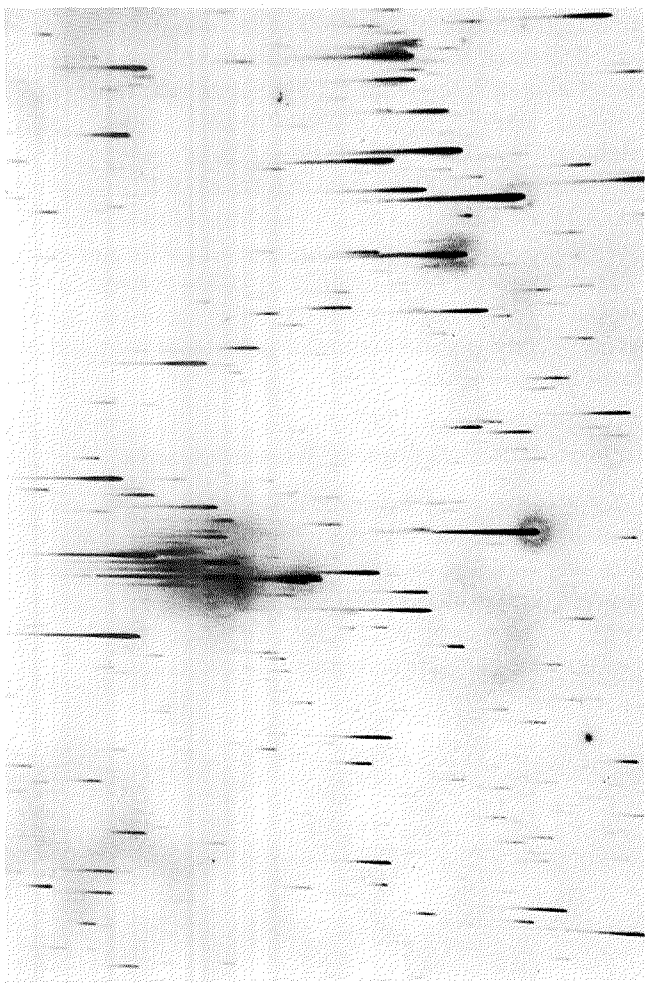

Figure 2-5.—Ultraviolet spectra obtained without a prism.

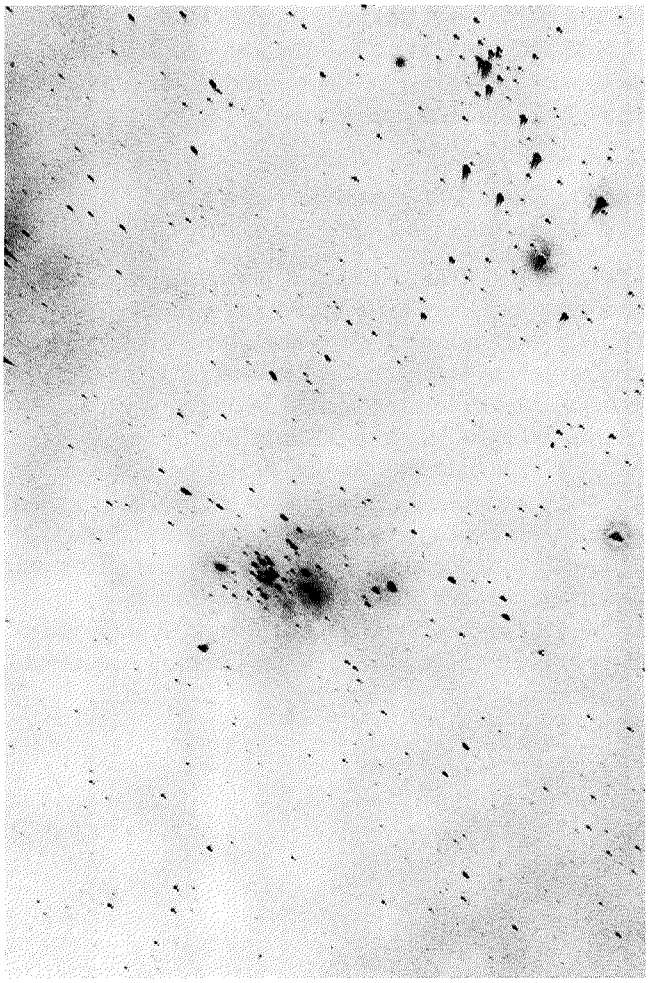

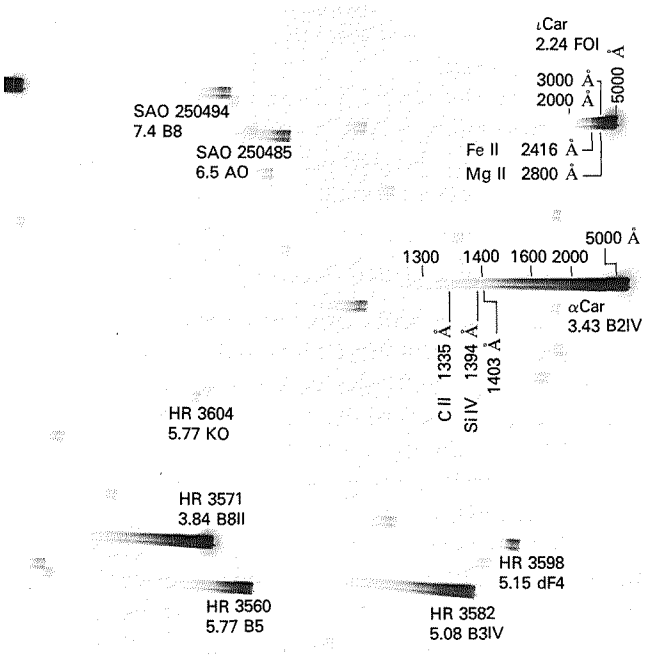

Figure 2-6.—Negative print of the widened ultraviolet spectra of a typical star field in the southern constellation Carina.

7000 K) is twice as bright as Alpha Carinae in visible light, its brightness diminishes rapidly between 3000 and 2000 Å, whereas Alpha Carinae (surface temperature 22 000 K), is still bright at 2000 Å and still measurable at 1300 Å. It is thus possible to gain a better knowledge of both the temperature and the absolute brightness of these stars by measuring the brightness distribution of their ultraviolet and visible spectra.

Peculiar Stars: The Ultraviolet Spectra of Wolf-Rayet Stars

Wolf-Rayet stars are stars whose outer layers have been stripped away by evolutionary processes and in which a very hot and disturbed core remains. Their spectra are very strong in the ultraviolet and show broad emission lines of ionized carbon, nitrogen, oxygen, and helium. Wolf-Rayet stars fall into one of two groups, WC and WN. For reasons not clearly understood, the WC stars show strong emissions of carbon and oxygen in their visible spectra but no nitrogen, whereas the WN stars show a strong emission of nitrogen and almost no carbon and oxygen.

Only two of these stars are bright enough in the ultraviolet to have been analyzed by the Orbiting Astronomical Observatory satellites. Skylab experiment S019 was able to obtain the ultraviolet spectra of 12 Wolf-Rayet stars. Figure 2-7 shows the spectra of six stars with strong carbon and oxygen emissions. The spectra of HD 156385, and possibly HD 165763 (the HD designation refers to the Henry Draper Catalog), show two lines (1718 and 1805 Å) that are best identified with nitrogen ions and may be the first unambiguous examples of the appearance of nitrogen in WC Wolf-Rayet stars.

The spectra of Gamma Velae and Theta Muscae are more like those of typical supergiant stars than like the emission-line-rich spectra of Wolf-Rayet stars. Both stars are known to have companions whose spectra are barely detectable at visible wavelengths. The ultraviolet spectrum of the companion star is stronger than that of the primary. The companion stars are thus even hotter than their primaries. Similar data for the WN stars show that three of the six have previously unknown companion stars. These discoveries give strong support to the concept that the observed characteristics of all Wolf-Rayet stars are partly attributable to effects of the companion stars.

Attenuation of Ultraviolet Light by Interstellar Dust

The plane of the Milky Way contains clouds of very minute particles known as interstellar dust. Starlight passing through these clouds is attenuated, with blue wavelengths being affected more than red. Thus starlight is "reddened" by the interstellar dust. The attenuation is greatest at about 2200 Å in the ultraviolet and then decreases somewhat at still shorter wavelengths. The effects of interstellar dust are shown in figure 2-8, in which star BS 6187 exhibits a pronounced dip in brightness at 2200 Å but slowly brightens again at wavelengths of 2000 to 1800 Å. BS 6188 is somewhat nearer to the Earth and shows very little of these absorption effects. (BS denotes Bright Star Catalog numbers.)

Since the effects of interstellar dust are greatest in the ultraviolet, ultraviolet spectra such as these should be useful in clarifying the nature of interstellar dust and its distribution in space.

Laboratory Rectification of Widened Spectra

Some of the recorded spectra were distorted by movement of Skylab during exposures. To compensate for this, the spectra were scanned with a computer-controlled microdensitometer in a series of very narrow strips. These measurements were then reassembled into a smoothed, geometrically rectified spectrum.

The rectification process is illustrated in figure 2-9. A print of the original spectrum is shown at the bottom of the picture; only two absorption lines are clearly evident. Trace 1 shows the rather noisy densitometer data from one 30-μm-wide strip. Trace 2 shows 20 such traces combined in their original positions along the wavelength scale. The noise is obviously reduced, but the wavelength resolution is degraded. Finally, trace 3 shows the result after adjustments ("wavelength shifts") have been made in each strip to obtain the best fit. The top portion of figure 2-9 is a "playback" of the rectified spectrum and shows a third line of moderate strength and several weaker features not seen in the original spectrum. However, care must be taken in interpreting such weaker lines since they may be remnants of photographic grain noise.

Broad Overview of the Ultraviolet Spectra of Hot Stars

An array of stars arranged vertically by spectral class (i.e., temperature) and horizontally by luminosity is shown in figure 2-10. The spectra have been rectified by the computer-controlled microdensitometer process described above.

Figure 2-7.—Far-ultraviolet spectra of WC Wolf-Rayet stars.

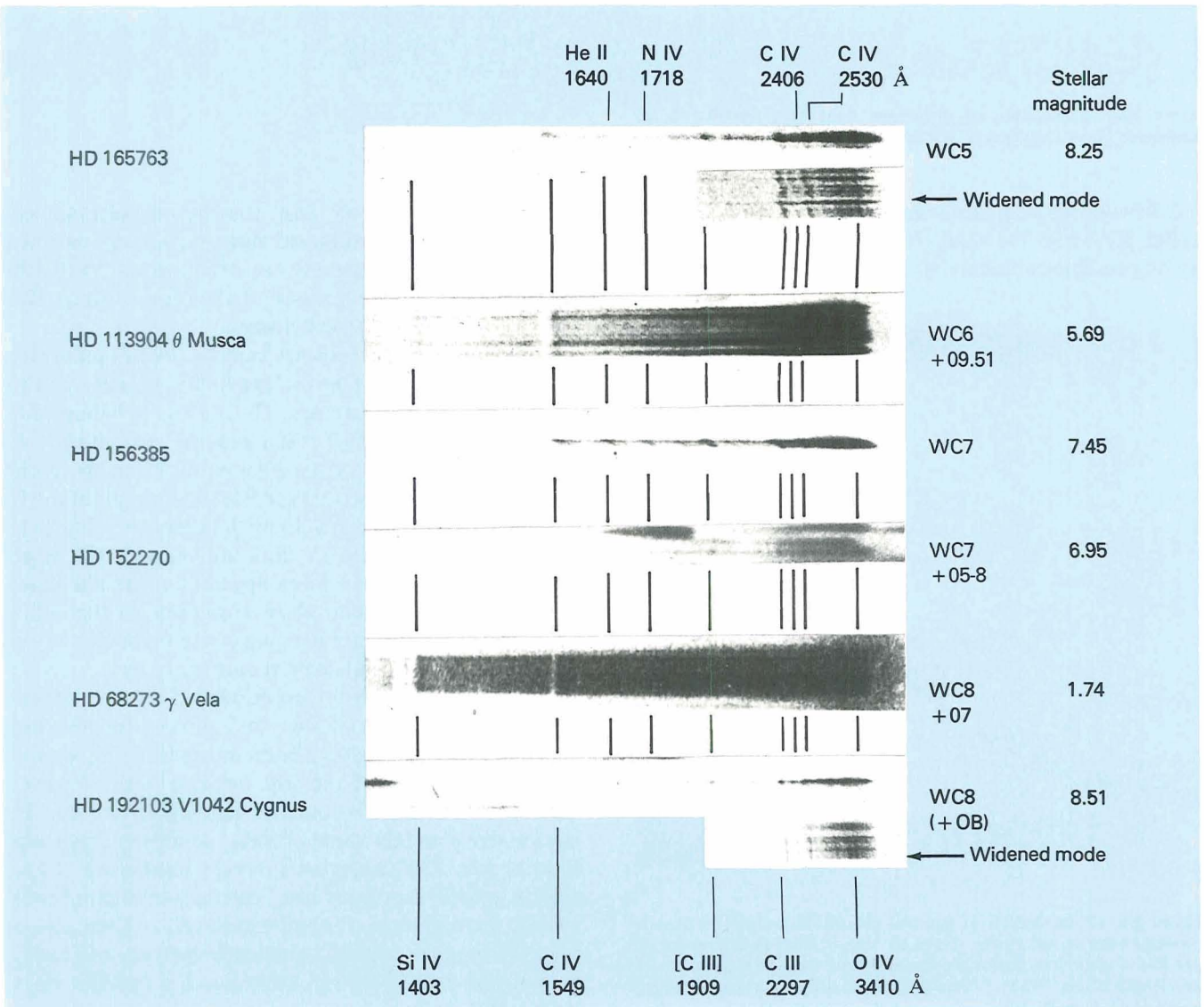

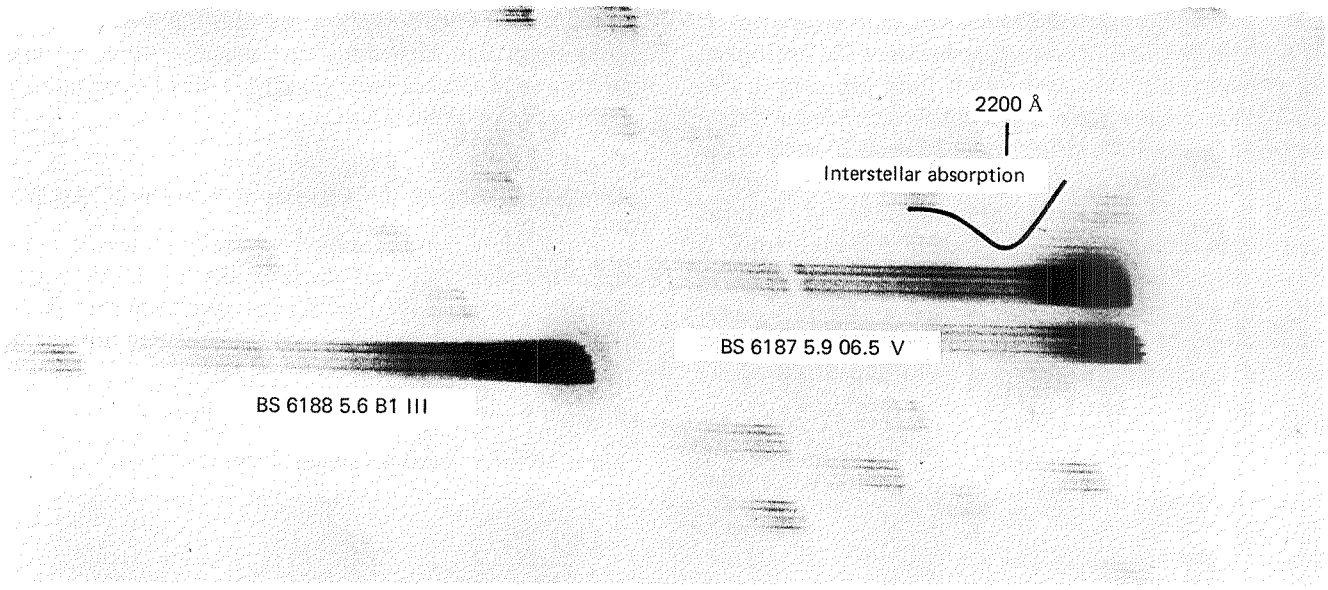

Figure 2-8.—Attenuation of ultraviolet light by interstellar dust, manifested in the spectrum of star BS 6187.

A B5 star has a surface temperature of approximately 16 000 K, while O7 stars have surface temperatures ranging to approximately 40 000 K. Luminosity class V stars are those, like the Sun, that lie on the main sequence of the color luminosity diagram. Class I stars are large-diameter supergiants with brightnesses 50 to 100 times greater (mainly because of their larger size). The class II and III giants lie between.

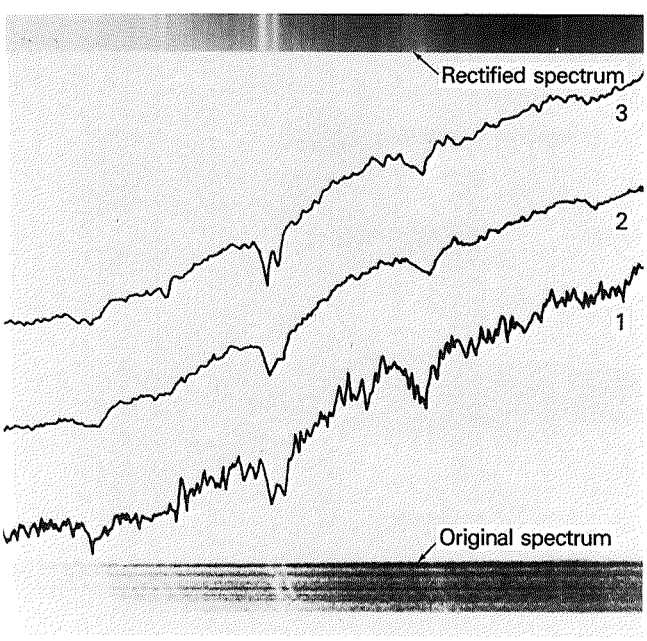

Figure 2-9.—Rectification of spectral distortions caused by Skylab movement during exposures. Trace 1: "noisy" densitometer trace of one 30-μm-wide strip. Trace 2: combined trace from 20 strips without wavelength shifts. Trace 3: combined trace after appropriate wavelength shifts in each strip.

Some interesting trends are evident. In all luminosity classes, the C IV line grows gradually stronger as the stellar temperature increases. The Si IV lines behave differently in class V and I stars, peaking very sharply at B1 in class V stars but remaining strong from B1 to O6 in class I stars. At spectral type B1, the strength of the C IV line increases dramatically with luminosity. Furthermore, the C IV and Si IV lines are wider in the more luminous stars, and emission appears on the red edge. The emission and broad absorption indicate that stars of higher luminosity are ejecting matter at such a rapid rate that it must affect their evolutionary cycle.

The Skylab data from experiment S019 and others covered a wide range of stars and showed for the first time that the rate of gas ejection depends mainly on the intrinsic brightness of the star summed over all wavelengths (the so-called bolometric magnitude) and that all stars above a certain value of total radiated energy seem to eject gas. The supergiants, whose luminosity is due chiefly to their enormous sizes, can eject matter at lower surface temperatures. (The surface layers of these giants are far from their centers, and hence the force of gravity is relatively weak.) On the other hand, a smaller, class V star must be much hotter before mass ejection begins.

The S201 Far-Ultraviolet Electrographic Camera

The S201 far-ultraviolet electrographic camera was sent aloft on the last Skylab manned mission, primarily to observe Comet Kohoutek. This camera was designed to take pictures in the far ultraviolet, including the region of the very strong Lyman-alpha line of hydrogen at 1216 Å. It was used during the Apollo 16 mission for both stellar and extragalactic photography from the Moon as well as for photographing the ultraviolet emissions of the Earth's upper atmosphere. The principal investigator for the Skylab experiment was Thornton Page, of the U.S. Naval Research Laboratory in Washington, D.C.

The electrographic camera was designed by George Carruthers, of the U.S. Naval Research Laboratory, to produce extremely sensitive photographs in ultraviolet wavelengths. It combines the light-gathering power of a telescope, the sensitivity of a photomultiplier tube, and the cumulative recording feature of film. It is therefore able to obtain wide-field pictures containing far-ultraviolet images of dim stellar sources.

Figure 2-11 is a schematic diagram of the camera. The incoming ultraviolet radiation passes through a corrector plate, which also serves as a filter. Either of two different wavelength regions can be photographed, depending on which corrector plate is used. A lithium fluoride plate permits radiation of wavelength longer than 1050 Å to pass; a calcium fluoride plate narrows the wavelength region to wavelengths longer than 1230 Å, thus excluding the Lyman-alpha radiation of hydrogen. The light is then reflected from a concave

Figure 2-10.—Ultraviolet spectra of hot stars arranged by spectral type and luminosity class.

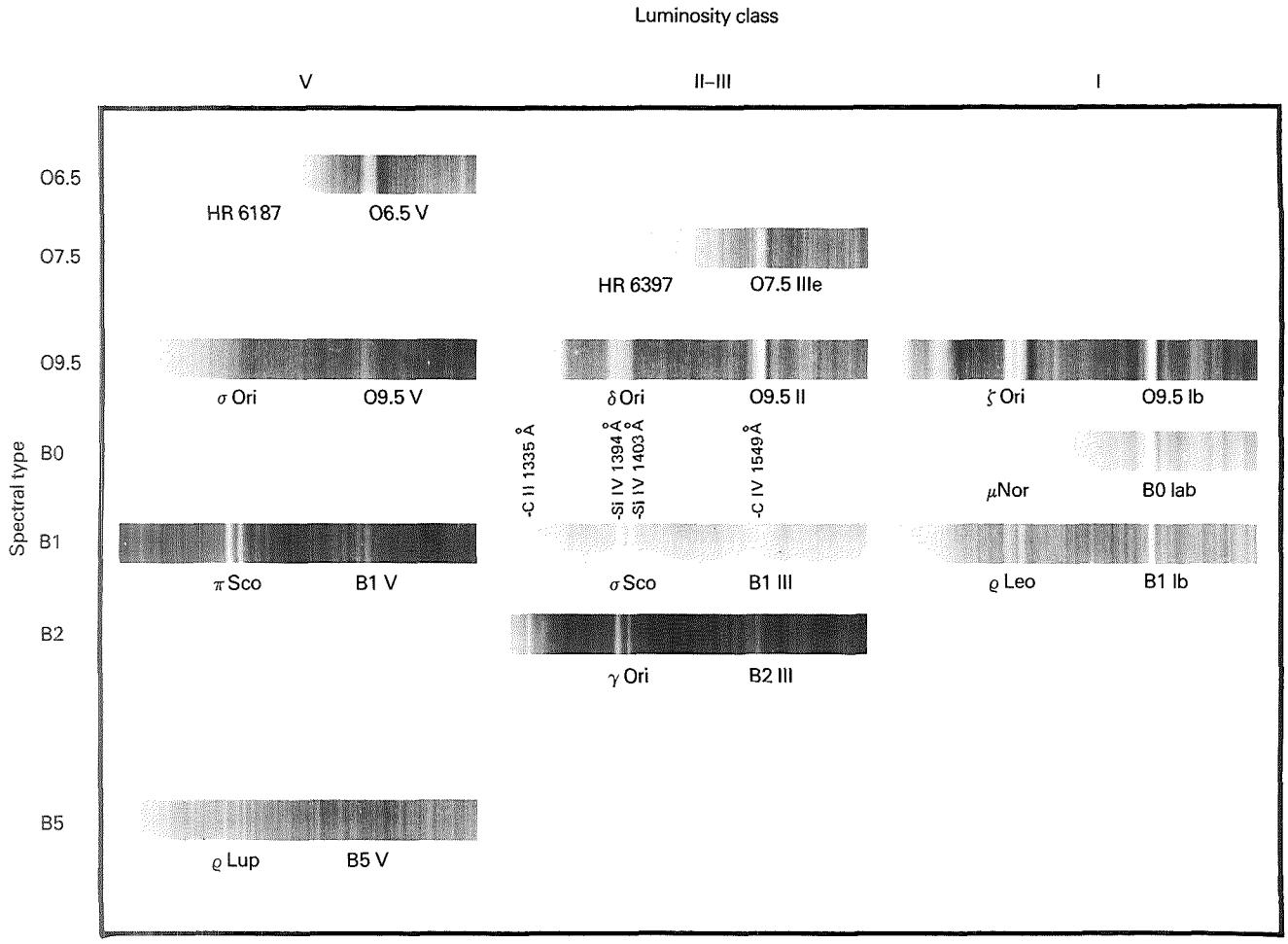

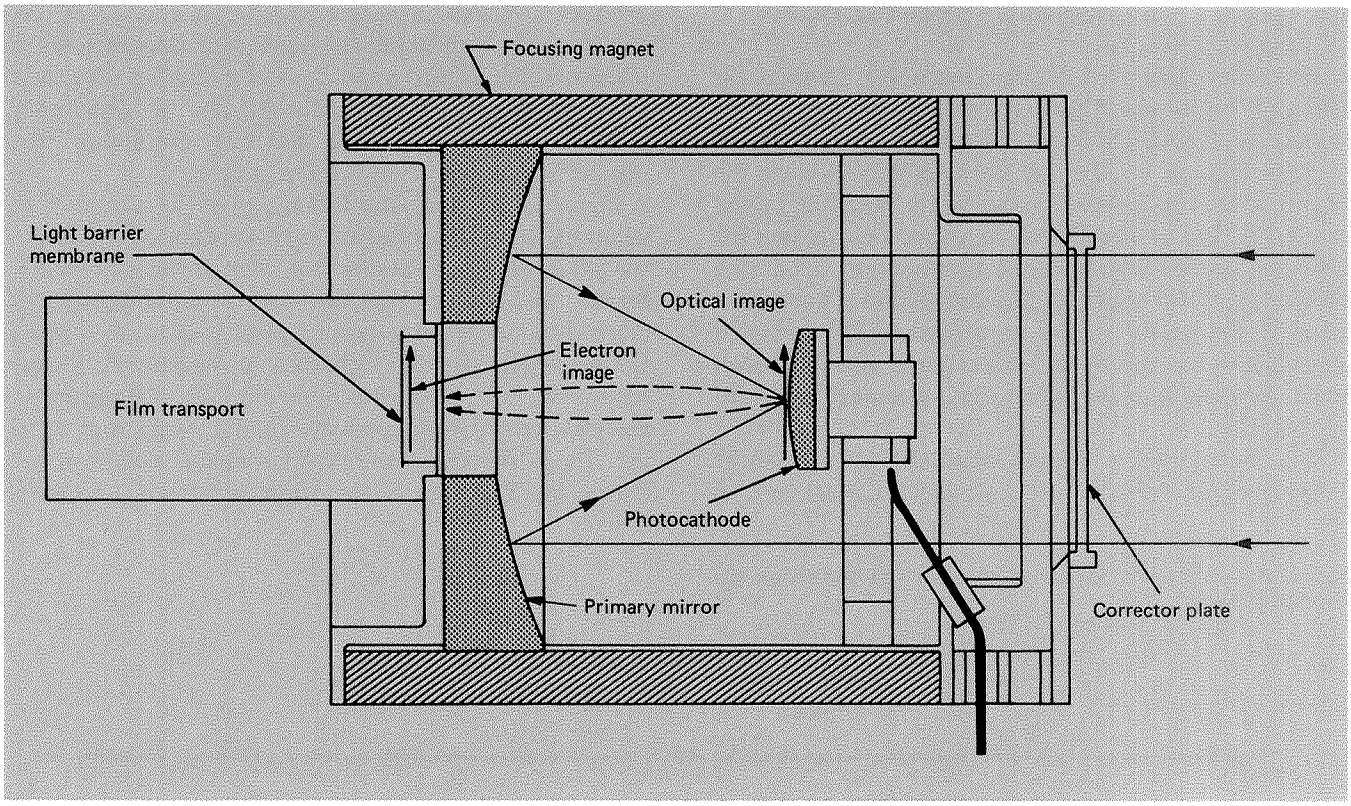

Figure 2-11.—Schematic diagram of the S201 far-ultraviolet electrographic camera.

mirror to form an optical image on a photocathode, a thin layer of potassium bromide that emits electrons from points at which star images are focused. Potassium bromide responds only to light of wavelengths shorter than 1600 Å. The net result is operation at one of two wavelength bands, 1050 to 1600 Å or 1230 to 1600 Å.

These electrons are accelerated away from the photocathode by a 25 000-V negative potential on it and are focused onto an electron-sensitive film by a 300-gauss magnetic field. This film thus records an electron image that is proportional in brightness to the photon image focused on the photocathode. A very thin aluminum barrier membrane keeps visible and ultraviolet light from reaching the film but is easily penetrated by the electrons. In summary, the camera has two unique advantages: densities in the developed film may be accurately related to the far-ultraviolet brightness of objects photographed, and it is "blind" to ordinary visible light and ultraviolet light of wavelengths longer than 1600 Å. The camera does have two operating constraints: the photocathode cannot be exposed to humid air, and exposures can be made only in a hard vacuum. Skylab's airlock enabled these conditions to be fulfilled.

Electrographic Data

One of the pictures returned from the electrographic camera aboard Skylab was of the Gum Nebula, a supernova remnant. It is shown in a 107-sec exposure (fig. 2-12) that illustrates the far-ultraviolet radiation of the hot blue stars in that region. A hazy glow fills the entire frame. Accurate measurements can reveal what portion of this background glow comes from gases in the Gum Nebula by comparison of this photograph with those of adjacent regions.

The star images on all the photographs were measured for far-ultraviolet brightness and "color" (difference in brightness between photographs taken with the two filters). Star positions allowed identification with those in catalogs of stars, nebulae, and galaxies photographed by Earth-based telescopes. Preliminary results showed that about 90 percent of the stars photographed were hot, blue stars in the Smithsonian Catalog. A few

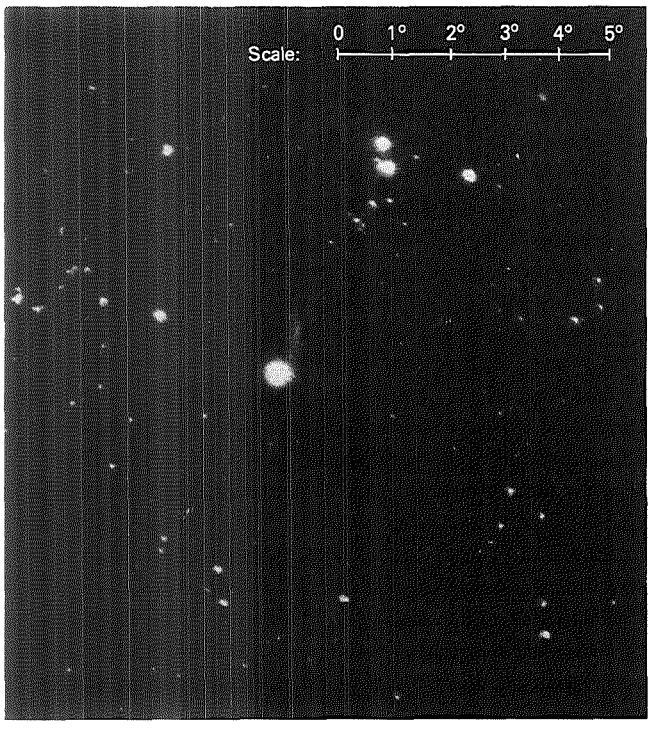

Figure 2-12.—Gum Nebula photographed by the S201 electrographic camera (107-sec exposure, 1250- to 1600-Å band).

others were nebulae and galaxies, but 5 or 10 percent were unknown objects—possibly faint stars of extremely high temperature or small gas clouds with strong far-ultraviolet emission lines.

Analysis Techniques

Quantitative variations in brightness can be emphasized by drawing isophote contours, lines that connect points of equal brightness. For example, figure 2-13 shows the Small Magellanic Cloud, a galaxy first observed by Magellan in his voyage in 1519. Four or five clouds of stars and gas in this galaxy can be compared with visible-wavelength data from ground-based photographs, allowing an estimate of the density distribution of interstellar gas in various regions of this small galaxy, which is quite near the Milky Way.

To make the isophote plot (fig. 2-14), a negative of the print (fig. 2-13) was scanned with a microdensitometer that measured film density at points only 2.5 μm apart. These millions of measurements were recorded on magnetic tape and then fed to a computer for connecting points of equal density or brightness. This chart was then compared with a similar one of the Large Magellanic Cloud, photographed during the Apollo 16 mission. Similarities and differences between these two nearest galaxies (about 100 000 to 150 000 light-years away) could thus be established.

Pleiades

Pictures of the Pleiades, better known as the Seven Sisters, show evidence of dust nebulosity around the brighter stars. The glow so produced is also evident in ground-based photographs. Figure 2-15 is an isophote plot made from a 15-sec exposure of the Pleiades taken

Figure 2-13.—Far-ultraviolet photograph (107-sec exposure) of the Small Magellanic Cloud.

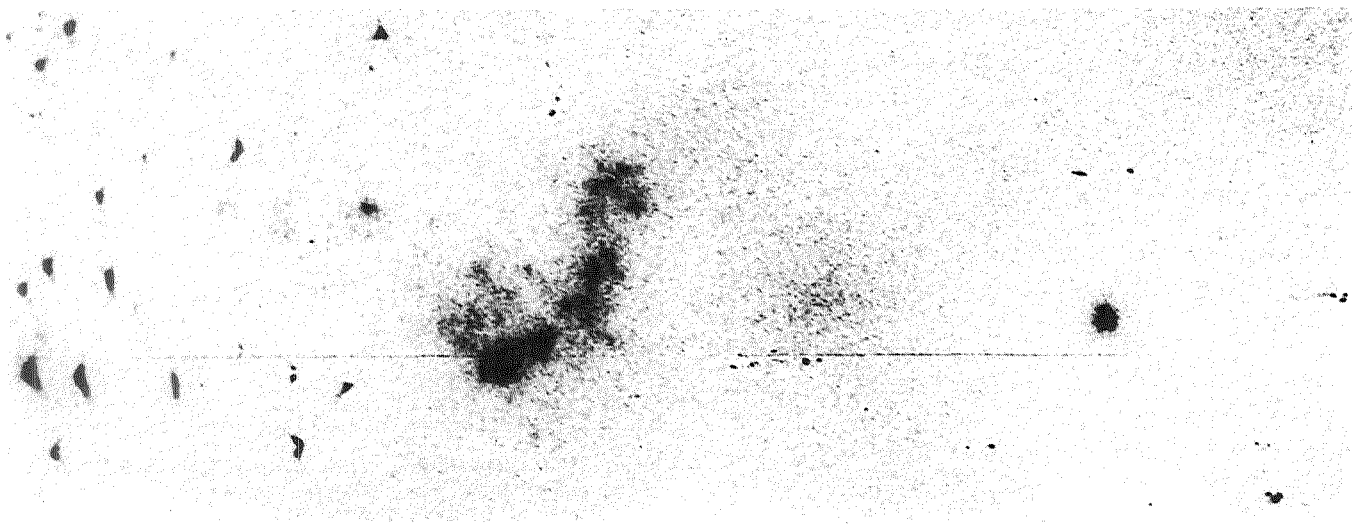

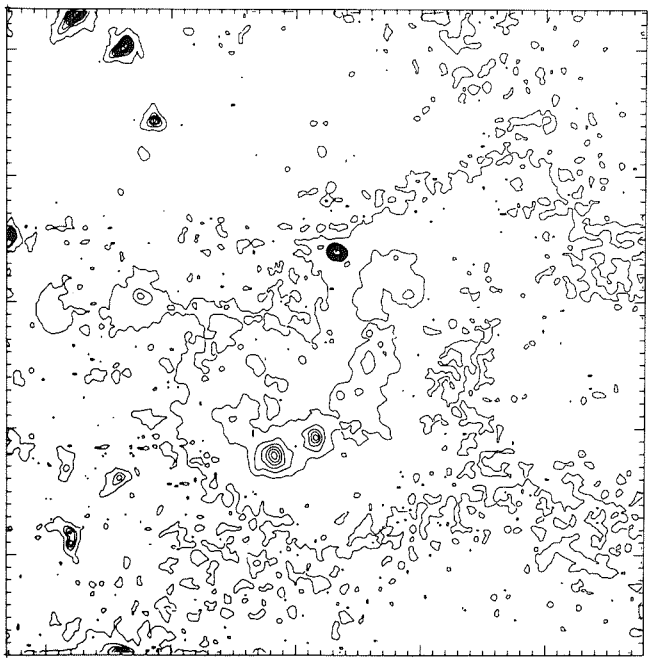

Figure 2-14.—Isophote plot of the Small Magellanic Cloud, constructed from the photograph shown in figure 2-13.

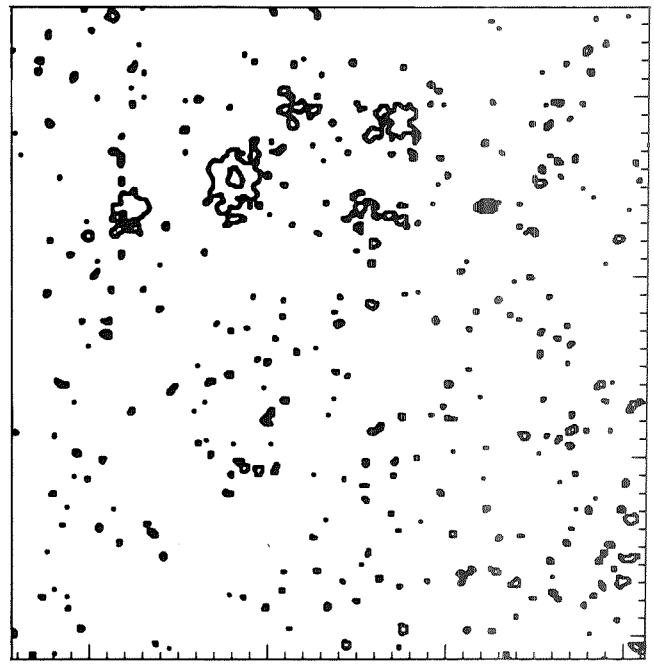

Figure 2-15.—Isophote plot of the Pleiades, constructed from a photograph taken by the electrographic camera with a lithium fluoride filter (15-sec exposure, 1050- to 1600-Å band).

with the electrographic camera, through the lithium fluoride filter. With that filter, the camera recorded wavelengths from 1050 to 1600 Å. Figure 2-16 shows the isophote plot of a 30-sec exposure through the calcium fluoride filter, which limited sensitivity to wavelengths from 1230 to 1600 Å. Differences between these two illustrations result from radiation in the interval 1050 to 1230 Å.

The S183 Ultraviolet Panorama Experiment

The S183 ultraviolet panorama experiment was conceived by Georges Courtes and his colleagues at the Laboratoire d'Astronomie Spatiale in Marseilles, France. It was based on previous experiments with sounding rockets. The objective was to obtain ultraviolet intensities, at three wavelengths, of hot stars, clusters of stars, large stellar clouds in the Milky Way, and nuclei of other galaxies. Data in two wavelength regions centered on 1878 and 2970 Å were recorded with high accuracy on glass plates by a photographic photometer. Data for the band centered on 2574 Å were recorded by direct, wide-field imaging with a 16-mm camera also used in Skylab for other experiments. The camera viewed the same area of the celestial sphere (with a slight offset) as the photometer. The two instru-

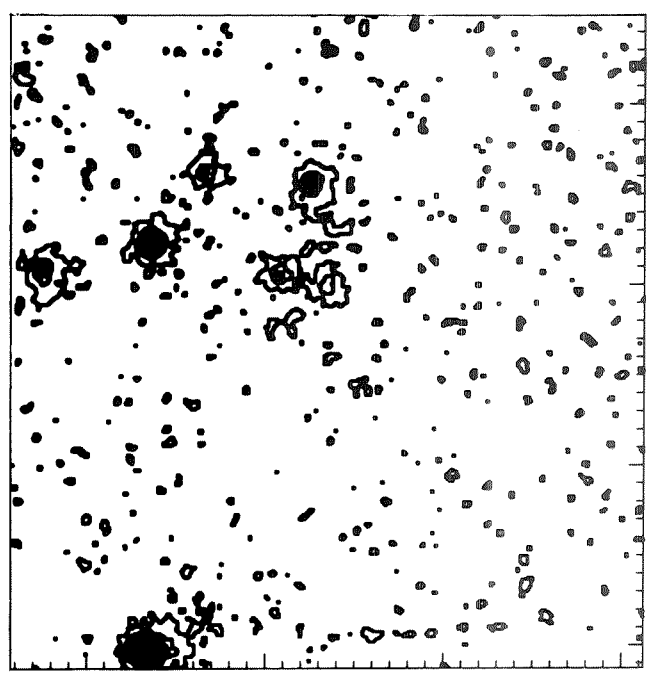

Figure 2-16.—Isophote plot of the Pleiades, constructed from a photograph taken with the electrographic camera with a calcium fluoride filter (30-sec exposure, 1230- to 1600-Å band).

ments were mounted in the same housing, shown in figure 2-17 in place at the airlock.

Photometer Design

The two-wavelength photometer employed a sophisticated optical design shown schematically in figure 2-18. The articulated mirror system common to several experiments and shown previously in figure 1-7 directs light from the selected 7° by 9° sky area into the photometer. This beam is focused onto a grating to achieve spectral dispersion, and the two spectral ranges (centered on 1878 and 2970 Å) are isolated by appropriately placed diaphragms. Immediately in front of the photographic plate, an array of cylindrical lenses made of magnesium fluoride form the light from a star into an

Figure 2-17.—Instrumentation for the S183 ultraviolet panorama experiment.

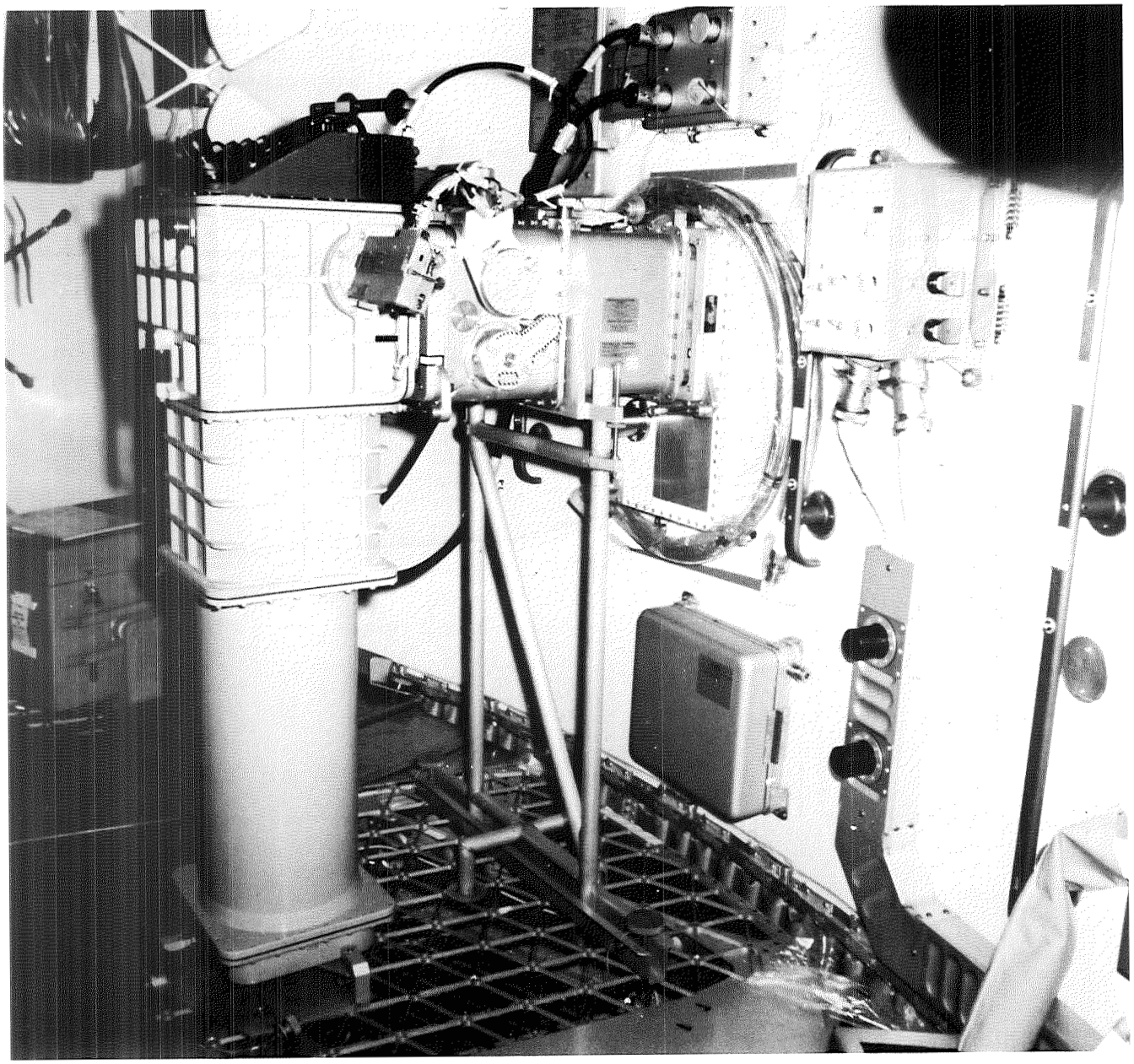

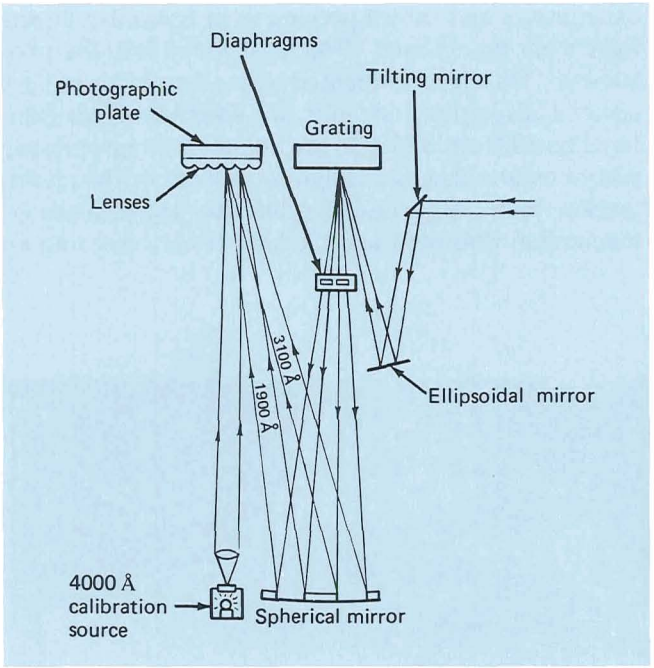

elongated rectangular image for each wavelength. The light from a calibration source is formed into a similar rectangular image on the photographic plate.

These spread-out, rectangular images are useful for accurate comparisons of the relative brightness of stars or other objects in the specified ultraviolet spectral ranges. Such images do not suffer from problems of photographic overexposure, such as may occur in the center of a tightly focused image of a star.

Schmidt-Cassegrain Camera System

The instrument for sky photographs in the 2574-Å region used a small Schmidt-Cassegrain telescope and a standard 16-mm data acquisition camera to record the

Figure 2-18.—Optical train of the S183 ultraviolet panorama experiment.

Figure 2-19.—Ultraviolet spectra recorded by the two-wavelength photometer in the S183 ultraviolet panorama experiment and corresponding microdensitometer traces. The spectral types and visual magnitudes of the stars are indicated above the tracings.

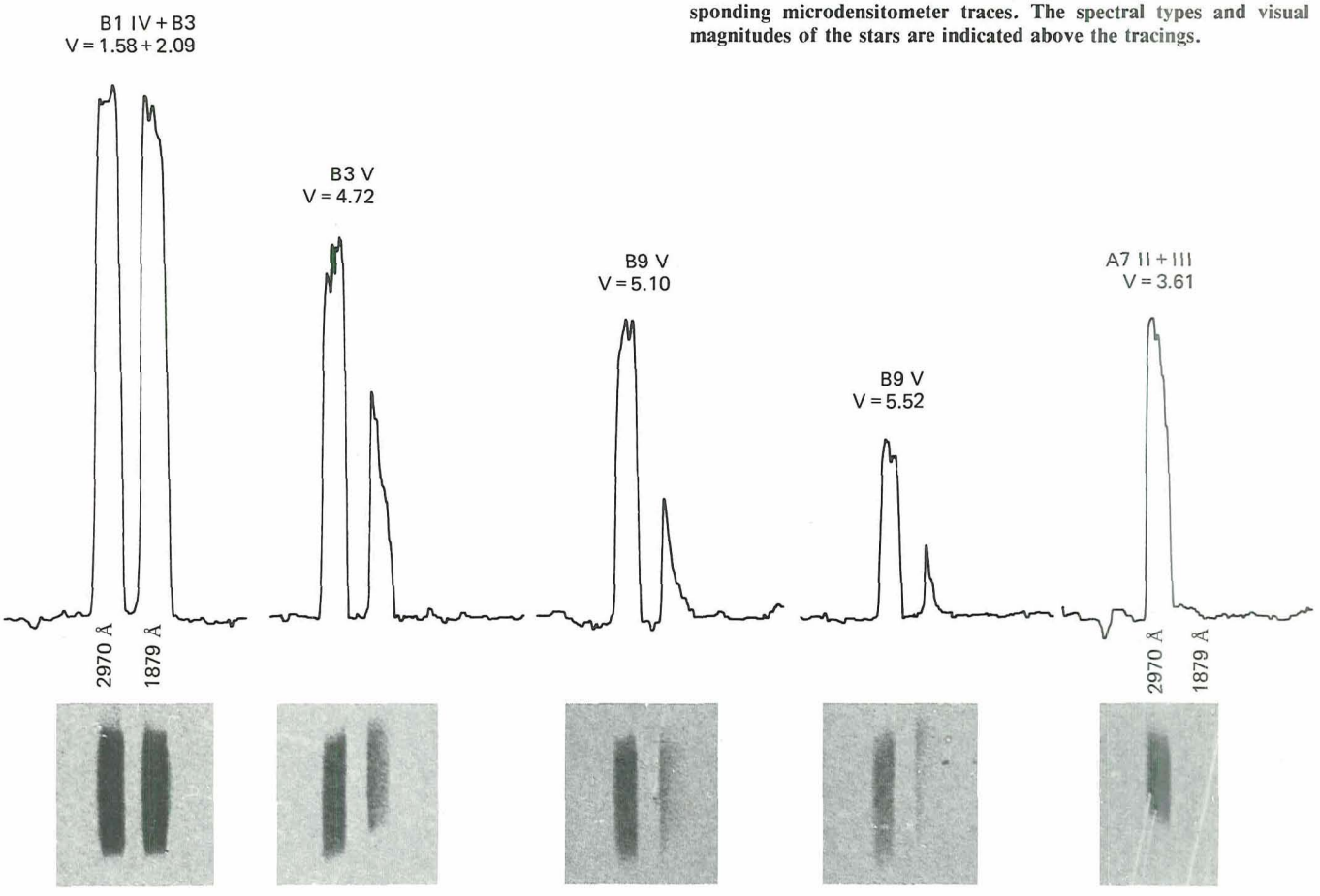

sources in a 5° by 7° field of view. The desired wavelength selectivity was obtained by multilayer interference coatings deposited on the two mirror surfaces of the telescope. The ultraviolet region used here lies between the wavelengths recorded by the two-wavelength photometer. Detailed structure of extended sources in the ultraviolet could be recorded by this camera system but this was sacrificed to gain accuracy in the photometer. The two instruments in the S183 experiment were thus complementary in the data they generated.

Photometer Results

An exposure (fig. 2-19) made during the first Skylab mission shows nearly rectangular images for brighter stars. For dimmer stars, the images are less well formed. Also shown in this figure are the corresponding photographic density traces. For each star, the bands centered around 1878 and 2970 Å are on the right and left, respectively. The spectral types and visual magnitudes of the stars are given above the tracings. The far-left example is the unresolved superposition of a pair of stars. The expected decrease in ultraviolet intensity for stars of increasing visual magnitude is apparent (in going from a first magnitude to a sixth magnitude star the intensity decreases by a factor of 100, or approximately 2.512 per step). The intensity plots show the relative weakening of the far-ultraviolet (1878-Å) band from the hottest star on the left to the coolest star on the right.

Camera Results

The Schmidt-Cassegrain camera system obtained ultraviolet pictures of 36 star fields. A typical observation target, the Pleiades (fig. 2-20), was photographed in a 21-min exposure. It is an example of a group of some 300 young, hot stars (not all seen here) formed about 60 million years ago. The stars are embedded in nebulous matter, which produces the haze seen around the bright stars. This haze is seen in the ground-based,

Figure 2-20.—Ultraviolet photograph of the Pleiades taken with the Schmidt-Cassegrain camera system (21-min exposure).

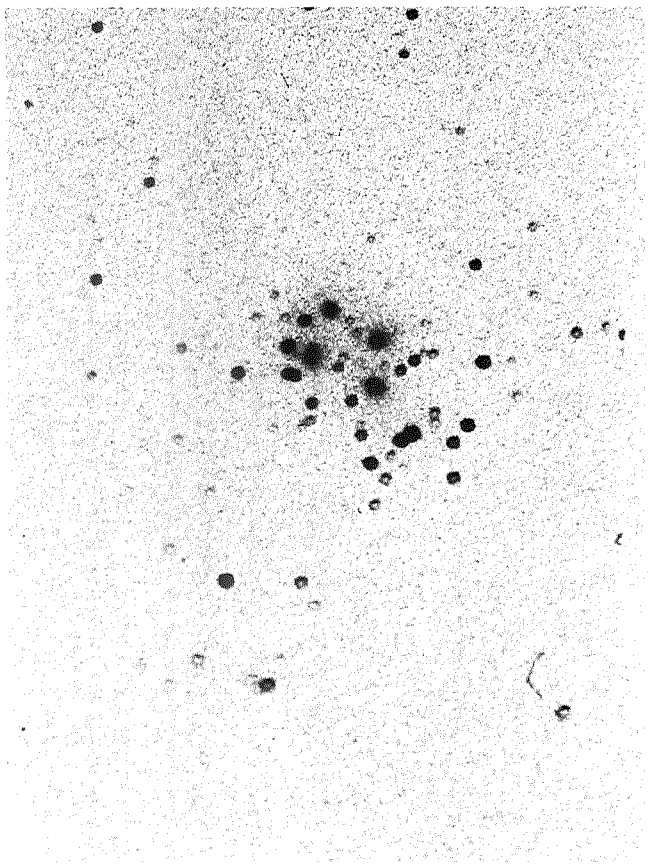

Figure 2-21.—Star field and nebula around Eta Carinae (21-min exposure).

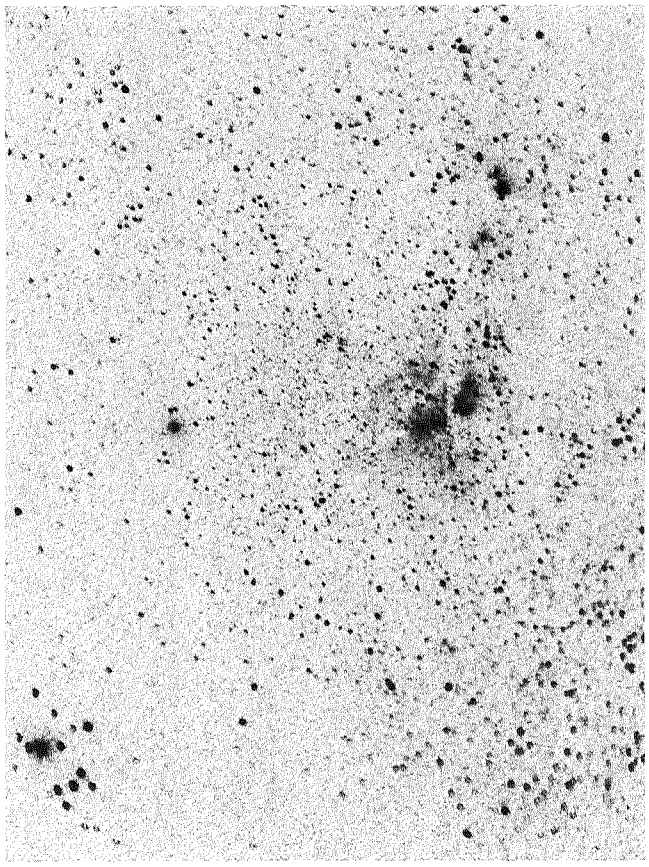

Figure 2-22.—Color isophote plot of the star field and nebula around Eta Carinae, constructed from the ultraviolet photograph shown in figure 2-21.

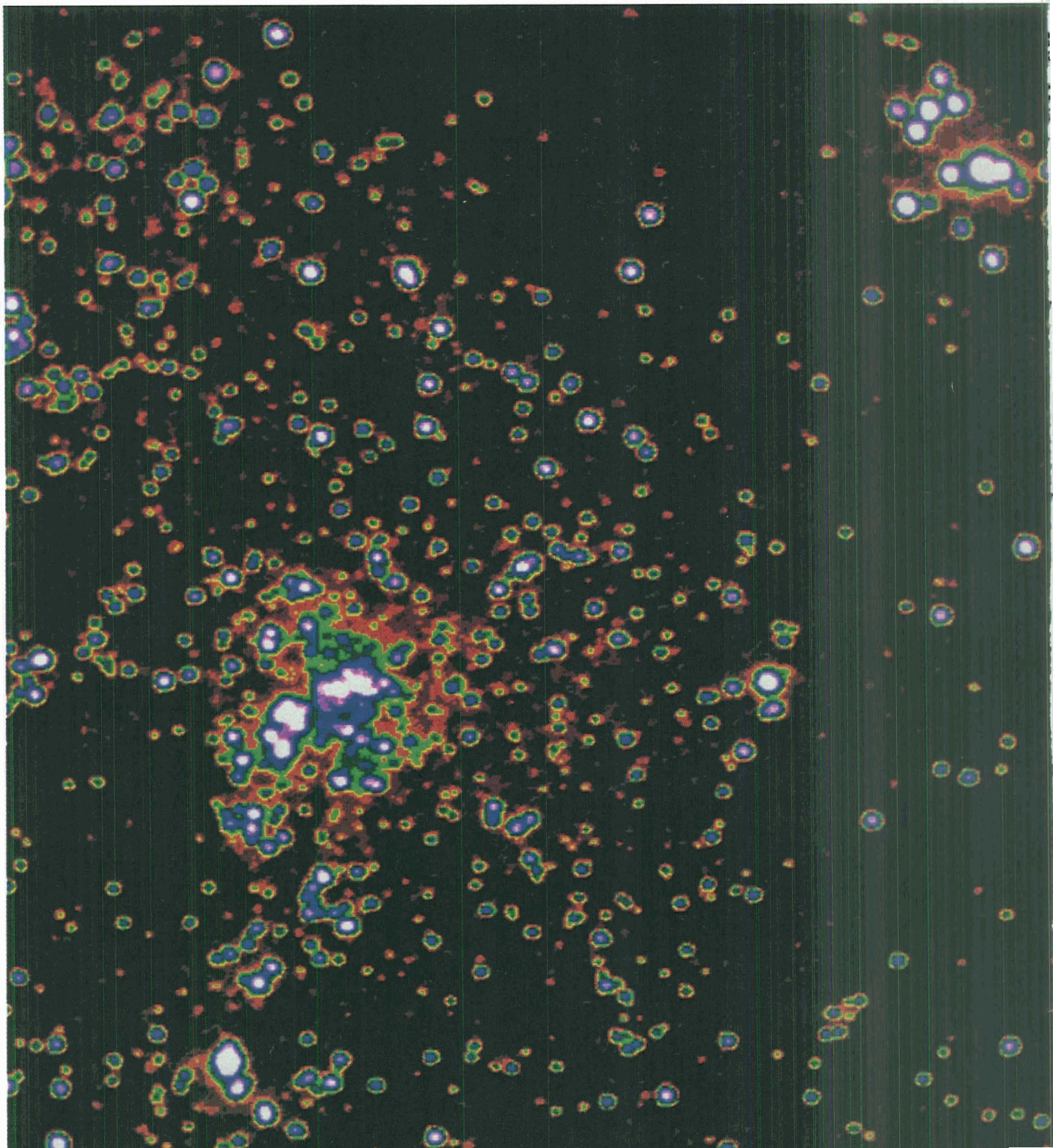

blue-light photographs as well as in the 2574-Å image obtained with the Schmidt-Cassegrain camera system. The fainter stars appear doughnut-shaped because of a slight misalignment of the optics in the 16-mm camera.

Ultraviolet Intensity Variations Emphasized by Color Isophotes

A useful and aesthetically pleasing series of photographs resulted from the S185 experiment. They were processed at the Marshall Space Flight Center's Image Data Processing Facility. The derived intensity differences are reproduced in several colors to emphasize temperature variations. The hotter and brighter stars and regions appear white, whereas the decreasing intensity of ultraviolet radiation is shown by the other colors.

An example is shown in figures 2-21 and 2-22. Figure 2-21 is a 21-min ultraviolet exposure of the stars and the nebula in the neighborhood of the star Eta Carinae; figure 2-22 is the isophote plot derived from it. The isophote plots dramatically emphasize the decreasing intensity of reflected ultraviolet light in the nebula outward from the hot stars shown in white.

These isophote plots are very useful in observing features and trends, which can then be studied more quantitatively by microdensitometry of the original negatives.

A Galaxy as Viewed by All Three Ultraviolet Instruments

The millions of galaxies known in the cosmos are classified into four basic forms: elliptical, spiral, barred spiral, and irregular. The Large Magellanic Cloud, one of a pair of galaxies that are relatively close companions of the Milky Way, is an irregular galaxy with some structural features suggestive of a barred spiral. It is evident that star formation is still taking place in this galaxy, for it is studded with numerous knots of hot, young stars. "Hot" stars are always equated with "young" stars because their energy is radiated so rapidly that it is exhausted within a few tens of millions of years. On the other hand, the cooler stars, like the Sun, radiate their energy slowly and may exist for billions of years.

Figures 2-23 through 2-26 show the value of ultraviolet observations in locating regions where stars are being formed, defining the extent of these regions, and showing their relationship to the overall structure of the galaxy. The first photograph (fig. 2-23) is a red-light picture taken from the Earth at the University of Michigan observatory by Karl G. Henize. The cool, red stars are emphasized more than the hot, blue, or ultraviolet stars. The dominant feature is a long central "bar" that consists mainly of faint yellow or red stars. Also conspicuous are several bright nebulosities that are clouds of hydrogen caused to glow in the red by ultraviolet light from hot stars embedded within them. Thus the nebulosities give some indication of the location of the hot stars. On comparing this photograph with figure 2-24, which is a far-ultraviolet photograph taken from the surface of the Moon with the electrographic camera (Apollo 16 mission), it is interesting to note that every nebulous patch in figure 2-23 has a corresponding far-ultraviolet patch in figure 2-24. However, not every far-ultraviolet patch in figure 2-24 is conspicuous in figure 2-23. For example, region A is the most prominent feature of figure 2-24 but is barely visible in figure 2-23. This indicates a lack of gas in region A and suggests that the gas and dust have been depleted and that star formation may be ended within this region. On the other hand, the 30 Doradus nebulosity, the most prominent feature in figure 2-23 other than the "bar," is rather weak in the far ultraviolet, which indicates the presence of a great mass of gas and dust from which only few stars have been formed so far. This region, therefore, is probably the youngest and most active of those in which stars are formed.

Figure 2-25 is an ultraviolet photograph taken in the S019 ultraviolet stellar astronomy experiment (no-prism mode, effective wavelength of about 2500 Å). The ultraviolet photograph in figure 2-26 was taken with the 16-mm camera of the S183 ultraviolet panorama experiment (effective wavelength 2574 Å); it shows an interesting transition between figure 2-23 (effective wavelength 6500 Å) and figure 2-24 (effective wavelength 1400 Å). For example, in figure 2-24, region B is slightly brighter than the complex around 30 Doradus, whereas it is slightly fainter in figures 2-25 and 2-26. This indicates that Region B has more hot, new-born stars than the complex around 30 Doradus, an observation that is not at all evident in photographs taken from the Earth.

Another interesting aspect of figure 2-24 is that the overall structure of the Large Magellanic Cloud differs considerably from that shown in figure 2-23. The ground-based photograph shows a 'bar" from which rudimentary spiral arms may trail. The far-ultraviolet picture suggsts that the dynamic center of the galaxy lies in region A and that one of its major arms spirals outward in a clockwise direction and splits into two arms near region C. Thus the ultraviolet morphology presents a totally new concept of the basic structure of the galaxy.

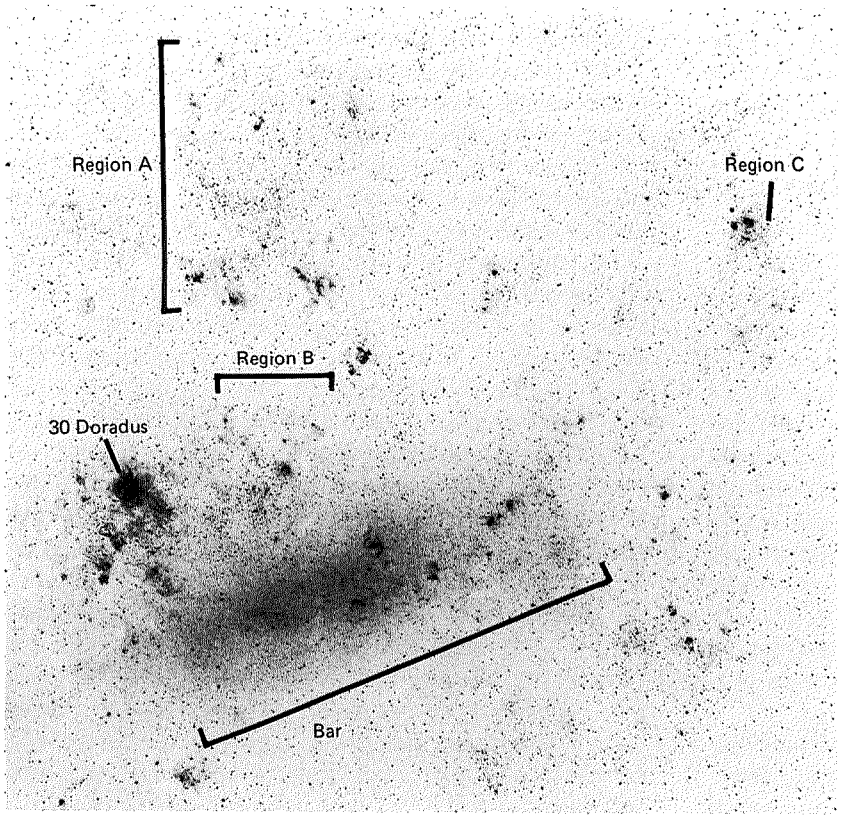

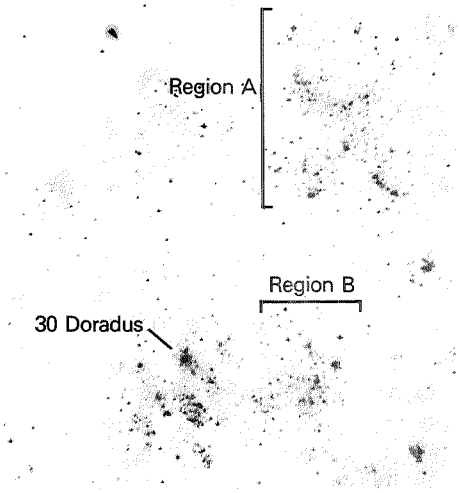

Figure 2-23.(top left)—Large Magellanic Cloud: red-light photograph (effective wavelength 6500 Å) taken from the Earth.

Figure 2-24.(bottom left)—Large Magellanic Cloud: far-ultraviolet photograph (effective wavelength 1400 Å) taken from the surface of the Moon with the electrographic camera (Apollo 16 mission).

Figure 2-25.(top right)—Large Magellanic Cloud: ultraviolet photograph taken during Skylab's S019 stellar astronomy experiment (no-prism mode, effective wavelength ~2500 Å).

Figure 2-26.(bottom right)—Large Magellanic Cloud: ultraviolet photograph (effective wavelength 2574 Å) taken by the 16 mm Schmidt-Cassegrain camera system during Skylab's S183 ultraviolet panorama experiment.

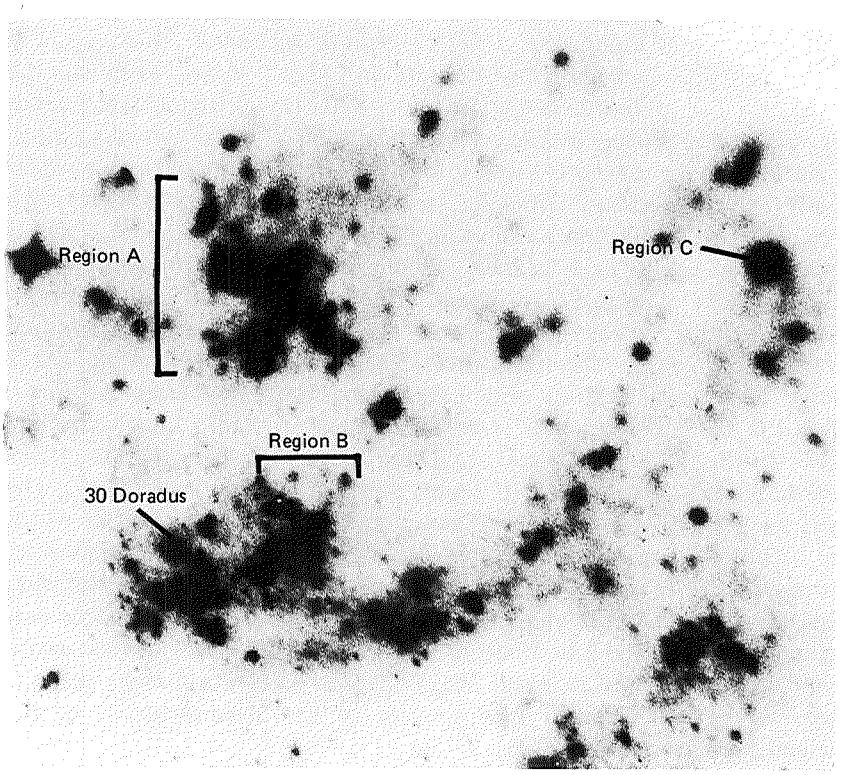

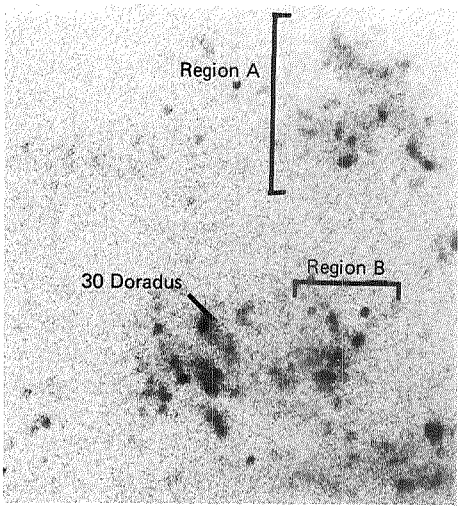

GALACTIC X-RAY EMISSIONS

X-Rays from Beyond the Sun

Nothing was known about the appearance of the sky in the soft-X-ray portion of the electromagnetic spectrum, at wavelengths of 1 to 100 Å, before NASA began experiments with equipment mounted in sounding rockets. These wavelengths are absorbed in the uppermost regions of the Earth's atmosphere, which even the most advanced research balloons cannot reach.

By 1962, X-rays from the Sun, which are produced in the solar corona and in flares, had been discovered and mapped in some detail. Astronomers concluded that, if other stars emitted X-rays at the same rate as the Sun, there was little hope of discovering any other sources of X-rays in the galaxy, the nearest star being over 250 000 times more distant than the Sun. It was therefore a major astronomical surprise when strong sources of X-rays were found, many at locations in the sky where only a distant, barely visible star, or no star at all, was known to exist.

Well over a hundred celestial objects emitting X-rays had been identified by 1973. One of the surprising results was the diverse nature of the discoveries. Sources of X-rays have been found both in and outside the Milky Way. Some of them are compact, almost point sources; others extend over large regions of the sky. More intriguing is the finding that some of them vary irregularly; some are pulsars and emit short pulses of X-rays on a regular schedule.

Moreover, a perplexing background glow of X-rays was found, coming almost uniformly from all directions. At the longest X-ray wavelengths observed (40 to 100 Å), this background glow, when integrated over the whole sky, amounts to more power reaching the Earth than from the brightest point source, Scorpius X-1. Even though sounding-rocket experiments continued until after Skylab, this diffuse glow has refused to admit resolution into individual starlike sources.

Skylab's Galactic X-Ray Mapping Experiment

The S150 galactic soft X-ray experiment was designed by William Kraushaar, Alan Bunner, and their colleagues at the University of Wisconsin for the difficult 40- to 100-Å band. An important objective was to extend the search for the origin of galactic X-rays beyond the sensitivity possible with short flights of small research rockets, by placing a large-area soft-X-ray detector in orbit to collect data for a much longer time.

Unlike the "hard" X-rays used by hospitals and industry to penetrate deep into materials, the "soft" X-rays are completely absorbed by even a very thin layer of the Earth's atmosphere. Even the tenuous neutral gas in interstellar space absorbs these soft X-rays. The S150 experiment had a plastic film entrance window 2 μm thick, yet still tough enough to hold back the gas pressure of the argon-methane mixture in the proportional counter. A sophisticated pressure regulator kept this gas mixture at constant density, in spite of a continual, slow leakage of gas through the thin window until eventually an inevitable direct exposure to the burning rays of the Sun melted the membrane.

The S150 X-Ray Instrument

The S150 instrument, shown in figure 2-27, was a single large proportional counter 1500 cm^2 in collecting area, electrically divided by fine wire ground planes into separate signal-collecting areas, and looking between collimating vanes (these vanes are the bronze-colored

Figure 2-27.—The S150 X-ray instrument.

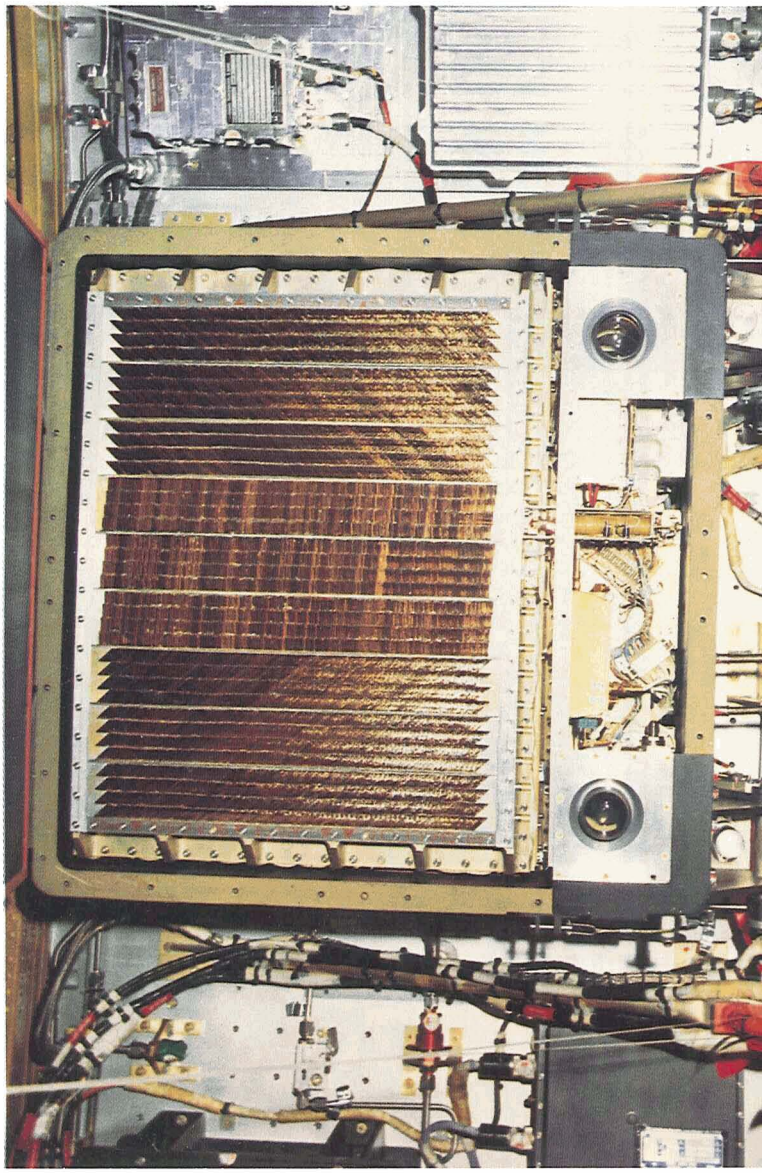

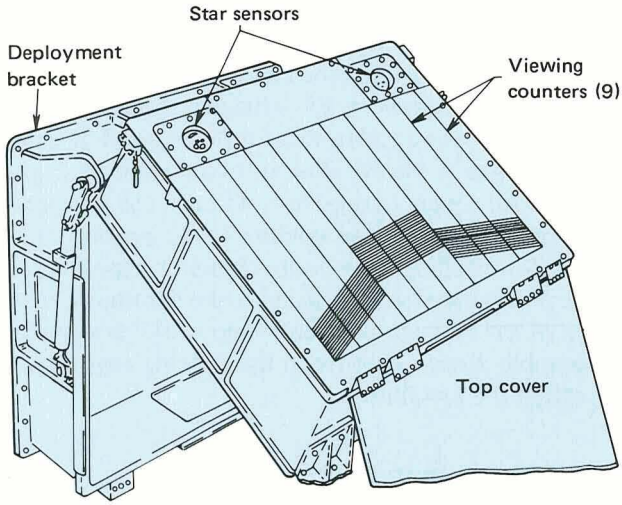

Figure 2-28.—The S150 X-ray instrument deployed in position.

objects in figure 2-27). These collimators, directed to different portions of the sky, defined three intersecting fields of view that allowed pin-point location of an X-ray star within 30 minutes of arc. The two star sensors on the side of the experiment feed pointing information to a computer.

The S150 instrument was not in Skylab but in the instrument unit of the second stage of the Skylab 3 Saturn IB rocket, which briefly orbited behind and below Skylab. The S150 experiment, therefore, could not be attended by the astronauts. It was activated only after the Command and Service Module carrying the crew toward linkup with Skylab had pulled away, exposing the experiment to space. The instrument then unfolded, as shown in figure 2-28, into its operating position and began automatically recording the X-rays on a tape recorder for later playback to ground tracking stations. The entire 130-ton second stage of Saturn IB was rolled and pitched by attitude-control thrusters to permit the X-ray instrument to scan selected areas of the Milky Way.

Figure 2-29 shows the Milky Way as seen from the solar system; the shaded regions are those scanned by the S150 experiment. The galactic center is approximately at the center of the map.

Because the experiment was designed to establish whether the seemingly diffuse X-ray emissions came

Figure 2-29.—The Milky Way as seen from the solar system. The three overlapping rectangles illustrate the fields of view of the three collimators at one instant of time.

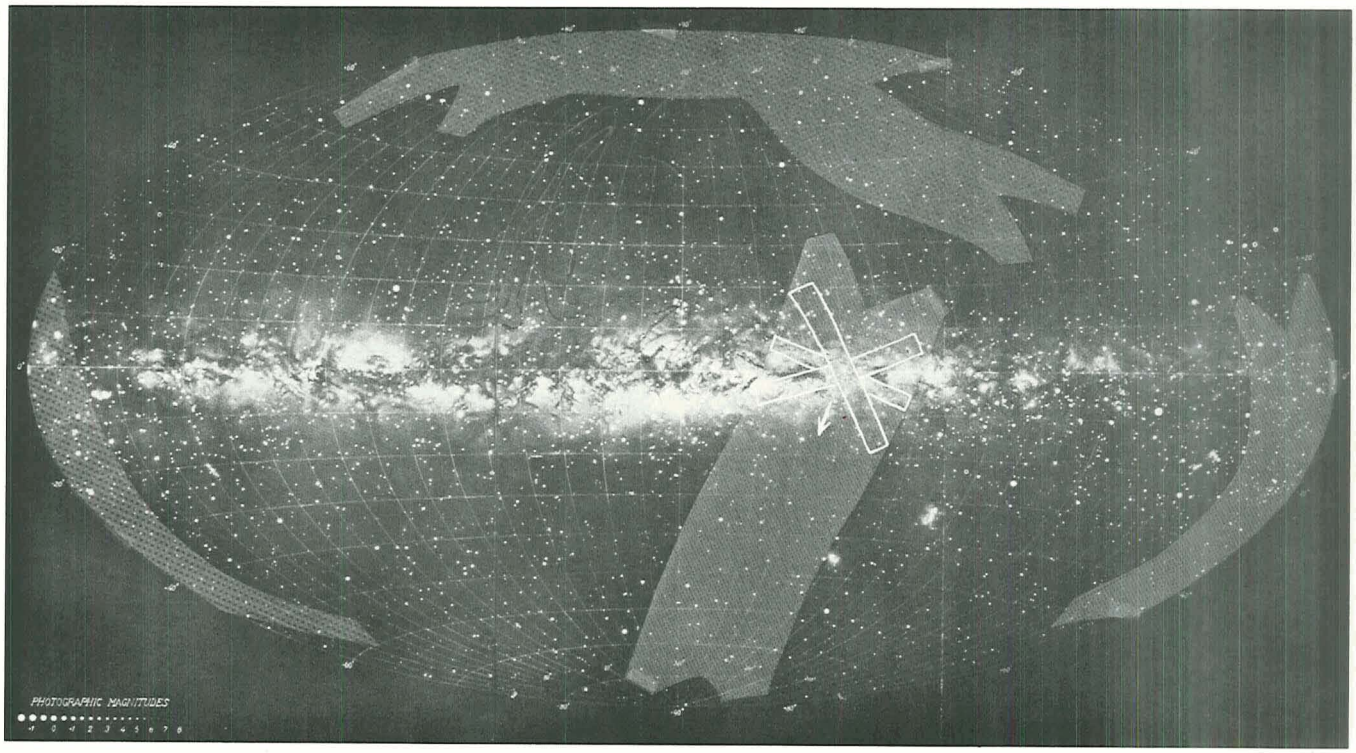

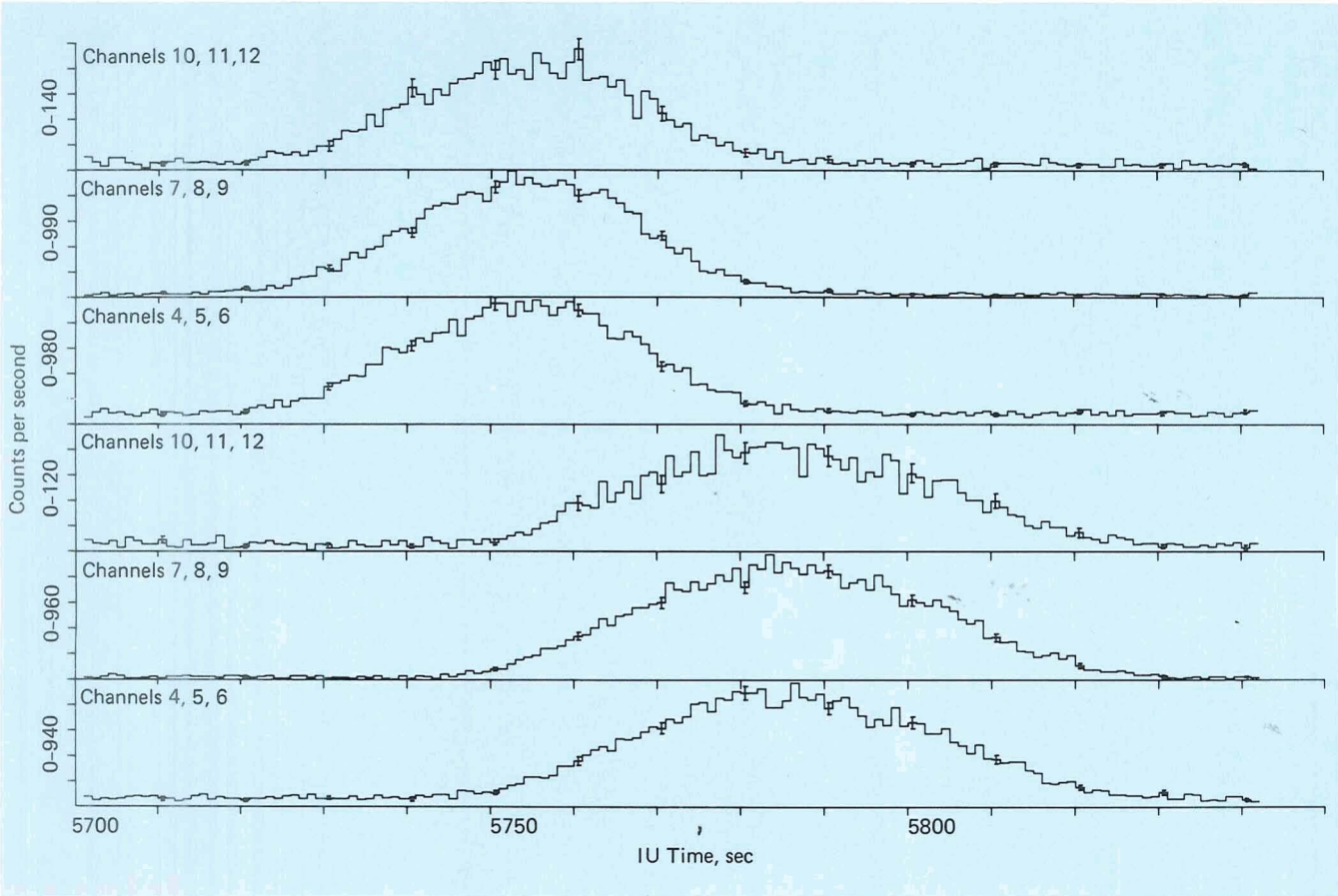

Figure 2-30.—X-ray emission from the Crab Nebula, for two collimator fields of view. Several energy channels were seen successively by two counters, each in three energy channels.

from many unresolved weak X-ray sources, the response of the instrument to localized sources was important. The strong source associated with the Crab Nebula provided a calibration of the instrument characteristics. Figure 2-30 shows a record from the Crab Nebula for two of the fields of view and several energy channels. The field of view of counter 3 swept across the target first; the field of view of counter 2 swept across it about 30 sec later.

Analysis of the data has provided strong evidence that the soft-X-ray background glow cannot be explained as the cumulative effect of thousands of unresolved X-ray stars. Thus it remains an enigma despite Skylab's efforts. Nearby representatives of every category of star known to exist in the Milky Way (in numbers sufficient to provide a possible class of closely spaced X-ray sources) passed slowly through the experiment's field of view, while the long-wavelength X-ray flux failed to reveal an X-ray star among even the closest candidates. Together with clues collected in other investigations, the Skylab experiment suggests that the soft-X-ray glow originates, not from stars of any kind, but from previously unsuspected hot plasmas in the vast reaches between the stars.

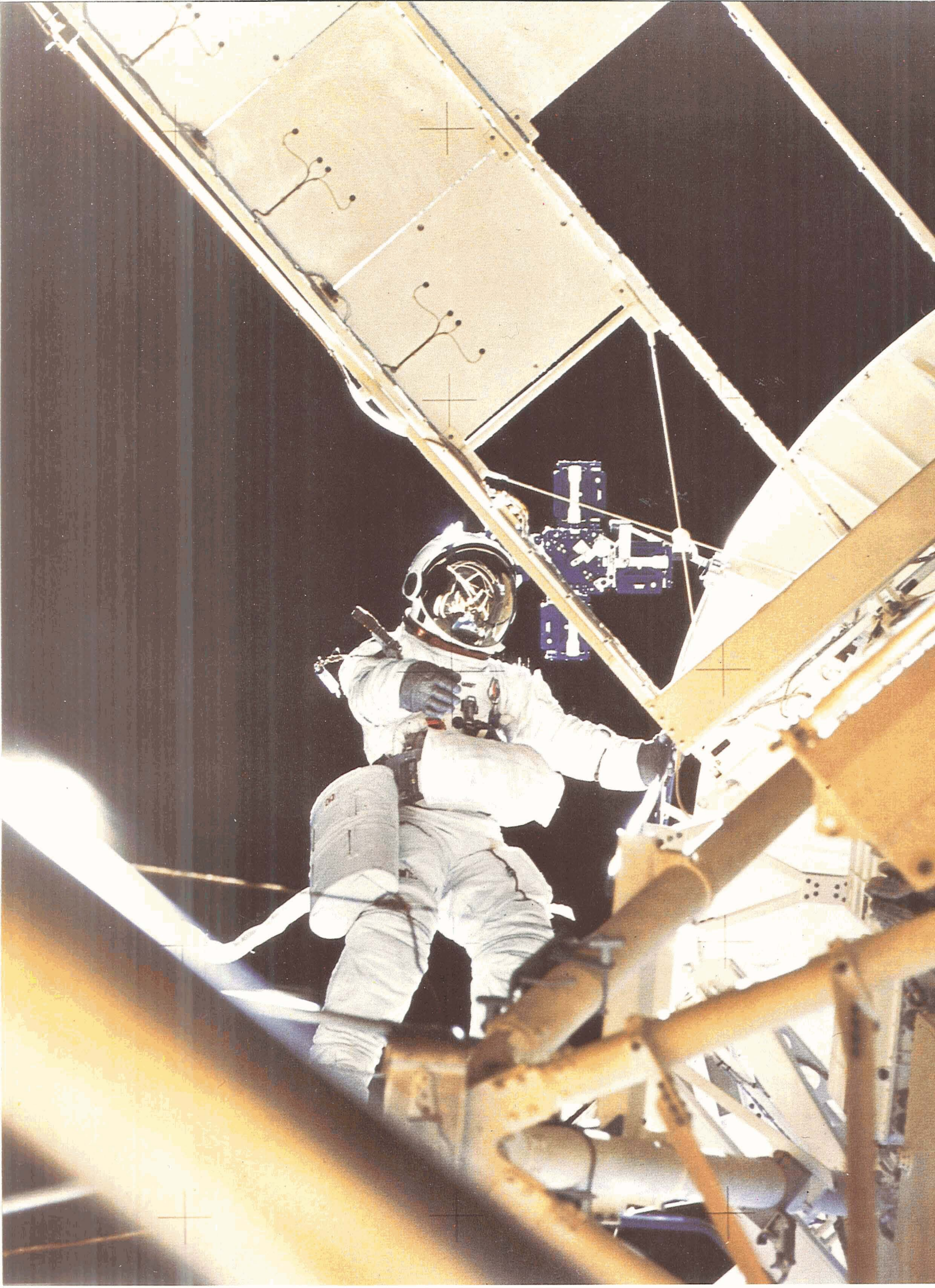

3
Interplanetary Dust

Meteors, or "shooting stars," were the first evidence of small solid objects in interplanetary space. They are caused by the passage through the atmosphere of chunks of solid matter that heat the air to incandescence by friction. The large remnants that reach the Earth's surface are called meteorites. Not all of these solid objects are big enough to cause shooting stars or to be conspicuous on the surface of the Earth after falling. Those smaller than about 0.1 mm in diameter are called micrometeorites when they are recovered from the surface of the Earth. Their surface-to-mass ratio is large and radiative cooling is so efficient that the object does not become hot enough to leave a trail of incandescent air. The terms "meteoroid" and "micrometeoroid" are used for individual solid objects in interplanetary space. The micrometeoroids, particularly the very small particles, are often called interplanetary dust. The mass of solid extraterrestrial matter reaching the Earth's surface has been estimated to be 10 000 metric tons per day, most of it as micrometeorites.

Meteorites recovered from the Earth's surface are of two types, stony and iron. About 61 percent are stony and about 35 percent are iron, with 4 percent being stony-iron. Over 90 percent of the stony meteorites are called chondrites because they contain small spherical inclusions called chondrules, which suggests that they formed from a rapidly cooling melt. Some 3 to 4 percent of recovered meteorites are black chondrites with a carbon content of about 3 percent and are called carbonaceous chondrites. Carbonaceous chondrites are sometimes very fragile; hence, many of them must be destroyed in the atmosphere before they reach the ground.

Meteors are classified as shower meteors or sporadic meteors. Sporadic meteors can occur at any time and can come from any direction. They are more common than shower meteors. Shower meteors are seen at about the same time each year from a particular direction in space.

Meteor showers are the trail of debris left by a comet along its orbit. The shower occurs when the Earth in its orbit around the Sun passes through the comet's trail. If the material in the trail is fairly evenly spread out, the Earth will pass through it and the shower will be seen each year. If the debris occurs in clusters along the trail, the Earth will sometimes pass through a gap between clusters and there will be no shower that year. An example of an annual meteor shower is the Orionids, so named because the meteors appear to originate from a point in the sky in the direction of the constellation Orion. The Orionids are in the orbit of Halley's comet and are observed each year around October 21.

The existence of micrometeoroids in space is indicated from studies of the zodiacal light. The zodiacal light is sunlight reflected from micrometeoroids orbiting the Sun near the ecliptic plane. Studies of it suggest that the number of micrometeoroids increases rapidly with decreasing size. Micrometeoroids presumably travel at the same speeds as meteoroids, about 12 to 72 km/sec.

Figure 3-1.—Micrometeoroid collection instrument (S149) deployed by scientist pilot Owen K. Garriott during the second manned mission. The collection cassettes are mounted on the rim of the solar observatory (in front of Garriott's head) and remained facing the Sun for 46 days before being retrieved.

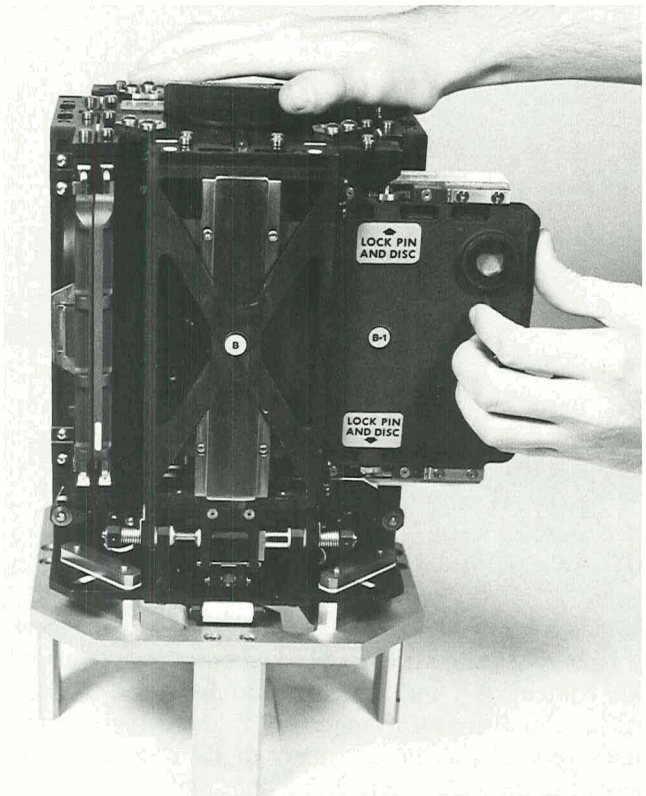

Figure 3-2.—Sample cassettes being loaded into the micrometeoroid collection instrument.

In the early days of space flight, therefore, it was thought that they might present a hazard to spacecraft even though they were very small. Zodiacal light is the best source of information about the average properties of in-place interplanetary dust as a whole, and particle impacts are the best source of data on the properties of individual micrometeoroids. Both the zodiacal light and micrometeoroid impacts were studied by instruments aboard Skylab.

The S149 Skylab Micrometeoroid Collection Experiment

Micrometeoroids in the near-Earth vicinity were expected to strike Skylab. To take advantage of the fact, C. L. Hemenway, director of the Dudley Observatory in Albany, New York, devised an experiment in which thin foils and polished metal plates were exposed in space to record penetrations by such particles. This experiment is shown deployed in figure 3-1. The exposed materials were returned to Earth and studied with optical microscopes and scanning electron microscopes.

Sample cassettes for the Skylab micrometeoroid collection experiment are shown being loaded in figure 3-2. A total area of 1200 cm^2 was exposed when the instrument covers were opened, deploying their sample surfaces and uncovering other samples in the pans around the cassette body (fig. 3-3). The surfaces included slides of stainless steel, copper, and silver. There also were stacked, aligned layers of thin carbon-coated nitrocellulose films on electron-microscope grids; nitrocellulose films over glass; and two layers of thin gold foil over stainless steel. The cassettes were opened, exposed, and sealed in the space environment before being retrieved and returned to Earth for analysis.

The micrometeoroid collection cassettes were deployed in two different locations on the Skylab vehicle, as shown in figure 3-4. For 34 days between the first and second manned missions, they faced away from the Sun on the end of a boom. This boom was also used to deploy and point a photometer that measured starlight and zodiacal light in another experiment. The cassettes were opened and closed by ground command after the Apollo spacecraft had left Skylab.

During the second and third manned missions, new cassettes were installed to face the Sun for 46 and 34 days, respectively. These cassettes were manually attached to the rim of the solar observatory and opened during spacewalks. A fourth set of cassettes was left on the rim of the solar observatory for later retrieval should there be a return visit to the Skylab. The letters A, B, C, and D indicate the orientation of the cassettes.

Table 3-I.—Distribution and Location of Craters

	Number of Craters				
	A	B	C	D	Total
Antisolar airlock—between first and second mission					
Covers	2(−Z)	1(−Z)	1(−Z)	2(−Z)	6
Pans	6(−Y)	5(+X)	2(+Y)	2(−X)	17
Observatory rim—second mission					
Covers	0(+Z)	0(+Z)	0(+Z)	1(+Z)	1
Pans	7(+Y)	3(+X)	3(−Y)	3(−X)	16
Observatory rim—third mission					
Covers	0(+Z)	0(+Z)	2(+Z)	1(+Z)	3
Pans	1(+Y)	1(+X)	13(−Y)	3(−X)	18

Note: The letters A, B, C, and D indicate the orientation of the cassettes (see fig. 3-4). The X, Y, Z directions are the directions perpendicular to the exposed surface with respect to the space station.

The distribution of craters in the various pans and covers of the micrometeoroid collection experiment is shown in table 3-I. The X, Y, Z directions are the directions perpendicular to the exposed surface with respect to the space station as shown in figure 3-4. The data are a summary of the results of scanning all metal surfaces once at magnifications of 200X and some of them at 500X. Because of Skylab's orientation, with the solar panels pointing at the Sun 99 percent of the time, the pans facing in the direction of Earth's motion around the Sun collected more particles per unit time than did the covers. The covers facing away from the Sun had

Figure 3-3.—Micrometeoroid collection experiment deployed.

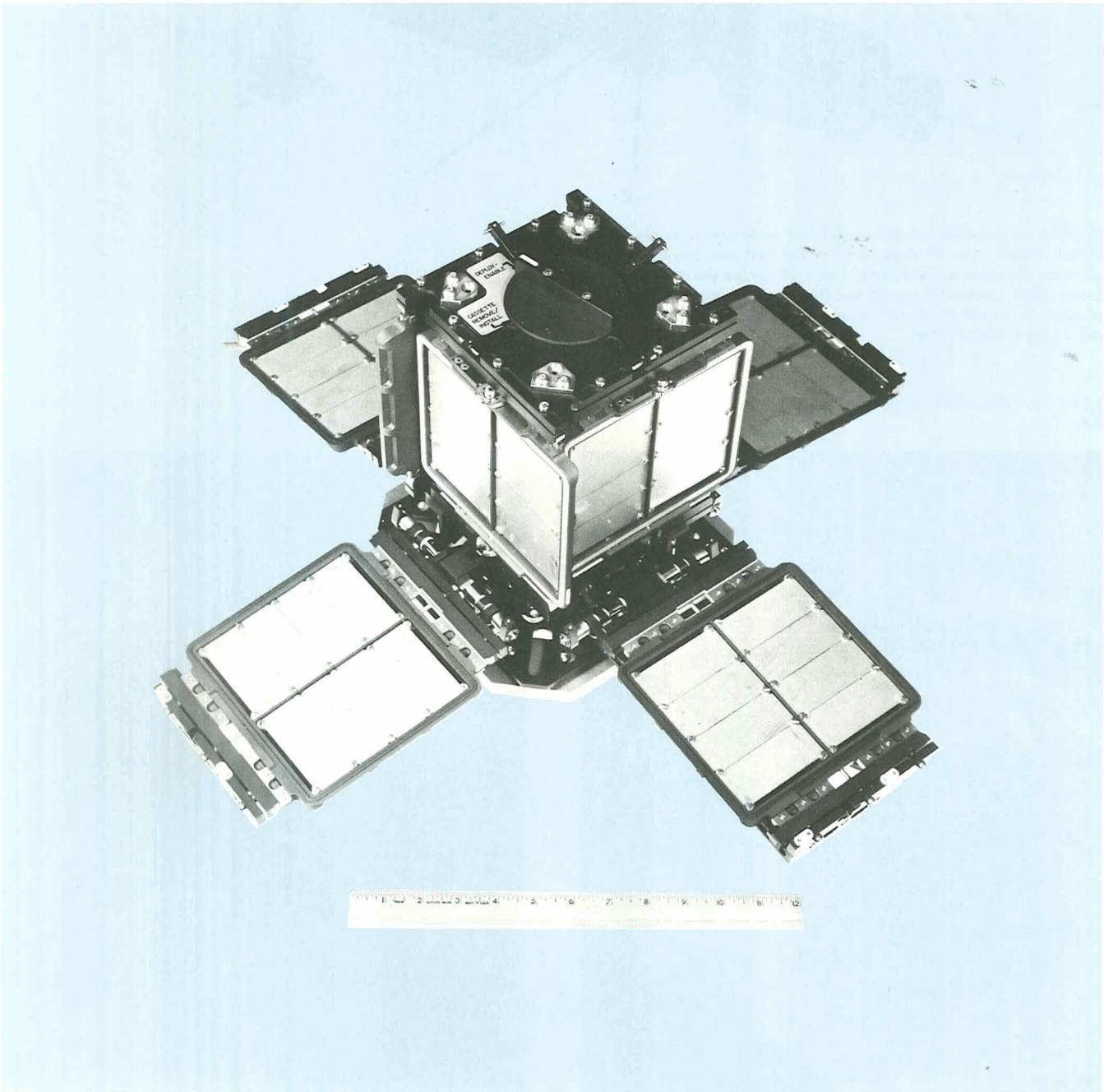

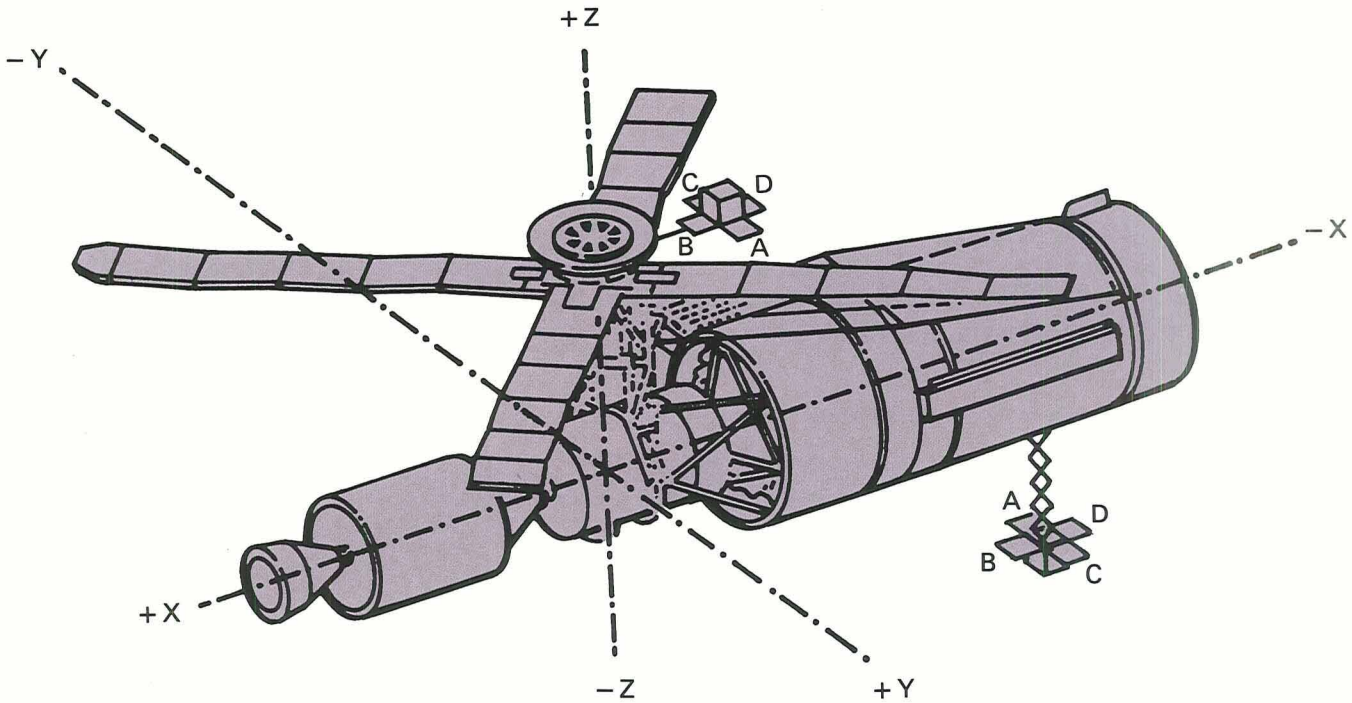

Figure 3-4.—Location of micrometeoroid collection cassettes on the Skylab vehicle. For 34 days between the first and second manned missions, the cassettes faced away from the Sun on the end of a boom (lower right). During the second and third manned missions, they were attached to the rim of the solar observatory and faced the Sun for 46 and 34 days, respectively.

Figure 3-5.—High-velocity micrometeoroid impact crater on a copper slide.

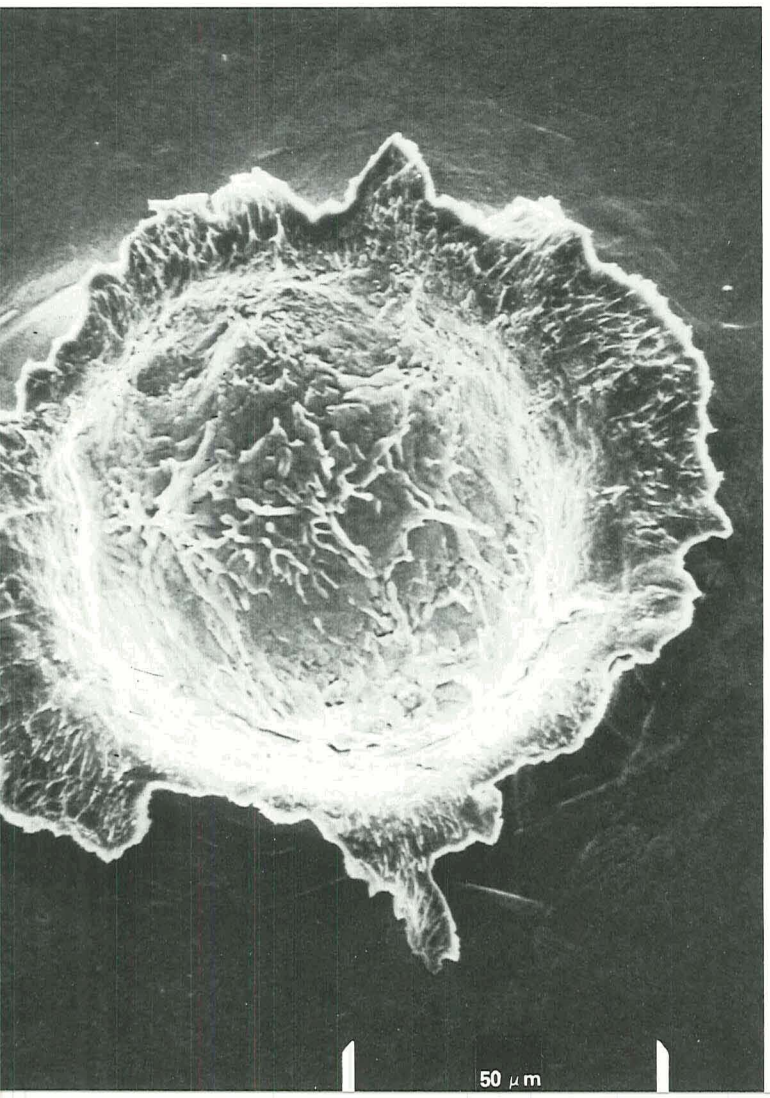

Figure 3-6.—Closeup of figure 3-5, showing the frozen droplet structure within the high-velocity impact crater.

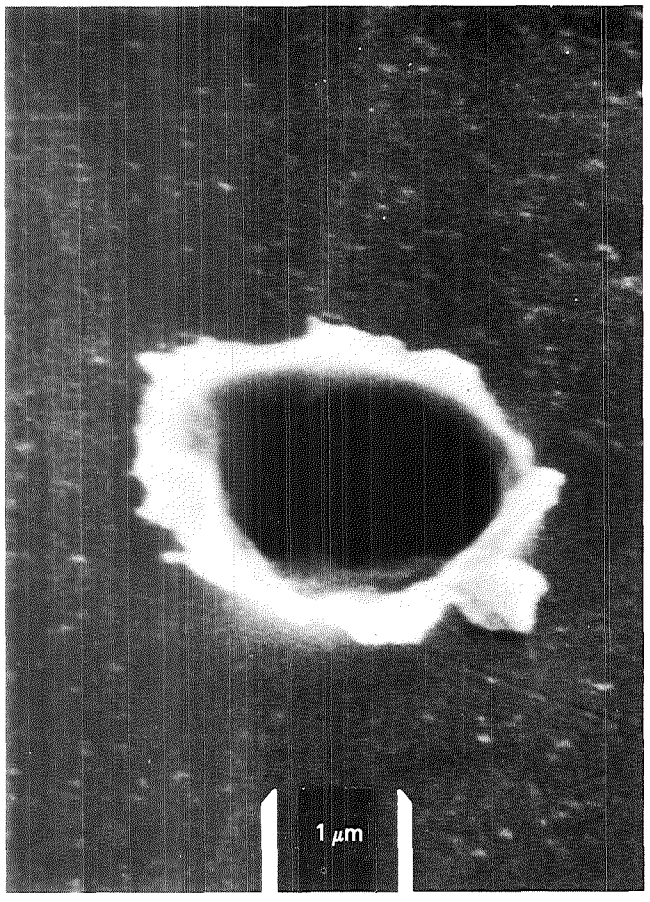

Figure 3-7.—Small, asymmetric impact crater in stainless steel, probably produced by a particle striking at an angle to the surface.

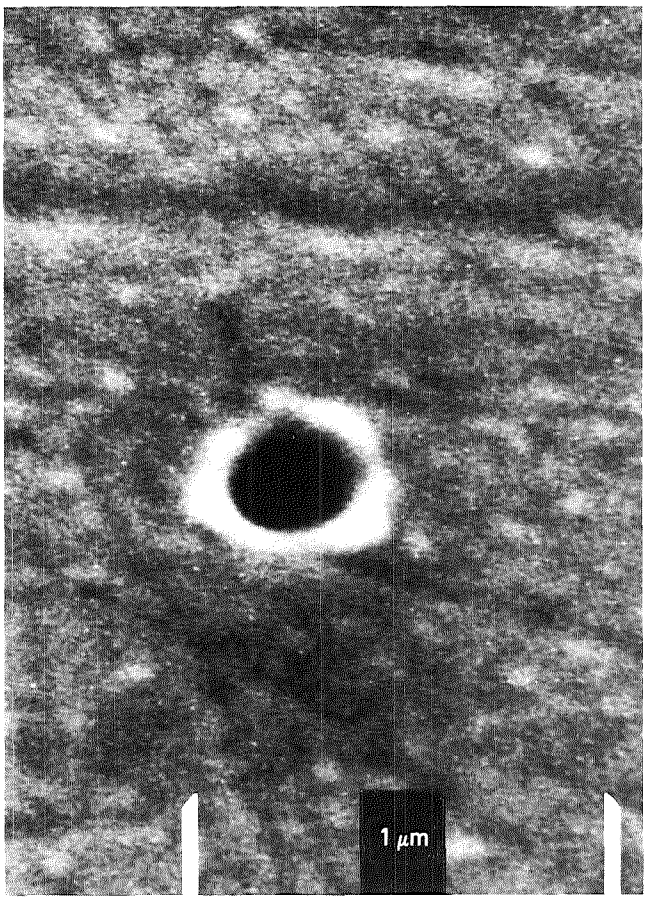

Figure 3-8.—Extremely small impact crater, produced by a micrometeoroid between 0.1 and 0.2 μm in diameter.

more craters than those facing the Sun, which is consistent with the concept that the dust particles are spiraling slowly inward toward the Sun.

Impact Craters

Typical high-velocity impact craters observed in stainless steel and copper slides with a scanning electron microscope are shown in figures 3-5 through 3-8. Figures 3-5 and 3-6 show the same crater in a copper slide. This was one of the largest craters observed in the micrometeoroid collection experiment; figure 3-6 is a closeup that shows the frozen droplet structure within the crater. The small, asymmetric crater in stainless steel, shown in figure 3-7, was probably made by a particle striking at an angle to the surface. Figure 3-8 shows one of the smallest craters observed, made by a particle believed to have been between 0.1 and 0.2 μm in diameter. The structure of the crater appears similar to that of larger craters.

Analysis of the craters produces information on the numbers, sizes, and velocities of the micrometeoroids and some information about their chemical composition. Considerable amounts of micrometeoroid residue were found in the bottom of rough-textured craters or on the lip of smooth craters. Elements found in such residue were aluminum, silicon, sulfur, chlorine, potassium, calcium, iron, and zinc.

Figures 3-9 and 3-10 are from a pair of stacked gold foils over a stainless steel substrate. A micrometeoroid struck the first gold foil and shattered into fragments, which in turn penetrated the second gold foil. The micrometeoroid must have been quite fragile, since it fragmented upon striking a foil much thinner than its dimension. In one case, two small craters were found in the stainless steel substrate after a particle penetrated two layers of gold foil. These pictures, incidentally, illustrate the principle of the micrometeoroid shield. Fragmentation of micrometeorites striking the shield

would greatly reduce the possibility of damage to the spacecraft wall. Although Skylab's 0.6-mm-thick micrometeoroid shield was lost, the orbital workshop's wall, 3.18 mm thick, was not penetrated, indicating that there is little meteoroid hazard to spacecraft in Earth orbit with such wall thickness.

Multiple Craters

Figure 3-11 shows two small craters close together, suggesting a clustering of micrometeoroids. Several such multiple events were observed. Figure 3-12 shows several penetration holes close together. As this picture indicates, debris from the impacting particle sometimes remained near the penetration hole. One of the best examples of the clustering of impacts was observed in a cover facing away from the Sun, where approximately 1000 penetration holes in the thin gold foil were observed in an area of only 8 mm^2.

"Evil Eyes"

Micrometeoroids penetrating the thin nitrocellulose films produced a cylindrical hole with a halo, giving it

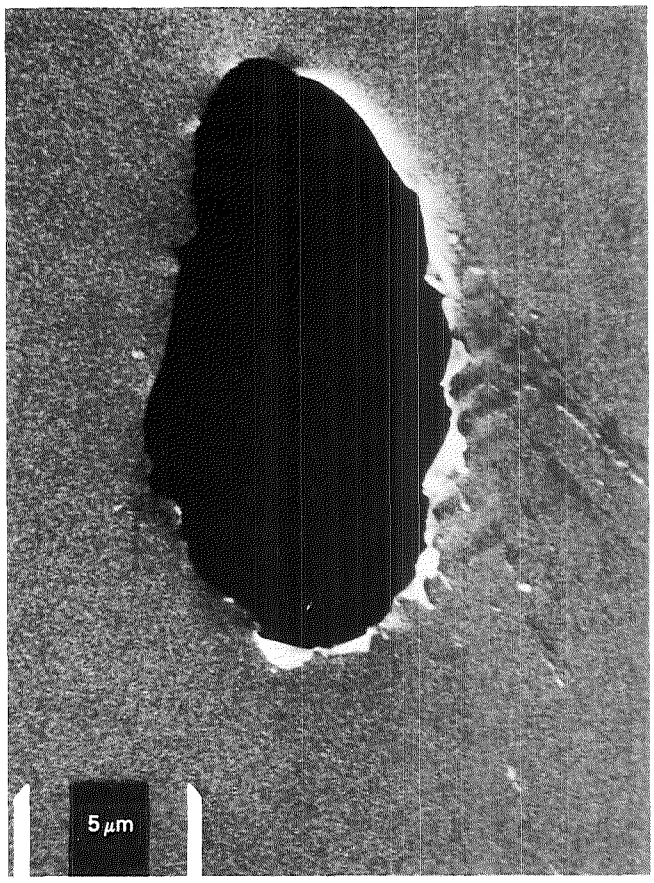

Figure 3-9.—Penetration hole in gold foil.

Figure 3-10.—Fine penetration holes in the second gold foil positioned beneath the gold foil shown in figure 3-9.

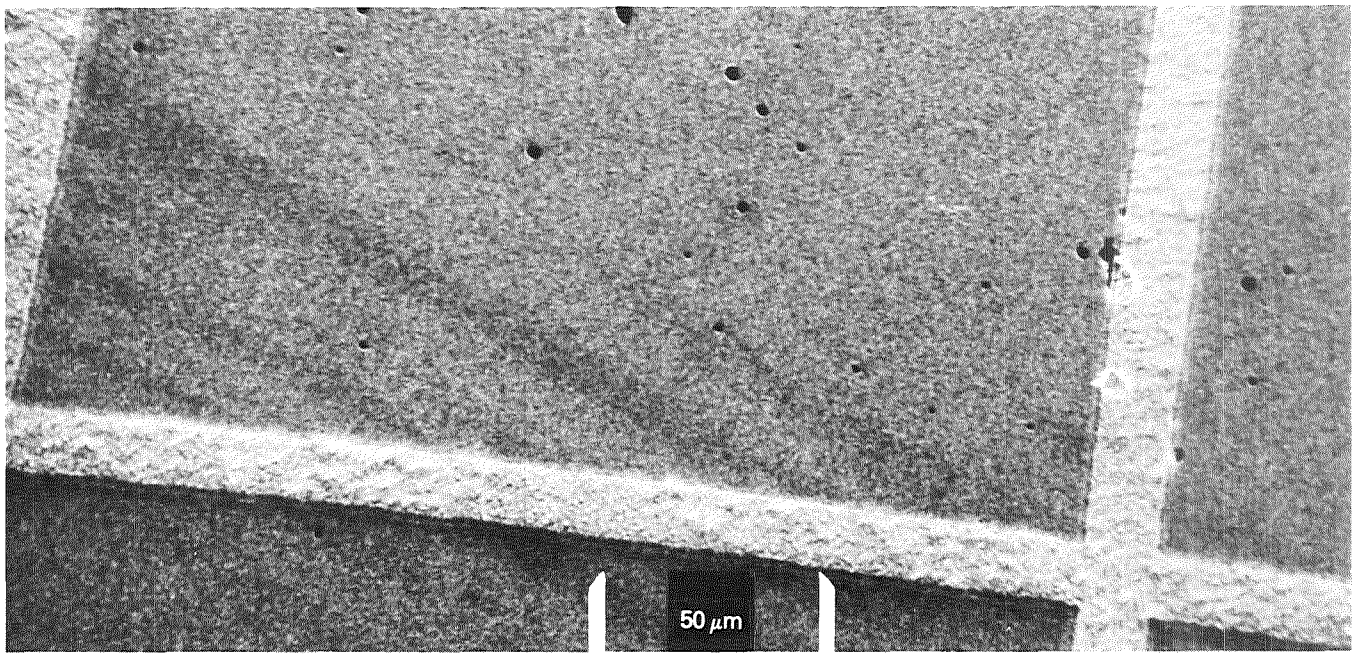

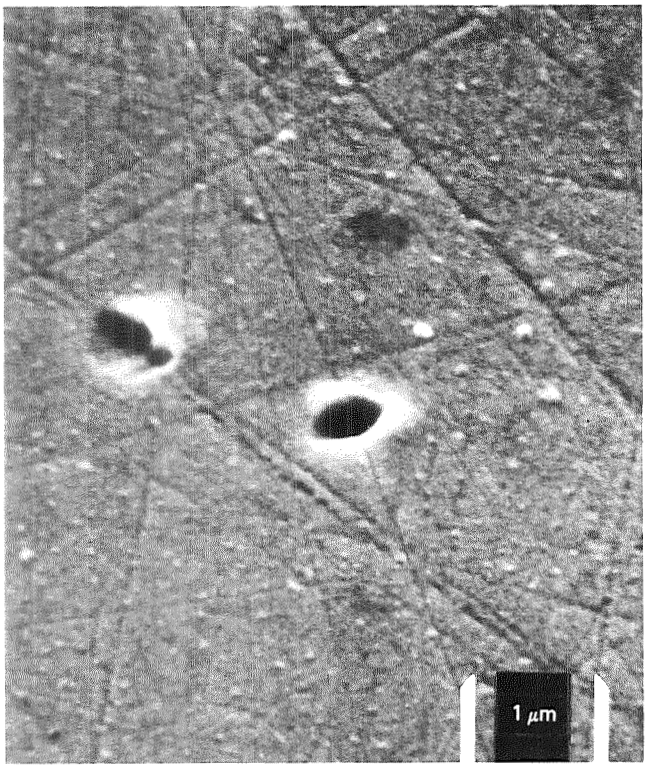

Figure 3-11.—Two small impact craters close together.

Figure 3-12.—Multiple penetration holes close together.

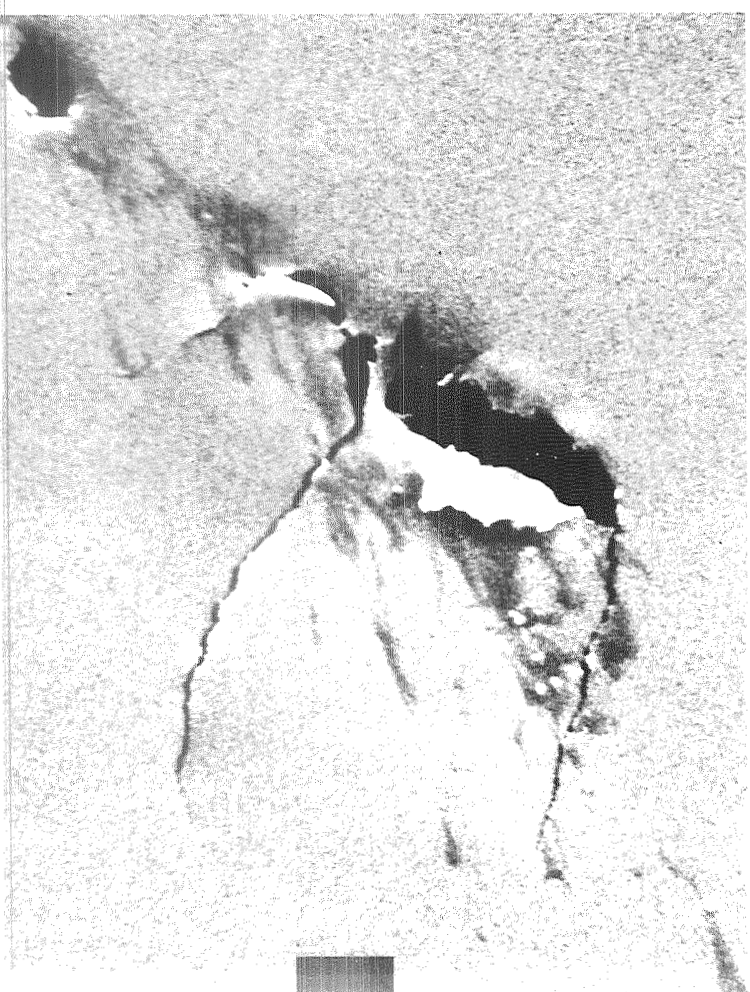

an "evil eye" appearance when viewed in an electron microscope (fig. 3-13). The halo around the "evil eye" is probably residue from the particle. The "evil eyes" were first seen in an exposure of a Gemini micrometeoroid collector but were unexplained. The particles causing them may consist of a hard core surrounded by soft material. The hard core produces the hole, and the soft material causes the halo.

Meteoroid Residue

An unrelated experiment (S228) by P. Buford Price on transuranic cosmic rays provided an unexpected additional observation of a micrometeoroid. A large micrometeoroid crater was found in the pure aluminum foil covering a detector stack that was deployed on the outside of the space station during the third manned Skylab mission and subsequently returned to the Earth. The crater is approximately 110 μm in diameter and 75 μm deep, as shown in figure 3-14. Donald Brownlee, of the University of Washington, found that the crater wall contained enough micrometeoroid residue to allow determination of the relative elemental composition by electron-microprobe techniques. It is thought that

Figure 3-13.—"Evil eye" hole produced in thin nitrocellulose film. The halo is probably residue from the impacting micrometeoroid.

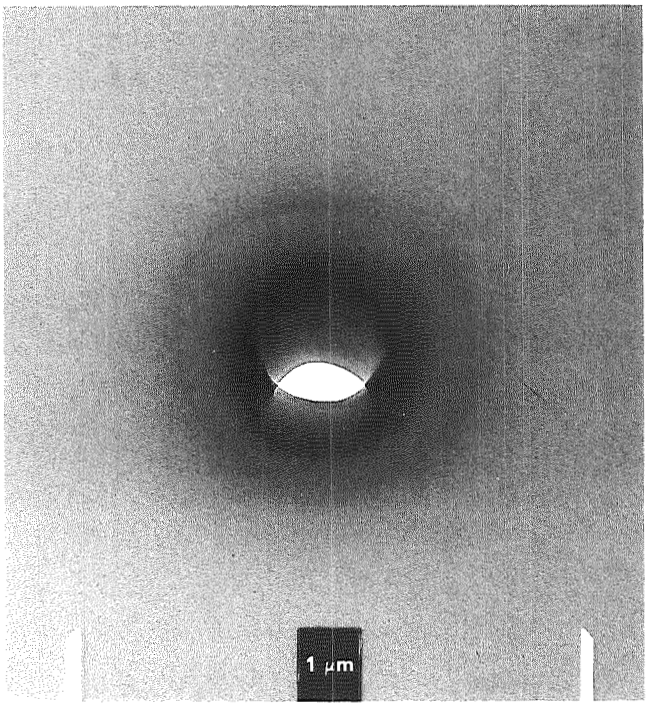

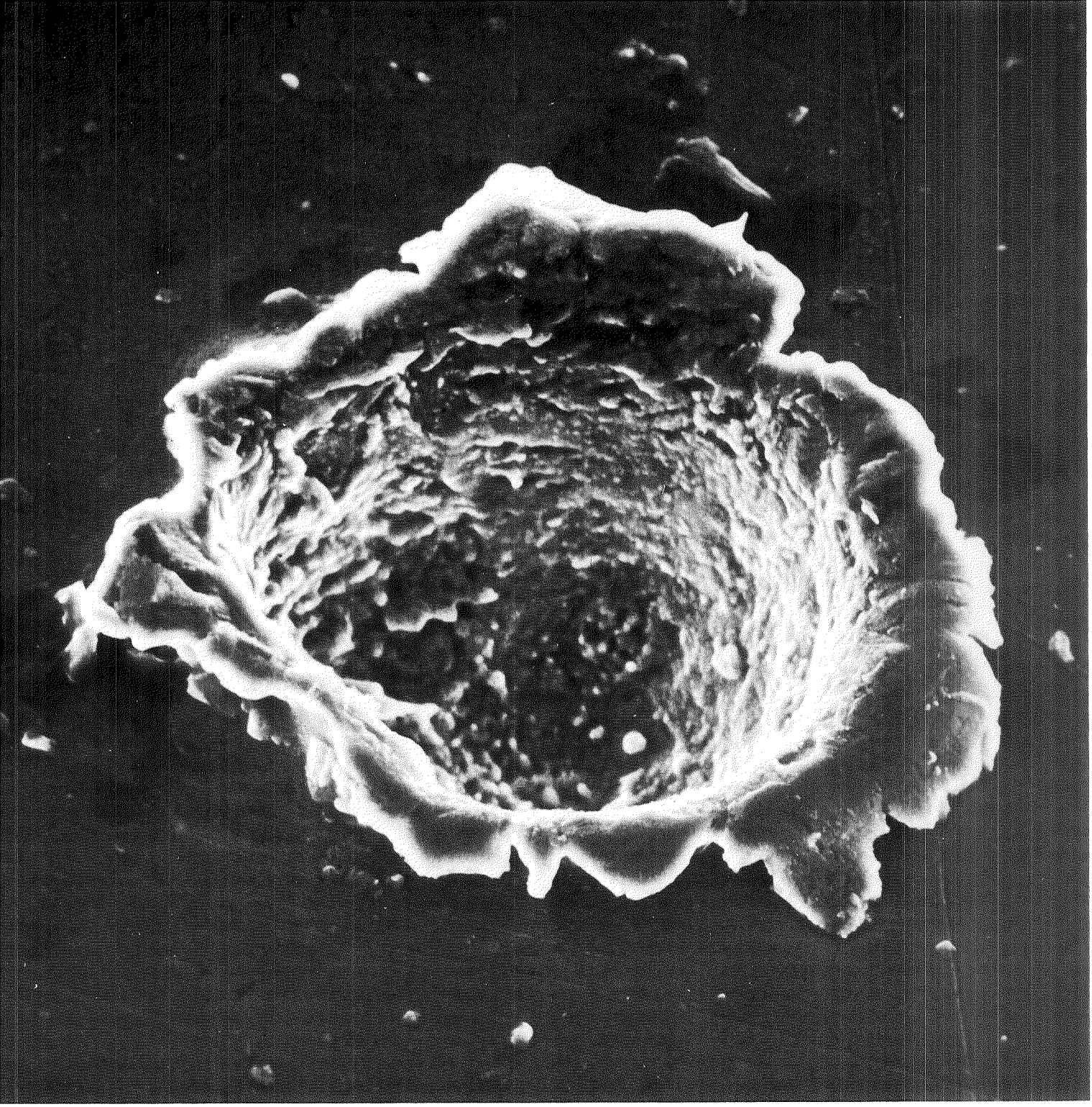

Figure 3-14.—Large impact crater (~110 μm in diameter, 75 μm deep) in pure aluminum foil.

micrometeoroids of this size (~30 μm in diameter) probably originated from comets, since meteor showers containing particles of this size or larger occur when the Earth crosses a comet's orbit. If so, this crater analysis provides a laboratory measurement of actual cometary material.

The results of two electron-probe analyses are shown in figure 3-15, the relative abundance being normalized to the amount of silicon found. Elements identified were iron, silicon, magnesium, calcium, nickel, chromium, and manganese. Upper limits were also obtained for titanium and cobalt. For comparison, the relative elemental abundances for two types of carbonaceous chondrite meteorites (C1 and C3) are also given. There is a

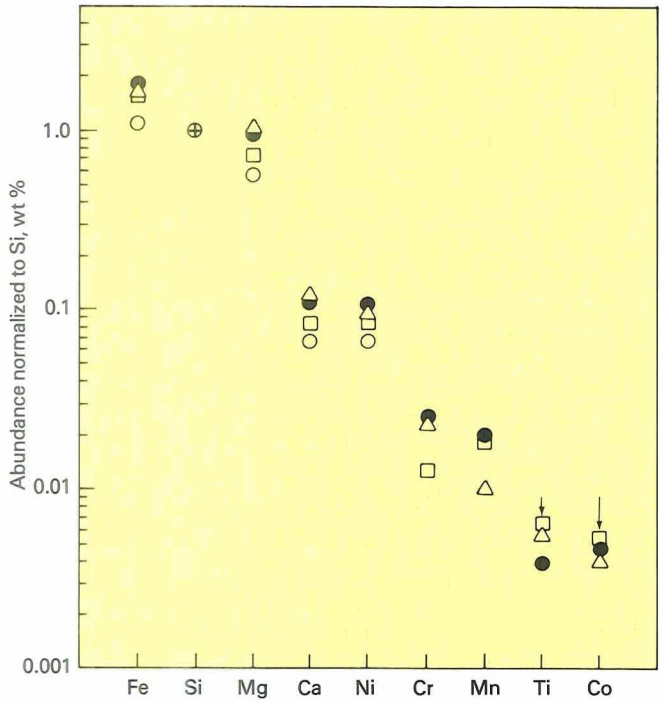

Figure 3-15.—Elemental composition (normalized to silicon) of micrometeoroid residue found in the crater shown in figure 3-14. The open squares and circles represent different electron-beam probe runs. The elemental compositions of two types of carbonaceous chondrite meteorites (C1 and C3), represented by solid circles and by crosses, respectively, are shown for comparison.

marked similarity, but this should not be construed as evidence that both objects have a common source. The similarities are possibly only a consequence of their both being primitive, well-preserved samples of early solar system materials. A sulfur analysis at a later date indicated that sulfur is also present in the crater with an abundance similar to the abundances of iron, magnesium, and silicon and also comparable to the abundances for carbonaceous chondrites.

Apparently the pure aluminum was a good material to trap the residue of the particle that caused the crater, since similar sensitive analyses of craters in lunar rocks failed to detect any micrometeoroid residue. Based on the analysis, it was estimated that approximately 10 percent of the particle survived as residue.

The successful detection of residue in the Skylab micrometeoroid craters suggests that, if other large craters can be analyzed, it may be possible to make a statistical estimate of elemental abundances in comet debris. Primitive meteorites found on Earth contain large (>30 μm) inclusions of materials such as the minerals olivine and magnetite, for which the relative elemental abundances are very different from the accepted cosmic abundances. Residue analysis of a large number of craters would show whether or not these types of materials are also in comets. The results of such a search would have implications regarding the interrelationships between comets and meteorites.

The Zodiacal Light

The zodiacal light is sunlight reflected from microscopic dust particles in orbit about the Sun and concentrated near the ecliptic plane. Figure 3-16 is a picture of the zodiacal light taken by P. Hutchinson from atop 3048-m Mt. Haleakala, Hawaii, in January 1967, just before sunrise. From the Earth, the zodiacal light is best seen when the ecliptic plane is approximately perpendicular to the horizon. In the Northern Hemisphere, the best times to view the zodiacal light are on clear, moonless nights after twilight in February and March and before dawn in September and October. In equatorial regions it is visible throughout the year. Figure 3-16 shows the rapid dimming of the zodiacal light at increasing angular distances from the Sun. At 30° from the Sun in the ecliptic, it is approximately three times brighter than the brightest part of the Milky Way.

The Gegenschein

The faint patch of light in the night sky directly opposite the Sun is called the Gegenschein, which is German for counterglow; it is an intensification of the zodiacal light. The phenomenon is difficult to observe or photograph from the ground because of interference from atmospheric airglow.

Figure 3-17 shows the Gegenschein photographed during the second manned Skylab mission. The photograph required a long exposure (6 min) using a very fast but grainy film (Kodak 2485) in a 35-mm camera. The camera was provided with occulting disks to blot out the Sun in an "artificial eclipse" when operated in a Sun-pointed mode (Experiment T025). The occulting disks and the supporting rod were rotated out of the way and are seen as the out-of-focus dark areas on the right. If the Gegenschein were due to a reflection from dust near the Earth, it might have been possible to see the Earth's shadow in the center of the Gegenschein in this photograph. Such a shadow is not seen, although a bright star (3.8 magnitude) near the center of the Gegenschein may have masked any existing shadowing to some degree. This result is in agreement with earlier ground-based observations.

The S073 Gegenschein-Zodiacal Light Experiment

Detailed study of the characteristics of the zodiacal light can in principle provide information on the dust particles that give rise to it: their numbers and sizes, distribution in space, refractive index, and shape. Ground-based observations have given discordant results, and it has not been possible to determine from these observations the nature or origin of the zodiacal dust.

The Skylab study of zodiacal light designed by Jerry Weinberg, of the State University of New York in Albany, used a photomultiplier photometer provided

Figure 3-16.—Zodiacal light observed just before sunrise on top of 3048-m Mt. Haleakala in Hawaii.

with filters and polarizers. The data are obtained as a plot of brightness and polarization at a number of wavelengths across the spectrum. The photometer was attached to the end of a boom that extended from the airlock in the wall of the orbital workshop. A 16-mm camera was mounted alongside the photometer in order to verify the direction in which it was pointed.

The two instruments were positioned at the end of the boom on a two-axis mounting that permitted a fixed-position or a scanning observation of selected areas of

Figure 3-17.—Gegenschein photographed during the second manned Skylab mission.

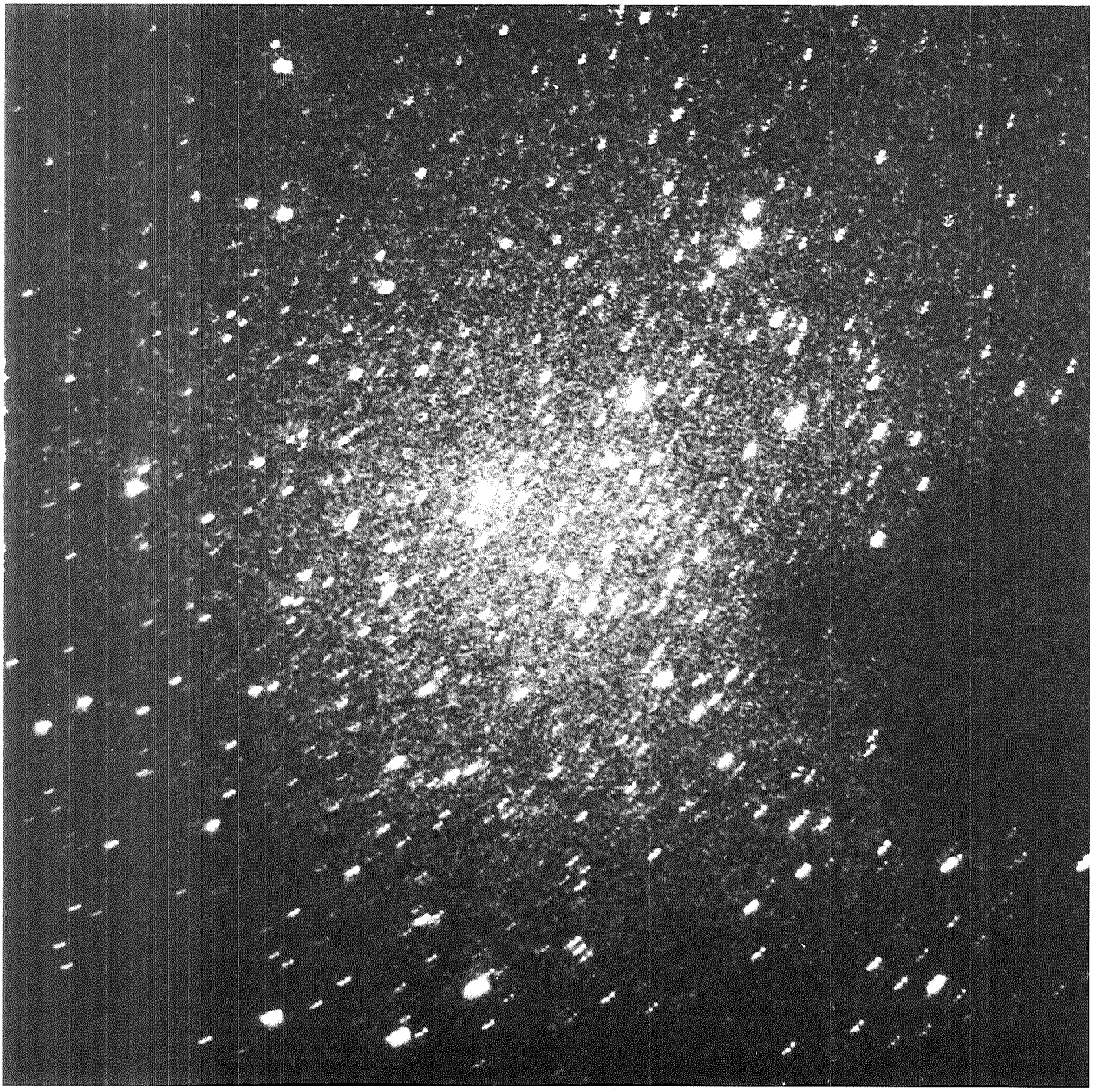

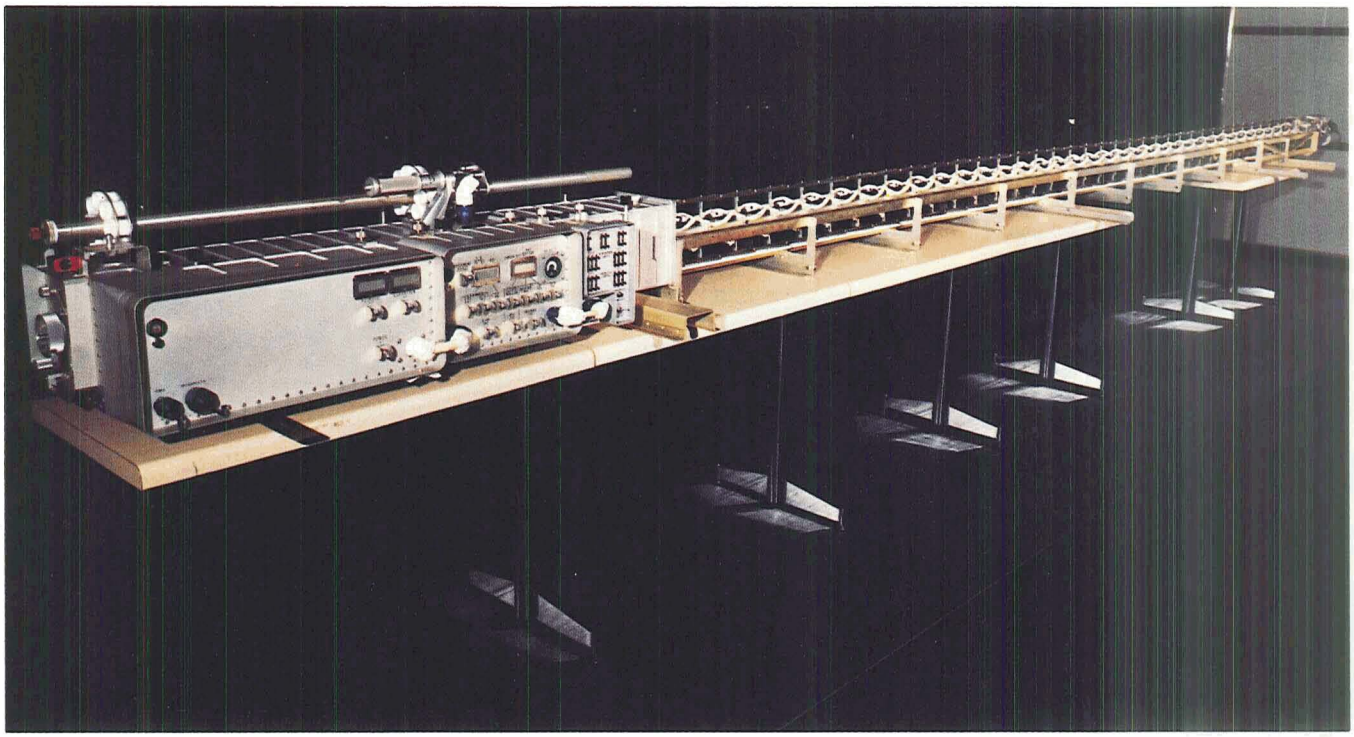

Figure 3-18.—Photometer deployed preflight as for the Gegenschein/zodiacal light experiment (S073).

the sky. The experiment measured the properties of the zodiacal light and starlight in the hemisphere of the sky centered in the antisolar direction. Before the mission, it had been hoped to scan the sunward area of the sky to within 15° to 20° of the Sun, where the zodiacal light blends into the outer corona of the Sun. The blockage of the Sun-facing airlock by the parasol deployed by the first crew, however, prevented such scanning.

The instrument is shown in figures 3-18 and 3-19. Figure 3-18 depicts it with the boom fully extended, which placed the photometer head some 6 m beyond the space-station wall. Figure 3-19 shows the photometer mounted in the airlock during the first Skylab mission. The long canister and panels contained power supplies, automatic and manual control equipment, and the extension mechanism. An astronaut's spacesuit is shown drying out alongside the photometer. Astronauts programmed the photometer scan pattern and scan limits so that it operated automatically, telemetering data on the observed region of the sky for up to 10 consecutive orbits while the astronauts slept or performed their duties.

When the meteoroid shield was torn off the spacecraft, the backup unit of the photometer canister was modified, launched with the first manned mission, and used at the solar airlock to deploy the parasol that shaded the vehicle.

The Poynting-Robertson Effect

Interplanetary dust particles, including those which give rise to the zodiacal light, are subject to gravitational and radiation forces. Gravitational forces cause them to orbit the Sun, while radiation pressure tends to push them away from the Sun. An additional force on the small micrometeoroids responsible for the zodiacal light is the Poynting-Robertson effect. The particles absorb sunlight from only one direction, but reradiate this energy in all directions. Calculations for small orbiting particles show that the result of this action is a drag force that, under most conditions, is greater than the radiation pressure and causes the particles to spiral inward toward the Sun. The Poynting-Robertson effect is greatest for particles of low density and small size. Consequently, after millions of years, first the smaller particles and then the larger ones will fall in toward the Sun, causing a sorting out process to occur, with the smaller particles being nearer the Sun. The particles will

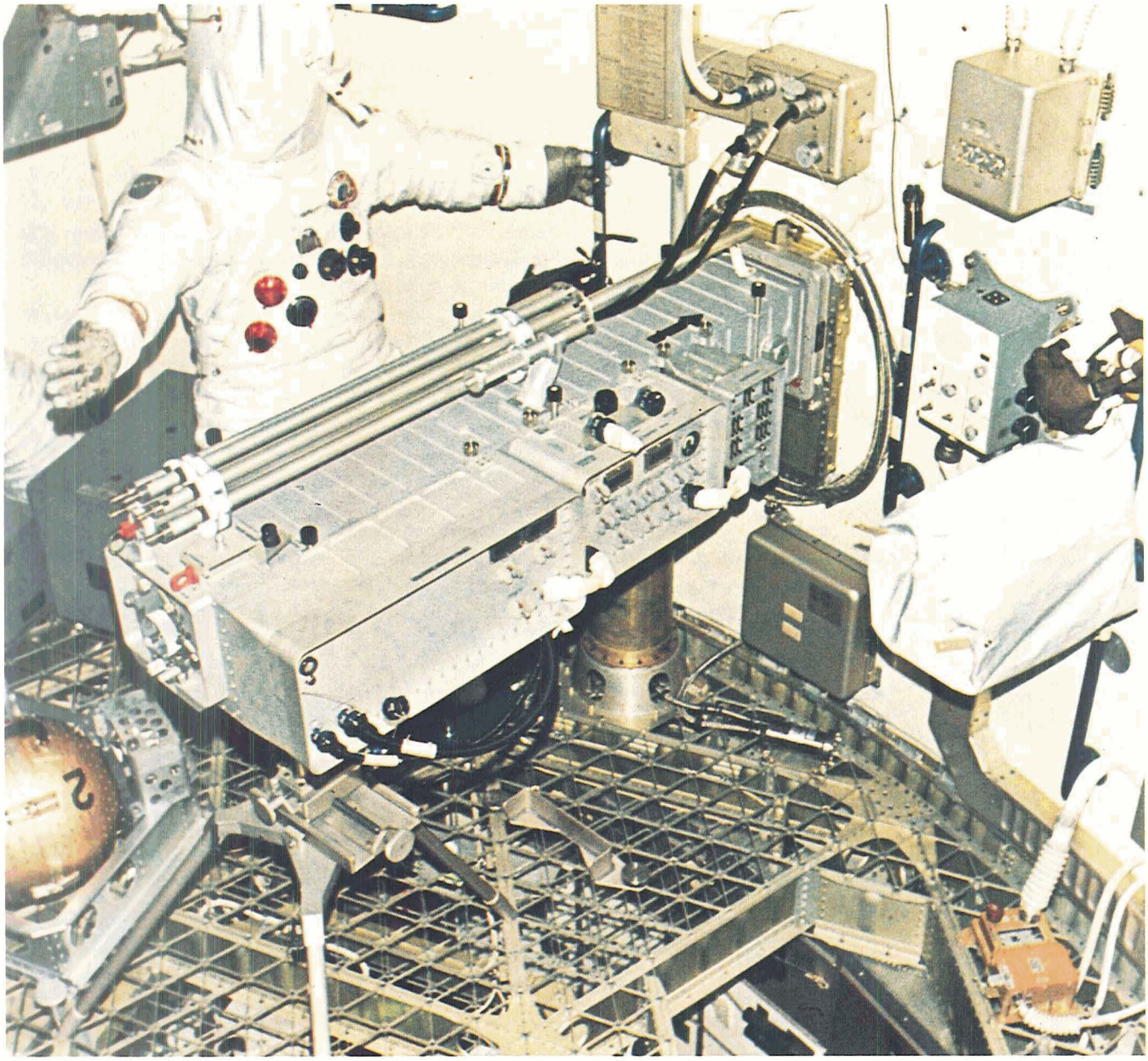

Figure 3-19.—Photometer mounted in the airlock during the first manned Skylab mission.

not actually fall into the Sun but will be partially or totally vaporized. The vaporized and the residual material are subsequently blown out of the solar system by radiation pressure. The fact that the dust is present, as is known from the zodiacal light, and is being depleted by the Poynting-Robertson effect means that there must be a source from which it is being replenished. Among the possible sources of fresh material are comets, with their long tails of ejected material, and fragments from collisions in the asteroid belt. Data on these effects were obtained from Skylab's sky-mapping observations, which were coordinated with observations from the zodiacal light experiments on the Pioneer 10 and 11 Jupiter probes, which passed through the asteroid belt. Weinberg's Pioneer data indicate that the interplanetary dust responsible for the zodiacal light does not

extend much beyond the asteroid belt. The rate at which the brightness decreases from the Sun out to the asteroid belt, combined with Pioneer and Skylab data on color and polarization, may make it possible to determine whether zodiacal dust has its origin in comets, in the asteroid belt, or in both.

Brightness of the Skyglow

Figure 3-20 is a color-coded brightness map of half a hemisphere of sky opposite the Sun. The colors show the variations in the level of brightness measured by the photometer through a red filter at a wavelength of 710 nm. The scan started in the center and worked outward in ever larger rings. Each block represents the average brightness in the area swept across by the photometer in 10 sec. The white rings are missing data due to automatic photometer shutdown caused by bright objects (e.g., Jupiter or the illuminated Earth). The lighter colored vertical band corresponds to the Milky Way, which intersects the ecliptic near the antisolar point, located at the center of the figure. The Gegenschein was in the Milky Way, in the region near the center colored dark red. This photometer scan was performed during the second manned mission. Similar maps were made at other wavelengths and for other periods of time.

Polarization of the Skyglow

Figure 3-21 is a color-coded polarization map for the scan program shown in figure 3-20. It shows the percentage of the total light that is polarized. Regions near the Gegenschein and in the Milky Way show the smallest amount of polarization.

Weinberg and associates report that the polarized brightness of the zodiacal light at intermediate elongations (i.e., when the apparent angle from the Sun is near 90°) has the same color as the Sun. Since the total brightness also has the same color as the Sun, the degree of polarization is independent of wavelength between 4000 and 8200 Å. This suggests that the zodiacal particles near the Earth's orbit are substantially larger than these wavelengths, in agreement with the results of discrete particle detectors and of lunar cratering studies, which find the size of the particles to be primarily in the range of tens to hundreds of micrometers in radius.

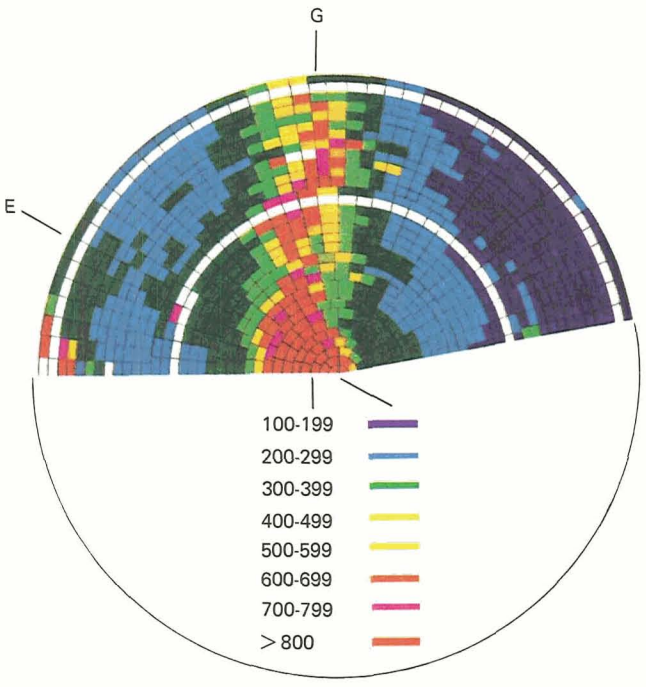

Figure 3-20.—Color-coded brightness map of half a hemisphere of sky opposite the Sun (red filter, 710-nm wavelength). The positions of the galactic equator and the ecliptic are indicated by G and E, respectively, and the lighter colored vertical band corresponds to the Milky Way.

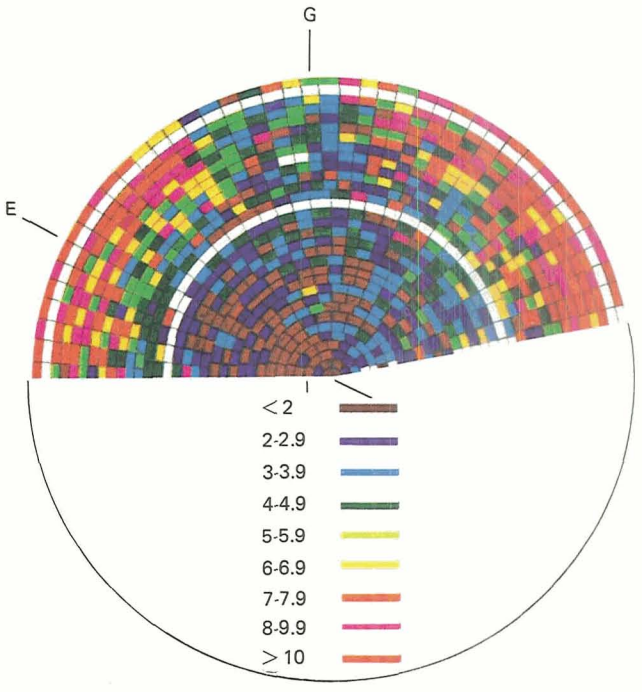

Figure 3-21.—Color-coded map showing the percentage of total light that is polarized (same scan program as in fig. 3-20).

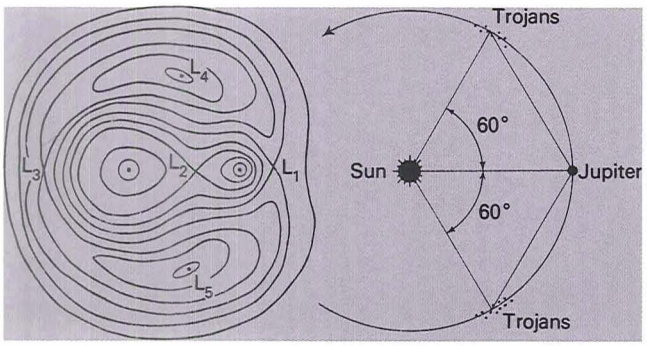

Figure 3-22.—Left: lines of constant gravitational potential for a small mass near two orbiting celestial bodies, one of which is comparatively large. The points L_1, L_2, etc., are the libration regions. Right: the Sun–Jupiter–Trojan asteroids system.

Lunar Libration Regions

Figure 3-22, left, shows lines of constant gravitational potential for a small mass near two orbiting celestial bodies, one of which is comparatively large. The points labeled L_1, L_2, L_3, L_4, and L_5 are called libration regions.

In the absence of perturbations by other celestial bodies, a small mass finding itself at rest near one of these equilibrium positions would tend to remain there. An example is the Sun-Jupiter-Trojan asteroids system. The Trojan asteroids are located near libration regions L_4 and L_5, as shown on the right in figure 3-22.

A number of ground-based observers have studied the L_4 and L_5 regions associated with the system Earth-Moon-particle. If small particles had accumulated in these regions, their presence might be detected by "excess" brightness from reflected sunlight. Since the light of the night sky is very faint and nonuniform, it is very difficult to identify the origin of localized patches of "excess" brightness. Both positive and negative results have been obtained in studies from the ground, where the L_4 and L_5 regions must be observed at large scattering angles.

At smaller scattering angles, the brightness from any material in these regions would be greater than that seen at the larger angle. Observation at these angles (near the Sun) is possible only from above the Earth's atmosphere. The brightness of the L_4 and L_5 regions at small Sun-region-Skylab angles was measured on photographs taken with the Skylab coronagraph (S052).

The photographs were examined by Robert MacQueen, of the High Altitude Observatory in Boulder, Colorado, the principal investigator of the coronagraph experiment, and by Alison Hopfield, of the Princeton Day School, Princeton, New Jersey. Miss Hopfield's suggestions that the lunar libration regions be studied was one of 25 experiments that were proposed by high school students and selected for the Skylab student experiment program. No excess brightness and hence no dust clouds could be distinguished against the solar coronal background in the photographs. An upper limit to the libration cloud radiance of 2.5×10^{-11} of the mean radiance of the solar disk was determined. When this upper limit was combined with past measurements of the back-scattered radiance of the libration region, certain candidates for the nature of the interplanetary dust could be eliminated. It was calculated that the radiance contrast of a possible libration cloud, composed of remaining candidate materials, would be maximum at about 30° from the Sun. However, that location was not within the field of view of the coronagraph. Thus the observations serve as a guide for future ground-based or spaceborne experiments.

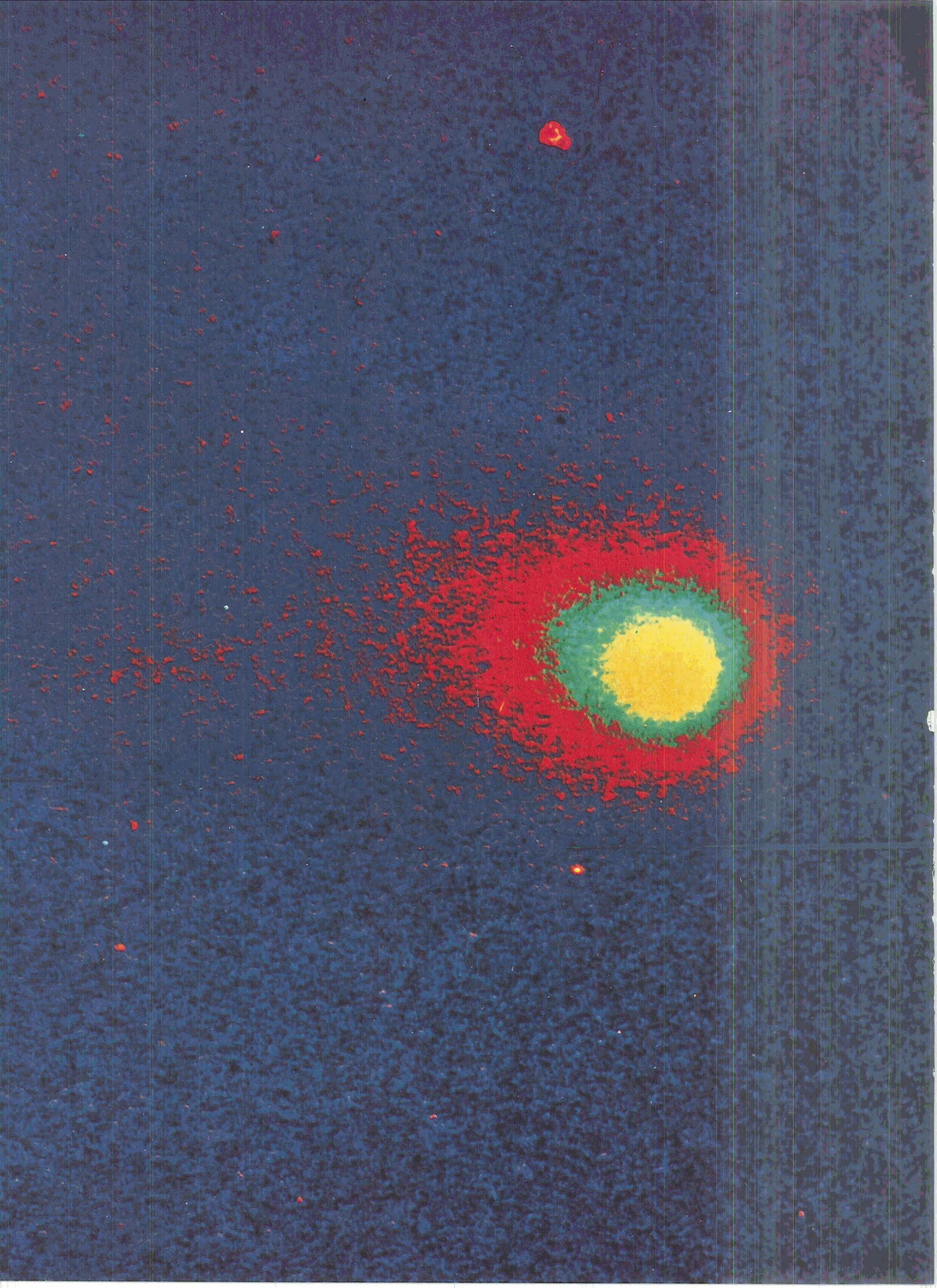

4
Observations of Comet Kohoutek

Comet Kohoutek (1973 XII) was discovered by Lubos Kohoutek during a search for asteroid images on photographic plates taken in early March 1973 at the Hamburg Observatory, in the Federal Republic of Germany. Calculations of its size and orbit showed it to be a large comet that would pass close to the Sun, reaching perihelion at the end of 1973.

This early discovery of a large comet in an orbit that would carry it close to the Sun prompted the National Aeronautics and Space Administration to initiate "Operation Kohoutek," a program to coordinate widespread observations of the comet from ground observatories, aircraft, balloons, rockets, unmanned satellites, and Skylab. This program was headed by Stephen P. Maran of the Goddard Space Flight Center. The third Skylab mission was rescheduled so as to make the best use of this opportunity—specifically to permit observations from Skylab during a period centered on perihelion. It is during this period that the most interesting and dramatic changes happen to comets, and it is also during this period that observations from the Earth's surface are hardest to make or even impossible because light from the nearby Sun is scattered by the Earth's atmosphere into instruments aimed at the comet.

Another factor making Comet Kohoutek an attractive subject for study was the fact that orbital calculations suggested it was a new comet—one that had never before passed close to the Sun and would therefore be expected to differ from comets that had periodically returned.

Figure 4-1 is a false-color contrast-enhanced picture of Kohoutek taken in Lyman-alpha light. It shows a hydrogen halo that is three times the diameter of the Sun. The brightest area (the center) is yellow, and the succession of colors outward indicate decreasing brightness.

Figure 4-2 shows Comet Kohoutek photographed on April 28, 1973, at the Kitt Peak National Observatory, Tucson, Arizona. The photograph was made with NASA's integrating vidicon system by astronomers Stephen P. Maran, Hong-Yee Chiu, and Robert W.

Figure 4-1.—Comet Kohoutek photographed with the far-ultraviolet electrographic camera during a Skylab spacewalk on December 25, 1973. It is shown here in a false-color reproduction of a black and white photograph.

Figure 4-2.—Comet Kohoutek (arrow) photographed at the Kitt Peak National Observatory on April 28, 1973, a few weeks after its discovery. North is toward the left; west is toward the top.

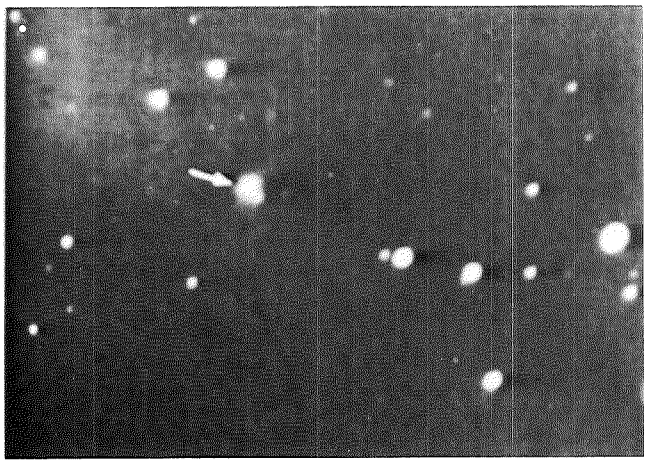

Hobbs of the Goddard Space Flight Center. At that time, a few weeks after its discovery, the comet was still 4.2 AU from the Sun, the magnitude of the nucleus was 17.2, and the estimated total magnitude was about 15.

The Comet as Seen from Earth

When a comet is first observed, sometimes at great distances from the Sun, it appears as a fuzzy object among the stars, as in figure 4-2. As the comet comes closer to the Sun, its appearance changes, and it is seen as having a bright center surrounded by a fuzzy cloud. The bright center is called the central condensation and surrounds the nucleus. The fuzzy cloud is called the coma. The change is real and is caused by the Sun's heat. Some of the surface material is vaporized and, together with dust that is liberated, forms a cloud. The remains of the original mass and the cloud both reflect or scatter light and are seen as the nucleus and coma, respectively.

As a comet approaches within a couple of astronomical units of the Sun, its most spectacular feature, the tail, gradually appears. Figures 4-3 and 4-4 show Comet Kohoutek photographed from the Joint Observatory for Cometary Research, South Baldy Mountain, New Mexico. The photograph in figure 4-3, taken on December 7, 1973, shows the comet about 3 weeks before its closest approach to the Sun (perihelion).

When it gets close to the Sun, the comet disappears from view against the bright background. Emerging on the other side of the Sun, it is again visible. Some of the visual differences observed among comets are attributable to relative distances and angular positions between comet, Sun, and Earth. Other differences are probably caused by the size and constituents of the comet.

Knowledge of the structure and composition of comets comes from spectral study and dynamic analysis. According to the most widely accepted theory of comet structure, the nucleus consists of a "dirty snowball," whose principal constituents are various frozen gases and solid particles of dust. The particles of minerals, or stony dust, range from perhaps a few millimeters in diameter to microscopic size and are held in place by the matrix of frozen gases.

As a comet approaches the Sun, its surface gradually heats up and the frozen gases begin to vaporize. Because of the low pressure in space, these materials will turn immediately from solid into gas and begin to form the comet's growing coma. The dust particles interspersed in the volatile matrix are released and initially mix with the gases in the coma.

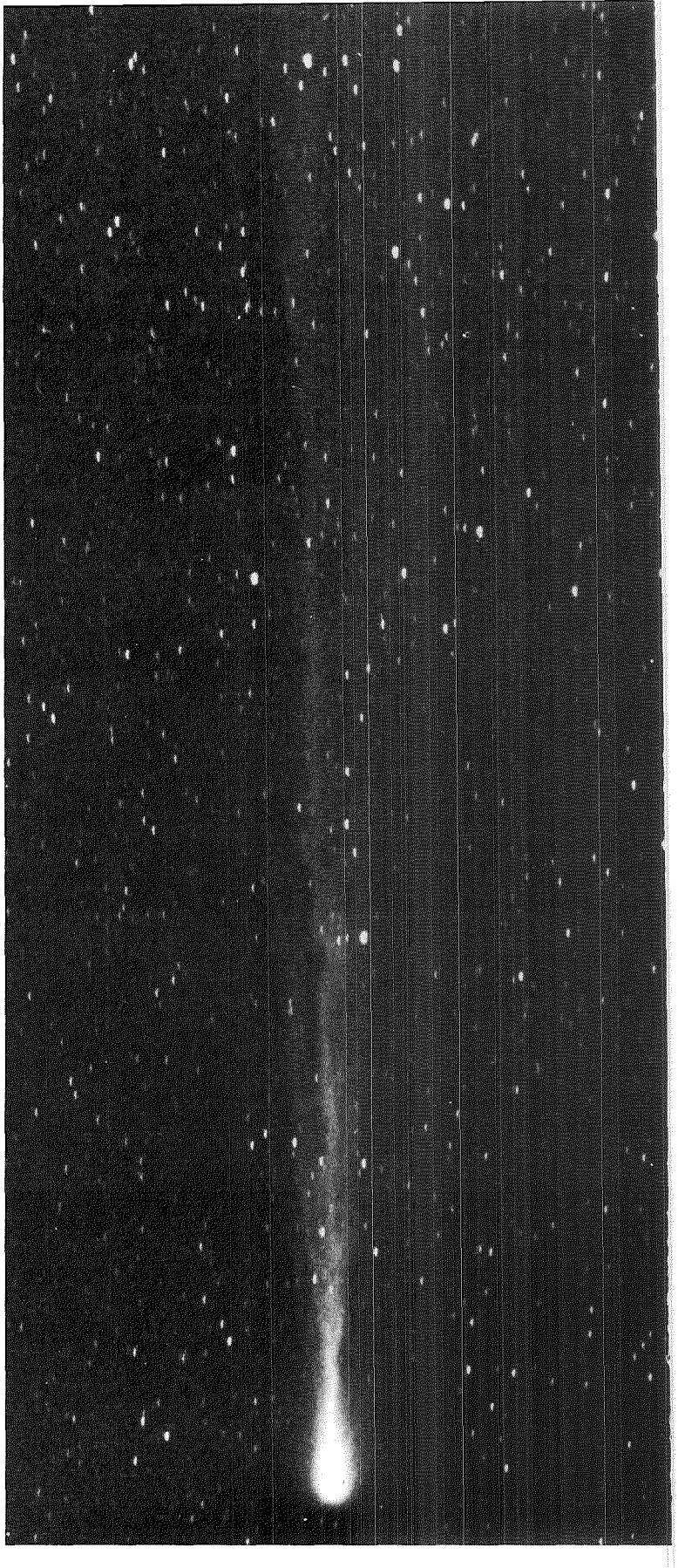

Figure 4-3.—Comet Kohoutek photographed from the Joint Observatory for Cometary Research, South Baldy Mountain, New Mexico, on December 7, 1973, about 3 weeks before perihelion.

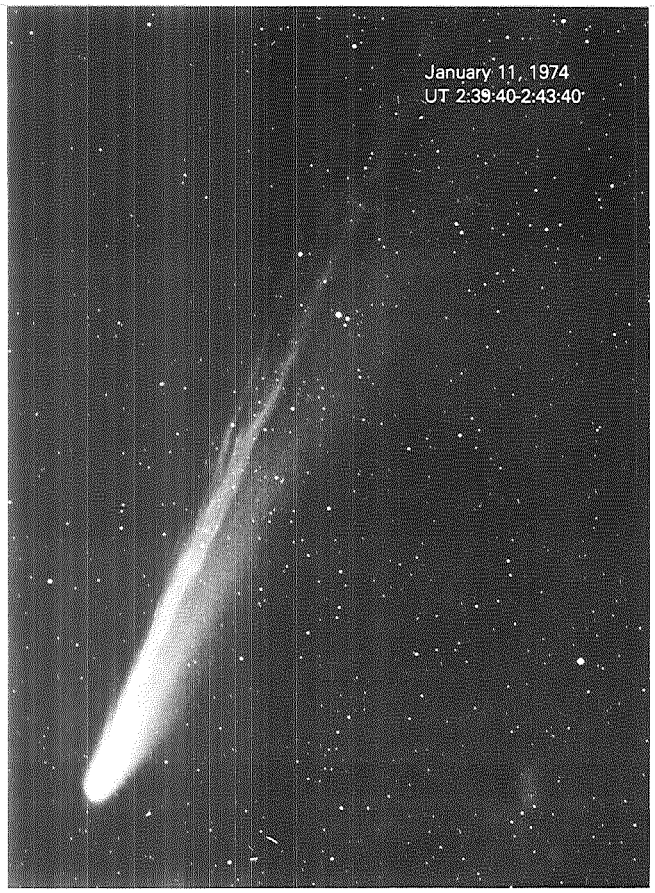

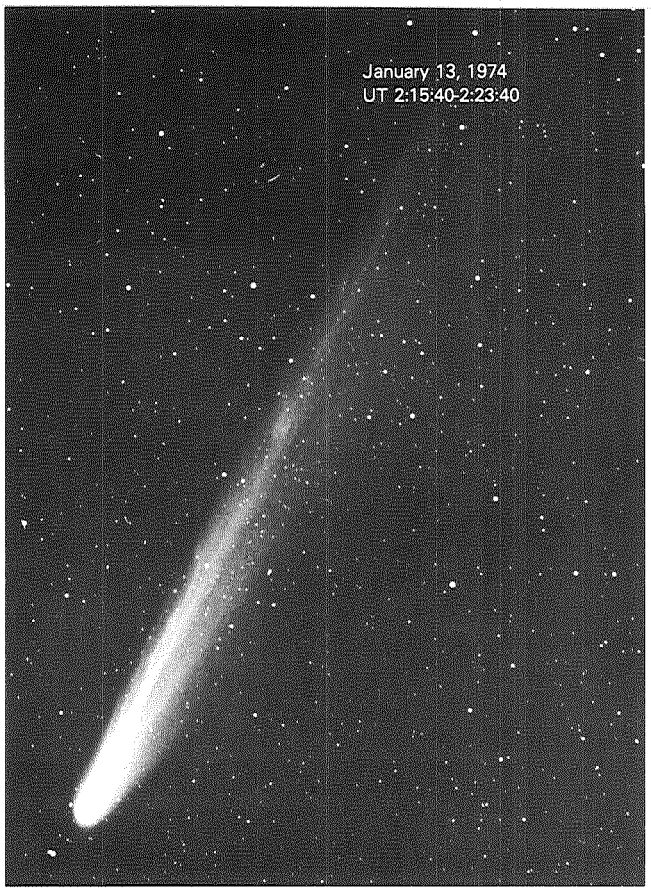

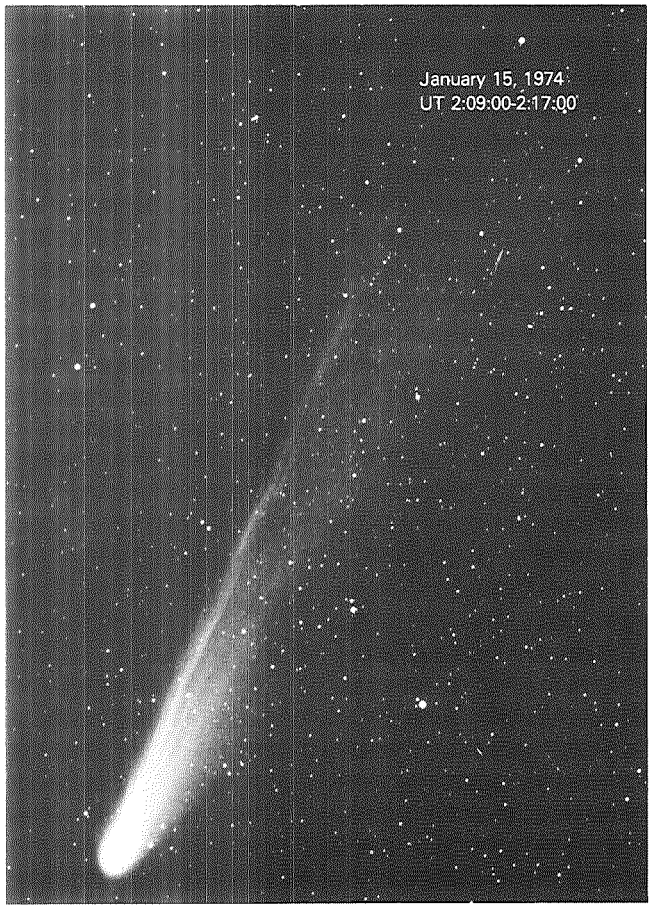

Figure 4-4.—Changes in the appearance of Comet Kohoutek from January 11 to January 20, 1974. Photographs taken at the Joint Observatory for Cometary Research.

The neutral gases continue to expand into an ever larger cloud about the comet. While this happens, sunlight dissociates some of the more complex molecules into simpler chemical species. One dissociation product is atomic hydrogen, which gives rise to the very large hydrogen halo observed around Comet Kohoutek (fig. 4-1). Dissociated water vapor is probably the principal source of this hydrogen.

Some gases released from the comet become ionized and interact strongly with the solar wind—the flow of ions streaming from the Sun. This ionized gas forms a plasma tail. Such a tail (type I) points away from the Sun. It is usually not appreciably curved, although some twisting and irregular motion within the tail may be present, as is the case in figure 4-3.

Sunlight pushes the microscopic dust particles released from the comet away from the Sun, and away from the comet, to form a tail. This tail of dust, known as a type II tail, points generally away from the Sun, regardless of the direction in which the comet is moving. However, the different motion of the dust particles released at different times will cause the tail to appear somewhat curved. This type of tail is generally white because it unselectively reflects or scatters visible light from the Sun.

When the Earth is near the orbital plane of the comet, part of the dust tail occasionally seems, in projection, to be pointing toward the Sun. This type III "antitail," which consists of large dust particles, is discussed later. Such an "antitail" on Comet Kohoutek was visible from Skylab shortly after perihelion, before it was possible to view it from ground-based observatories.

Pictures of Comet Kohoutek shown in figure 4-4 were taken at the Joint Observatory for Cometary Research

Figure 4-5.—Typical comet spectrum (box) and the spectral capabilities of Skylab instruments (identified by experiment number at left).

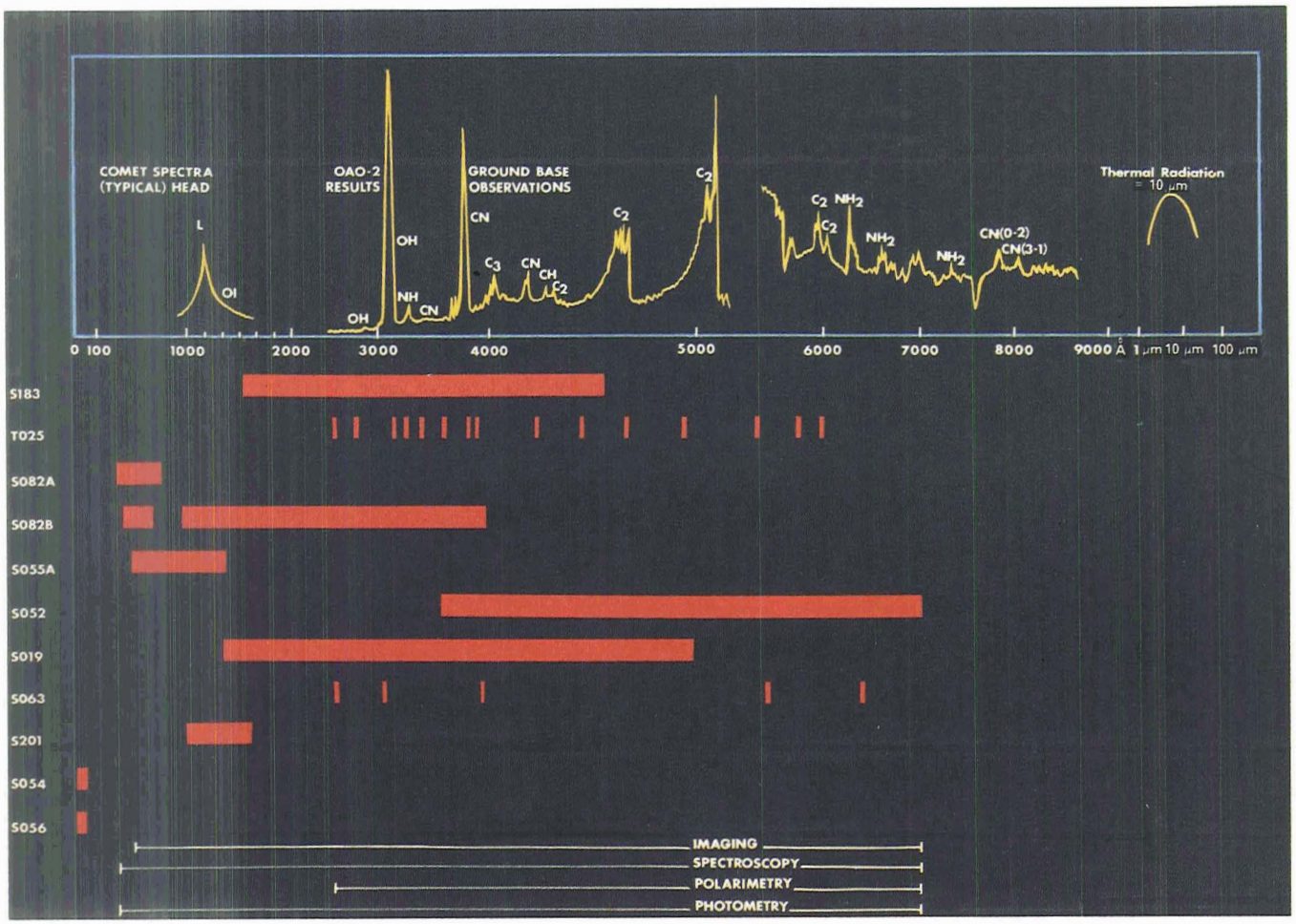

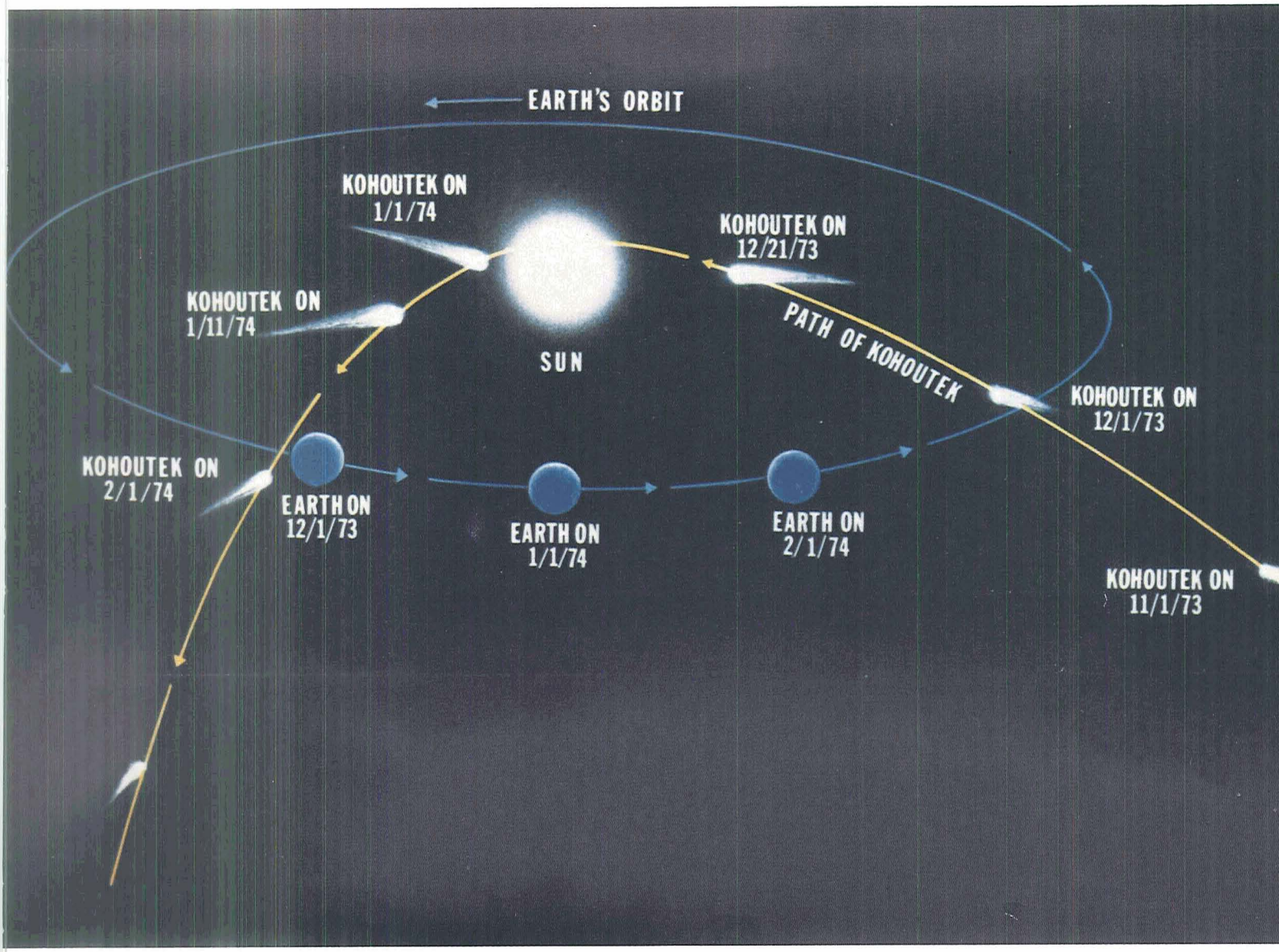

Figure 4-6.—Comet Kohoutek's path around the Sun.

and show the changes in appearance from day to day, and in some cases from hour to hour, of an active comet. The curved dust tail reflects and scatters the light of the Sun and therefore appears white to yellow on a color photograph. The plasma tail shows many branches and numerous waves and whorls, indicating the irregular fluctuations of the solar wind. Studies of such plasma tails gave rise to the first ideas of the existence of the solar wind. In color photographs, the plasma tail appears bluish. In order to bring out details of the tail structures, these photographs were taken at exposures that overexposed the head, and therefore no details are visible in the central region of the comet.

Instrument Selection

During the preparations to observe Comet Kohoutek, it was determined that some of the instruments already on board Skylab for other experiments could be used to study the comet (fig. 4-5). Some of these instruments were designed to view the bright Sun, and their use to observe the comet was considered to be exploratory in

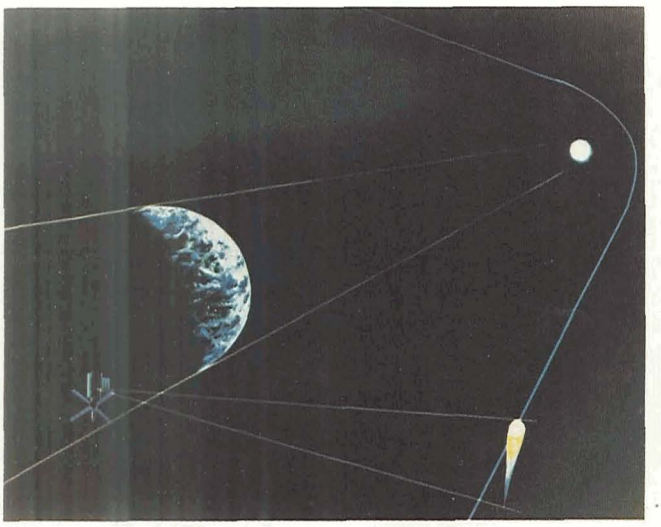

Figure 4-7.—The geometry of observation of Comet Kohoutek—preperihelion.

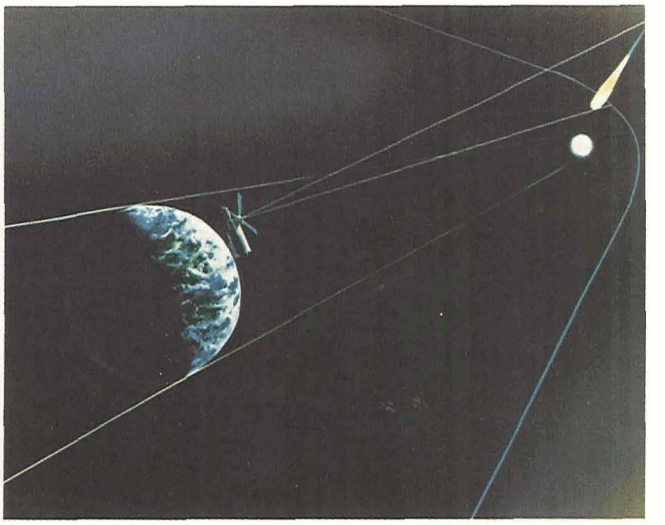

Figure 4-8.—The geometry of observation of Comet Kohoutek—perihelion.

nature. To design, build, test, and launch new instruments was not possible since such a process generally takes 2 to 3 years. However, one instrument, the backup far-ultraviolet electrographic camera (S201) used on Apollo 16, was available. After minor modifications, it was taken up to Skylab by the third crew.

The far-left column of figure 4-5 lists the instruments on Skylab, identified by experiment numbers. As individual instruments are discussed, these numbers will be given for reference. To the right of each number is shown the portions of the electromagnetic spectrum in which the instrument makes observations. The wavelength scale for this spectral response is given in angstroms or micrometers along the bottom of the blue box. Within the box a typical comet spectrum is shown, with indications of several of the molecules responsible for individual features. Thus figure 4-5 illustrates which Skylab instruments could be expected to measure the various spectral features of a comet.

Comet Orbits

The path of a comet is essentially an ellipse, sometimes of such great eccentricity that it is very nearly a parabola. An ellipse is a closed curve, and a comet with an elliptical path may be expected to have a finite period of revolution about the Sun. Early predictions for Comet Kohoutek indicated it had an elliptical orbit with a period 50 000 to 200 000 years for one such journey. A part of this uncertainty was associated with the difficulty of making an early determination of the comet's position in space. Also significant are the perturbations experienced by the comet in its long journey, especially those caused by the gravitational force of Jupiter.

Kohoutek's closest approach to the Sun (fig 4-6), at a distance of 0.142 AU, was made on December 28, 1973, although to an Earth observer the comet appeared closer on December 27. The orbit was inclined to the ecliptic plane by 14°, and the Earth passed through this plane on December 9, 1973. Another interesting circumstance occurred on January 15, 1974, when the dust tail's position relative to the Earth gave an observer on Earth the best view of its entire length.

Skylab's Location

Because Skylab was above the Earth's atmosphere, its instruments were in a favorable position to photograph Comet Kohoutek as it swung around the Sun. Because Skylab orbited the Earth approximately 15 times daily, the viewing opportunities were shorter, but more frequent, for the astronauts than for observers on Earth.

Observations by instruments in the airlock module were made during the brief periods that the comet was visible but the Sun was not (because Skylab was in the Earth's shadow). The observations also required maneuvering Skylab. Before perihelion, Kohoutek was viewed between "cometrise" and sunrise (fig. 4-7). This observation period varied from 0 to 26 min, as determined by the positions of the comet, the Sun, and the space station.

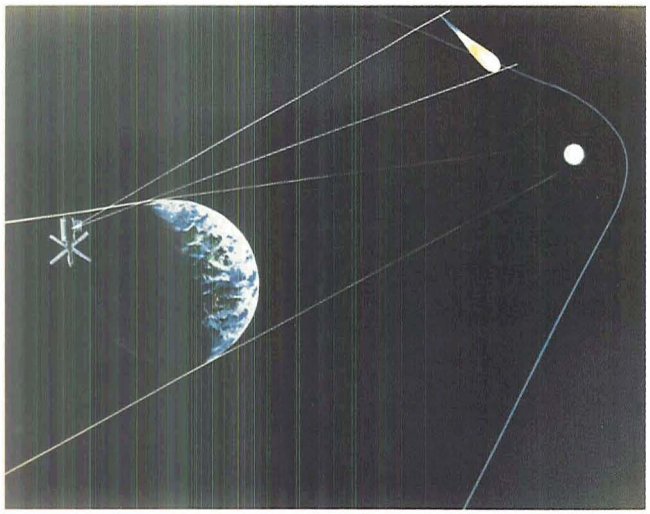

Figure 4-9.—The geometry of observation of Comet Kohoutek—postperihelion.

When the comet was nearest the Sun, the astronauts focused the solar observatory instruments on the comet (fig. 4-8). This was done almost continuously during 21 consecutive orbits centered around the closest angular approach, as seen from the Earth and Skylab, on December 27, 1973.

Like the preperihelion observations, the postperihelion measurements required shadowing and had to occur after sunset but before "cometset" (fig. 4-9). The maximum postperihelion time available for viewing Kohoutek was approximately 17 min during each orbit.

Hydrogen Halo

Photographs of the halo about the comet were taken in hydrogen Lyman-alpha light with the electrographic camera (S201) aboard Skylab and are shown in figure 4-10. The size and brightness of the halo are plotted in

Figure 4-10.—Comet Kohoutek's halo photographed in hydrogen Lyman-alpha light with the electrographic camera aboard Skylab. In all photographs the Sun is toward the bottom. All times are GMT. A. 11-26-74, 23:29; B. 12-5-74, 22:08; C. 12-12-74, 01:46 (near horizon); D. 12-16-74, 17:41 (near π, δ Scorpio); E. 12-23-74, 16:03 (near θ Ophiuchus); F. 12-25-74, 21:33.

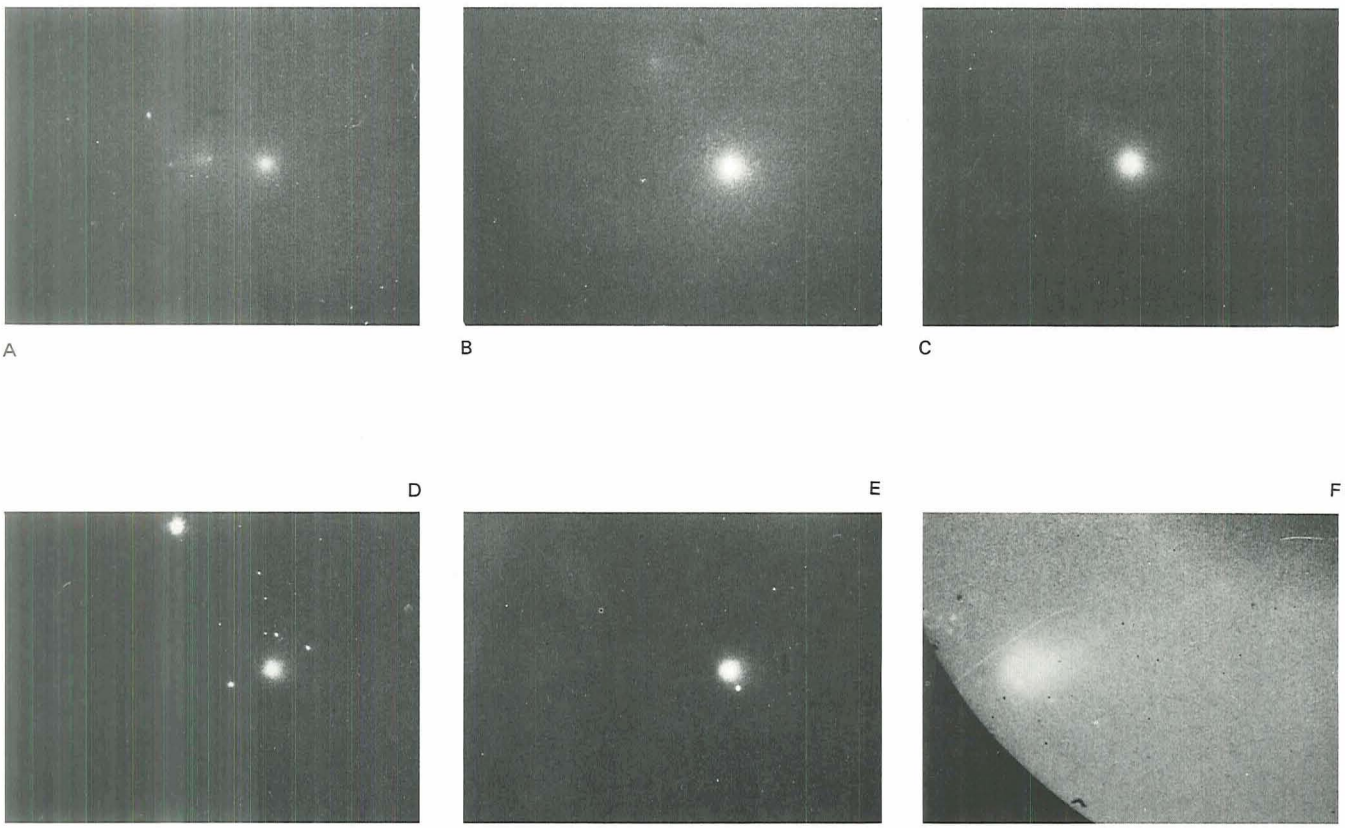

figure 4-11 and are shown to have reached a preperihelion maximum on December 12, 1973. On the basis of a simplified comet model, and allowing for changes in camera sensitivity and Earth-to-comet distances, Thornton Page, principal investigator for these observations, suggests that a layer of volatile material in the comet nucleus boiled off just before December 12.

The general behavior of the hydrogen cloud surrounding the comet confirms earlier findings and gives support to the current "dirty-snowball" model. Data on the growth and morphology of the halo gathered by Skylab represent the first extended observation performed on any comet.

The curves in figure 4-12 illustrate how the comet's calculated hydrogen production rate varied with the comet-to-Sun distance. They are based on the S201 Skylab data and results of a similar experiment conducted from an Aerobee rocket. The outflow velocity of hydrogen atoms from the nucleus of the comet was calculated to be approximately 8 km/sec.

Figure 4-11.—Size and relative brightness of Comet Kohoutek's hydrogen halo as a function of comet-to-Sun distance.

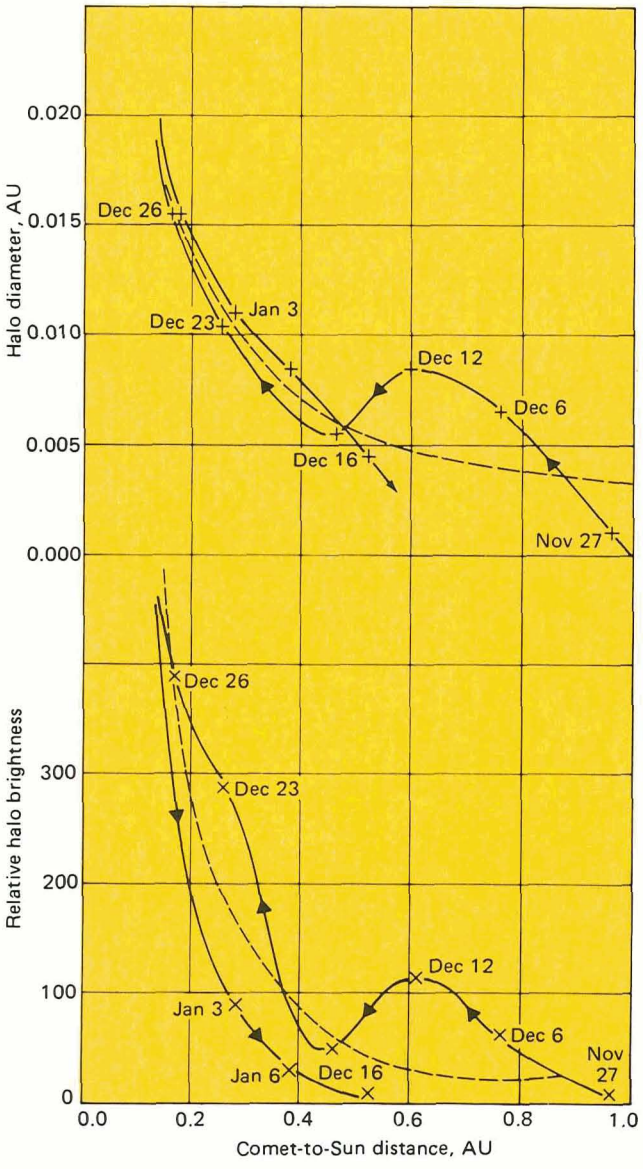

Figure 4-12.—Calculated rate of hydrogen production by Comet Kohoutek as a function of comet-to-Sun distance.

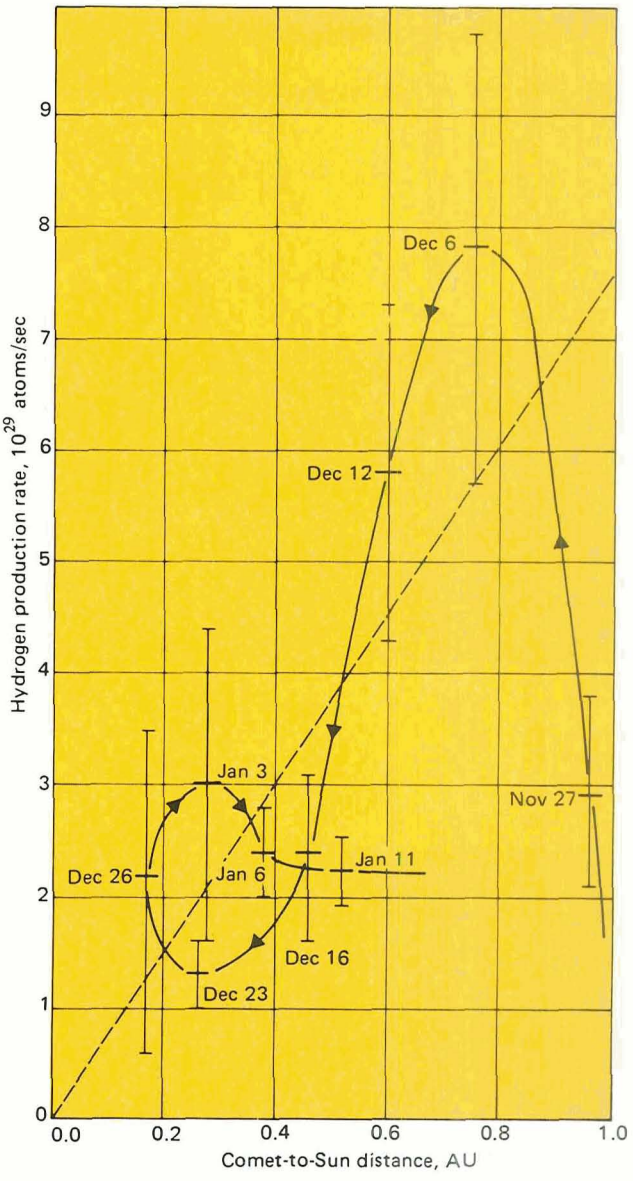

Figures 4-13 through 4-15 illustrate the use of sophisticated image-processing techniques to reveal information not readily obtained from simple images. Figure 4-13 is a conventional image of the sky obtained on December 25, 1973, with the electrographic camera at wavelengths from 125 to 160 nm. Figure 4-14 was obtained from an enlargement of part of figure 4-13 by a photographic technique in which the varying optical density of the film (the "brightness" of the sky) is translated into various colors. The original image, of course, has a continuous gradation of density, but the processed image is divided into a few zones of color corresponding to ranges of density. Despite this loss, the false-color image reveals more detail to the human visual system than does the original.

In figure 4-15, the same result was obtained by a much more elaborate method. The original image was scanned with a microdensitometer, and the density of the film was measured digitally at millions of points on a regular grid. From those millions of numbers, recorded on magnetic tape, a computer produced a "contour map" in which the lines are lines of equal intensity in the original image.

Figures 4-13 to 4-15 show a longer tail than do the other photographs at these wavelengths. The source of the light, however, is still an unsolved puzzle. The first conjecture was that it came from atomic oxygen radiating at 130.4 and 135.6 nm. Atomic oxygen, however, has too short a half-life under these conditions to give a tail of this length. It would not last long enough to travel that far at the calculated velocity. Another suggestion is that an unidentified molecule is absorbing and reemitting the far-ultraviolet light. Thornton Page suggests that the visibility of the extended tail in the far ultraviolet may result from scattering by dust particles.

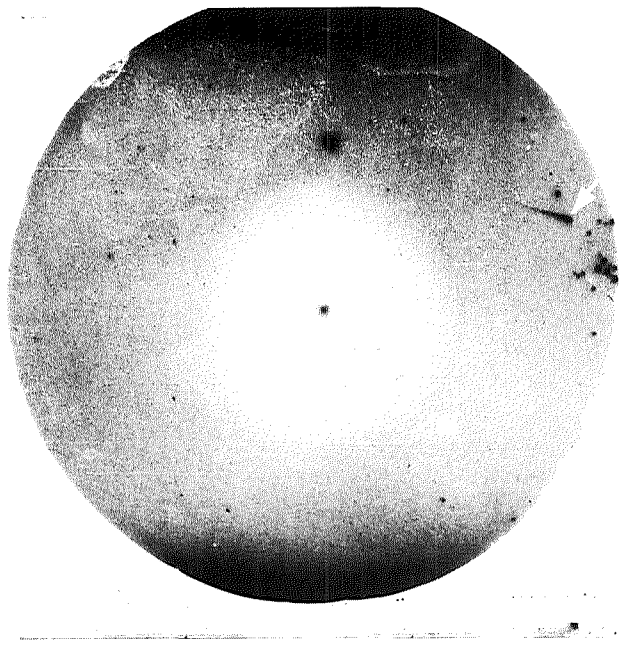

Figure 4-13.—Comet Kohoutek and stars photographed on December 25, 1973, by Skylab's electrographic camera filtered for wavelengths from 125 to 160 nm.

The Ultraviolet Spectra of Kohoutek

Skylab's ultraviolet objective-prism spectrograph (ultraviolet stellar astronomy experiment, S019) obtained nine images of Kohoutek; five of these are shown in figure 4-16. Data analysis was performed at the University of Texas. The objective-prism spectrograph was designed to produce the ultraviolet spectra of stars at wavelengths of 130 to 500 nm. The second photograph shows several dispersed stellar images in which visible light lies at the right and far-ultraviolet light lies at the left of each highly elongated image. The bright core of the comet's image shows only a slight elongation because there is no significant ultraviolet radiation from the comet. The comet's images were formed by light with wavelengths from 300 to 500 nm and indicate a surprisingly sharp cutoff of ultraviolet radiation below 300 nm.

The comet nucleus in figure 4-16 appears double on the first three dates. This double structure is confirmed in figure 4-17, which is an isophote map of the comet's appearance on December 13. The two knots in the nucleus represent the wavelength separation of the two strongest emission bands in the 300- to 500-nm region of the spectrum—namely, the emission from OH at 309 nm and the emission from CN at 388 nm. The fact that the double structure is not so clearly seen in the last two photographs in figure 4-16 is evidence that the OH emission was considerably weaker on those dates.

Kohoutek Visually Observed

Figure 4-18 shows sketches of Comet Kohoutek made by Edward G. Gibson, scientist pilot of the third crew. These sketches are based on the crew's collective impressions of the comet's appearance on December 29, 1973, as observed through 10-power binoculars. The upper drawing was made just after perihelion and shows the long, yellow-white "antitail" pointed toward the Sun. The head of the comet is extremely bright, and the tail is pointing away from the Sun. The lower drawing

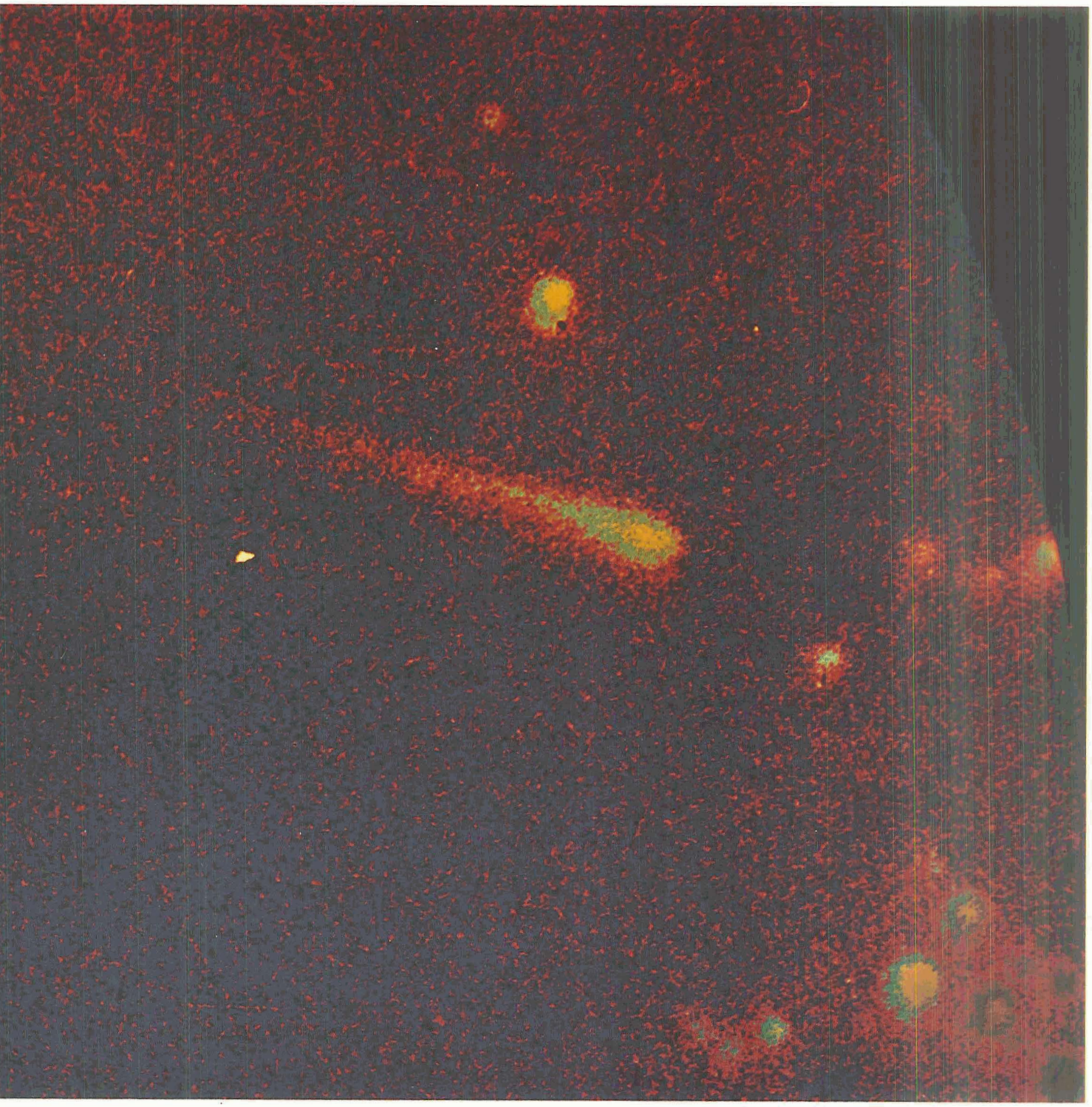

Figure 4-14.—False-color enhancement of the photograph shown in figure 4-13.

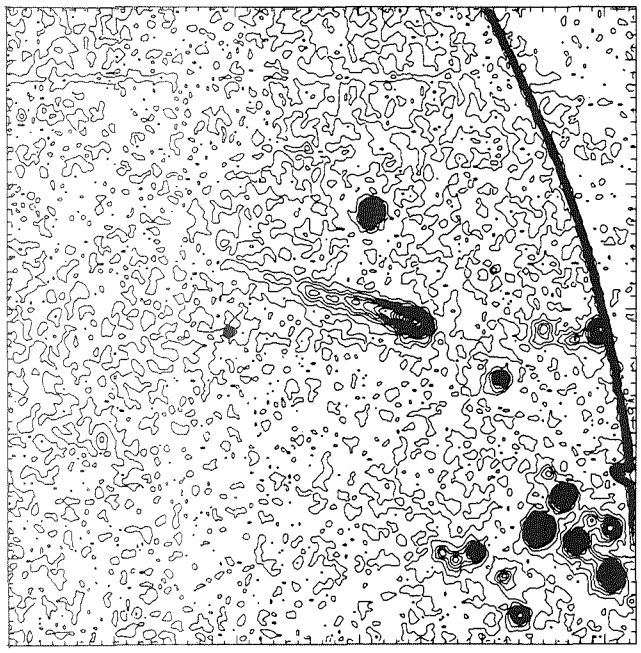

Figure 4-15.—Isophote plot of the photograph shown in figure 4-13.

illustrates isophotes (lines of equal intensity) with the comet brightest at the nucleus and least at the outer edges. The length of the visible comet was determined from the angle it subtended, estimated from the amount of the field it filled in binoculars with a 7° field of view.

Pencil sketches and notes were made of the color, shape, size, and intensity of the comet on 10 different days. The color sketches shown in figure 4-19 were made by an artist after the mission, utilizing Gibson's notes and recollections.

Kohoutek Passing the Sun

The solar observatory's control and display panel is shown in figure 4-20. It was from this panel that the astronauts oriented Skylab to point the solar instruments at the comet as it passed near the Sun.

The white-light coronagraph (S052), designed for solar corona observations by R. MacQueen and associates at the High Altitude Observatory in Boulder, Colorado, was used to obtain measurements while the comet appeared closest to the Sun. This instrument made more than 1600 photographs from December 14, 1973, to January 6, 1974, at wavelengths of 350 to 700 nm. Analysis of the photographs provided data on dust-production rates and grain-size distribution in the comet.

A 27-sec exposure of Comet Kohoutek (fig. 4-21) was made at 2353 GMT on December 28, 1973. The instrument was not pointed directly at the Sun. The picture shows the "antitail," or "sunward spike," of the comet approximately 13 hr after perihelion passage. Instrumental vignetting has reduced the brightness of the tail so that it does not appear. Detailed photometric measurements of these images provide data that permit the size, distribution, and production rate of the dust particles that make up the spike to be estimated as a function of time. Images of distant stars as faint as visual magnitude 7.4 are visible in the original photographs.

Figure 4-22 shows a series of photographs taken by the white-light coronagraph on December 27 and 28, 1973, when the comet was passing the Sun. The first picture was taken at 0441 GMT on December 27 and the last at 0201 GMT on December 28. The coronagraph was designed to improve photographs of the corona by

Figure 4-16.—Ultraviolet images of Comet Kohoutek obtained with Skylab's objective-prism spectrograph. Dates and exposure times (from left to right): December 13, 200 sec; December 16, 270 sec; January 7, 400 sec; January 8, 500 sec; and January 12, 720 sec.

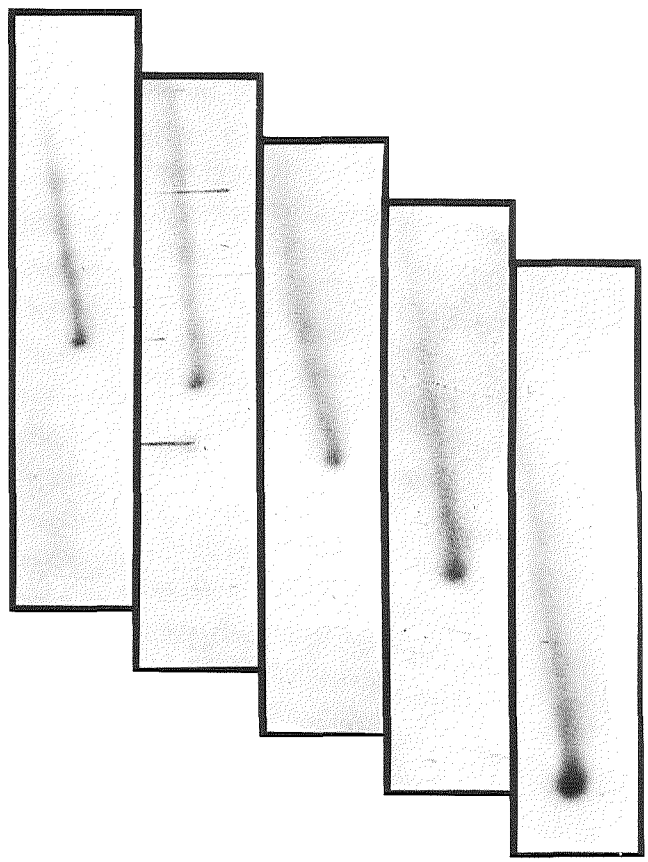

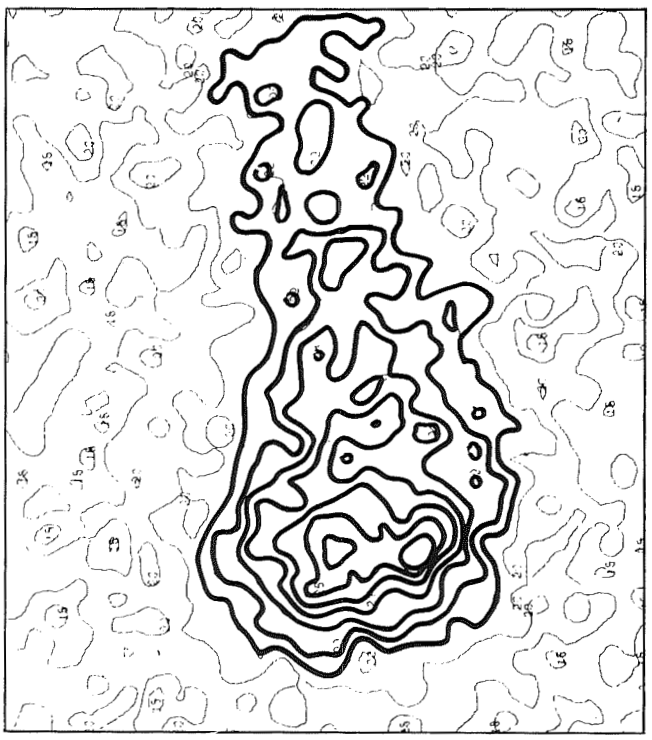

Figure 4-17.—Isophote plot of the ultraviolet photograph of Comet Kohoutek taken on December 13, 1973 (see figure 4-16).

flattening the intensity gradient through deliberate vignetting. Because of this designed characteristic of the instrument, the image of the comet shows reduced brightness when the comet is near the occulting disk. Photometric analysis of the white-light coronagraph data for this period provided information on Kohoutek's brightness variation with time and filled the gap in Earth-based observations between preperihelion and postperihelion.

Other Solar Observatory Results

Five photographic plates exposed in the solar observatory's ultraviolet spectrograph (S082B), operating in the spectral range of 97 to 394 nm, resolved the line profile of 121.6-nm Lyman-alpha light reflected and scattered by Comet Kohoutek. However, any other emission lines in this waveband were not detected because of basic limitations of the instrument's sensitivity, Skylab's pointing capability, and the comet's brightness. Richard

Figure 4-18.—Sketches of Comet Kohoutek made by Edward G. Gibson, scientist pilot of the third Skylab manned mission, illustrating the crew's collective impressions of the comet's appearance on December 29, 1973. The scale is E–M units (Earth–Moon distance, ~380 000 km).

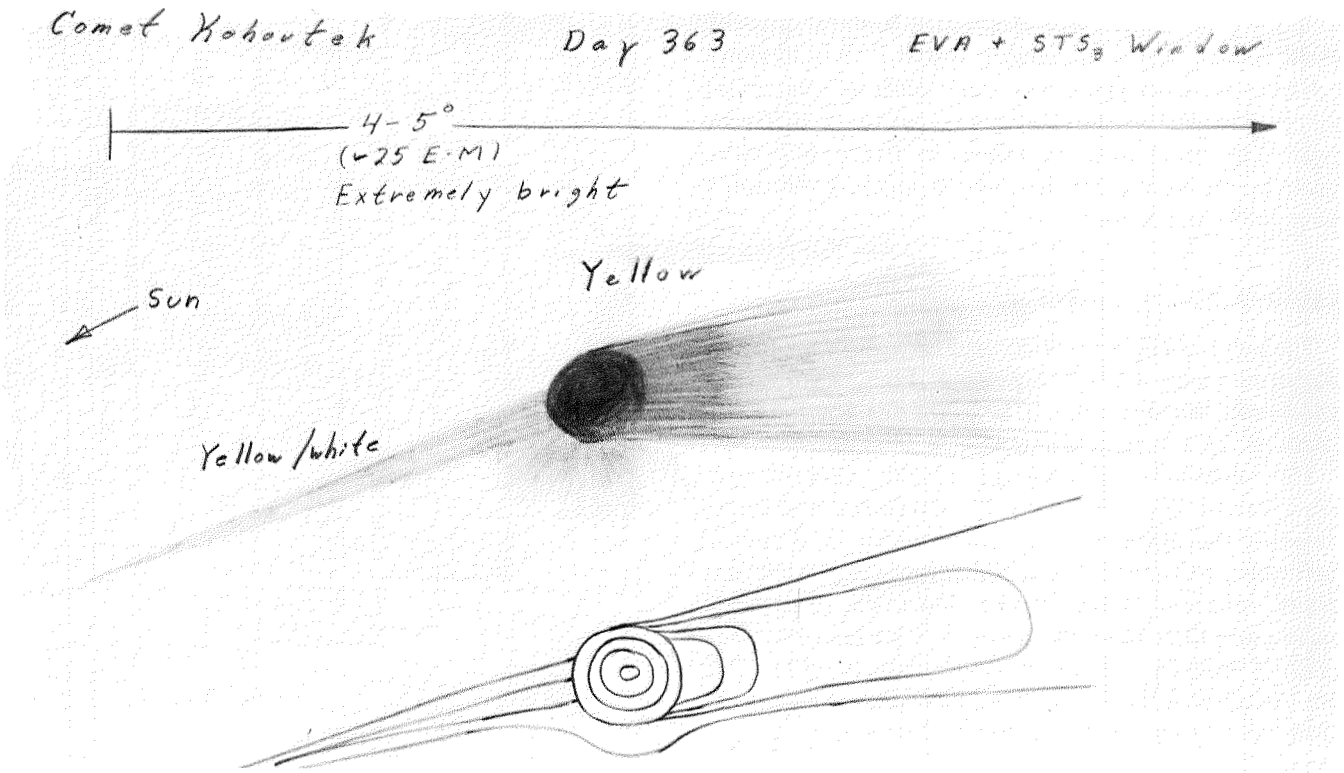

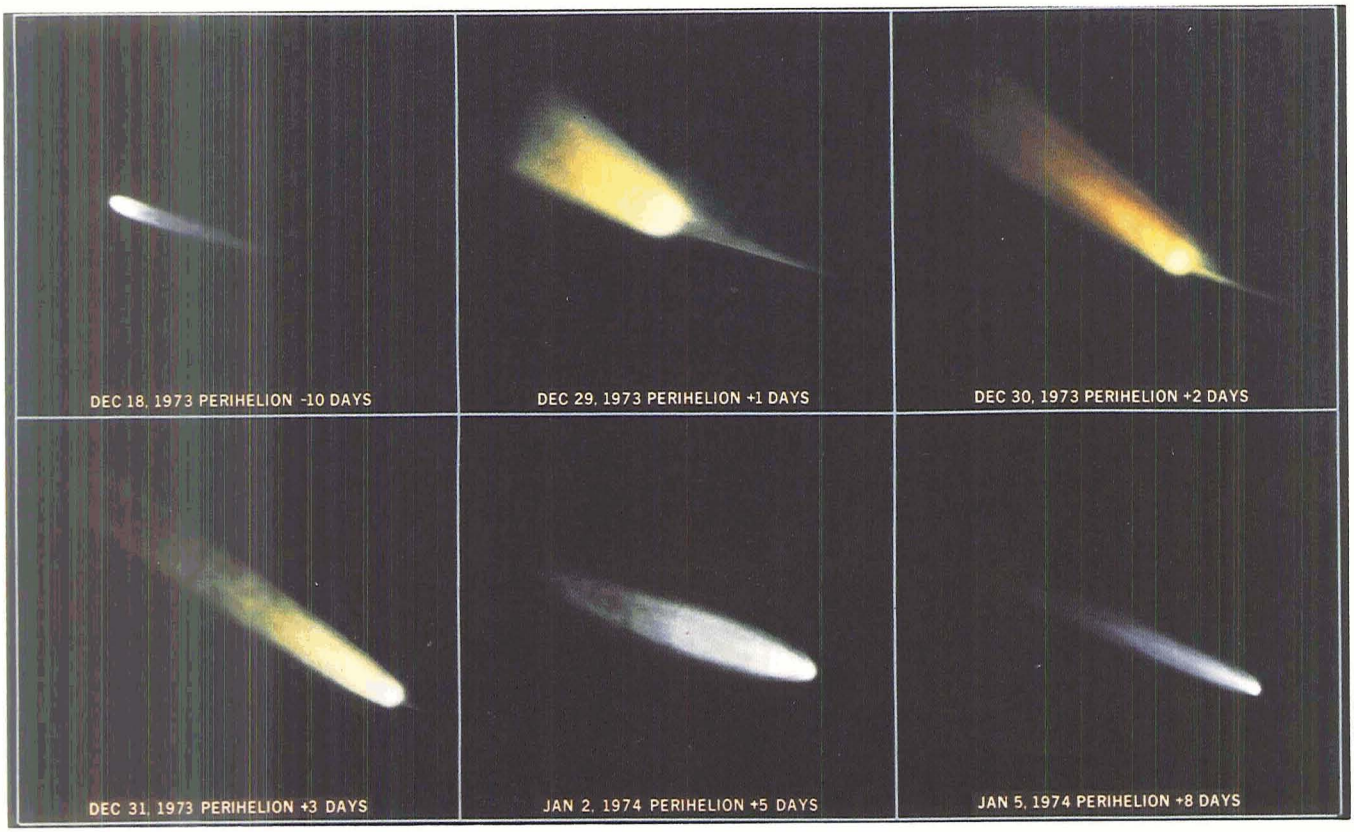

Figure 4-19.—Artist's conception of a changing Comet Kohoutek, based on sketches and descriptions by scientist pilot Edward G. Gibson.

Figure 4-20.—Astronaut Gibson at control and display panel of the solar observatory aboard Skylab.

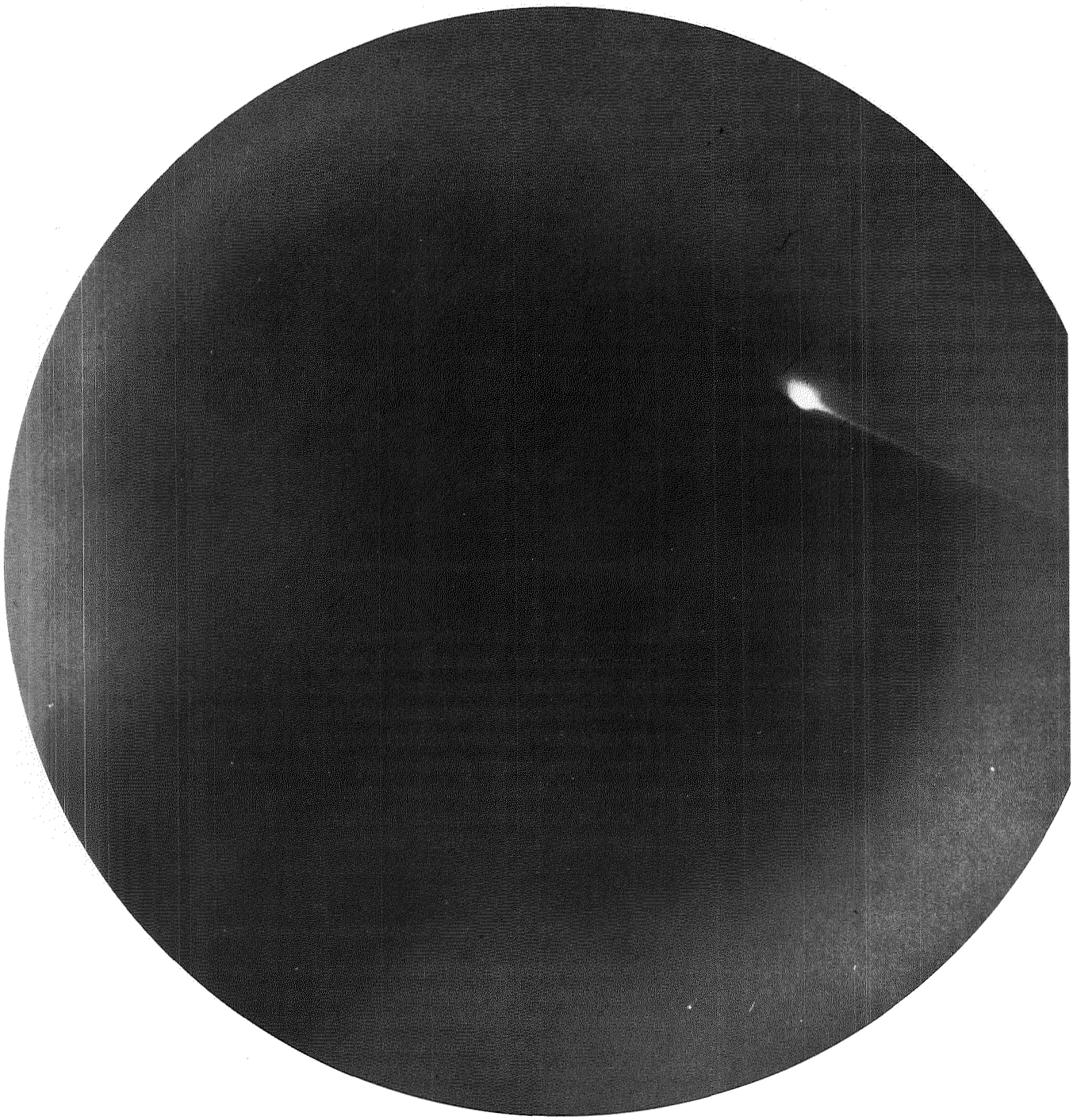

Figure 4-21.—The "antitail" (sunward spike) of Comet Kohoutek seen in a 27-sec exposure made at 2353 GMT on December 28, 1973, about 13 hr after perihelion passage. The instrument was not pointed directly at the Sun.

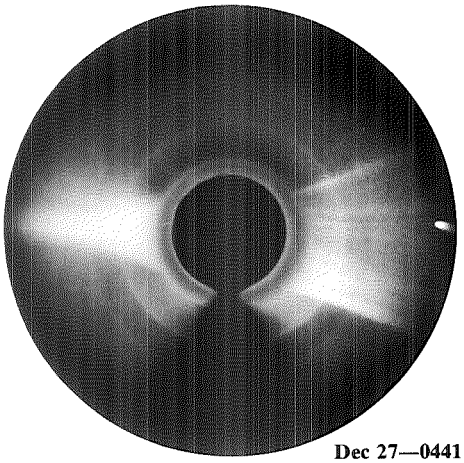

Dec 27—0441 GMT

Figure 4-22.—Series of photographs taken by the white-light coronagraph on December 27 and 28, 1973, when Comet Kohoutek was passing the Sun.

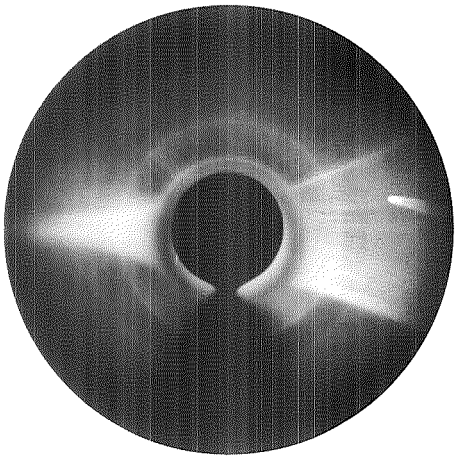

Dec 27—0710 GMT

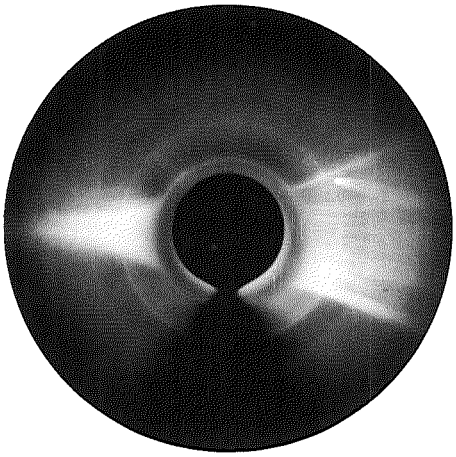

Dec 27—1020 GMT

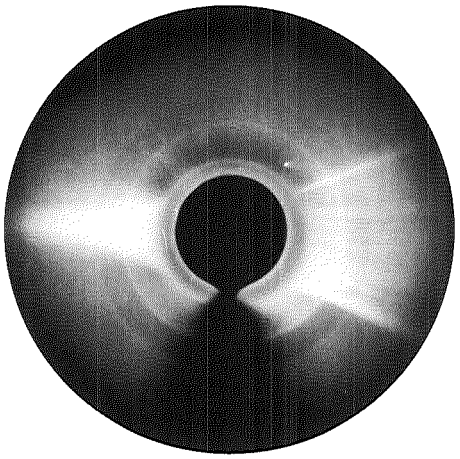

Dec 27—1327 GMT

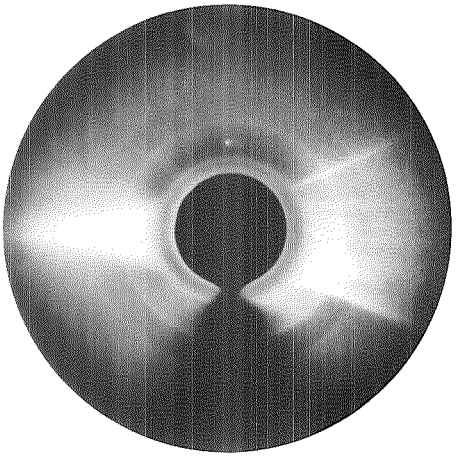

Dec 27—1630 GMT

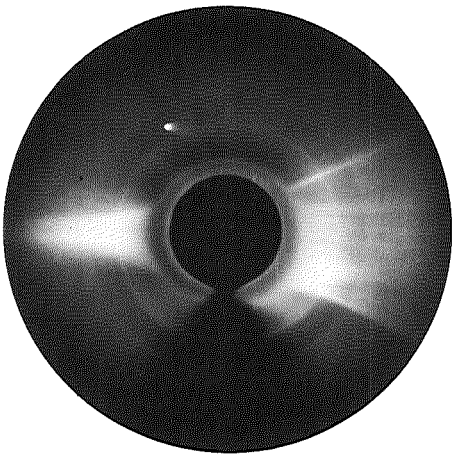

Dec 27—1938 GMT

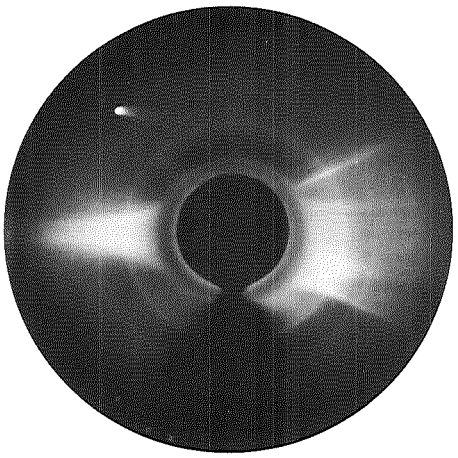

Dec 27—2242 GMT

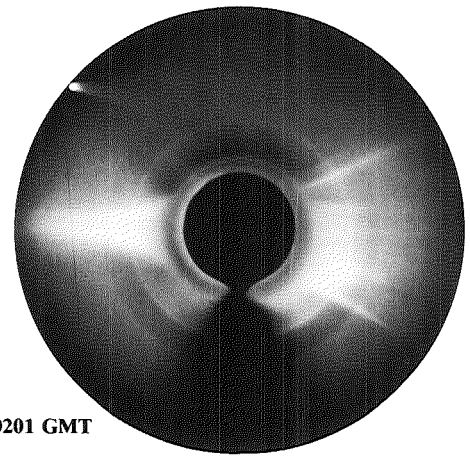

Dec 28—0201 GMT

Tousey and David Bohlin of the U.S. Naval Research Laboratory reported that the full width at half maximum intensity of the Lyman-alpha line was 0.013 nm. H. Uwe Keller of the Laboratory for Atmospheric and Space Physics, University of Colorado, showed that this linewidth was consistent with a hydrogen outflow velocity of 8 to 10 km/sec, which agrees with other observations of Kohoutek's hydrogen halo.

Figure 4-23.—Theoretical trajectories (syndynes) at 2400 GMT on December 29, 1973, of dust particles leaving the comet under the influence of a constant radiation pressure (zero initial velocity relative to the comet). The calculations were made for four sizes of particles. Top: calculations for the comet's orbital plane: Bottom: calculations to the skyplane (i.e., an idealized observer's view from the Earth). The term $1-\mu$ is the acceleration exerted on a particle by solar radiation pressure, expressed as a fraction of solar gravity on the particle. The term t is the time in seconds since the particles left the nucleus.

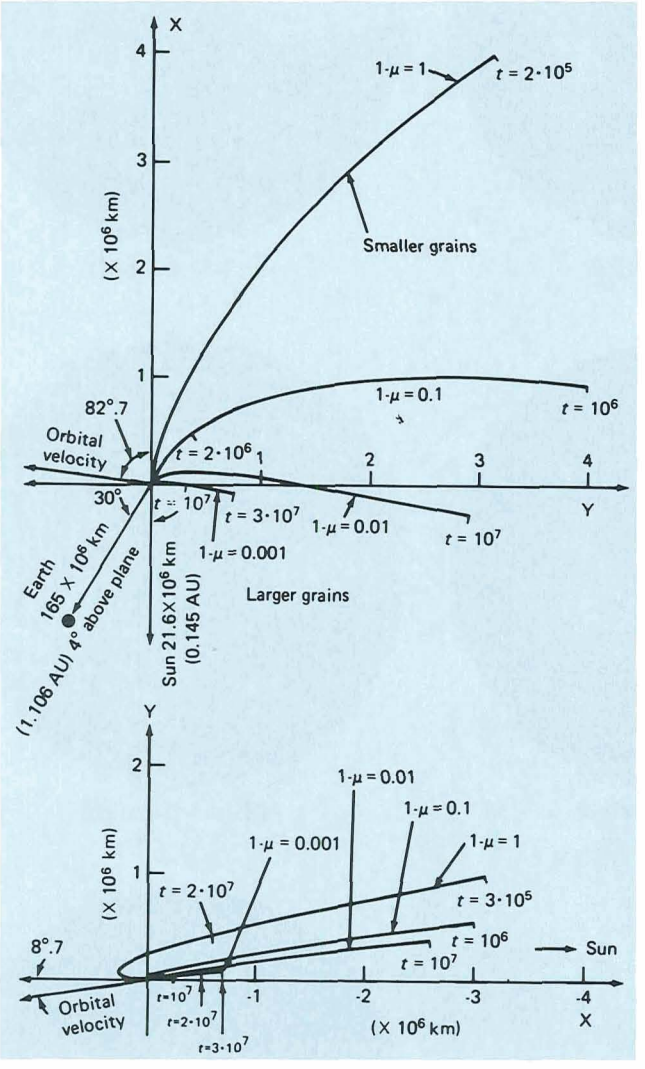

An ultraviolet photoelectric scanning instrument (S055) in the solar observatory operated in the spectral range of 29.6 to 135.0 nm. This instrument was used to detect emission by hydrogen in the coma for correlation with other instruments. Edmond Reeves of the Harvard College Observatory reported that the intensity of the Lyman-alpha line of atomic hydrogen was measured on a number of occasions during scans of the comet.

Search for Helium

An attempt was made with the extreme-ultraviolet spectroheliograph (S082A) to photograph the comet in the radiation from neutral and singly ionized helium at 58.4 and 30.4 nm, respectively. Although it was believed most unlikely that Comet Kohoutek would produce a helium halo, a long exposure with the extreme-ultraviolet spectroheliograph was made during the comet's closest approach to the Sun. The Naval Research Laboratory team reported that no image was detected. The instrument's sensitivity therefore sets an upper limit for the column density of such a helium halo.

Search for X-Rays

Attempts to measure the emission of X-rays were made with two solar observatory X-ray instruments. The exposure was considered exploratory in nature. The instruments were capable of measuring wavelengths of 0.2 to 6.0 nm. Kohoutek was not expected to give off any X-rays, but some possibility existed that more energetic radiation from the Sun might have caused the comet to fluoresce, yielding information on the nature of cometary material. However, Skylab's X-ray instruments recorded no such emission from Kohoutek.

Kohoutek's Antitail

As mentioned earlier, Comet Kohoutek displayed an "antitail" (sunward spike) just after perihelion. The astronauts' sketches and the white-light coronagraphs provided data that helped to clarify the antitail's development and the distribution of particles in the comet.

A theoretical analysis was made by H. Uwe Keller of the paths of dust particles leaving the comet under the influence of a constant radiation pressure (zero initial velocity relative to the comet). The calculations were made for dust particles of four sizes. The smaller particles are driven relatively large distances away from the comet; larger particles move smaller distances away from the comet. As the comet nears perihelion, the trail

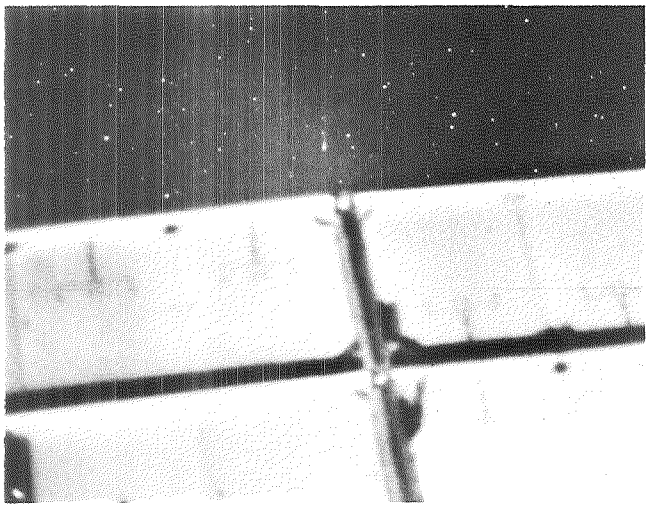

Figure 4-24.—A 120-sec exposure made on December 5, 1973, showing the comet with a slight tail. (A solar panel is seen in the foreground).

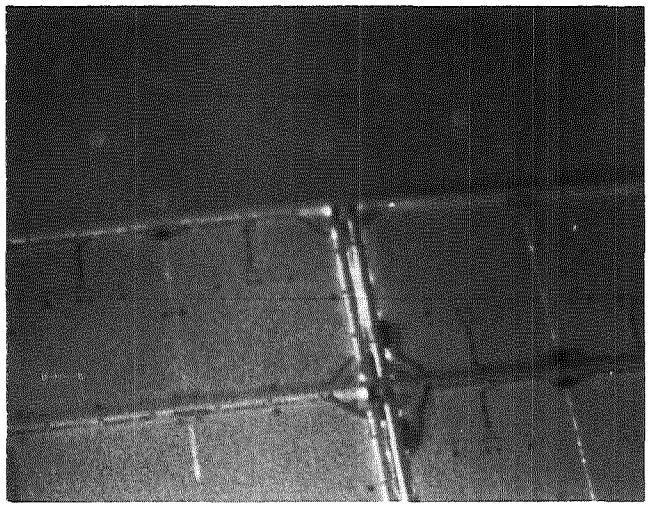

Figure 4-25.—A 60-sec exposure made immediately after the photograph in figure 4-25, with the lens purposely focused at 15 ft.

of larger particles emitted earlier becomes visible by scattered and reflected sunlight. Its position is such that it appears as a "sunward spike." Figure 4-23 shows the loci of particles as calculated for 2400 GMT on December 29, 1973. This time happens to be close to those of the white-light photographs shown in figure 4-22. The curves in the upper diagram are in the comet's orbital plane; those in the lower diagram are in the skyplane (i.e., an idealized observer's view from the Earth).

Before the mission, Z. Sekanina of the Smithsonian Astrophysical Observatory predicted that a "sunward spike" would probably develop just after perihelion. The astronauts' observations were consistent with his prediction, indicating that Kohoutek's preperihelion dust emission was very high. From the deviation in the direction of the sharp leading edge of the spike from the sunward direction (some 5° to 7°), he estimated that the part of the spike near the comet's head contained dust particles of submillimeter or even millimeter size and that the material in the spike was produced by ejections beginning at least some 2 months earlier.

G. A. Gary and C. R. O'Dell of the Marshall Space Flight Center described the appearance of the sunward spike as evidence of large particles being ejected near the perihelion. They showed that the basic features of the antitail are explained by the detailed theory of particle trajectories developed by Finson and Probstein. They also related the finite apparent spike length to the mass of the heaviest particles that overcame the gravitational attraction of the nucleus. Their analysis of the spike length made use of data from the Skylab astronaut observations.

Photometric Studies

When Comet Kohoutek became visible through Skylab's windows, a program to photograph it twice a day was begun, using a 35-mm camera equipped with a 55-mm, $f/1.2$ lens. The purpose of this activity was to determine the brightness of the comet as often as possible. Information about changes in its nucleus and coma resulting from its close passage by the Sun could be deduced from such a brightness history. The experiment (S233) was conducted for Charles A. Lundquist and associates at the Marshall Space Flight Center.

Figure 4-24 is a 120-sec exposure made on December 5, 1973, and shows the comet with a slight tail. A solar panel, slightly out of focus, is in the foreground. Photographs, with the comet in focus, were used to locate the comet exactly and to record a sharp image of its tail.

Figure 4-25, a 60-sec exposure, was made immediately after the picture in figure 4-24; however, the lens of the camera was purposely focused at 15 ft. Defocusing the lens facilitated measuring the total exposure recorded by each image, by ensuring that most of the images were not overexposed. The brightness of the comet was found by comparing the density of its image with those of stars of known brightness.

The photograph in figure 4-26 was taken on December 22, 1973, and was the last 35-mm photograph made

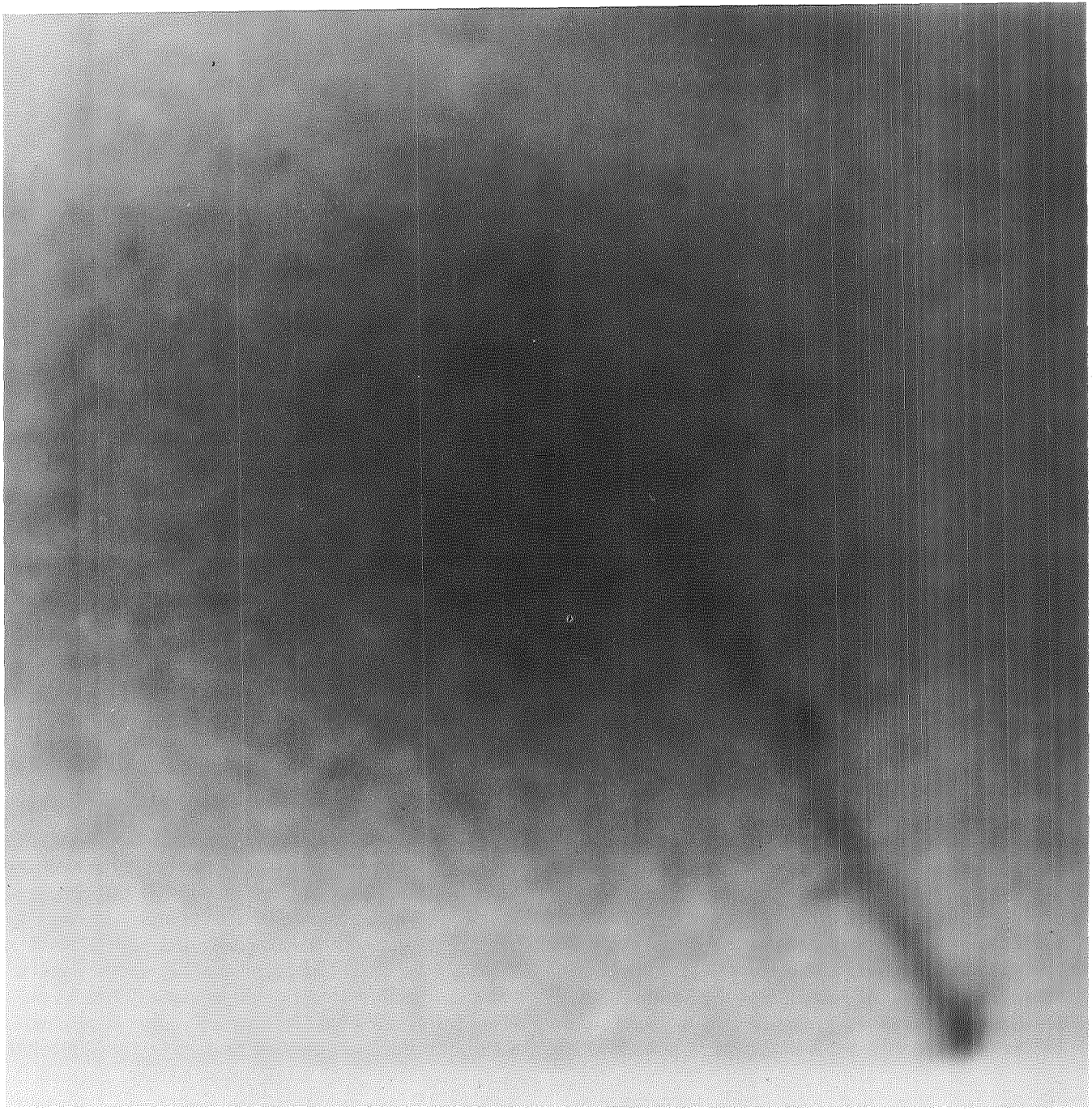

Figure 4-26.—Comet Kohoutek on December 22, 1973, before perihelion, with approximately 5° of its tail visible.

before perihelion. Approximately 5° of Kohoutek's tail is visible. Later, the comet was too close to the Sun for this type of photography. The picture in figure 4-27 was obtained from figure 4-26 by the false-color enhancement process discussed earlier. In it, colors are assigned different levels of brightness, from brightest to least bright: red orange, dark red, blue, and black. The extremely bright area at the top of the photograph, making it difficult to see where the tail actually ends, is caused by reflections from a strut of the Skylab.

Figure 4-28 is a 120-sec exposure made on January 10, 1974, 13 days after perihelion. Approximately 7° of the comet's tail can be seen. Streaking of the star images was caused by motion of the space station during the exposure.

Kohoutek's Visual Magnitude

William A. Deutschman of the Center for Astrophysics, Harvard College Observatory, and the Smithsonian Astrophysical Observatory studied the changing visual magnitude of Comet Kohoutek as it approached and passed the Sun. He concluded that the postperihelion magnitude was dimmer and decreased more rapidly with

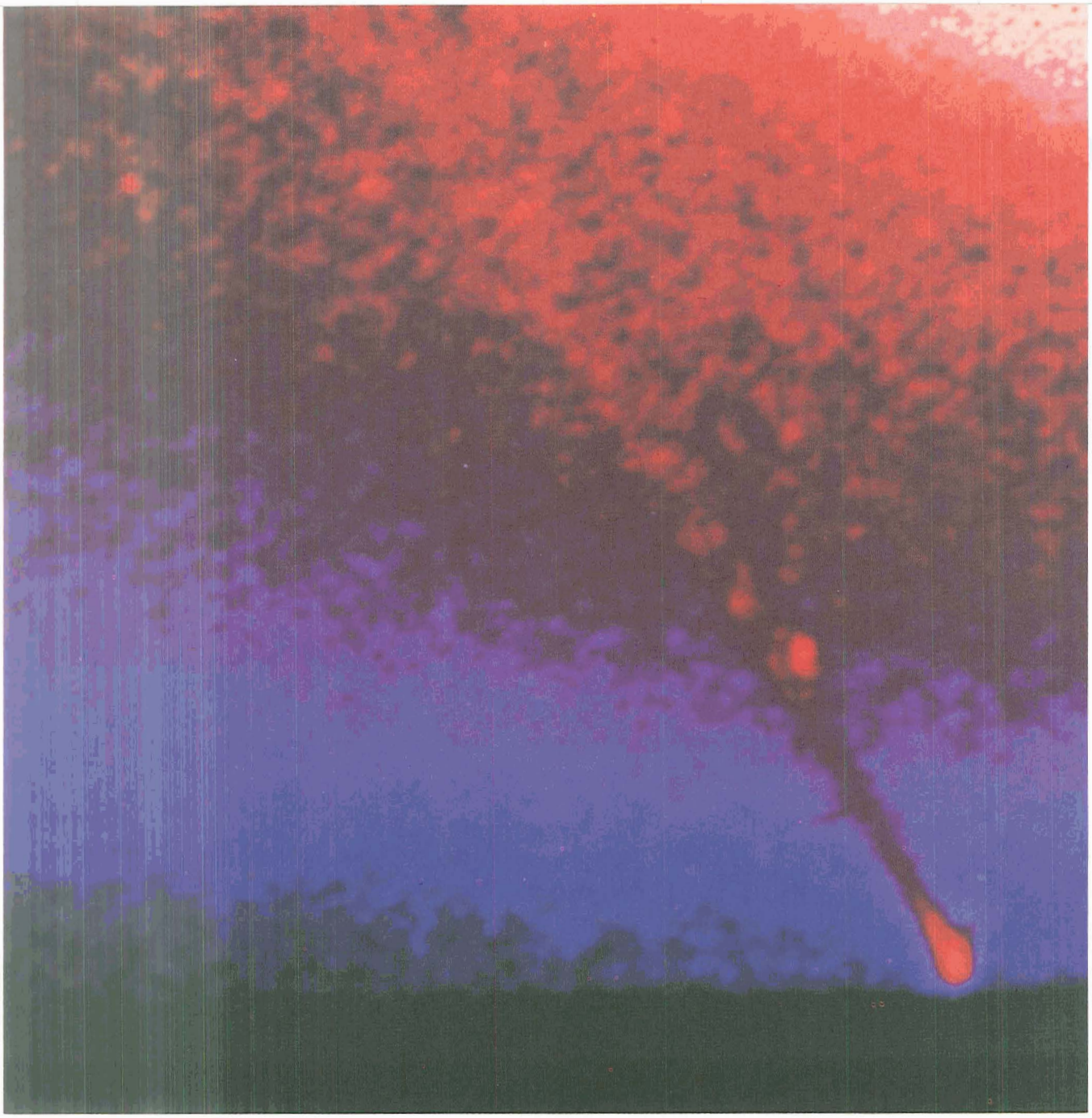

Figure 4-27.—False-color enhancement of the photograph shown in figure 4-26.

distance from the Sun than did the magnitude before perihelion. His result is confirmed by the photographs from Skylab. This behavior is opposite to that of some comets, which are brighter after perihelion than before, for the same distances from the Sun. Deutschman's curves (figs. 4-29 and 4-30) are based on 476 observations by 62 observers on Earth. The data are divided into 231 preperihelion and 245 postperihelion observations. The magnitude points have been corrected for the variation in distance between the Earth and the comet, and by a standard aperture correction for individual observers. The quantity R is the distance between the Sun and Kohoutek in astronomical units. Observation dates are plotted, superimposed with values of log R. The curves represent a best fit to two theoretical treatments of comet magnitudes.

Best Observed Comet

By good fortune, the Skylab operation overlapped the passage of Comet Kohoutek through the inner solar system. This circumstance and the extensive observational capability of Skylab instrumentation were catalysts for a worldwide effort to measure all aspects of the comet.

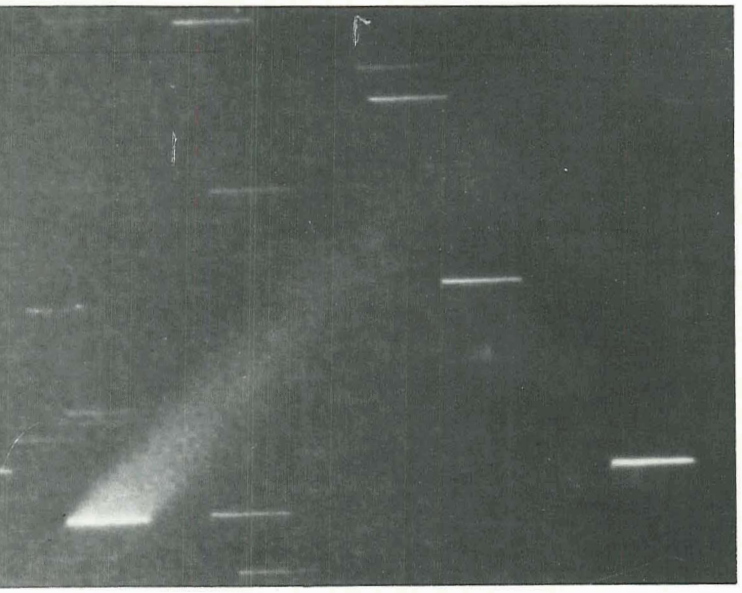

Figure 4-28.—Comet Kohoutek photographed in a 120-sec exposure on January 10, 1974, 13 days after perihelion.

This effort was indeed successful to the degree that Comet Kohoutek became the best observed and studied comet in history. Directly, through unique measurements made on board, and indirectly, through stimulus to others, Skylab can be credited with this success.

Figure 4-29.—Comet Kohoutek's visual magnitude before perihelion based on 231 ground-based observations from September 1 through December 28, 1973. The +, x, and o symbols are, respectively, visual, photographic, and image tube observations.

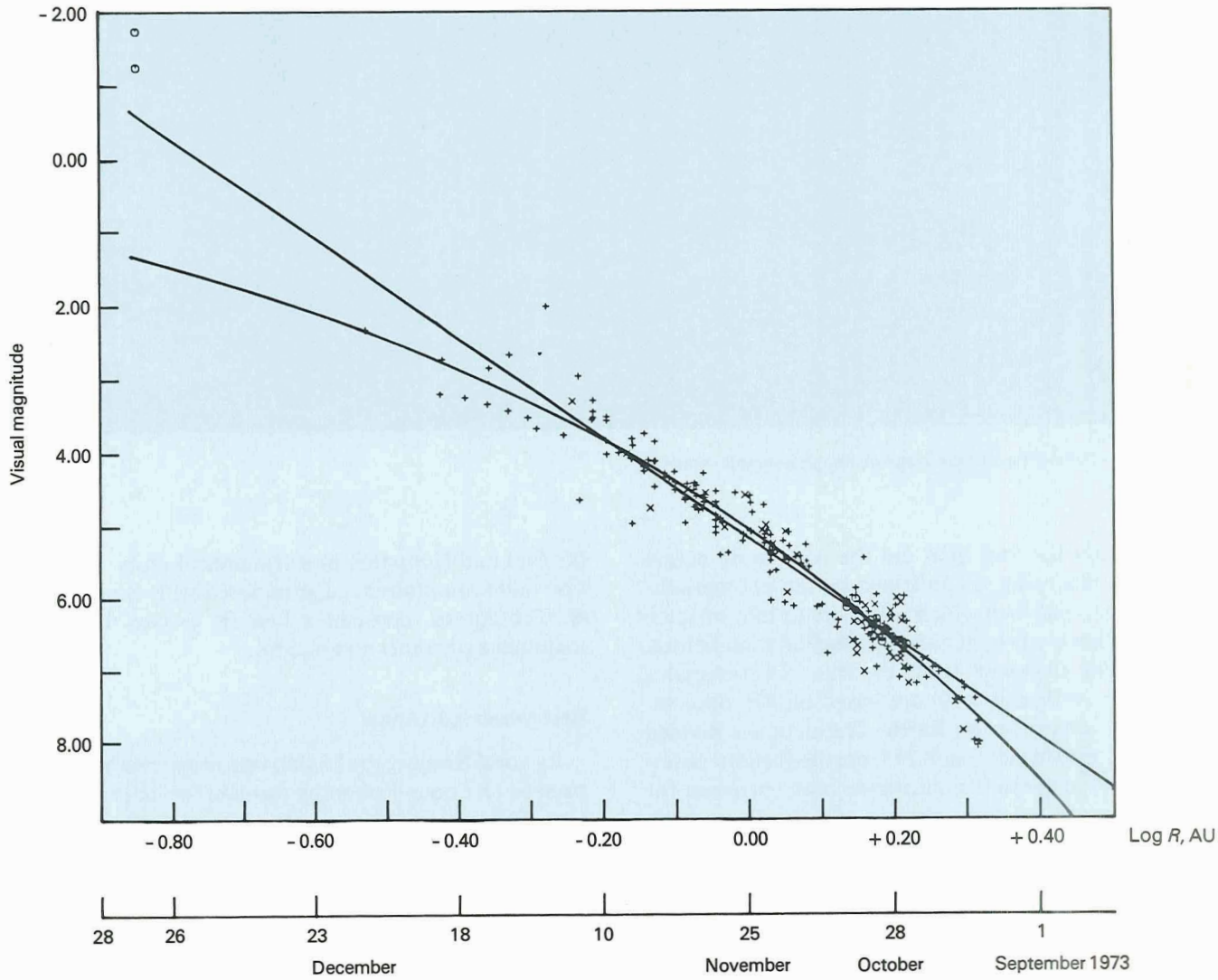

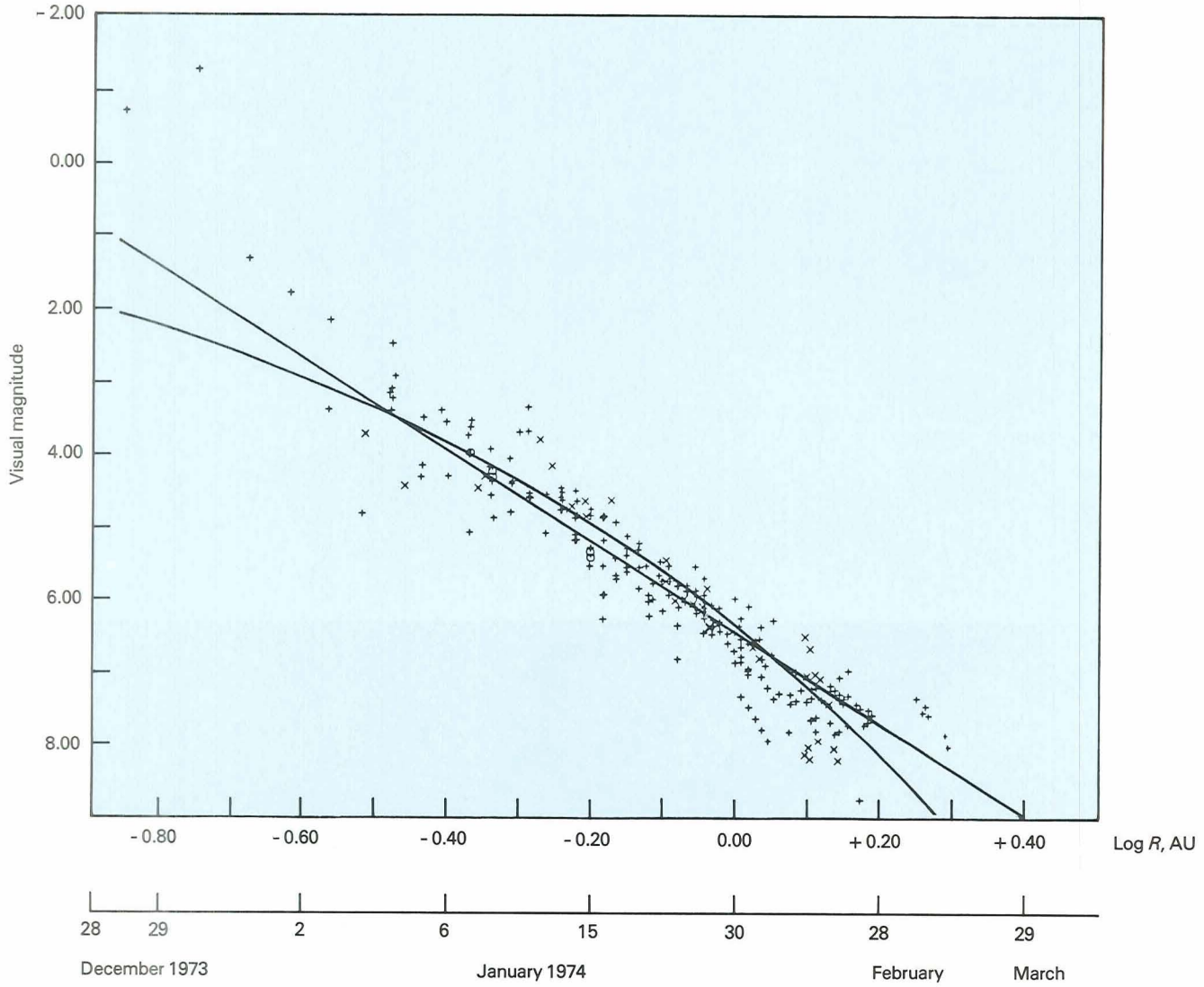

Figure 4-30.—Comet Kohoutek's visual magnitude after perihelion (based on 245 ground-based observations between December 28, 1973 and March 29, 1974).

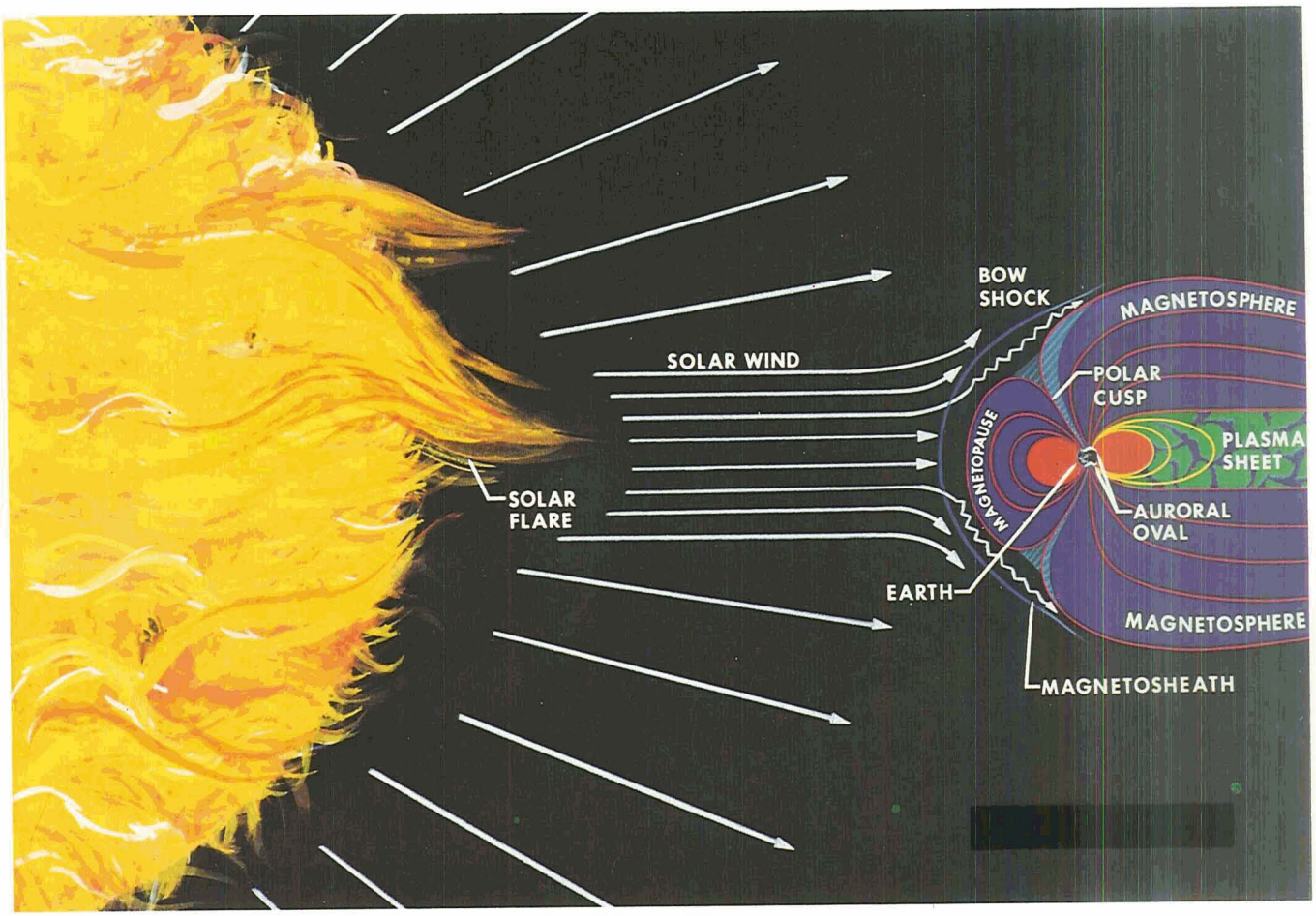
BOW
SHOCK
MAGNETOSPHERE
SOLAR WIND
POLAR
CUSP
MAGNETOPAUSE
PLASMA
SHEET
SOLAR
FLARE
AURORAL
OVAL
EARTH
MAGNETOSPHERE
MAGNETOSHEATH

5
Energetic Particles

At about 100 km above the Earth's surface the magnetosphere gradually begins. It contains ions and electrons whose density is very low and whose behavior is strongly influenced by the Earth's magnetic field. The upper boundary of the magnetosphere is not spherical. On the dayside it is about 60 000 km above the Earth; on the nightside it is on the order of a million kilometers.

The particles within the magnetosphere have various origins and some have complex histories. Among those observed by instruments on Skylab were galactic cosmic rays, trapped particles probably originating in the solar wind, and neutrons formed by the reaction of high-energy particles with the atmosphere. In addition, there were secondary particles produced by high-energy particles striking the structure of Skylab itself.

Skylab's orbit was entirely within the magnetosphere (fig. 5-1).

Origin and Composition of Magnetospheric Particles

A magnetospheric particle experiment (S230) was designed by Don Lind of the Johnson Space Center and Johannes Geiss of the University of Bern, Switzerland, to determine the numbers and kinds of atomic particles impinging on Skylab and, from their isotopic abundance, to gain insight about their origin.

Figure 5-2 shows a cuff-shaped collector used to measure the fraction of various atomic species within the total flux of magnetospheric particles. It carried strips of thin aluminum and platinum foils mounted on fabric. Some strips consisted of a single metal; others were multilayered composites of both metals. The foils trapped the energetic atoms that struck them and were returned to Earth for analysis.

The collectors were mounted on an external truss of the Skylab structure (fig. 5-3). The foils were able to trap particles approaching from almost any direction.

Collector assemblies were stacked so that the outer one collected while protecting the inner one. At intervals

Figure 5-1.—Earth's environment in space.

Figure 5-2.—Collector cuff for the magnetospheric particle composition experiment.

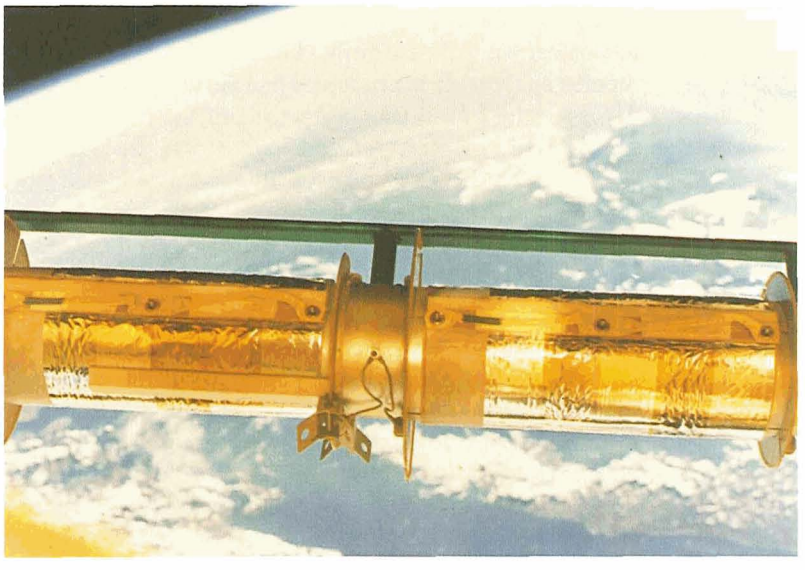

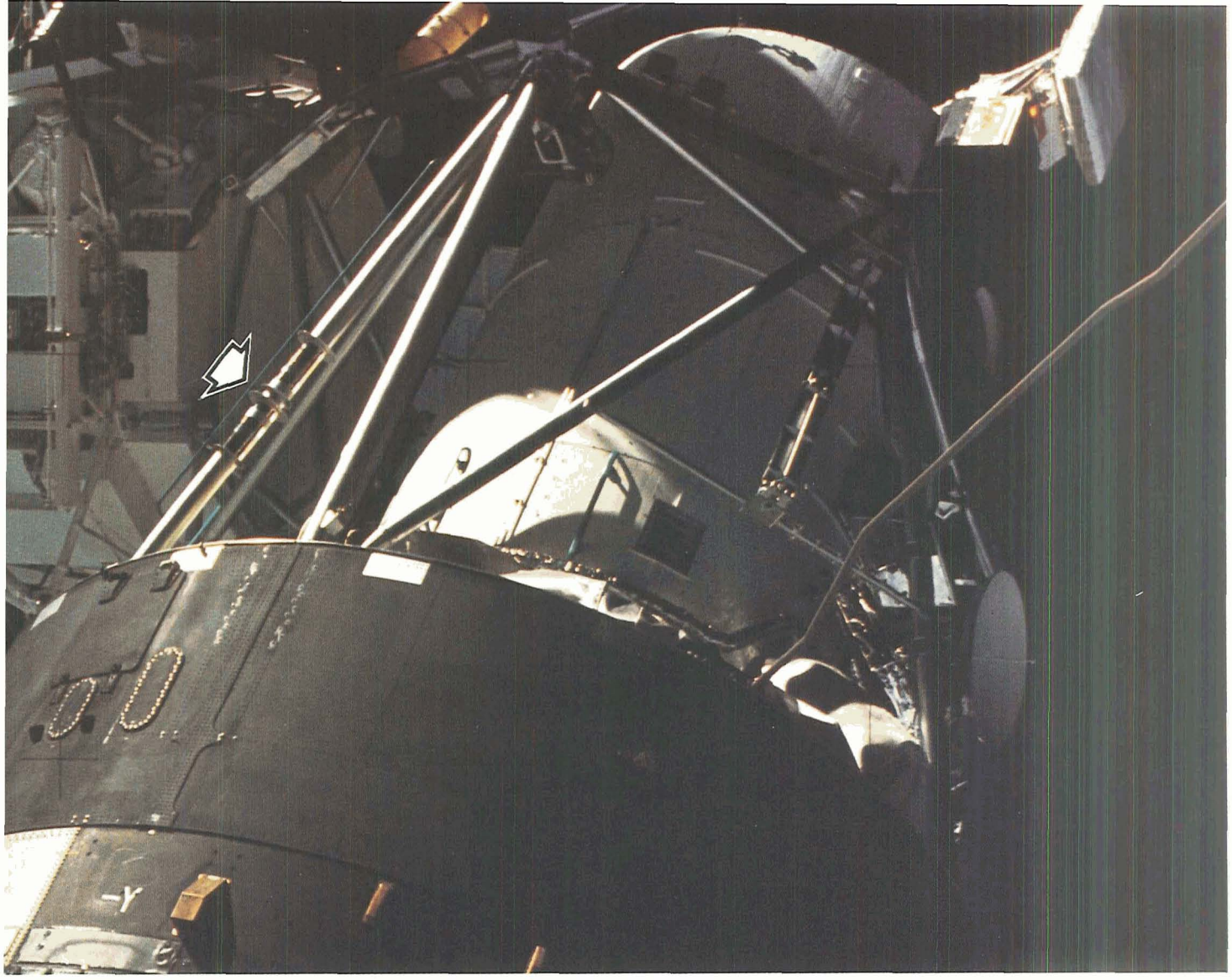

Figure 5-3.—Collector cuff deployed on Skylab.

the astronauts removed outer collectors, exposing the inner ones. In this way a time series of collections was obtained. The mounting spools (fig. 5-4) were designed to protect the delicate foils. The exhaust plumes of the Apollo spacecraft attitude-control thrusters could have damaged the foils during maneuvers if the flanges of the spools had not shielded the collectors. In addition, shields clipped on the edge of the spools covered portions of the foils at specified times. These shields were used as "shutters" to limit exposure to certain areas of the foils.

After the metallic foils had collected particles for the planned period, they were brought back to Earth for analysis in an extremely sensitive mass spectrometer at the University of Bern (fig. 5-5). Sections of the foils were removed and heated to drive off the trapped particles. All extraneous atoms were discounted, including those from a thin layer of contamination, seen as a colored film on the collector. (The contamination environment of Skylab is described further in Chapter 7.) Specifically, the trapped noble gases—helium, neon, and argon—were carefully measured because the relative abundances of their various isotopes are sensitive indicators of the origin of the particles.

Results of the experiment indicated, for example, that the majority of helium atoms impinging on Skylab with energies greater than 3 keV are transported to the Earth by the solar wind, and are accelerated in the magnetosphere. This conclusion is supported by the recognition that the $^{3}He/^{4}He$ ratio in the solar wind is greater by a factor of 300 than that in atmospheric helium and by the finding that the collected helium has nearly the solar wind ratio.

Also from measurements on neon, Lind and Geiss detected, for the first time, isotopic fractionation in the upper atmosphere. This process occurs because a lighter isotope of neon (^{20}Ne) tends to diffuse higher in the atmosphere than does a heavier isotope (^{22}Ne).

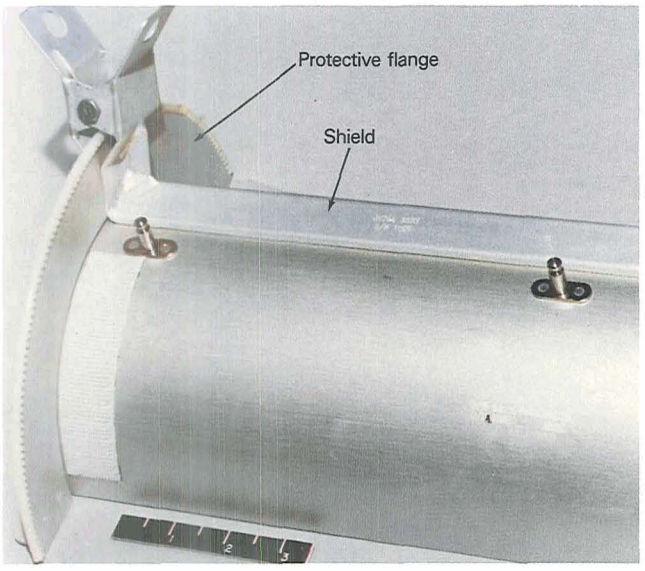

Figure 5-4.—Detail of collector spool, showing the protective flange and shield.

The two square test patches shown on the collectors are sections of foil bombarded with a known number of particles before flight. Any loss of these particles as a result of solar heating would have been detected, and the trapped particle data would have been corrected accordingly. However, no such losses were found.

Neutron Radiation

Neutrons are somewhat more difficult to detect than energetic protons, nuclei, or electrons, largely because they have no electrical charge. This absence of charge limits the interaction of neutrons with matter. They lose no energy through ionization or atomic excitation as they pass through matter and are thus able to penetrate matter much more easily than can charged particles with the same energy.

Figure 5-5.—Collector foils after return to Earth. The test patches are sections of foil bombarded with a known number of particles before flight.

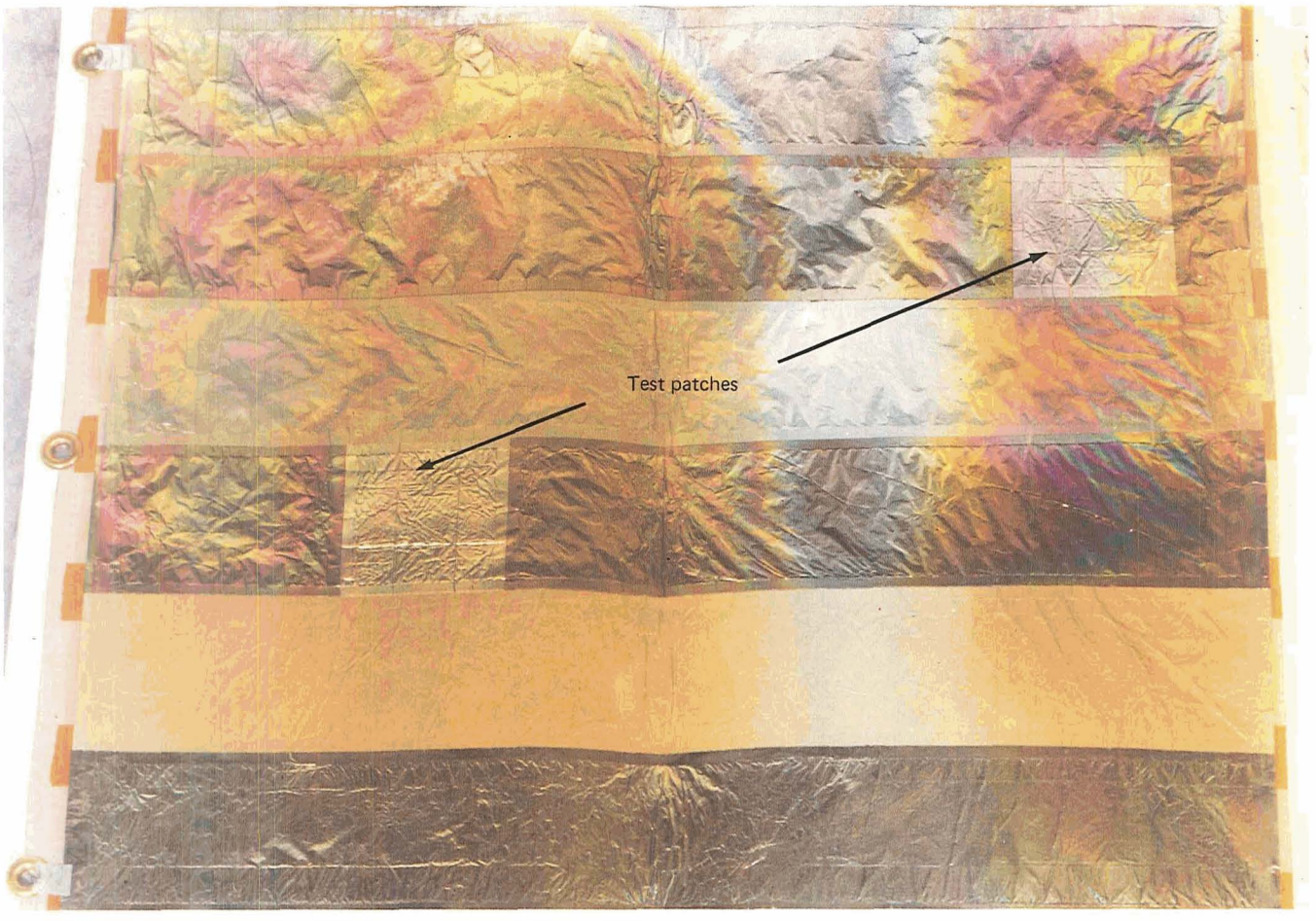

A free neutron is not a stable particle; it decays with a half-life of 11 min into a proton and an electron. Therefore, the vast majority of the neutrons detected in Skylab must have been generated either within the spacecraft or within the Earth's atmosphere. These neutrons are products of nuclear reactions initiated by primary radiation striking the spacecraft or the atmosphere.

When an energetic neutron collides with a proton (i.e., a hydrogen nucleus), there is a high probability that the neutron will exchange substantial momentum with the proton. Since human beings are largely composed of hydrogen-rich compounds such as proteins, fat, and especially water, neutrons passing through the human body have a substantial probability of reacting with it. Therefore, a knowledge of the ambient neutron fluxes within a manned space station is essential in order to assess the total radiation dosage encountered by the astronauts.

Neutron-flux measurements are important for other reasons. Interactions by high-energy neutrons can damage film and sensitive experimental equipment. Furthermore, neutrons are a complicating factor in sensitive X- and gamma-ray astronomy observations since their potential interactions with nuclei can result in secondary emissions.

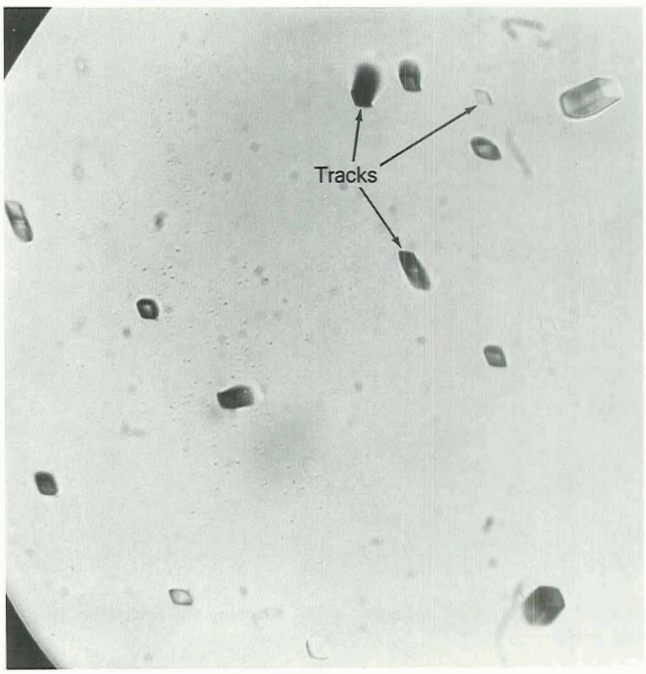

Figure 5-6.—Uranium fission tracks in muscovite mica.

Figure 5-7.—Neutron detector. The multiple-foil dielectric assembly (the symbol "TN" indicates cellulose triacetate).

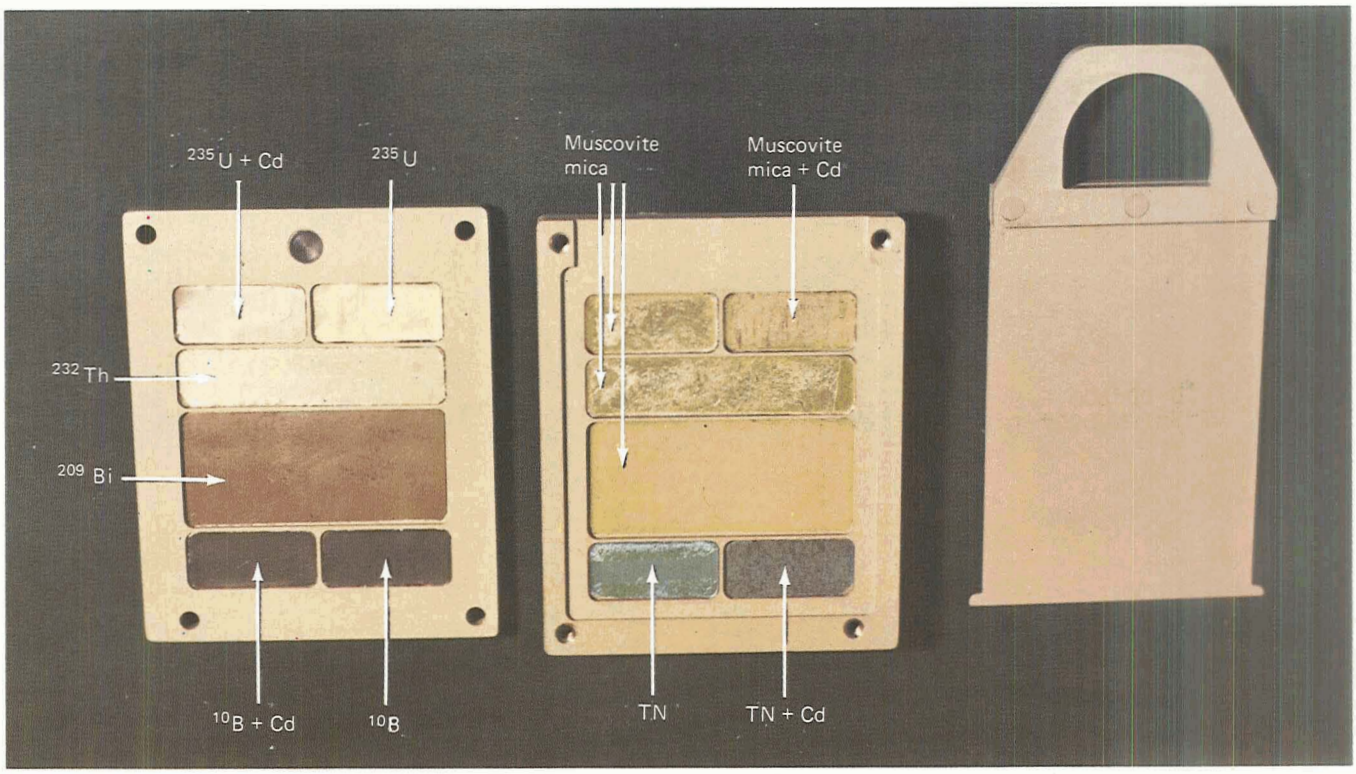

Earth-Orbital Neutron-Analysis Experiment (ED-76)

The measurement of neutron fluxes inside Skylab was an experiment proposed by Terry Quist, a participant in Skylab's high school student program. The objective was to measure the neutron fluxes present in Skylab, to determine the energies of the neutrons and to establish the origins of the particles observed.

The experimenter chose to detect neutrons with a "solid-state track recorder." In this technique, a target material and a recording material are used side by side. The target materials are foils of metals that have a relatively large neutron cross section; that is, they present a good target for the particles. When a neutron strikes the nucleus of an atom in such a foil detector, the target nucleus is fissioned into fragments. The recording medium, in contact with the detector foil, is typically a dielectric material such as natural muscovite mica or a manufactured polycarbonate material (e.g., Lexan or cellulose triacetate). The fission fragments from the detector foils pass through the recording sheets, disrupting the polymer chains in the plastic or disturbing the crystal lattice in the muscovite. In either case, etching with appropriate chemicals makes the fission tracks visible for counting under a microscope.

Figure 5-6 shows tracks from fission in a uranium foil recorded in muscovite and developed by etching with hydrofluoric acid. The energy range of the neutrons was differentiated into thermal, intermediate, and fast by means of a multiple-foil dielectric assembly shown in figure 5-7. The target foils were made of boron, bismuth, thorium, and uranium. The recording media were cellulose triacetate and muscovite mica. Each detector was activated by withdrawing an aluminum shield, shown on the right, which was interposed between the target foils and the recorders.

Ten of these detectors were deployed by the first Skylab crew at various locations throughout the space station (see, for example, fig. 5-8). Four of the detectors were returned to Earth by the first Skylab crew. Analysis by Terry Quist, under the supervision of Donald Burnett of the California Institute of Technology, indicated that

Figure 5-8.—Neutron detector deployed in Skylab.

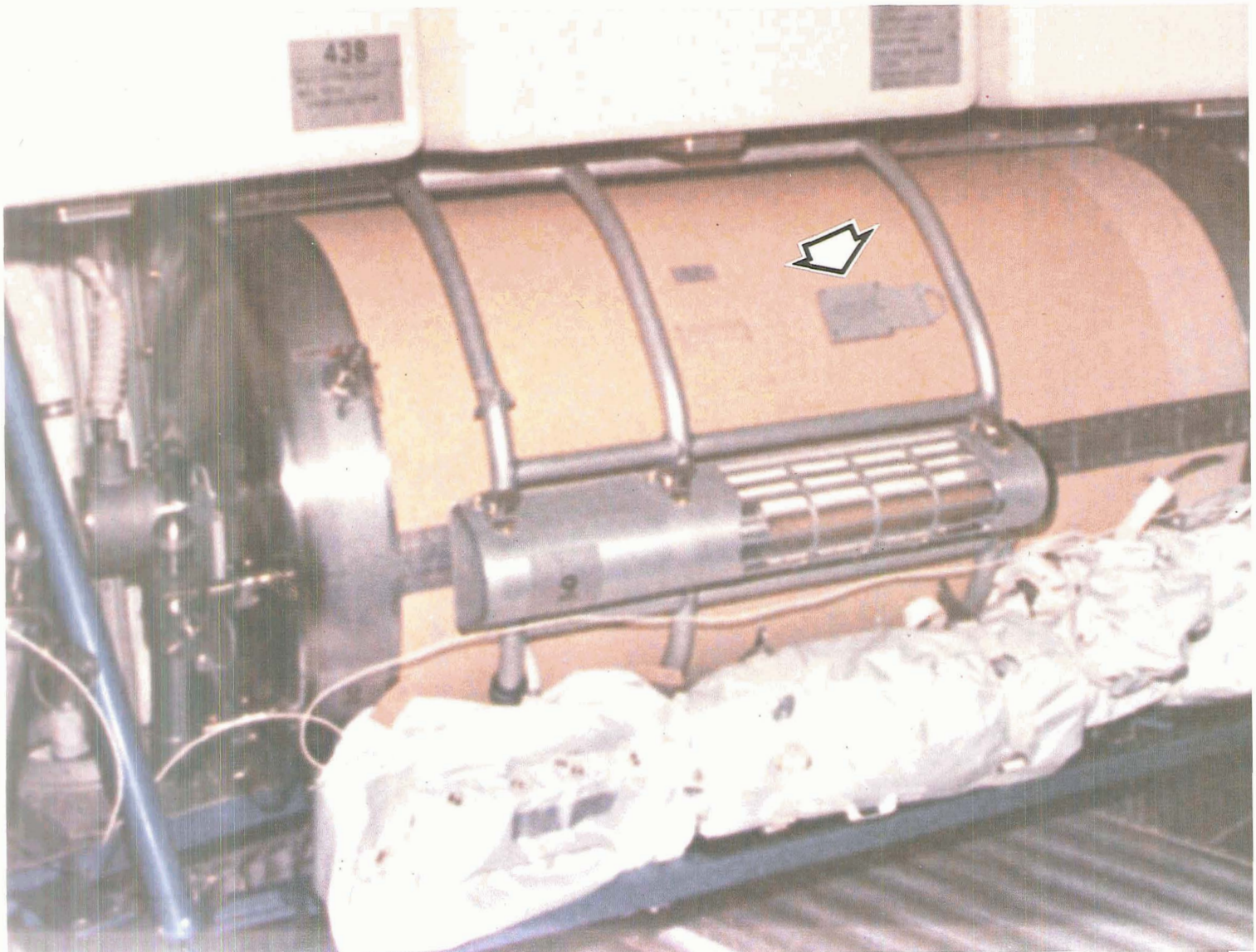

Figure 5-9.—Neutron detector packages containing samples of tantalum, nickel, titanium, hafnium, and cadmium-covered tantalum in fireproof bags.

the neutron flux was much higher than had been expected. As a result, one of the four returned detectors was refurbished for the third mission. Ultimately, all detectors were returned, four having been exposed to the Skylab environment for 24 days, six for 251 days, and one for 81 days.

The high neutron fluxes observed were attributed to secondary neutrons produced by bombardment of Skylab by charged particles (mostly protons) from the Van Allen belts. Although not nearly as energetic as cosmic rays, these protons are still energetic and numerous enough to generate the secondary neutrons observed in the space station by nuclear reactions with its structural materials.

Neutron Environment Demonstration (TV-108)

A different technique for measuring the neutron flux aboard Skylab was used by Gerald Fishman of the Mar-

Figure 5-10.—Neutron detector package mounted on the outside wall of the sleep compartment.

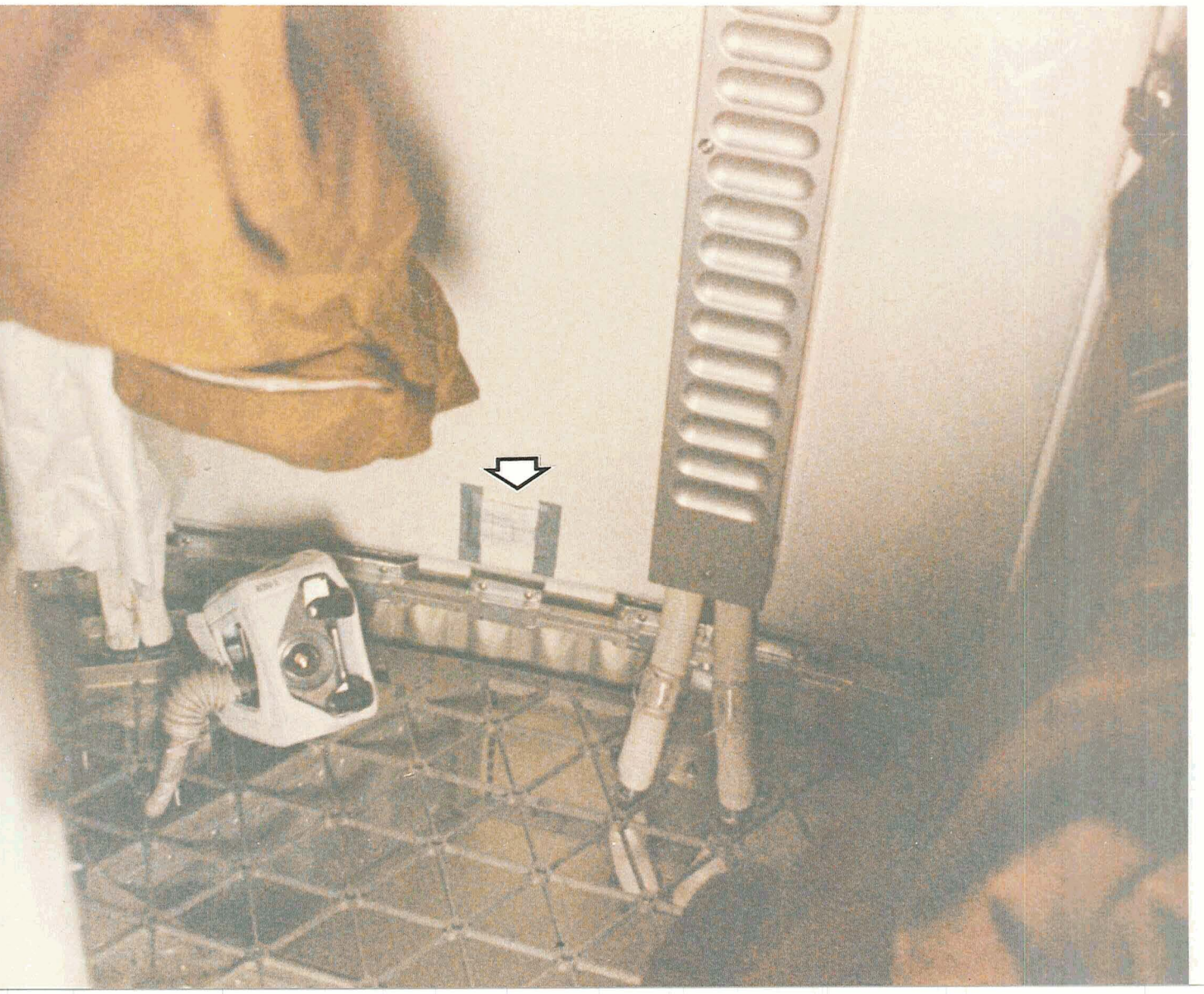

shall Space Flight Center. Fishman's method used specimens of stable elements whose nuclei readily react with neutrons. In each case a radioactive nucleus is formed which decays with a known half-life by the emission of a gamma ray of known energy. Measurements of the gamma rays can thus be used to calculate the flux of neutrons to which the samples of stable elements were exposed.

Four "activation packets," containing samples of tantalum, nickel, titanium, hafnium, and cadmium-covered tantalum, were launched with the third Skylab crew. Figure 5-9 shows the samples contained in cloth bags. They were deployed in the Skylab orbital workshop in a film-vault drawer, on the outside of a water storage tank, on the dome of the forward compartment of the workshop, and on the outside wall of the sleep compartment at the location shown in figure 5-10. The packets remained in place for 76 days and were then returned to Earth. In addition to these specially designed activation packets, analyses were made of a large sample of stainless steel from an experiment container and samples of tantalum and indium antimonide from other Skylab experiments.

Some of Fishman's activation packets were designed to enter into nuclear reactions with the neutrons, while others were expected to react with the protons that penetrated Skylab's wall. The amount of activity traceable to each of these components was further studied by the differences in behavior at various locations within the space station. The production of radioisotopes by proton reactions should have been greatest in locations with least shielding from the outside, since the protons came from the exterior. Radioisotopes produced by neutron reactions would logically show the reverse behavior, since the samples would be more heavily irradiated by neutrons in the densely shielded locations, assuming such neutrons were generated almost entirely by interactions in the space station material itself. The plot of activity against shielding, figure 5-11, shows the expected pattern. The proton-induced reactions fell off with increasing shielding, while the neutron-induced radioactivity increased in locations of high-shield density.

A gamma-ray spectrometer system was used to measure the gamma-ray decay rates of all the samples over an extended period of time after their return to Earth. All induced radioactivities were very weak, as expected. Nevertheless, the neutron fluxes derived from these measurements agreed well with those obtained from Quist's experiment. In essence, Fishman's results confirmed that the neutron environment of a space station the size of Skylab, and in its orbit, is dominated by high-energy (fast) neutrons and that their flux is higher than had been predicted.

Conclusions

Together, the two neutron experiments have led to important conclusions for the design of future space stations. First, the flux of neutrons observed in Skylab was much too high to be attributed to solar neutrons, Earth albedo neutrons, or even neutrons induced by cosmic rays in space-station materials. The other conclusion is that the higher neutron flux must come primarily from bombardment of space-station material by trapped protons in the Van Allen belt. However, the neutrons did not pose a biological hazard to the crew, nor did they produce significant film fogging.

Cosmic Rays

Cosmic rays are atomic nuclei moving at velocities approaching the speed of light. The commonest are the nuclei of hydrogen and helium. The abundance decreases generally with mass except for elements close to iron in

Figure 5-11.—Neutron- and proton-induced radioactivity as a function of shielding in various locations within Skylab.

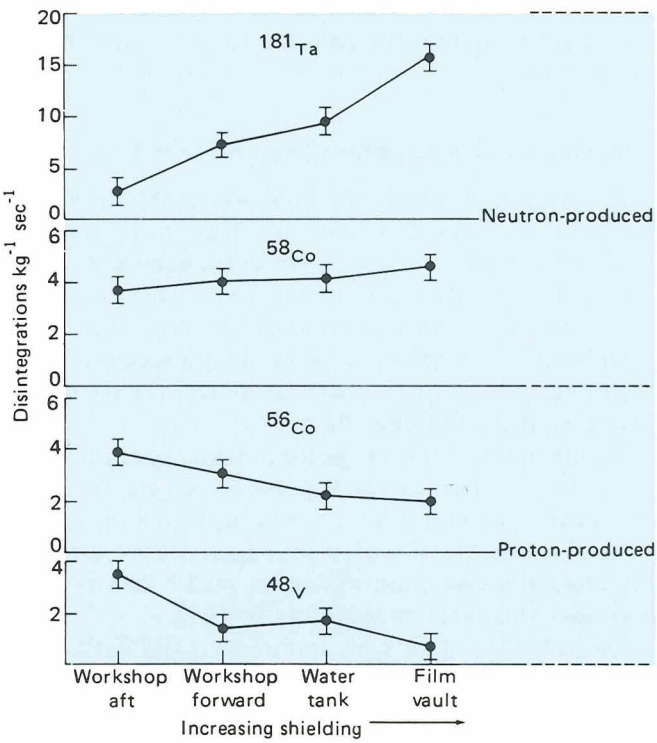

the periodic table, which are present in excess. The heaviest are among the most interesting. The effects of cosmic rays are due primarily not to the number of particles but rather to the prodigious individual particle energies, in some instances up to 10^{20} electron volts. This is an amount of energy per particle that, if converted to mechanical work, could lift this book a meter or so. In fact, the total energy contained in cosmic rays in the Milky Way may be comparable to the energy stored in the galaxy's magnetic fields or to the turbulent kinetic energy of its gaseous clouds. Astrophysicists are presented with an intriguing puzzle in trying to determine the natural processes that can concentrate so much energy in such a small amount of matter.

One example of a prodigious energy source on an astronomical scale was noted as early as 1054 AD by Chinese astronomers who witnessed the cataclysmic death of a star, a supernova explosion. The remnant of this explosion is still conspicuous in the sky today as a huge, irregular shape some 3500 light-years away, the Crab Nebula. It is widely believed that each supernova event produces cosmic rays that speed out into the galaxy, where they may wander for millions of years, deflected first one way and then another by magnetic fields.

Skylab performed two important cosmic-ray experiments; the first used nuclear emulsion film stacks to track heavy atomic nuclei close to iron in atomic mass. The other used large plastic sheets to record the rarely encountered, ultraheavy particles close to uranium in atomic mass.

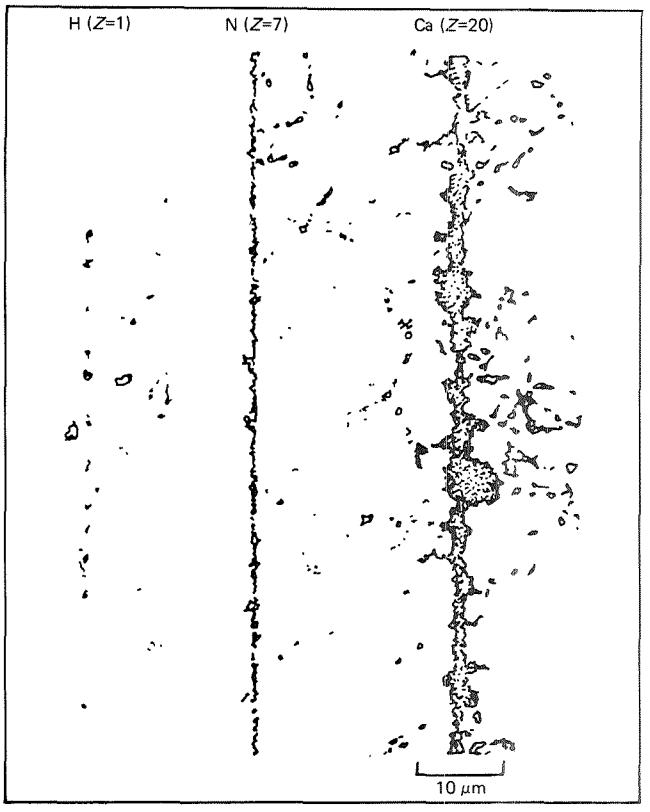

Figure 5-12.—Cosmic ray tracks on photographic film. Left to right H, $Z=1$; N, $Z=7$; Ca, $Z=20$.

Nuclear Emulsion Experiment and the Iron Peak

An interesting feature resulting presumably from the later stages of the formation of elements (known as nucleosynthesis) is a large relative abundance of iron nuclei. This is referred to as the iron peak in the universal elemental composition of matter. An iron peak is prominent in the galactic cosmic ray population. Furthermore, iron is often observed among the energetic nuclei emitted from solar flares.

The abundance of iron ejected in solar flares can only partly be explained by the hypothesis that the Sun is a second-generation star (i.e., one formed from the debris of heavy elements of a previous supernova explosion). Preferential acceleration of heavier nuclei such as iron may also be at work in some of the flares.

The galactic cosmic rays approaching the Earth still possess an iron peak, but they also have a far larger than universal abundance of elements just below iron in atomic number. The breakup of cosmic ray iron by collisions with interstellar matter during millions of years of traveling through the galaxy could contribute importantly to the buildup of elements lighter than iron. Analysis of Earth-arriving cosmic rays for elemental constituents in this part of the periodic table was a prime objective of the Skylab nuclear emulsion experiment (S009). The experiment was prepared by Maurice M. Shapiro and colleagues at the U.S. Naval Research Laboratory, Washington, D.C., and used a refined version of the nuclear emulsion detection method first used in high-altitude balloons and later employed on a Gemini space mission.

The nuclear emulsion detector flown on Skylab consisted of stacks of special photographic film. The emulsion layers differ from ordinary photographic film principally in being thicker and having a higher density of silver halide grains. On passing through the stack, a cosmic ray particle activates the tiny silver crystals in its path and makes them developable. The silver ions become specks of metallic silver after development. The tracks are typically several micrometers or less in width;

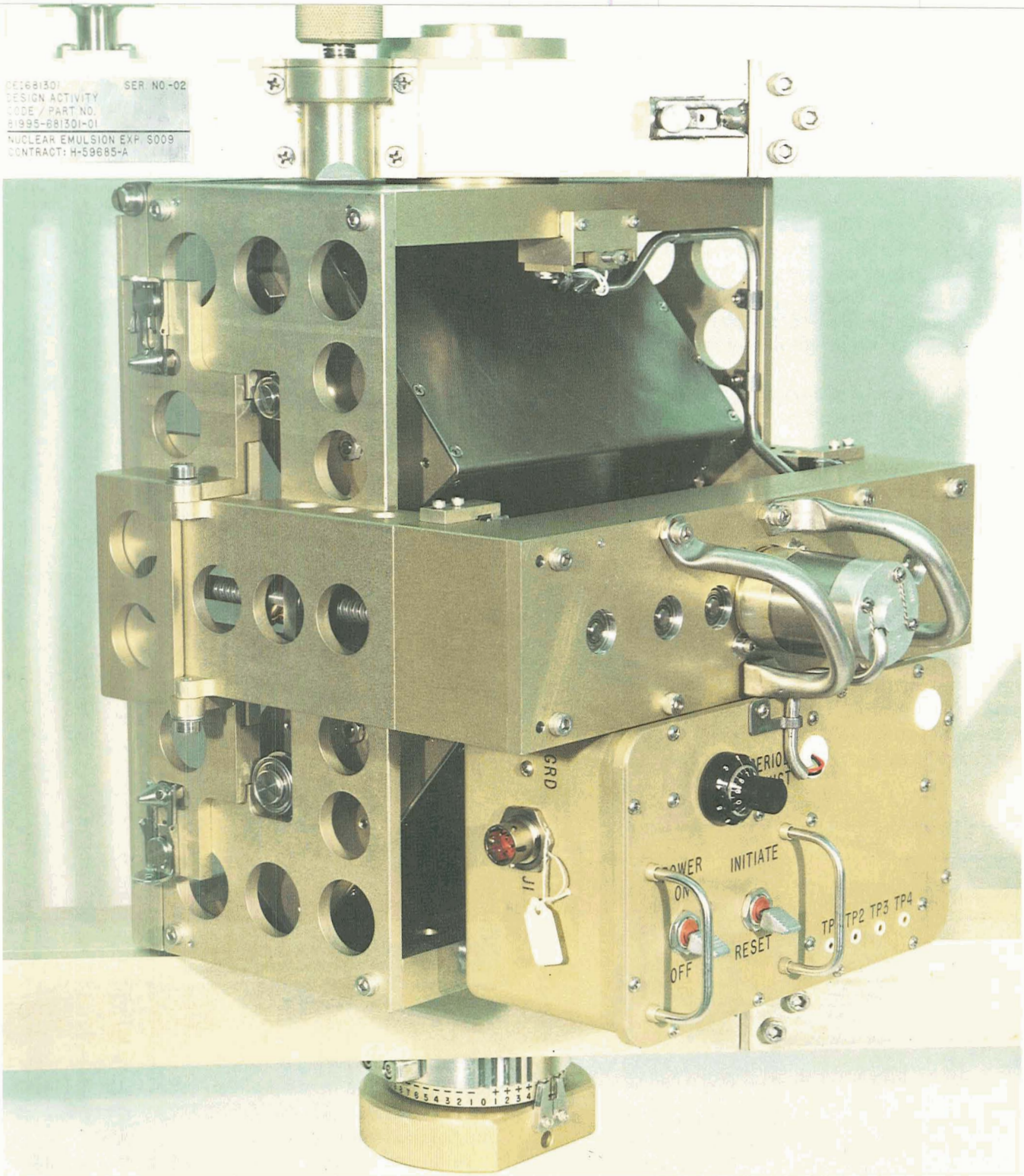

Figure 5-13.—Skylab nuclear emulsion package.

hence magnifications greater than 1000x are commonly used to examine their details. Figure 5-12 shows some typical microscopic tracks formed by various cosmic ray nuclei moving with relativistic velocities through such emulsions. The densest track was left behind by a calcium nucleus, the next one by a nitrogen nucleus, and the thinnest track by a hydrogen nucleus.

The Skylab nuclear emulsion package (S009), shown in figure 5-13, was activated by the crew of the third mission. It remained inside Skylab for 38 days at a location chosen to give it an unobstructed view of deep space through a section of the skin of the docking adapter purposely milled down to minimize the amount of matter between the incoming cosmic rays and the package.

Two operational constraints had to be met during the experiment. First, the exposure faces of the emulsion package had always to point away from the Earth to avoid collecting albedo particles from its atmosphere. This was accomplished by a daily readjustment of the mechanism by the crew to compensate for the slowly changing tilt of Skylab's orbit relative to the Earth-Sun line.

Second, the package was built in two parts and hinged like a book (fig. 5-14). This permitted a timer to open and close the package. Data were collected when Skylab was in the equatorial zone between 30°N and 25°S, where only the highest velocity cosmic ray nuclei, of interest to the experiment, could penetrate the Earth's magnetic field to Skylab's altitude and leave tracks in the detector package. At higher latitudes (both north and south), where the magnetic field bends closer to the Earth, heavy—but slower—nuclei also penetrated to the space station's altitude and left tracks in the package. Since these nuclei were of lesser interest, the package was closed in those regions. Sufficiently penetrating particles recorded at those latitudes were recognizable because they crossed the two faces of the closed package and could be subtracted out during analysis.

Figure 5-14.—Nuclear emulsion pack in the open position.

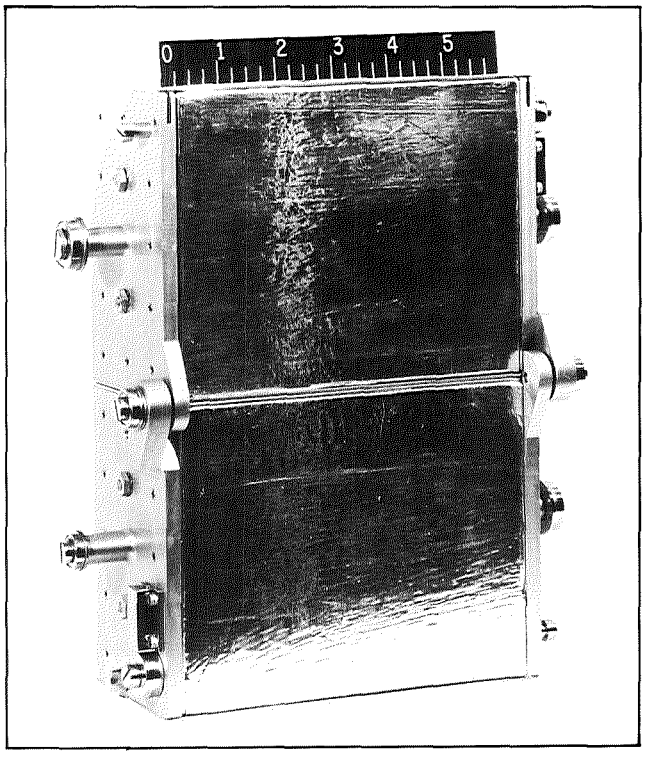

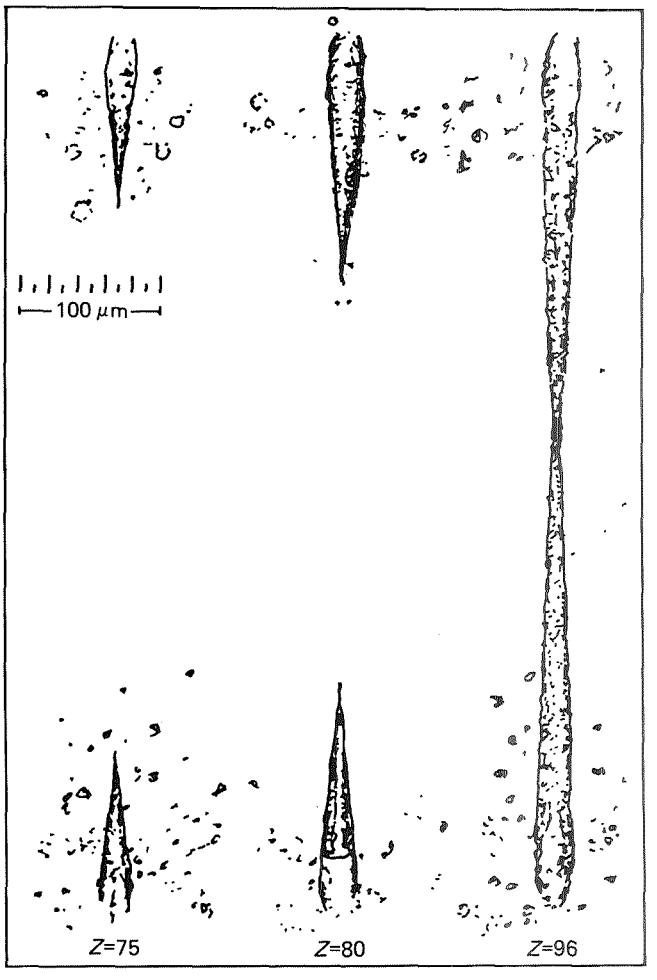

Figure 5-15.—Photomicrograph of etched pits showing the path of ultraheavy cosmic rays. The three penetration depths correspond to cosmic rays with atomic numbers of approximately 75, 80, and 96, respectively, from left to right.

Package closure south of 25° latitude also provided partial shielding from the Van Allen belt radiation, which penetrated Skylab's skin as Skylab passed through the South Atlantic anomaly.

At the end of the mission, the nuclear emulsion package was returned to Earth for development and analysis of the recorded tracks. The large volume of data obtained (estimated to be more than 4000 tracks) added a great deal of knowledge about the composition of cosmic rays and provided insight into the cosmological significance.

Transuranic Cosmic Ray Experiment (S228)

Although the iron peak is a conspicuous feature of the cosmic rays that impinge on Earth, most cosmic rays

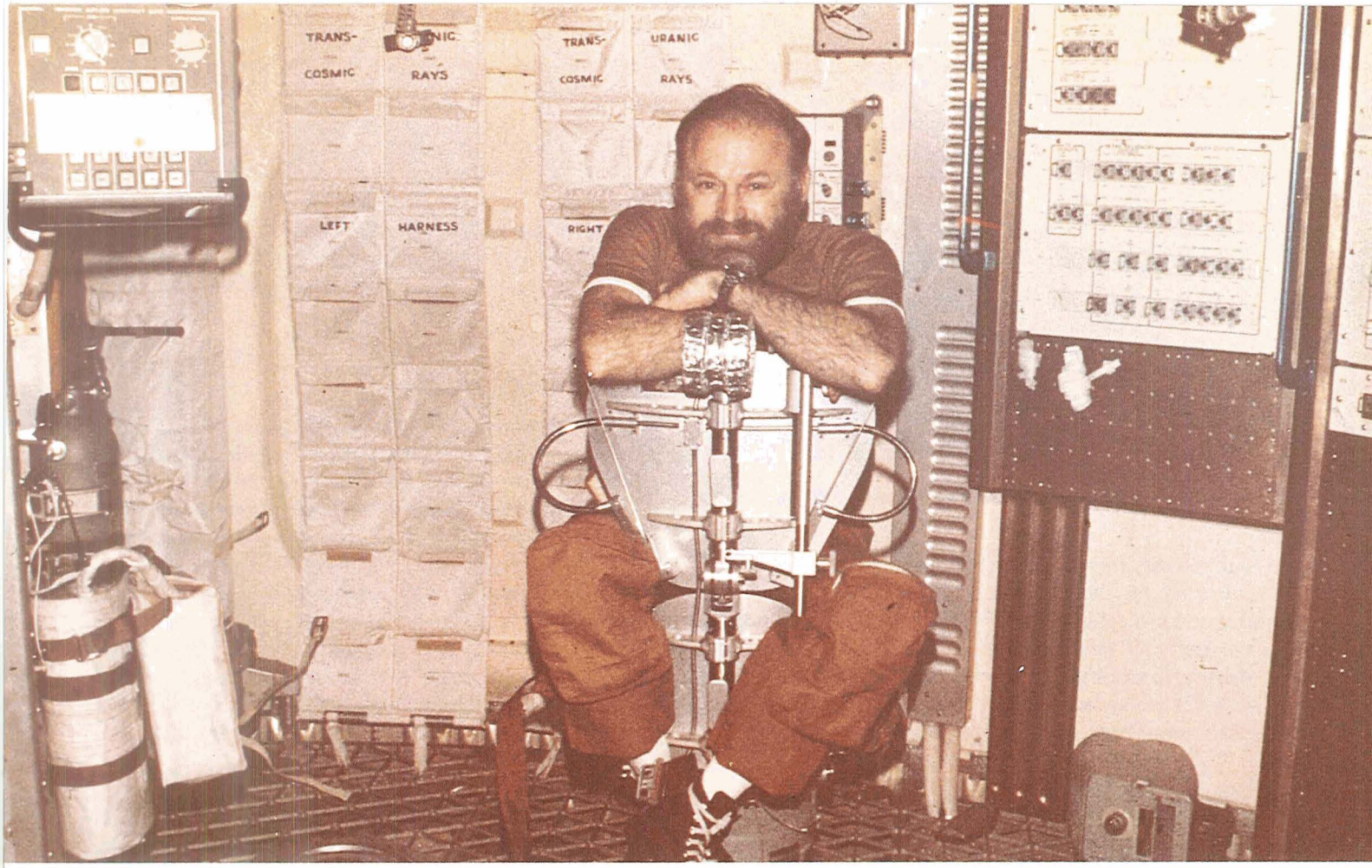

Figure 5-16.—Cosmic ray detectors mounted on the wall of Skylab's workshop, behind and to the left of astronaut Gerald P. Carr.

are protons. Helium is the next most abundant element. Heavier nuclei become progressively rarer with increasing mass. Skylab was the first vehicle that was capable of deploying a large enough detector, for long enough to record a statistically significant sample of ultraheavy nuclei and then return the experiment to Earth for analysis.

The second Skylab cosmic ray experiment, searching for ultraheavy cosmic rays, was designed by P. Buford Price and E. K. Shirk of the University of California at Berkeley. They have had considerable experience in the detection of heavily ionizing cosmic ray particles in meteorite fragments and have pioneered in the use of plastic detectors, such as Lexan, for experiments flown first in balloons and later in space. After exposure to energetic radiation, the Lexan is treated with a chemical that preferentially etches tracks of radiation damage left behind by heavy nuclei.

Figure 5-15 is a photomicrograph of etched pits showing the paths of ultraheavy cosmic rays such as those detected aboard Skylab. It shows three different penetration depths, corresponding to cosmic rays with atomic numbers of approximately 75, 80, and 96.

The Lexan detectors for the transuranic cosmic ray experiment were arranged in 36 stacks with a total detector area of 1.3 m^2. A harness, with pockets containing the detectors, was attached to the wall of the workshop, as shown in figure 5-16.

One module was returned to Earth on September 25, 1973, after a 119-day exposure. At the end of the final mission, 34 of the modules were brought back to Earth, having had a 253-day exposure. One was left behind in the space station's docking module, conveniently located for retrieval by any astronauts who might someday visit Skylab.

The sheets of Lexan in the returned modules were chemically etched and then scanned under a low-power microscope for tracks of cosmic rays with atomic number $Z>65$. Approximately 150 separate events (etched pits) were located. Three events were found for which the best estimates of charge correspond to those of transuranic elements ($Z\geq 94$). This is 4 percent of the 77 events from nuclei in the range $74\leq Z\leq 87$. No nuclei with atomic number greater than 110 were detected.

The transuranic cosmic ray experiment also permitted the determination of other abundance ratios of astrophysical significance without the need to correct for atmospheric interactions. The ratios thus obtained shed

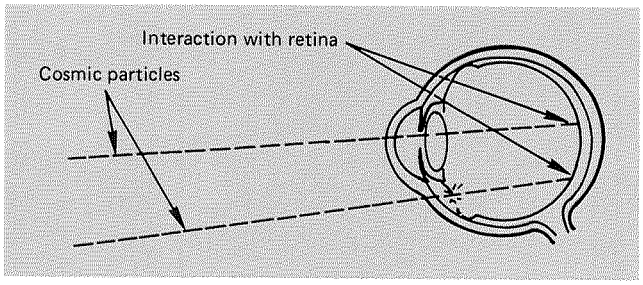

Figure 5-17.—Light flashes produced by energetic particles.

light on theories of the birth of elements in the universe. For example, the elements close to platinum ($Z=78$) in the periodic table are generally formed in processes involving rapid neutron capture, such as in high-neutron-density reactions in supernovae. Those close to lead ($Z=82$) are associated with slow neutron capture reactions, more typical of helium-burning phases (e.g., in red-giant stars). The thorium–uranium ratio is an indication of origin since it should vary from less than 1 in newborn stars to about 3 in older systems such as the Earth.

Light-Flash Observations

The observation of visual phenomena termed light flashes during manned space flight was first reported by Edwin Aldrin during the Apollo 11 mission. Similar observations were made on subsequent Apollo missions. No flashes were reported during earlier Mercury or Gemini flights, previous Earth-orbital Apollo missions, or the circumlunar flight of Apollo 8. Why no flashes were observed before Apollo 11 has not been explained. The most likely reason appears to be that the eye must be adapted to darkness and the observer must be reasonably relaxed and free from distracting activities. These conditions, by and large, did not obtain in flights pre-

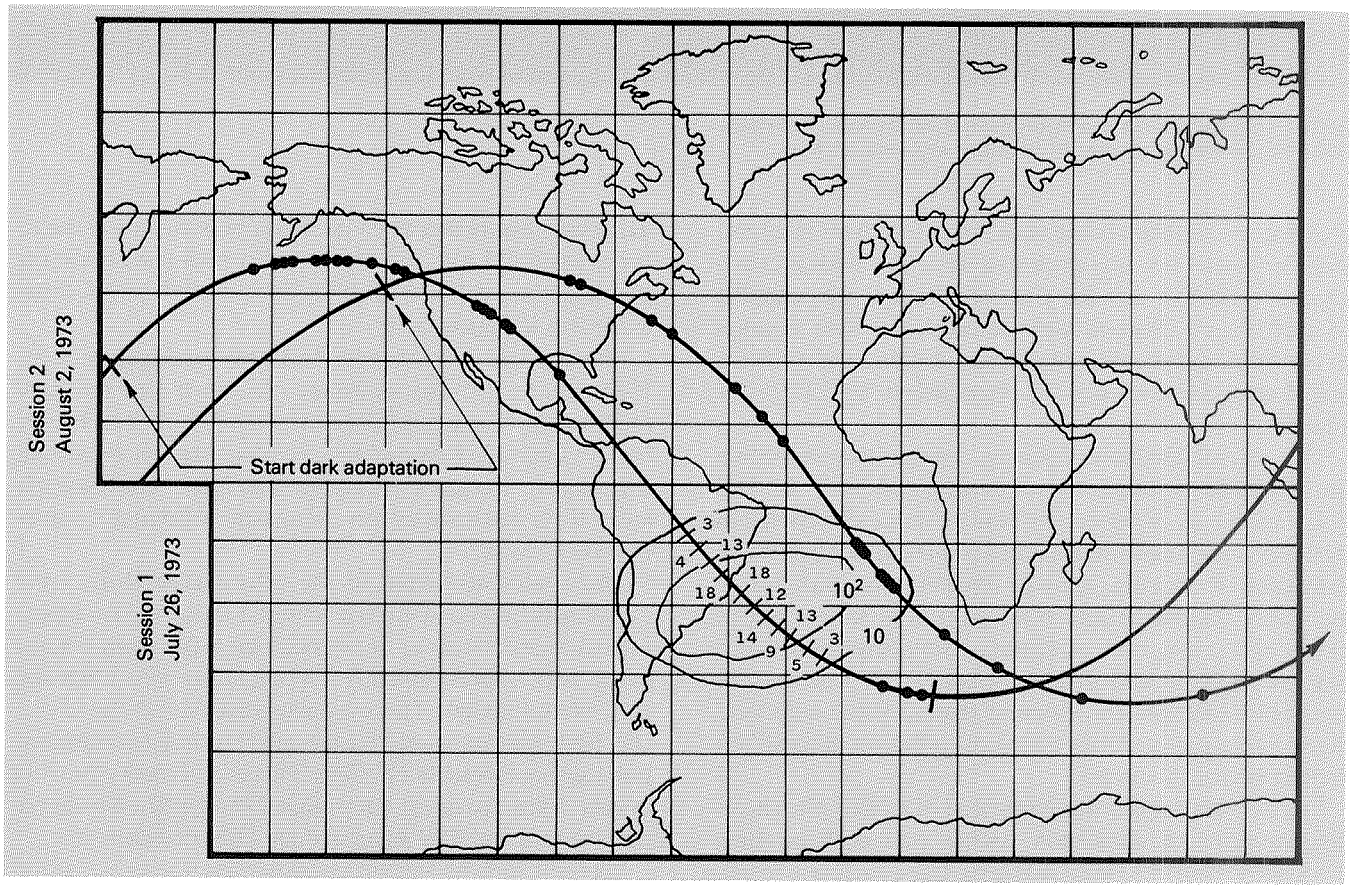

Figure 5-18.—Light flashes observed during two particular orbits selected to provide data on the effects of latitude and the South Atlantic anomaly.

ceding Apollo 11. A special effort was made to observe them on Skylab.

Although the cause of the flashes is not certain, the interaction of heavily ionizing particles with the visual apparatus, most probably the retina itself, appears to be the most likely explanation, as illustrated in figure 5-17.

If cosmic rays were the cause, there would be a latitude effect on the light-flash rate for an observer orbiting Earth because of the geomagnetic cutoff of charged particles and the steep energy spectrum of primary cosmic ray fluxes. Near the Equator, only cosmic particles with very high energy penetrate Earth's magnetic field to Skylab's orbital altitude; nearer the magnetic poles, particles of much lower energies reach comparable altitudes because the magnetic lines bend toward the Earth.

The primary objective of a study designed by R. A. Hoffman of the Johnson Space Center was to investigate the frequency and character of visual light flashes in near-Earth orbit as Skylab's path passed from northern to southern latitudes. Because the path periodically passed through the South Atlantic anomaly, a well-known region where the Van Allen belt bends closer to the Earth, another objective was to determine whether light flashes would occur as a consequence of the many energetic particles trapped there.

Figure 5-19.—Light flashes counted in and outside the South Atlantic anomaly, calculated cosmic ray flux, and Van Allen belt dosimeter response in the anomaly.

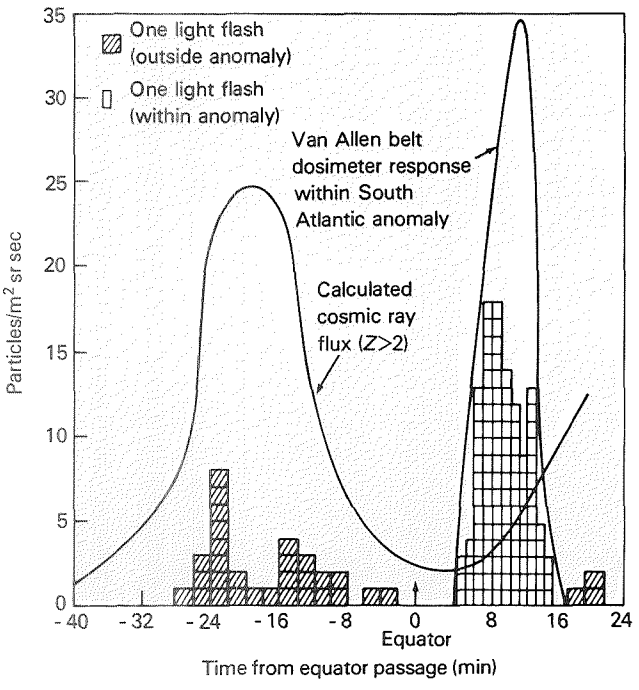

During the last Skylab mission, two separate light-flash observation sessions were conducted by astronaut William Pogue. Two particular orbits were selected to provide data on the effects of both latitude and the South Atlantic anomaly. The first session provided the best latitude conditions, but the space station passed only through the edge of the anomaly. During the second session, it passed through the center of the anomaly but did not achieve optimal geomagnetic latitudes. During each session, the astronaut, while in his "bed," donned a blindfold, allowed 10 min for adaptation to darkness, and then began to voice record his observations of each flash experienced before falling to sleep.

Figure 5-18 depicts the light flashes observed as the Skylab passed from the northern to the southern latitudes in its orbit. Each point represents the occurrence of a flash. Because of the high frequency of flashes detected during one of the two passes through the South Atlantic anomaly, the numbers shown for that case represent the number of flashes observed per minute.

Figure 5-19 represents the flashes observed before and after equatorial passage on session 1 of figure 5-18, a plot that roughly indicates latitude position. For example, Skylab was at the highest magnetic latitude approximately 20 min before and 30 min after equatorial passage. The calculated cosmic ray fluxes at the latitudes corresponding to the times on the abscissa are also shown.

Two conclusions are apparent. The occurrence of light flashes correlates with the flux of cosmic particles. However, the greatly increased number of flashes in the South Atlantic anomaly is not fully understood; they must result from either trapped protons in this region or possibly from trapped heavier nuclei.

Particle Research Continues

The first United States satellite, Explorer I, carried an experiment prepared by James Van Allen to measure cosmic radiation. However, the primary result of the experiment was the discovery of the belts of trapped particle radiation around the Earth. These radiation belts subsequently became the subject of intense research. Features of the belts now have become so well known that they have acquired a name, e.g., the South Atlantic anomaly. Still, many aspects of the energetic particle flux above the atmosphere remain to be understood. The fact that samples could easily be returned to Earth for analysis after long exposures in space allowed Skylab experimenters to make significant advances in this important, continuing topic of investigation.

6
The Earth's Atmosphere

The atmosphere is an extremely complex and variable structure. It has been studied from the ground and from various vehicles. Skylab's position above the atmosphere and the long duration of the missions enabled the crews to gather information about the atmosphere that could hardly have been obtained in any other way.

Figure 6-1 shows a sunrise photographed from Skylab. Orbiting the Earth once every 93 min, the astronauts of Skylab saw 15 sunrises during every 24-hr period.

The atmosphere is almost homogeneous up to some 95 km. The composition is fairly constant and much the same as at sea level. The principal constituents are nitrogen (78%), oxygen (21%), argon (1%), and minor constituents (~0.04%). Water vapor, aerosol particles, and an ozone layer are also present. Above the homogeneous zone the gases separate according to their masses

Figure 6-1.—Sunrise at Skylab.

Figure 6-2.—Characteristics of the Earth's atmosphere.

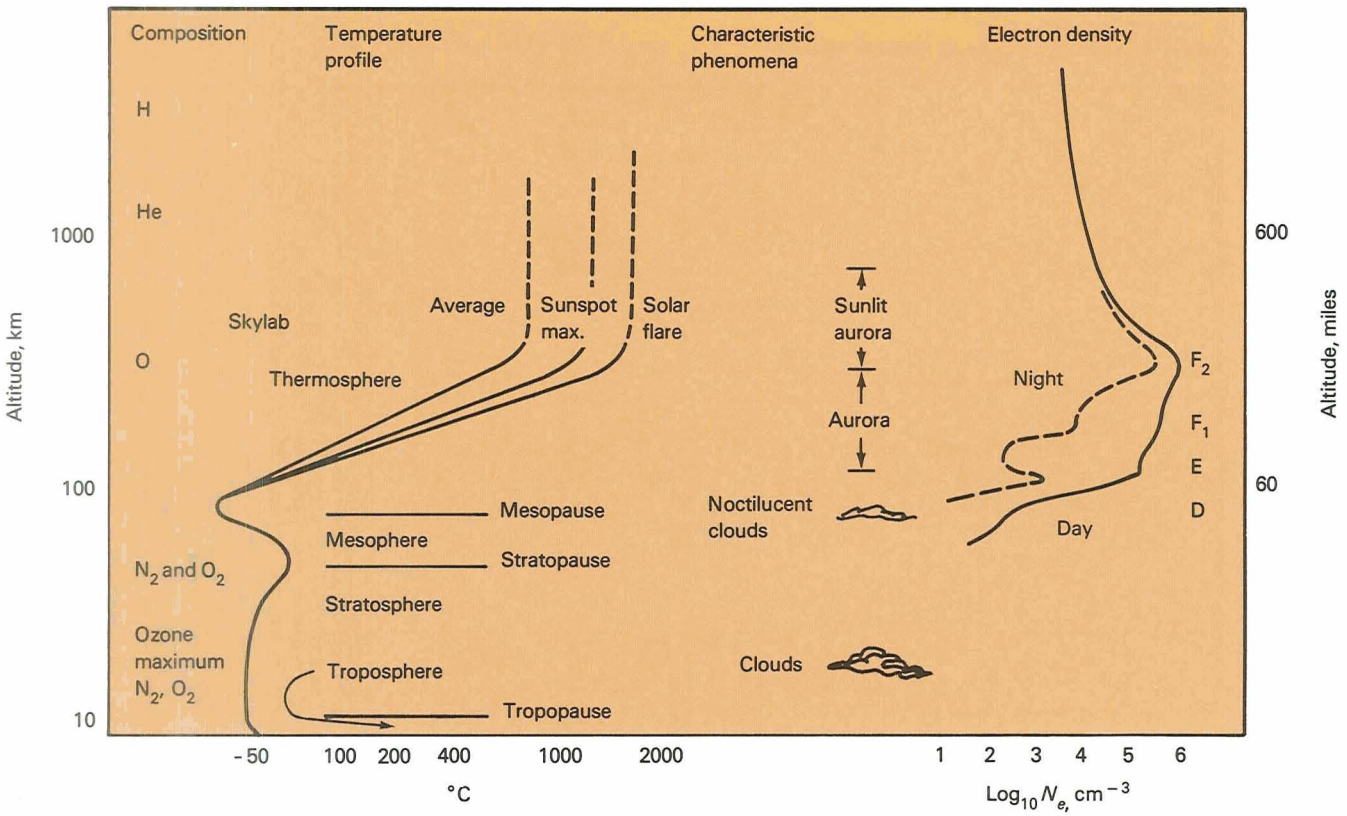

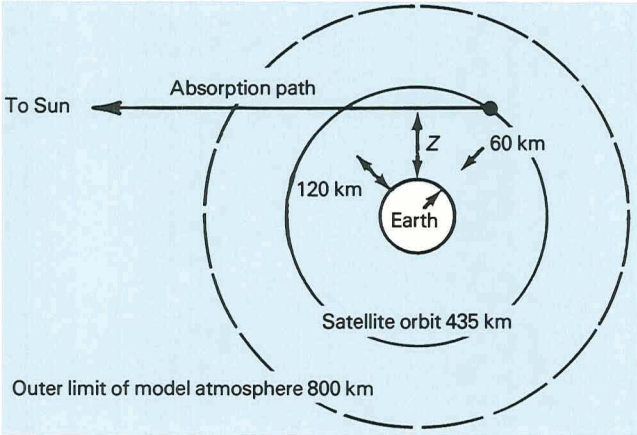

Figure 6-3.—Geometrical relationship of the Sun, Earth, and Skylab for atmospheric studies.

under the influence of gravity. Molecular oxygen and nitrogen occupy the lowest levels, whereas helium and hydrogen dominate at the highest levels. Between them lies a level of predominately atomic oxygen, which has an intermediate mass.

Ionosphere

In the thin upper reaches of the atmosphere, above 50 to 55 km, is the ionosphere where sunlight ionizes the air, producing free electrons and ions of the gases. The density of electrons fluctuates between night and day, from season to season, and from place to place above the Earth's surface. Some of these variations are predictable, and the general structure of the ionosphere is fairly well understood.

The ionosphere is subject to many disturbances. One of these results in the emission of visible light called the aurora, a condition that occurs when high-energy particles interact with air at high altitudes.

Figure 6-2 shows diagrammatically the composition, temperature, characteristic phenomena, and electron-density profile of the atmosphere.

Horizon Observations

Many Skylab experiments concerned the Sun and observed it directly without interference from the atmosphere. In other experiments, the Sun's light was used as a probe to study the atmosphere itself.

The geometry of the experiments is seen in figure 6-3. As Skylab moves toward the Earth's shadow, the sunlight reaching Skylab begins to pass through the uppermost reaches of the atmosphere. As the orbit continues, the distance traveled by the light through the atmosphere becomes greater, and the light passes through lower and lower layers of the atmosphere. The reverse sequence is observed at dawn. Moonrise and moonset offer the same opportunity for study of the various layers of the atmosphere. Since Skylab made about 15 revolutions in 24 hr, there were many sunrises and sunsets each "day," occurring over widely different

Figure 6-4.—The curvature of the Earth and Skylab's altitude.

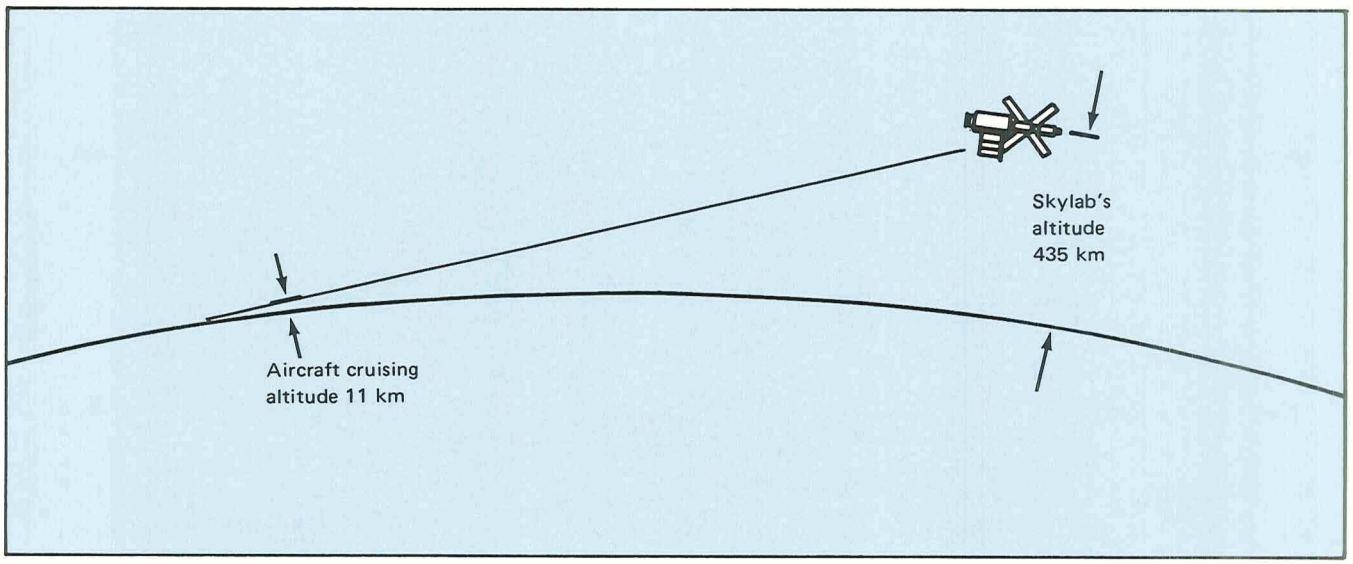

Figure 6-5.—The Moon through Earth's atmosphere.

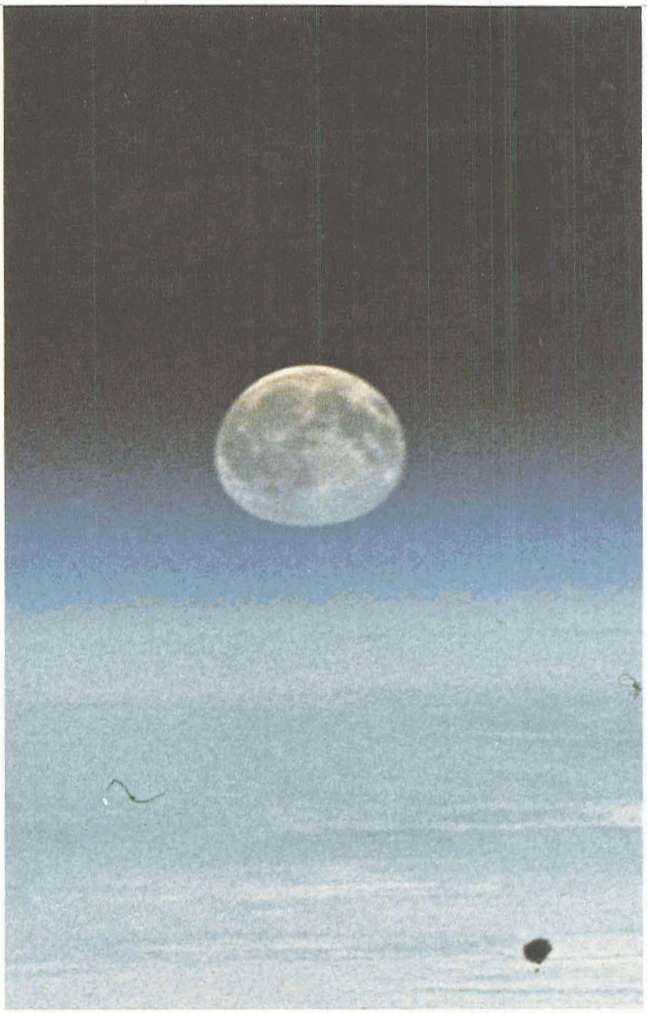

Figure 6-6.—The Moon rising higher on the horizon, seen almost without interference by the atmosphere.

locations. Because of the speed at which Skylab was traveling, the sunset or sunrise occurred so rapidly that atmospheric conditions did not change much.

Several methods have been developed for calculating altitude profiles, that is, changes in atmospheric properties throughout its height. Measurements of absorption of sunlight were made at several wavelengths from Skylab, to assist in establishing such profiles.

Figure 6-4 shows the curvature of the Earth and the space station's altitude to approximately true scale. For scale purposes, the typical altitude of a conventional airplane is shown as 11 km.

Moonrise

Photographs from Skylab of moonrise illustrate several features of the Earth's atmosphere. Figure 6-5 shows the illusion that the lower rim of the Moon has been lifted up or flattened. This is because the atmosphere's density increases rapidly toward lower altitudes. A ray of light traversing the dense, lower part of the atmosphere is bent (refracted) more than a ray traversing the less dense higher atmosphere.

In this picture the details of the Moon's surface

Figure 6-7.—The Moon above the atmosphere.

features are washed out. This is due to the scattering of light in the atmosphere. Scattering diminishes rapidly with altitude as the density decreases; therefore, more detail is visible on the upper part of the Moon than on the lower part, and the upper part is clearly brighter. The air above the horizon appears generally bluish because blue light is more strongly scattered than is red light. Since the Moon is full, the Sun is behind the space station, and the blue light in the atmosphere is backscattered sunlight.

Figure 6-8.—Sunrise seen from Skylab.

1

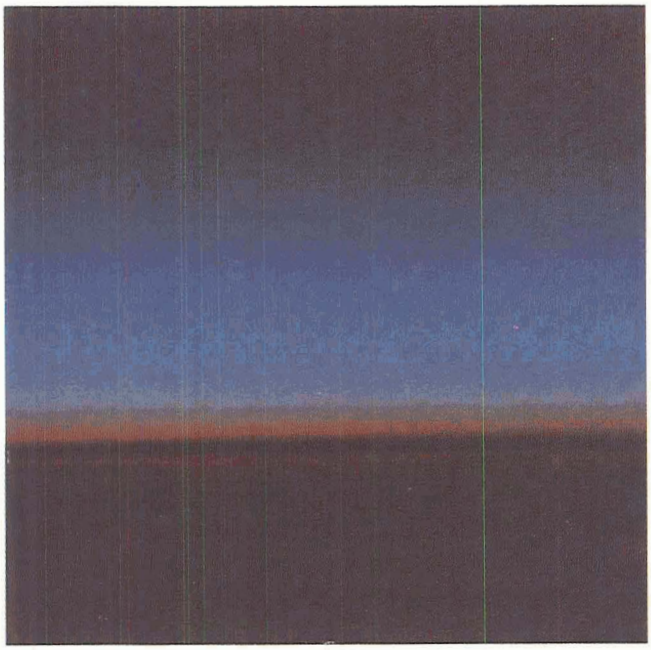

2

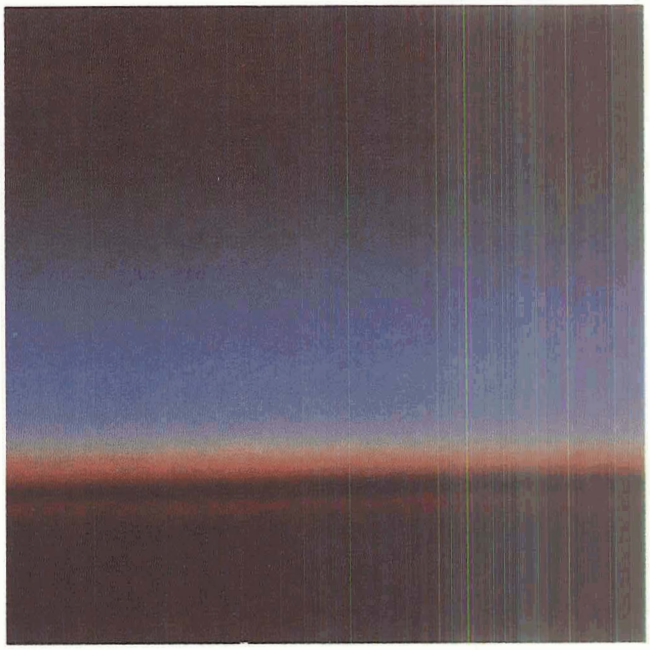

4

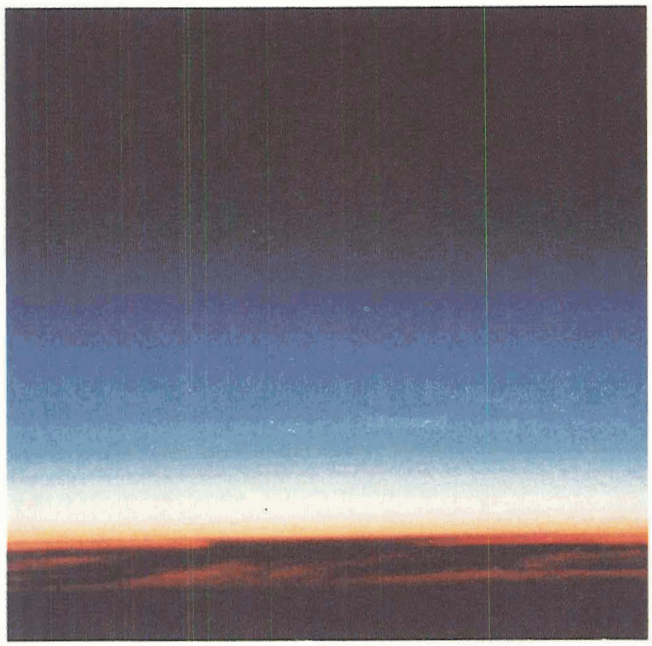

5

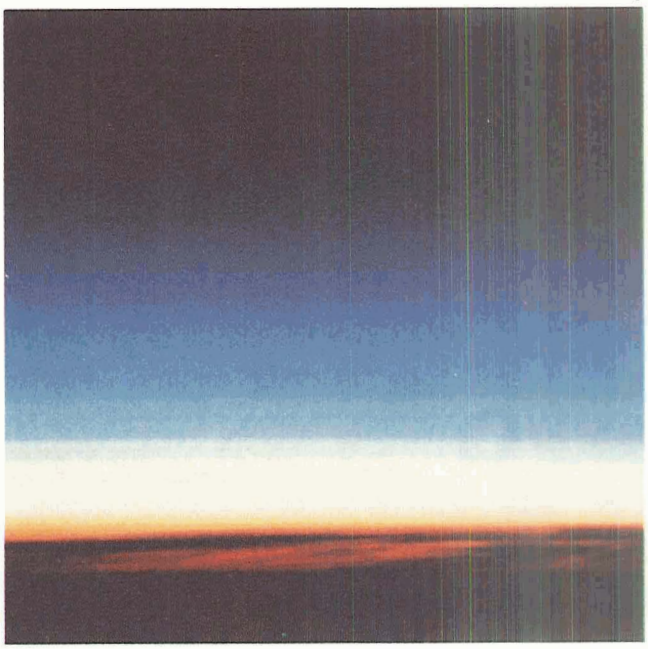

Figure 6-6 shows the Moon higher on the horizon. The distortion has largely disappeared; the surface details have become visible; and the usual, although slightly reddened, color has begun to appear at the top. The next photograph (fig. 6-7) shows the Moon well above the horizon with no apparent atmospheric effects.

3

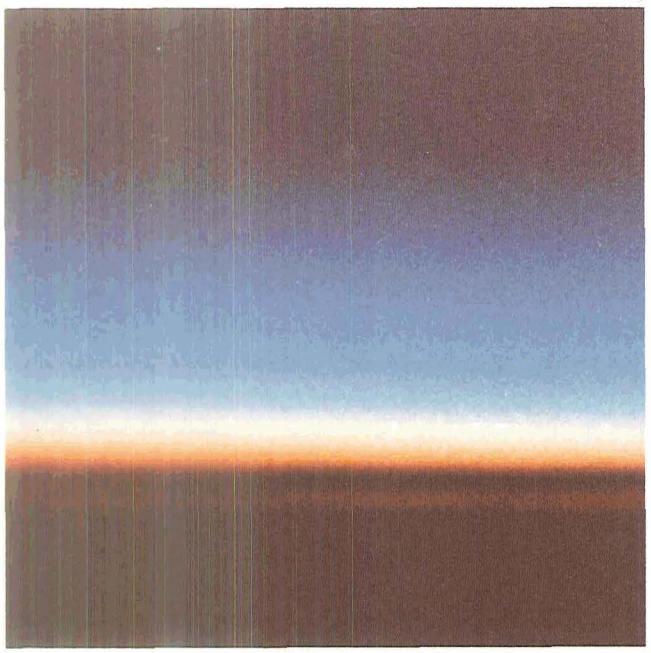

6

Sunrise

To the jetplane traveler, beautiful sunrises are a common sight. They display layers of various colors and thicknesses, indicating dust and pollutants in the air. Not much is known about local and global distribution of these manmade and natural constituents of the air.

Skylab maintained an enormous global overview and mapped many of the occurrences and changes in these atmospheric phenomena. Examples of such observations are shown in figure 6-8.

The series of photographs in figure 6-8 shows the progress from the first faint glow of sunrise to the point where the Sun can actually be seen underneath the cloud cover near the horizon. These photographs were taken for investigations by Donald Packer of the Naval Research Laboratory in Washington, D.C.

The exact interpretation of the various colors and strata is complicated because absorption in the ozone and oxygen layers cannot immediately be separated from scattering from aerosol or dust layers that may be present. For example, volcanic eruptions inject massive amounts of dust into the atmosphere.

The Earth's Limb in Ultraviolet

The Earth's atmosphere was also investigated with a Skylab coronagraph T025, a camera with a central disk to occult the Sun so that the region around it (the corona) can be seen without interference from the extremely bright disk of the Sun. Figure 6-9 shows the circular field of view of this instrument. In the center is the occulting disk covering the Sun. Toward the lower right is the illuminated curved Earth showing the Earth's atmosphere as an ill-defined edge. The crescent-shaped feature is an instrumental ghost image, not a real feature of the atmosphere. The object shaped like a bowling pin reaching toward the lower left is the occulting-disk support, which is out of focus.

Figure 6-10 is an enlarged negative print of the Earth's limb and atmosphere taken in 250 nm ultraviolet light with this coronagraph for Mayo Greenberg of the Dudley Observatory, Albany, New York. The atmosphere is seen "edge on," and the amount of radiation passing through each level of the atmosphere can be investigated. It shows that a horizontally layered structure is present. A height scale has been superimposed on the photograph. At 250 nm, atmospheric ozone absorbs much of the radiation. The investigators compare photographs such as figure 6-10 with corresponding photographs at wavelengths (e.g., 360 nm) where the

influence of ozone is negligible. From quantitative determinations of the differences, atmospheric composition values can be deduced.

The observed atmospheric radiation at 360 nm is primarily due to scattering by air molecules. A smaller portion may be scattered by very small (less than 0.1 μm) particles in the atmosphere. Since the changes in brightness, as a function of angle from the sun, can be calculated for air molecules, brightness variations from those calculated indicate the presence of very small particles as a function of height. The occulting disk was used in these experiments because the aerosol or particulate matter in the atmosphere is detected more easily when one looks toward the Sun, that is, when the particles are illuminated from behind.

Figure 6-9.—The Earth's limb in the ultraviolet. The center (A) is the occulting disk covering the Sun. The illuminated Earth (B) shows the atmosphere as an ill-defined edge. The crescent shape (C) above it is an instrumental artifact.

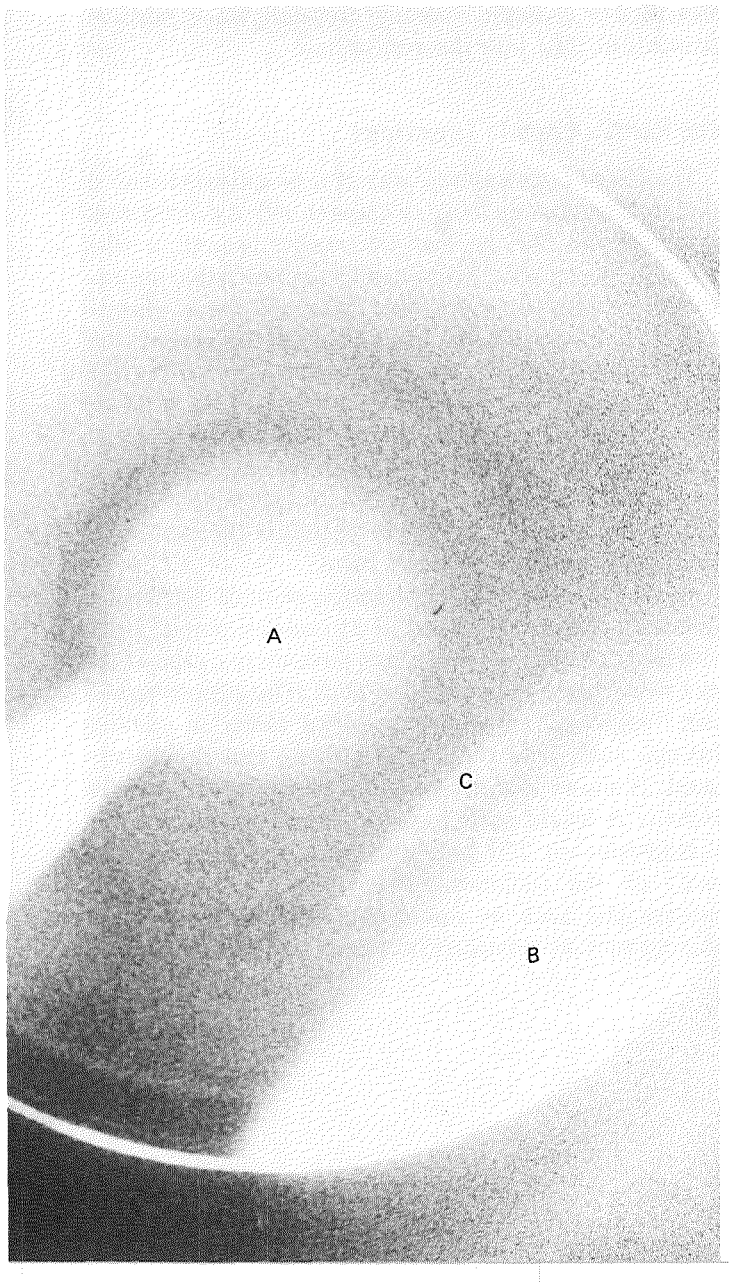

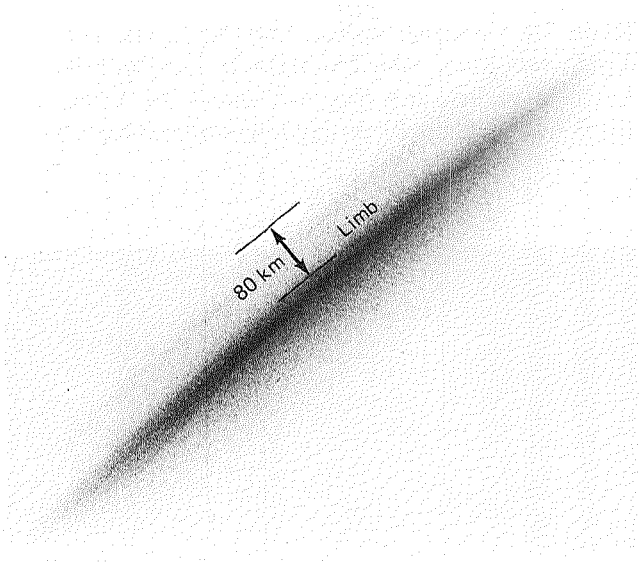

Figure 6-10.—Enlarged negative print of the Earth's limb in the ultraviolet, edge-on view.

Atmospheric Absorption of the Sun's Extreme Ultraviolet Radiation

A more detailed and sophisticated picture of atmospheric properties can be obtained by studying the extinction, or gradual disappearance, of specific spectral lines of the Sun as it slowly sets beneath the horizon. During a sunrise or sunset, it was possible for Skylab to observe the atmospheric absorption profiles at a number of extreme ultraviolet (EUV) wavelengths using the solar observatory instruments.

The reason for the strong interest in these wavelengths is that the solar EUV radiation at wavelengths below 125 nm is the principal source of energy for heating and ionizing Earth's upper atmosphere. In particular, solar EUV radiation is absorbed at altitudes between 80 and 300 km.

One instrument on Skylab using this technique was an EUV spectroheliometer (S055) that was part of the solar instrument array and used primarily for studies of the Sun. That photoelectric instrument was designed to obtain up to seven simultaneous spectroheliograms in the range 28 to 135 nm with a spatial resolution of 5 sec of arc and also to perform spectral scans with a resolution of 0.16 nm over the same wavelength range. Because of its large size, the instrument had a sensitivity far greater than that of any photoelectric EUV spectroheliometer used in space up to the time of Skylab.

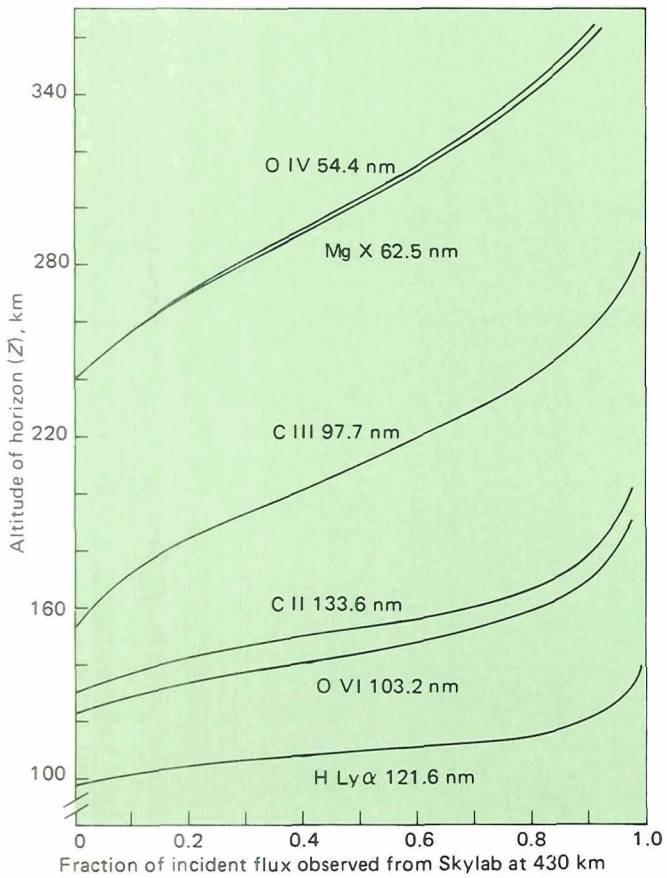

Figure 6-11.—Atmospheric extinction profiles at 45.7°S 118.8°E, December 6, 1973, 1135 GMT (sunset).

Examples of atmospheric extinction profiles, recorded at sunset on December 6, 1973, are shown in figure 6-11. Each spectral line in the figure is identified with the ionized element in the solar atmosphere emitting the line. The altitude at the horizon is the quantity designated Z in figure 6-3. From these profiles, investigators at the Harvard College Observatory found that it was possible to determine the temperature and composition of the Earth's upper atmosphere over the altitude range from about 100 to 360 km. The quantitative data were obtained by applying sequentially the known absorption characteristics of atmospheric constituents, starting with the longest wavelengths. Since the three longest wavelengths (133.57, 121.57, and 103.19 nm) are absorbed solely by molecular oxygen, which has a different absorption cross section for each wavelength, absorption at these wavelengths can be used to determine its density in the range 100 to 170 km. For example, the 133.57 nm line has the greatest cross section and hence less molecular oxygen is needed to absorb it. Light of this wavelength will therefore be completely absorbed higher in the Earth's atmosphere.

Solar radiation from doubly ionized carbon at 97.7 nm is absorbed both by molecular oxygen and by nitrogen. Once the oxygen density as a function of altitude has been determined, this profile can be used to determine its absorption of the 97.7 nm radiation. Subtracting this from the observed absorption gives the nitrogen absorption, from which can be calculated the nitrogen density in the 170- to 250-km region.

Finally, the two solar wavelengths from triply ionized oxygen (55.4 nm) and nine-times ionized magnesium (62.53 nm) are absorbed principally by atomic oxygen, with a small amount of absorption by nitrogen. These profiles can thus be used to determine the density of atomic oxygen over the altitude range 250 to 360 km. The temperature of the neutral gas can then be determined from the variation of density with altitude.

Figure 6-12 shows the number density of molecular oxygen determined from a set of absorption profiles taken during one Skylab sunset on September 15, 1973. The densities predicted by a theoretical model of the upper atmosphere are shown for comparison with the measured data.

Spectral Line Absorption

The composite illustration in figure 6-13 was reconstructed from data obtained with a solar ultraviolet spectrograph (S082) by investigators from the Naval Research Laboratory. These spectrograms of the setting Sun were taken on August 18, 1973, as Skylab's line of sight passed through progressively lower and more dense layers of the Earth's atmosphere. The minimum altitude Z of the light path above the Earth's surface is given in the scale at the left.

Molecular oxygen is the principal absorbing species, although the absorbance varies a great deal over the spectral region from 121.6 to 192.5 nm shown in figure 6-13. At 155 nm, absorption by molecular oxygen is the strongest, and the line pair (154.8 and 155.1 nm) due to triply ionized carbon is completely obliterated at an altitude of 145 km. Wavelengths above 190 nm are least affected, and the Sun's emission at these wavelengths penetrates much deeper into the atmosphere, down to altitudes that can be reached by high-altitude balloons.

The Lyman-alpha radiation from the Sun is broadened by turbulence and pressure in the Sun's atmosphere. The sharp absorption line seen at the center of this line is due principally to absorption by Earth's geocorona of hydrogen. Similar absorption "notches" can

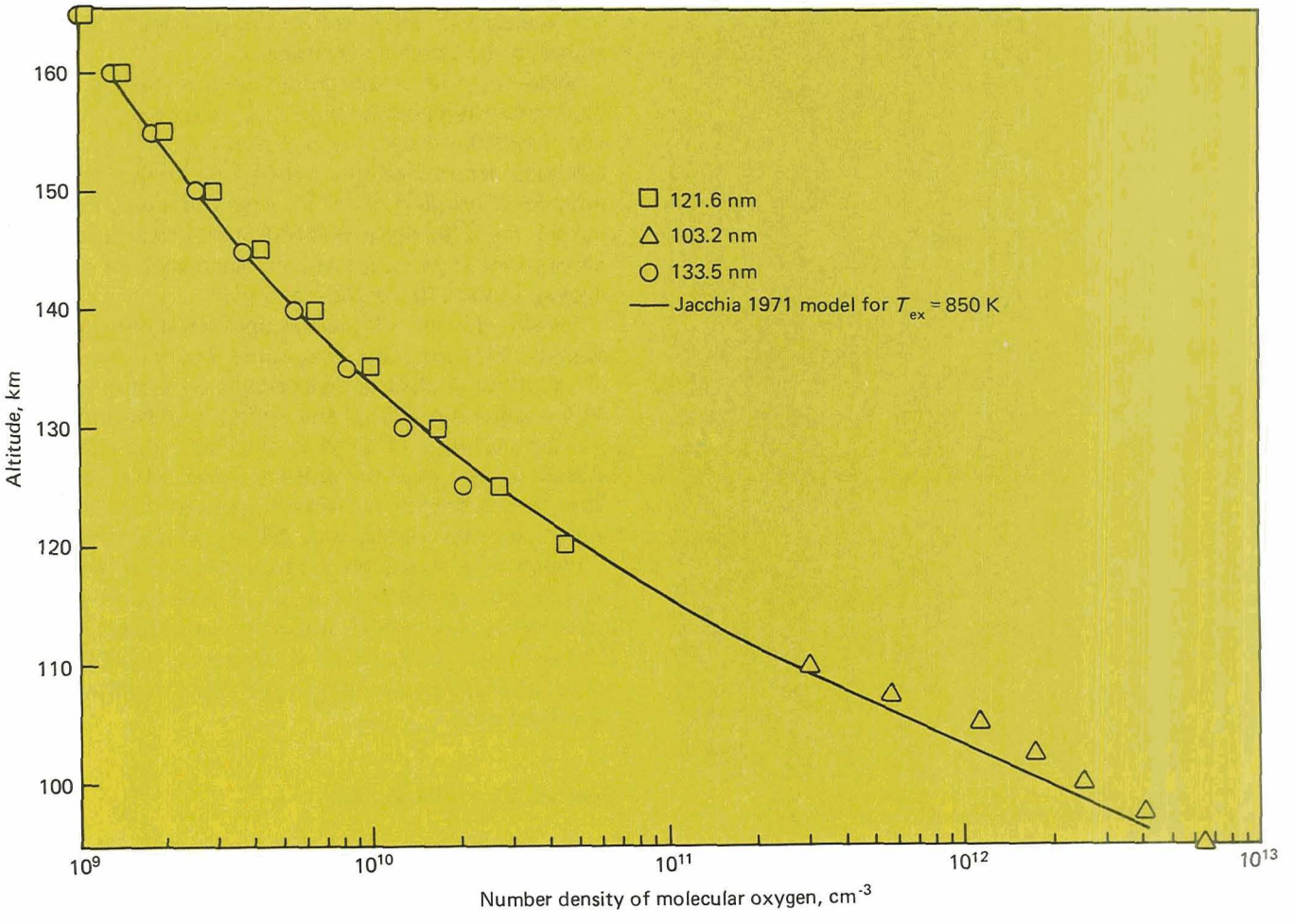

Figure 6-12.—Number density of molecular oxygen determined from absorption profiles taken at a sunset on September 15, 1973.

be seen in the atomic oxygen lines near 130 nm; they are caused by the atomic oxygen in the Earth's atmosphere.

Measurements of spectral absorption by the Earth's atmosphere, such as those shown in figure 6-13, are the starting point for detailed atmospheric composition determinations. Results on the molecular oxygen distribution, for example, show large variations with time and geographic location.

The Aurora

Photographs of aurorae were made as part of a study (S063) of the upper terrestrial atmosphere by Donald Packer of the Naval Research Laboratory. Auroral displays are produced by charged particles that precipitate downward along geomagnetic lines of force into the high atmosphere in a zone circling each magnetic pole. The formation of aurorae is related to geomagnetic disturbances, which in turn are often triggered by solar events and resulting changes in the solar wind.

One such solar event was a spectacular solar flare that began at 1140 GMT on September 7, 1973. About 2½ days later, the particles ejected from the Sun during the flare began impinging on the magnetosphere, as indicated by a sudden decrease in the cosmic ray flux and rapid rises in geomagnetic activity indices, quantities measured throughout the world on a routine basis. Skylab's orbits carried it into the southern auroral zone at night during this period of atmospheric disturbance. Owen D. Garriott, the scientist pilot of the second manned mission, photographed some of the spectacular aurorae that occurred. Two pictures taken during this period are shown in figures 6-14 and 6-15. These photographs were made with a hand-held camera with a

55-mm lens on Kodak High Speed Ektachrome. Exposure times ranged between 1 and 4 sec.

Figure 6-14 was taken at 2140 UT on September 9, 1973. It shows a very intense emission from the 557.7-nm green atomic oxygen line extending in a band parallel to Earth's horizon. Some discrete auroral forms are also present. Emission from atomic oxygen at 630.0 to 636.4 nm is also prominent as a red glow extending upward from the green band to beyond 250 km. Auroral rays above the main layer are parallel to the geomagnetic lines of force.

The photograph shown in figure 6-15 was taken at a shorter exposure 1 min later and slightly displaced from it. The aurora has evolved somewhat, now showing folds extending toward and away from the observer.

Approximately 2 days later, a discrete rayed arc appeared at night (fig. 6-16), with a thin shell of quiet luminescence viewed "edge on" at the left. The sharp upper boundary of this layer is characteristic of airglow, but the overall intensity appears to be excessive for airglow and probably includes radiation induced by particle bombardment. The full Moon illuminates the Earth in the foreground.

Approximately 1 min later, the complete rayed arc

Figure 6-13.—Altitude dependence of the absorption of solar emission lines by atmospheric constituents. The numbers at the left refer to the altitude index *Z* at which each spectrum was taken. (A) Absorption of 1216 Å (Lyman-alpha) by molecular oxygen. The conspicuous absorption in the core is by atomic hydrogen in the geocorona. (B) Absorption of three lines (1302, 1305, 1306 Å) in their cores by atomic oxygen and in the whole line by molecular oxygen. (C) Absorption of 1548 and 1551 Å by molecular oxygen. These lines are near the absorption maximum of molecular oxygen and are almost entirely absorbed above 150 km. (D) Absorption by bands of molecular oxygen is much weaker at 1900 to 1925 Å. The Sun's emission can therefore penetrate even to balloon altitudes.

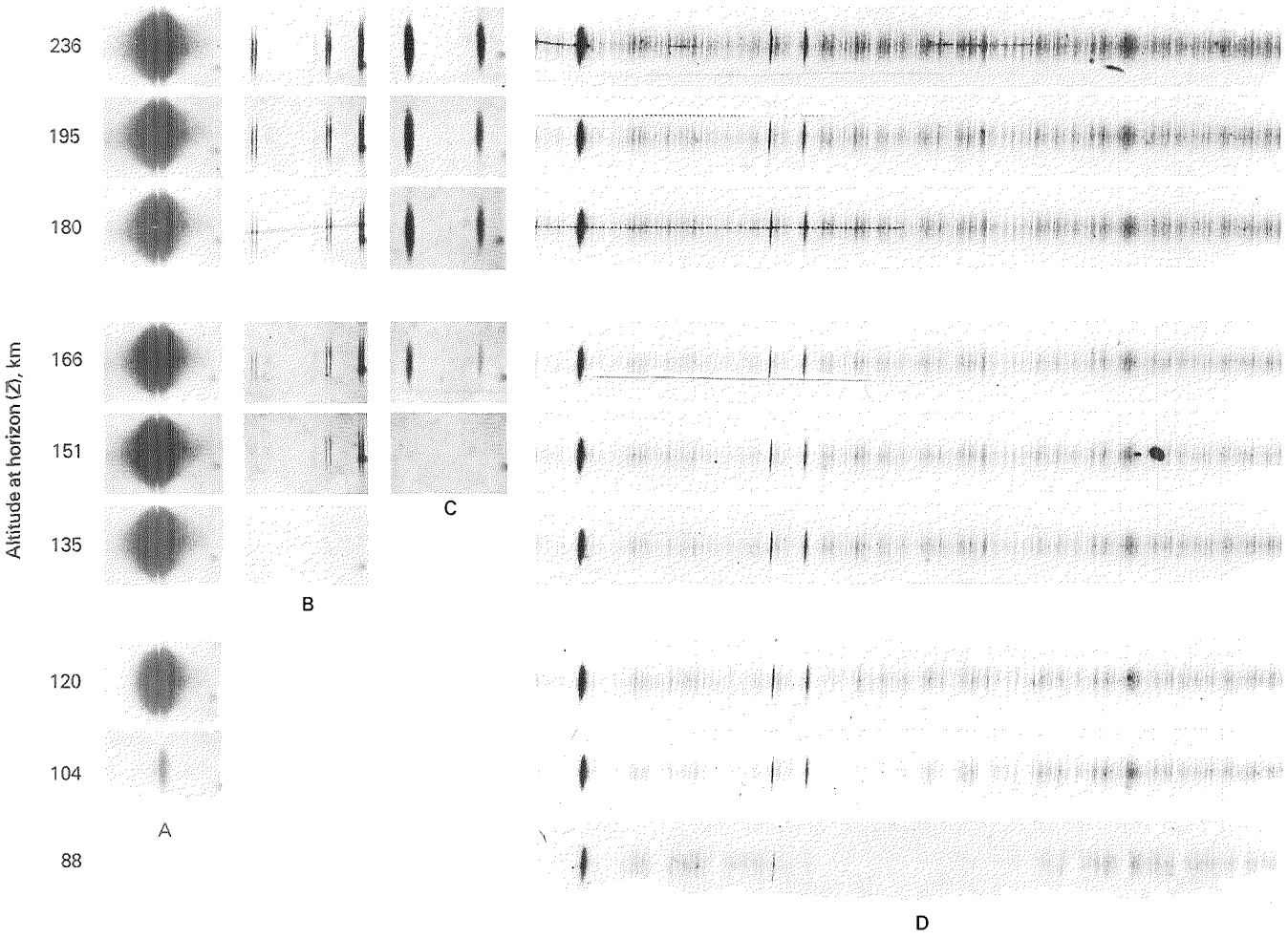

Figure 6-14.—Southern aurora at 2140 UT, September 9, 1973.

Figure 6-15.—Aurora at 2141 UT, September 9, 1973.

was seen (fig. 6-17). It extended over 400 km in length. The lower border at 120 km coincided with that of the luminous layer seen edge on at the right. Not visible in figure 6-17, but visible in the original, is another band extending to the left and 20 km lower in altitude. The lower band is at the same altitude as the luminous layer seen in figure 6-15.

Figure 6-18 was taken two orbits later on the same day, when Skylab was back close to the same position relative to the Earth and the Sun, but the Earth had rotated about 45° to the east (Skylab was therefore about 45° further west than it had been when the photograph shown in figure 6-17 was taken). Figure 6-18 shows an intense, green-rayed arc folded back on itself and merging into a thin, less bright homogeneous band extending toward the horizon.

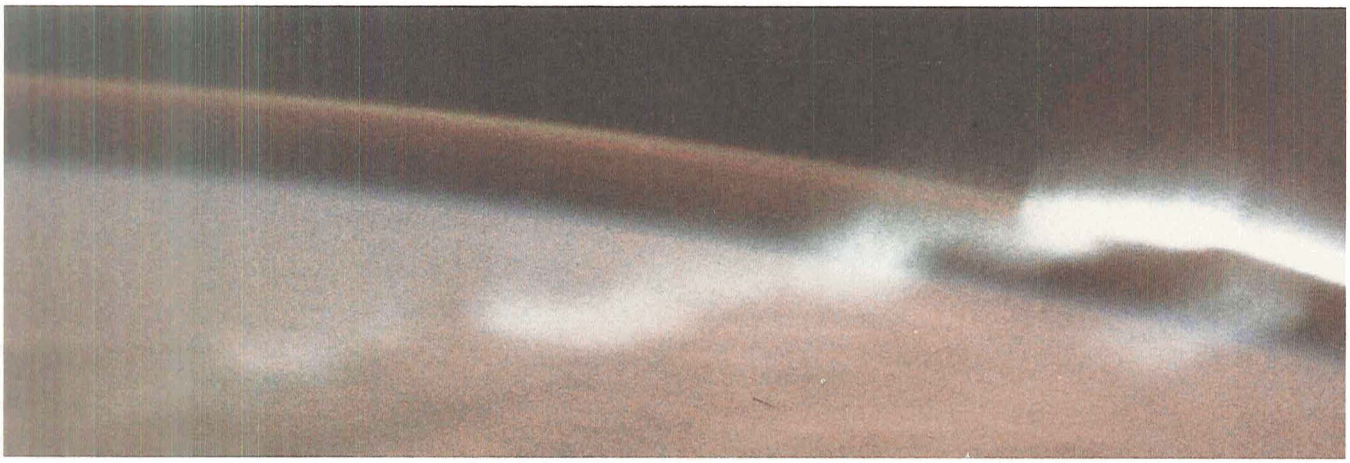

Figure 6-16.—Aurora at 1843 UT, September 11, 1973.

Figure 6-17.—Aurora at 1844 UT, September 11, 1973.

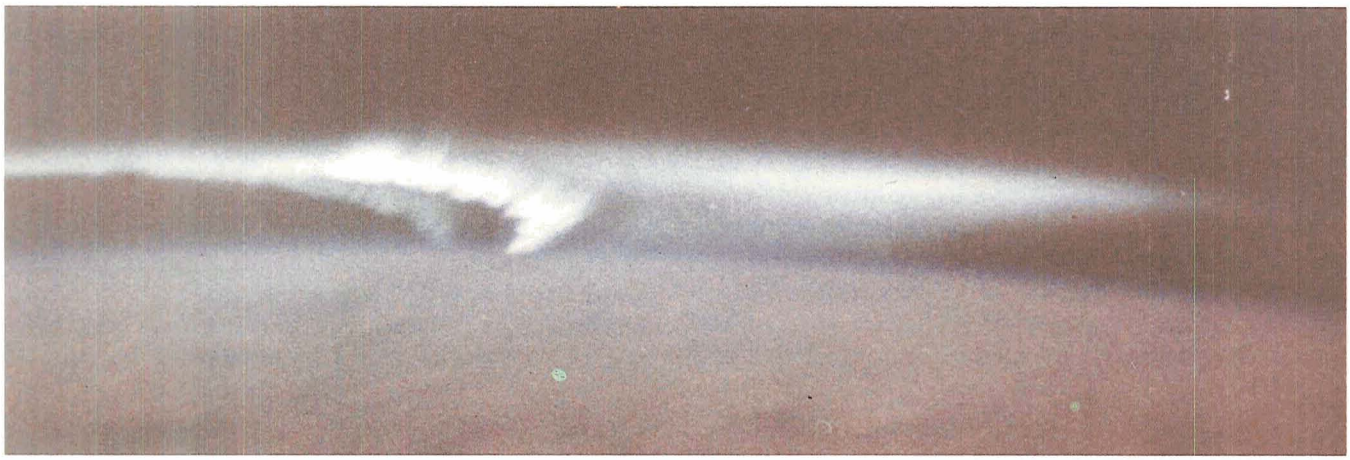

Figure 6-18.—Aurora at 2152 UT, September 11, 1973.

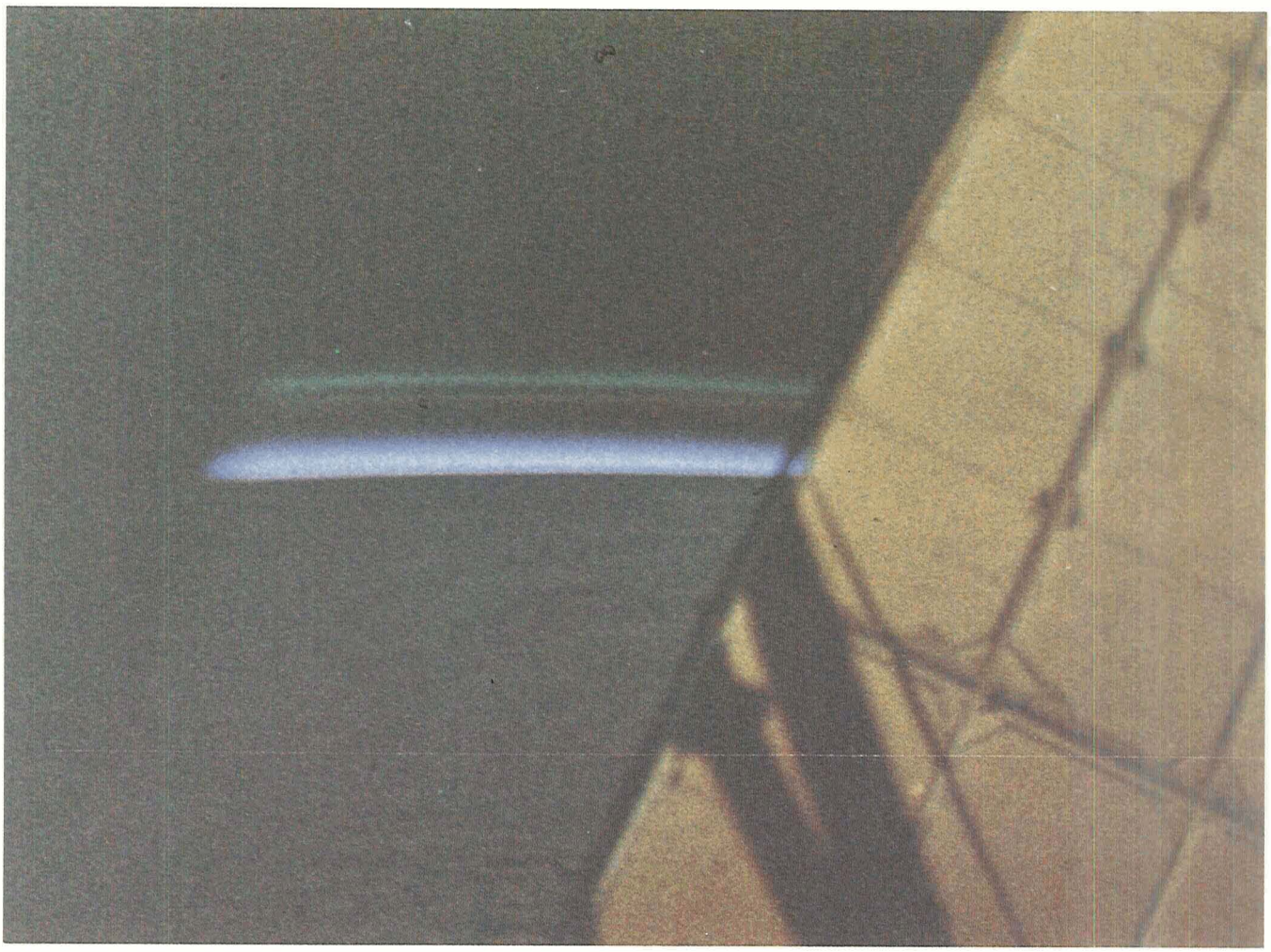

Figure 6-19.—Luminous layers above illuminated lower atmosphere.

Figure 6-19, taken 20° farther west at early dawn, shows two distinct luminous layers above the brightly illuminated lower atmosphere. These layers are similar to those shown in figures 6-16 and 6-17, and are at 100 and 120 km. No discrete auroral forms are present. The top layer is whitish, and its intensity is twice that of the lower layer, which appears generally reddish.

The series of photographs in figure 6-20, taken during the second manned mission, show a fairly constant northern polar cap layer of aurora with a surprisingly persistent pattern of aurora over the horizon. The bright spots in the foreground are lightning; the yellowish light patterns are city lights showing diffusely through clouds. The location of the lightning flashes varies from picture to picture, whereas the cities form a constant pattern on the ground.

Significance

The atmosphere is very complex and changeable; despite the many techniques that have been used in the past to study it, it has been very imperfectly understood. Skylab has permitted observation from a new perspective and also the use of new techniques.

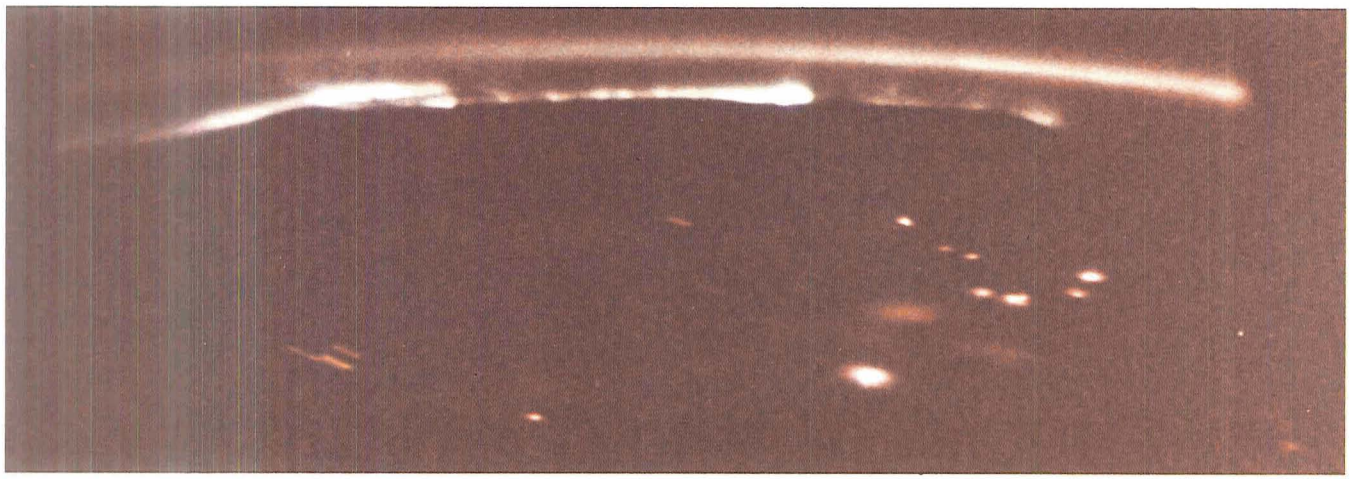

1

2

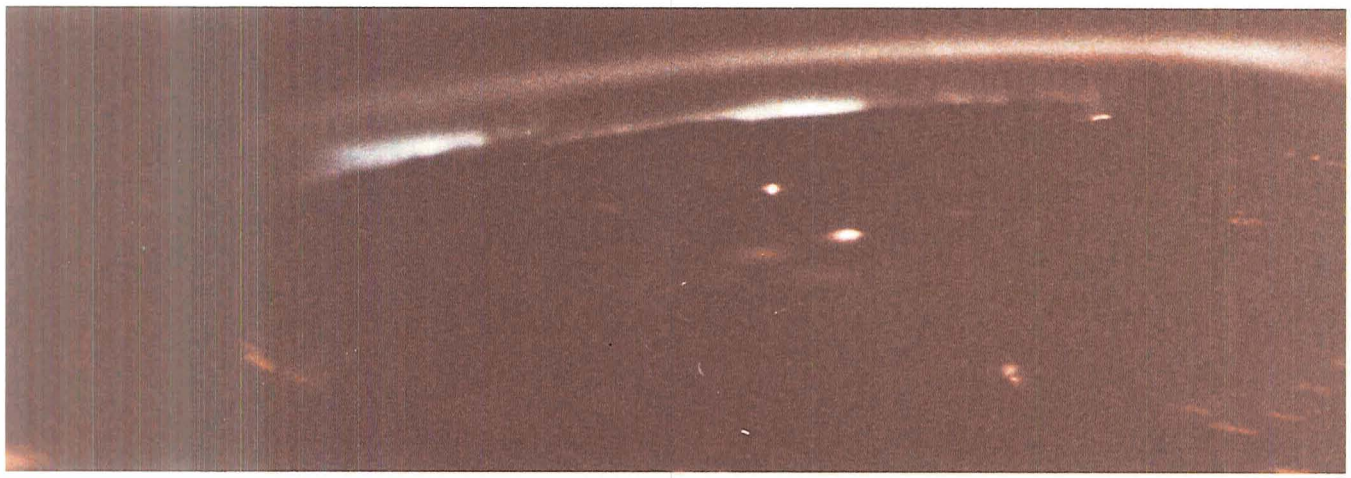

3

Figure 6-20.—Polar cap aurora.

7
Orbital Environment

During the first U.S. orbital flight of Mercury 6, astronaut John Glenn observed particles outside the spacecraft which he called "fireflies." They were later identified as condensed ice crystals from the small hydrogen peroxide rockets used for altitude control. Since this early observation, it has been established that a spacecraft creates a small cloud of debris or contamination around itself. The cloud is formed from gas released by external material surfaces, minor vehicle leaks, control rocket firings, and vented waste materials. It can cause degraded "vision" for any viewing instruments that must observe through it and can produce a deterioration of external surfaces by the deposition of contaminants.

Figure 7-1 shows a darkening of Skylab's external white-painted surfaces, which resulted from such contamination. The contaminants are characteristic of gases released from nonmetallic materials.

Contamination Studies

Skylab, the first true space laboratory with an extended flight time (several months), provided an opportunity to study the contamination cloud and the effect of its surface deposition over a long period. The space station contained monitors of external contamination, experiments to evaluate the effects of the space environment on materials, and experiments to investigate contaminant deposition on typical external materials in the space station.

Figure 7-1.—Contamination-induced darkening of Skylab's painted exterior.

Contamination information was also obtained, as secondary data, from instruments designed for other purposes. Furthermore, the astronauts visually observed contamination both inside and outside Skylab.

Skylab had several sensitive optical instruments that were susceptible to contamination. Design criteria were generated before the mission to select materials that would produce minimum contaminants in space. Mathematical models were developed and laboratory tests were made to simulate the orbital environment of the space station. On this basis, optimum locations were chosen for experiments and vents, covers were installed over susceptible apertures and windows, and operational procedures were generated to minimize contamination of critical surfaces. During the mission, these procedures permitted controlled venting activities and the performance of experiments with minimum possibilities for contamination.

Contamination-Measuring Instruments

The deposition of contaminants was measured with a device called a quartz-crystal microbalance. Two quartz crystals vibrate mechanically, driven by electronic circuits. The frequency of vibration depends on the effective mass of the crystal. The addition of foreign matter to the surface of a crystal increases its effective mass and decreases its frequency of vibration. The crystals are as nearly identical as they can be made and vibrate at

almost the same frequency. An electronic circuit compares the frequencies of the two crystals and generates a signal that depends on the difference. One crystal is exposed to the environment being studied, the other is at the same location (same temperature, etc.) but shielded from contaminants. Under these circumstances, the signal produced depends entirely on the mass of material deposited on the exposed crystal.

The device is extremely sensitive. An idea of its sensitivity is conveyed by the fact that a monolayer (a layer of contaminants one atom thick) will produce a signal (frequency difference) of 1 Hz, which is quite substantial with modern techniques. Figure 7-2 shows the device.

In all, there were six quartz-crystal microbalances placed in critical locations, including two mounted on the solar observatory sunshield looking directly at the Sun and four located beneath the docking adapter, near the Earth resources instruments (fig. 7-3). Of these, two were pointed away from the vehicle and the other two were pointed along the vehicle, one toward the command and service module and the other toward the orbital workshop.

Data from these devices were telemetered to the ground and were monitored throughout the mission. If contamination rates rose to a level that would interfere with a particular experiment, that experiment was postponed until a more suitable time. In addition, during the time that the externally mounted solar observatory or airlock instruments were operating, controlled vents were closed. Conversely, the optical surfaces were cov-

Figure 7-2.—Quartz-crystal microbalance used to measure contamination deposition.

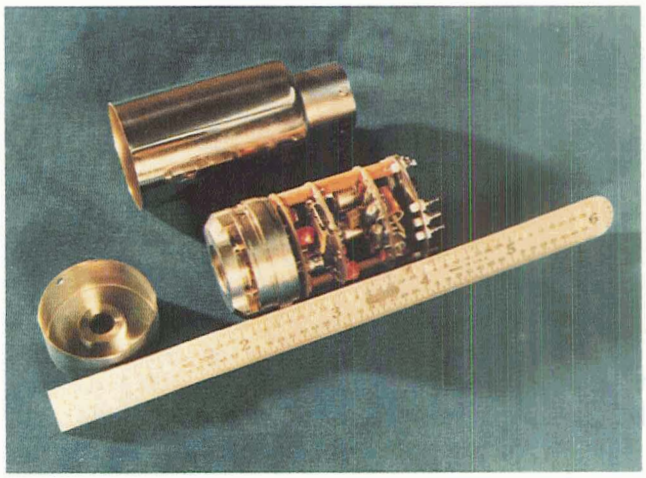

Figure 7-3.—Locations of quartz-crystal microbalances on Skylab.

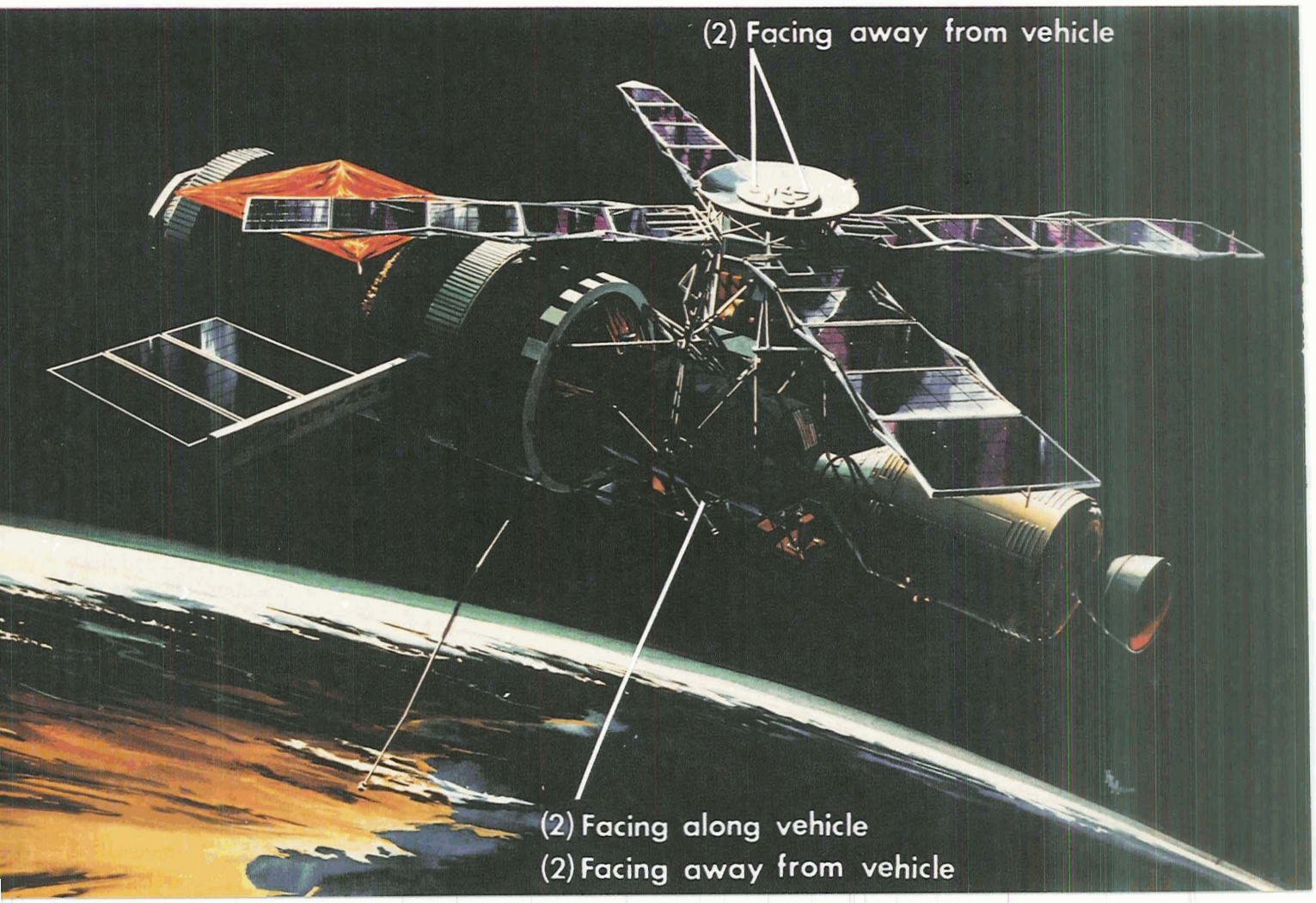

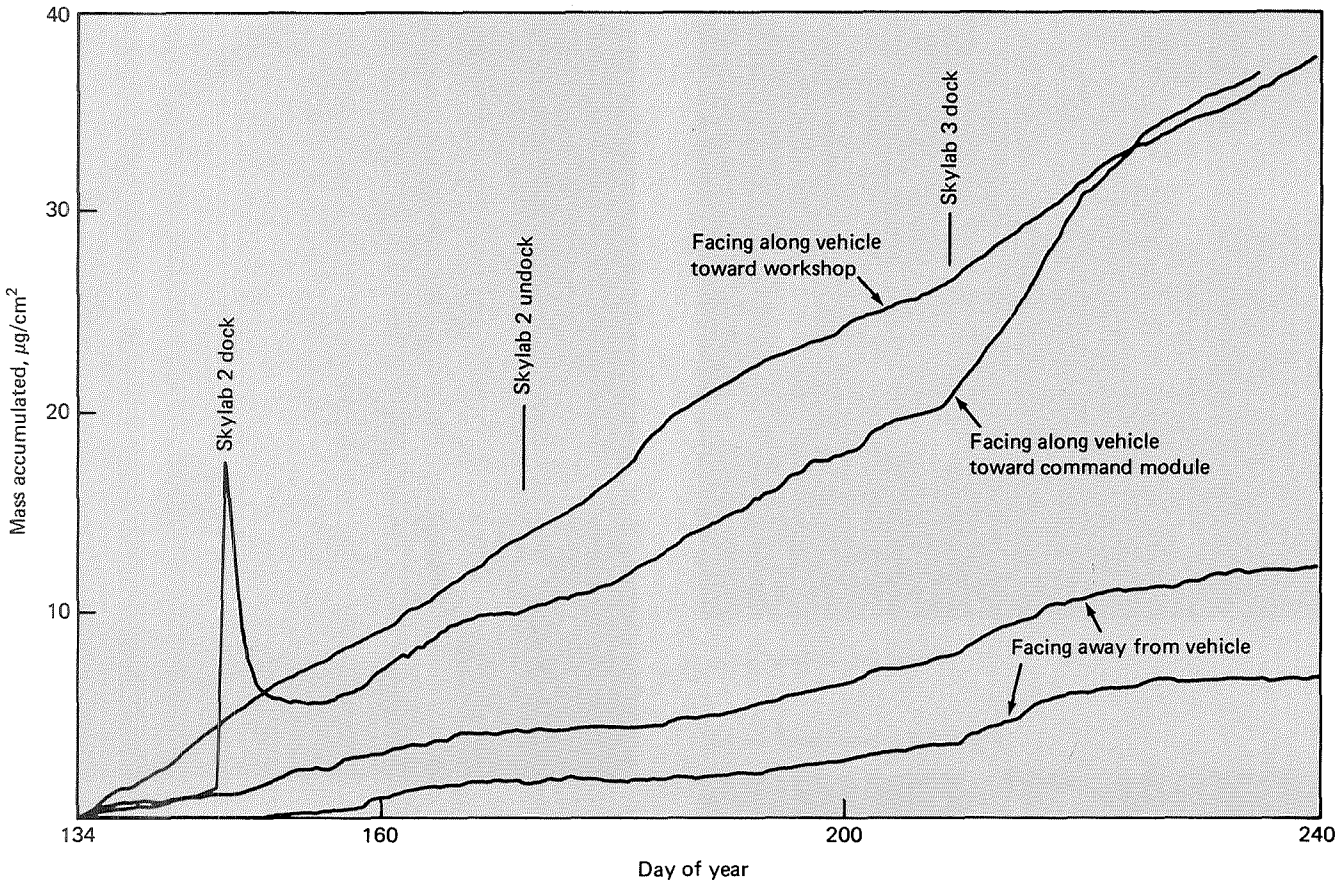

Figure 7-4.—Contamination buildup as a function of time as measured by microbalances on docking adaptor.

ered by doors except during periods when they were in use.

The time history of mass accumulation on the quartz-crystal microbalances is shown in figure 7-4. Crystals facing along the Skylab's longitudinal axis registered the highest contamination rates. It is believed that structures in the line of sight of these crystals released gases and caused the deposition. Crystals that faced away from the vehicle collected deposits presumably consisting of contaminants which originated from the space station and whose molecules were backscattered by the atmosphere around the space station. Gases released from wire bundles in the field of view of these crystals were also a source of contamination. Early in the mission, the crystal facing the command module was contaminated by the steering-rocket exhaust. The two crystals mounted on the solar telescope were much warmer than the others and did not show any deposition, because the contaminants did not adhere well to warm surfaces.

Sun-Tanned Vehicle

For temperature control, large areas of the external surfaces of Skylab were painted with a special white thermal-control paint. These surfaces were photographed by the first Skylab crew from the command and service module, before they boarded Skylab. At that time all the surfaces were still pristine white (fig. 7-5). Later, it was reported during a spacewalk that some brownish discoloration was visible on the underside of the solar observatory's solar panels. Photographs taken by the following two crews showed that this surface darkening increased with time (fig. 7-6). The brownish color appeared darkest near the hatch through which the astronauts went in and out for spacewalks (fig. 7-7). The airlock, in which the spacesuited astronaut went through decompression immediately before his walk in space, normally maintained cabin pressure. During a spacewalk the materials in the airlock were subjected to space vacuum and these apparently emitted gases that

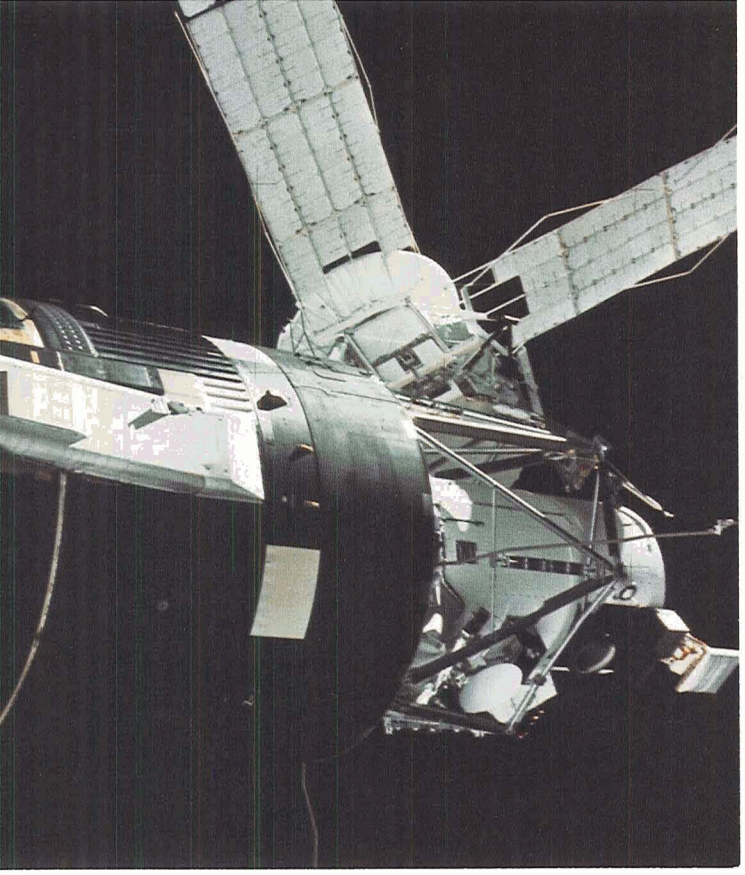

Figure 7-5.—Skylab clean.

Figure 7-6.—Sun-tanned Skylab.

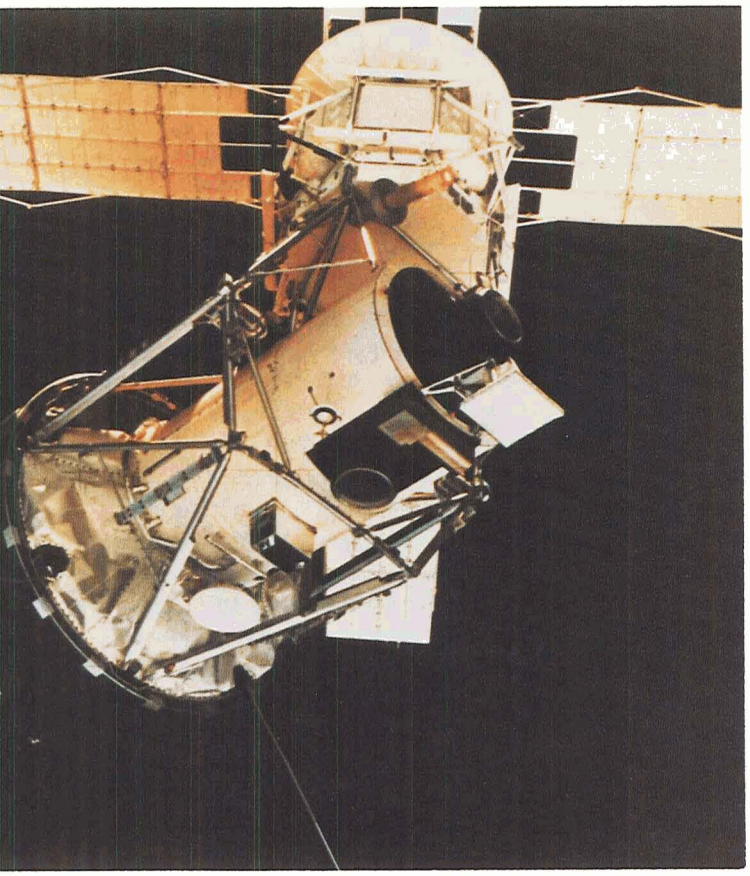

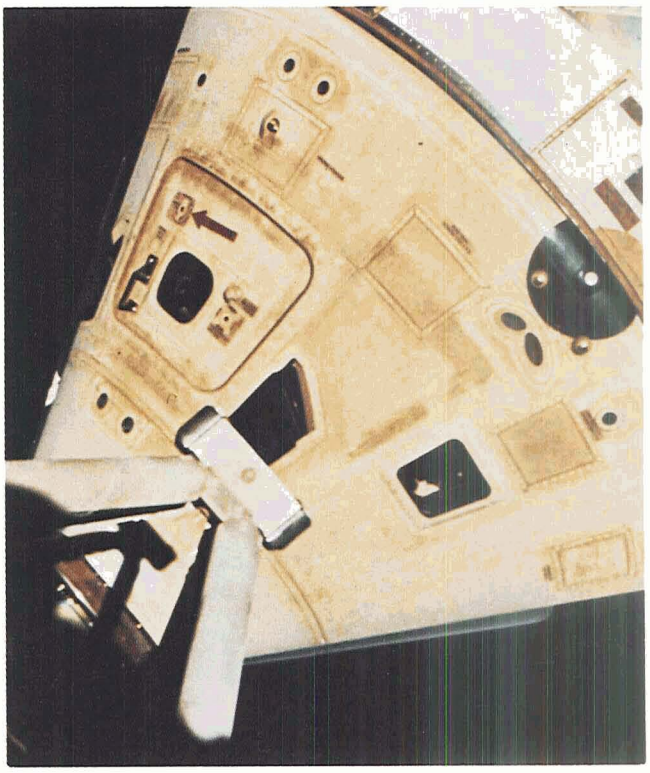

Figure 7-7.—Discolored hatch.

condensed on surfaces near the hatch, causing the discoloration.

Discoloration was particularly heavy along seams (fig. 7-8) in the airlock's meteoroid curtains, as though material had leaked from inside them. During the mission, a leak developed in the vehicle's coolant system. The molecules had an affinity for surfaces covered with silicone-based paints. In the presence of solar radiation, and water vapor in the external Skylab environment, a nonvolatile material resembling silica gel formed on the surfaces. The ultraviolet radiation from the Sun caused a color change from clear to golden brown in this material.

Some darkened spots appeared on painted surfaces of the sunshield, the sides of the solar observatory, and the command module. These spots were probably localized contaminants introduced during touch-up work or other ground handling and became visible as they underwent chemical change in the space environment. Most organic or silicone materials will polymerize in the presence of ultraviolet or energetic-particle radiation, and such polymerization affects the optical properties, generally resulting in a brownish appearance. Surfaces that are partially shadowed from sunlight show distinct differ-

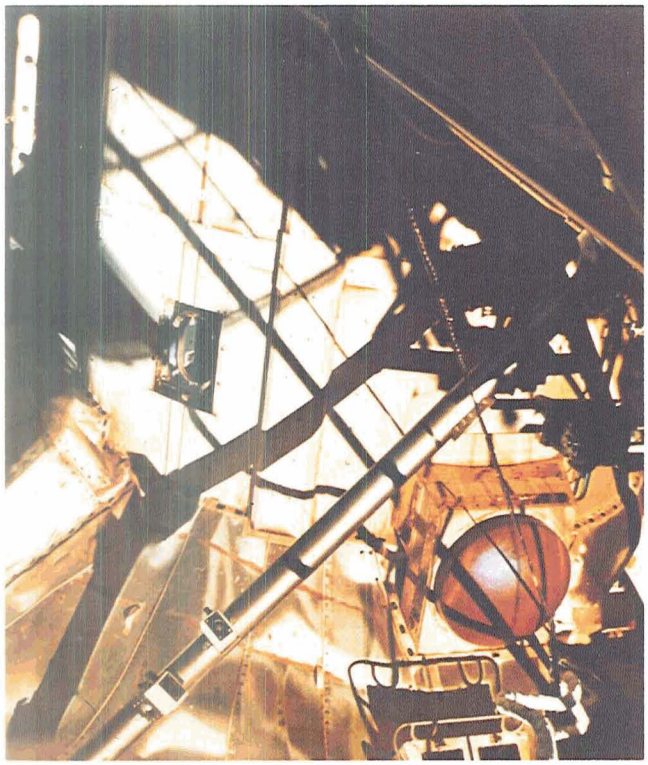

Figure 7-8.—Contaminated micrometeoroid curtains in the airlock.

ences in coloration between the exposed and the shadowed areas. Either the contaminants on the surface in the shadow remain unchanged or they migrate along the surface until they are exposed, whereupon they become immobilized.

Despite the visible contamination on the sunshield paint, neither the quartz-crystal microbalance on the surface of the solar observatory nor the optics of its instruments detected the presence of any contaminant. The solar observatory's optics were covered when not in use (fig. 7-9) and had an acceptance angle for contamination 100 times less than that of the quartz-crystal microbalances. Apparently, the contaminants that deposited did not readily adhere to warm bare-metal surfaces but had a much greater affinity for cold painted surfaces, whose molecular structure resembled that of the contaminants.

Effects of the Space Environment on Materials

The fact that Skylab was of long duration and its crew could return samples made it easy to experiment with materials and to study the effect of the external environment on these materials.

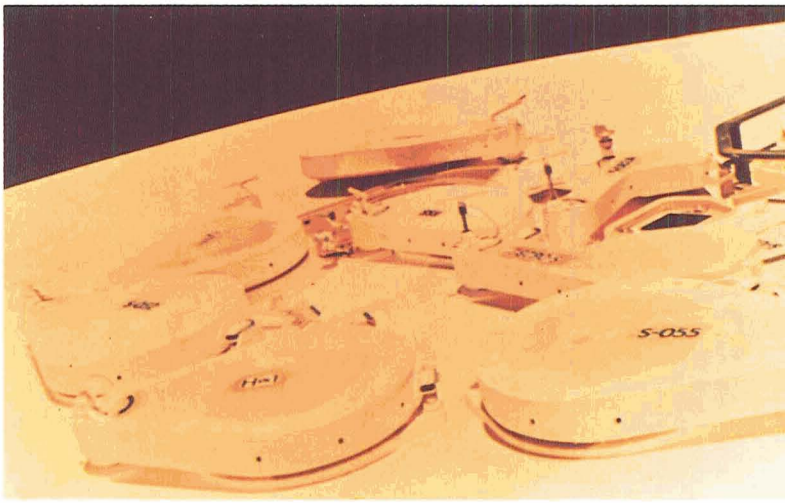

Figure 7-9.—Covers on the solar observatory's optics.

A thermal control and polymeric film experiment (D024) was conducted for William L. Lehn of the Wright-Patterson Air Force Base, Ohio (fig. 7-10). Samples of thermal control materials and of polymeric films were exposed to the environment outside the space station. The thermal control materials are used on space equipment to control its temperature by controlled absorption and re-radiation. The polymeric films studied were of the type used for thermal insulation of spacecraft. On each of the three manned Skylab missions, samples of thermal-control materials and polymeric films were deployed externally and returned by the crew for laboratory evaluation.

The experiment (fig. 7-11) used four sample panels: two duplicate sample trays each containing 36 individual sample buttons coated with 27 different thermal control coating materials, and two duplicate sample trays each holding eight different polymeric film specimens. The four specimen trays and two hermetically sealable return containers were mounted on the exterior (fig. 7-12) of Skylab and were retrieved during a scheduled spacewalk by the crew.

Figure 7-13 shows four sets of thermal control coatings: an unexposed set not flown in Skylab (left) and one set returned from each of the three manned Skylab missions. The specimens returned with the first crew (second from left) were exposed for approximately 550 hr (35 days) of solar radiation. The specimens returned with the second crew (third from left) were retrieved after approximately 2040 hr (131 days) and returned to Earth for analysis. Severe contamination on the first two manned missions tended to obscure the desired

Figure 7-10.—Thermal control experiment on Skylab truss.

measurements. The experiment was therefore repeated on the last flight. These specimens (extreme right) show the effects of approximately 1150 hr (74 days) of solar exposure, but no exposure to fly-around by the command and service module.

Since this experiment was located near the EVA hatch, the sources of the contaminants are most likely those discussed previously: outgassing from the materials in the airlock and vapor from leaks in the cooling system. A postmission analysis of the contamination indicated the presence of organic silicon compounds and traces of phosphorus and other elements. The vast variety of silicone materials used on the spacecraft, together with the fact that the space environment causes chemical changes in the contaminant deposits, makes it impossible to identify the specific source. A significant finding in the analysis was the total lack of nitrogen. This rules out the hypergolic thrusters as sources because they operated on monomethylhydrazine nitrate.

Clearly defined "shadow" patterns (fig. 7-14B) on the returned polymeric film trays gave a clear indication of the contamination and the degree of solar orientation that was maintained by Skylab. These "shadow" patterns were also observed on the containers and the

Figure 7-11.—Device used in the thermal control coating experiment.

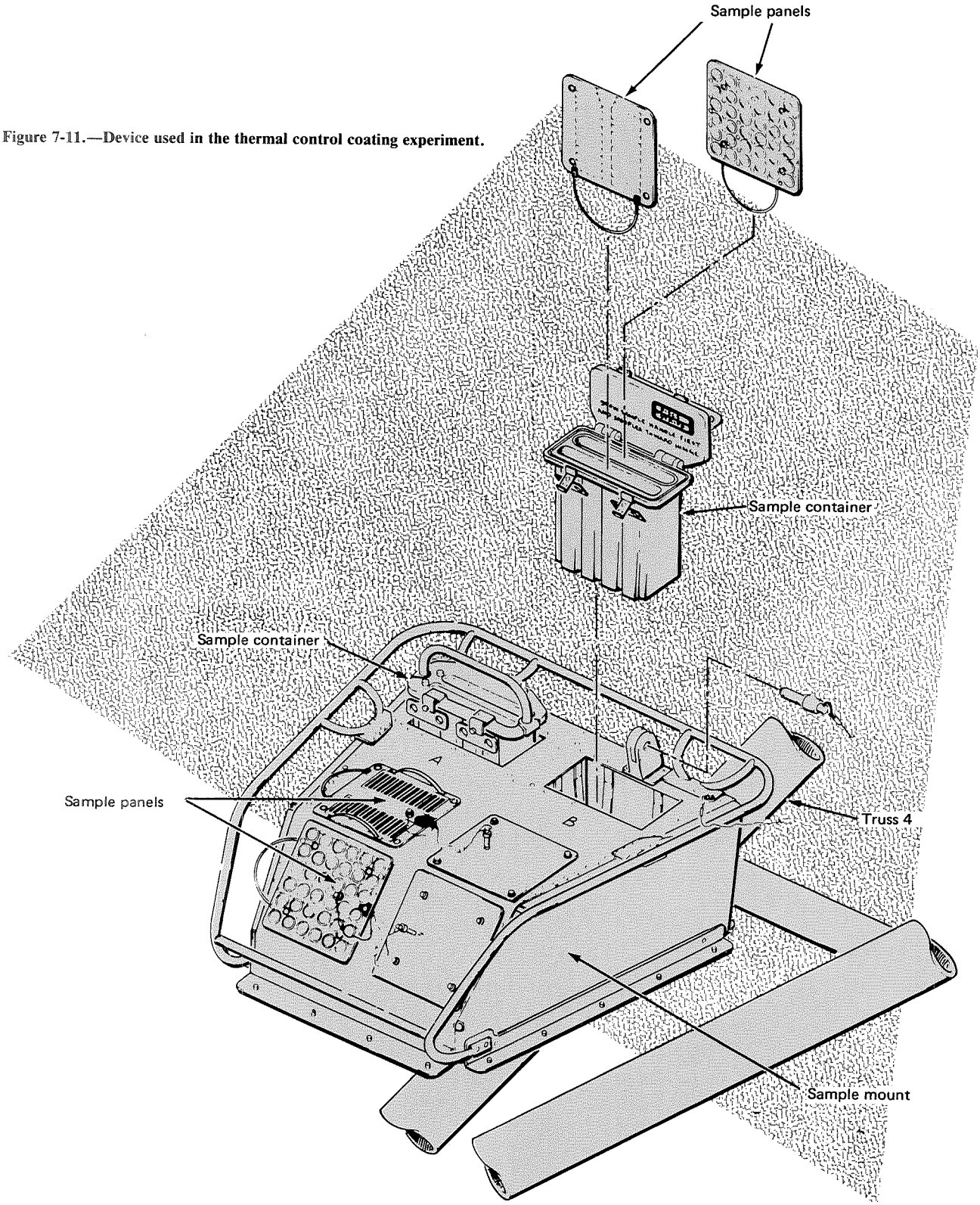

Figure 7-12.—Thermal control coatings mounted on the exterior of Skylab.

Figure 7-13.—Thermal control coating specimens: unexposed set not flown on Skylab (left) and sets returned from each of the manned missions.

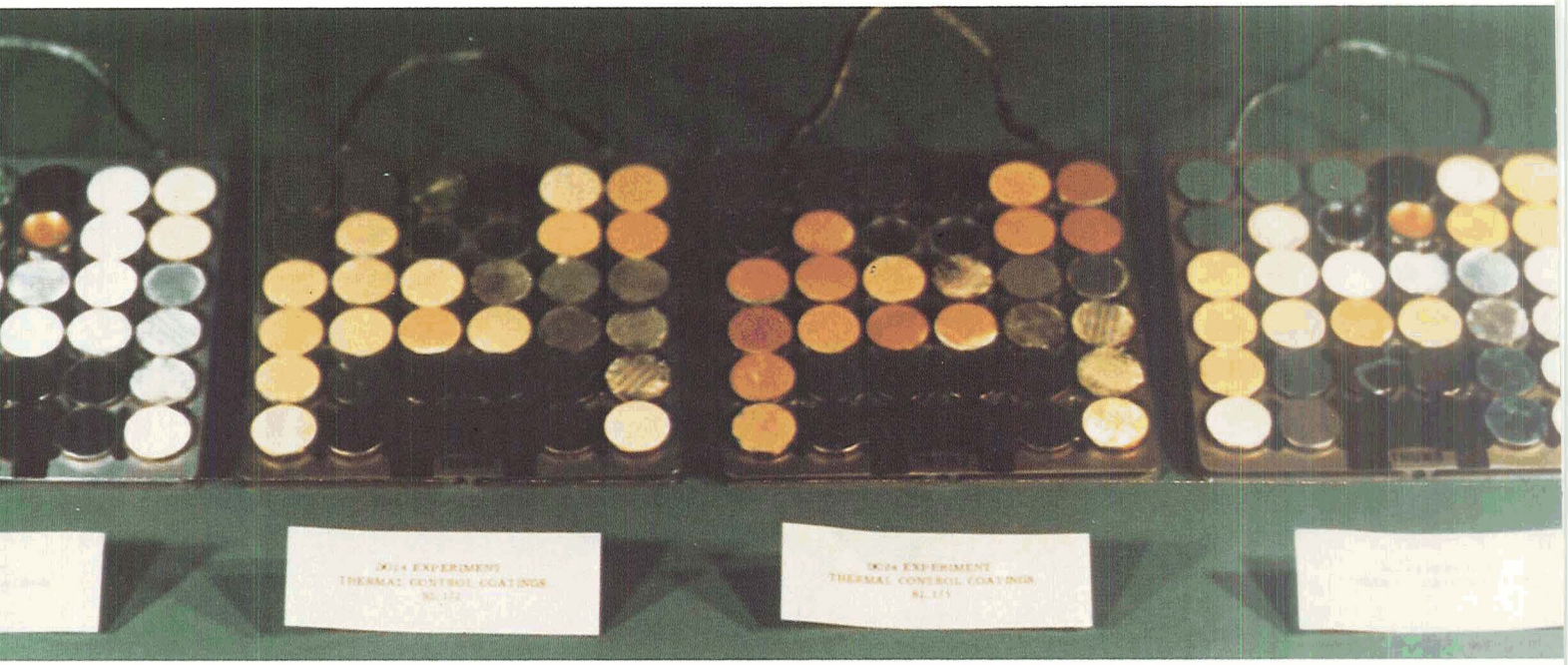

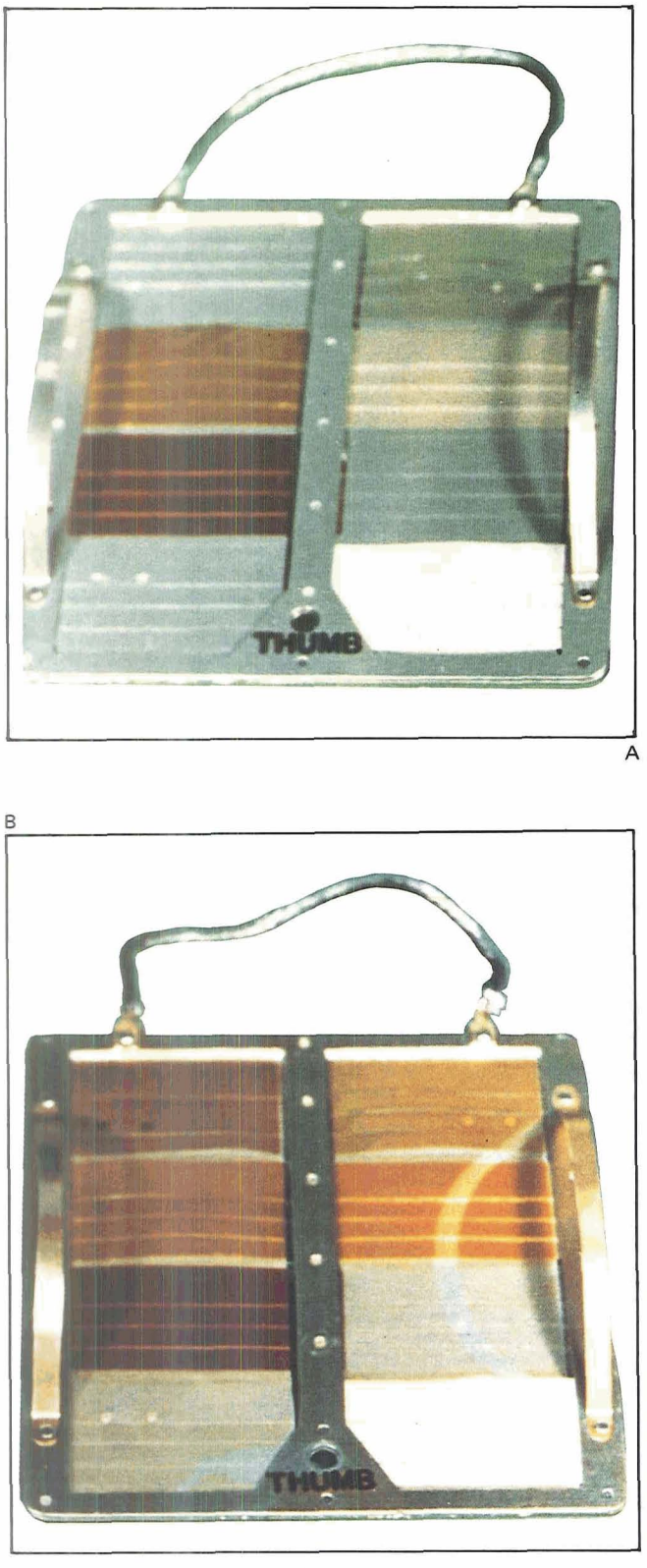

Figure 7-14.—Polymeric films before (A) and after (B) mission.

thermal control coatings returned to Earth. The apparent absence of contamination in the shadowed area of the returned samples indicated that the contaminants either did not polymerize, were able to deposit and reevaporate, or could migrate along the surface until irradiated and fixed by sunlight.

Curves of reflectance versus wavelength (fig. 7-15) were based on optical measurements made before and after the flight. The samples of thermal control coatings generally showed gross changes in solar absorbancy explicable only on the basis of contamination and solar degradation.

Optical Surfaces Experiments

Many instruments expose optical surfaces to the orbital environment. An experiment was conducted in which samples of various optical surfaces on various materials were deliberately exposed to the orbital environment. Although the purpose of this experiment, designed by Joseph A. Muscari, of the Martin Marietta Aerospace Corporation, Denver, Colorado, was to study the behavior of optical surfaces in the orbital environment, it furnished valuable data on the deposition of contaminants. Figure 7-16 shows the exposed samples. Twenty-five different kinds of optical surface, such as transmissive windows, mirrors, and diffraction gratings, were used on a total of 248 optical samples. These were mounted on an extendable boom and exposed to the space environment through the antisolar airlock of the orbital workshop during the first manned Skylab mission. The optical surfaces had varied characteristics and exposure durations. The entire experiment lasted 46.5 hr. From the extremely small amount of contaminant deposition observed on the samples, it was concluded that the antisolar side of the vehicle was very clean.

Preflight and postflight laboratory measurements of optical transmission from 0.28 to 15 000 nm and reflection from 0.834 to 21 000 nm were made to determine the effects of surface contaminants. Computer programs were developed to determine the variations in deposition of contaminants due to surface material, solar radiation, period of exposure, and direction of exposure. Spectral and polarization and spectral measurements were used to determine the thickness and composition of the contaminants. Only trace amounts of surface contamination were found, near the sensitivity limit of the laboratory instrumentation. The maximum thickness was less than 1 nm. Some indication of silicone was present in the spectroscopic data, but the data obtained were inconclusive.

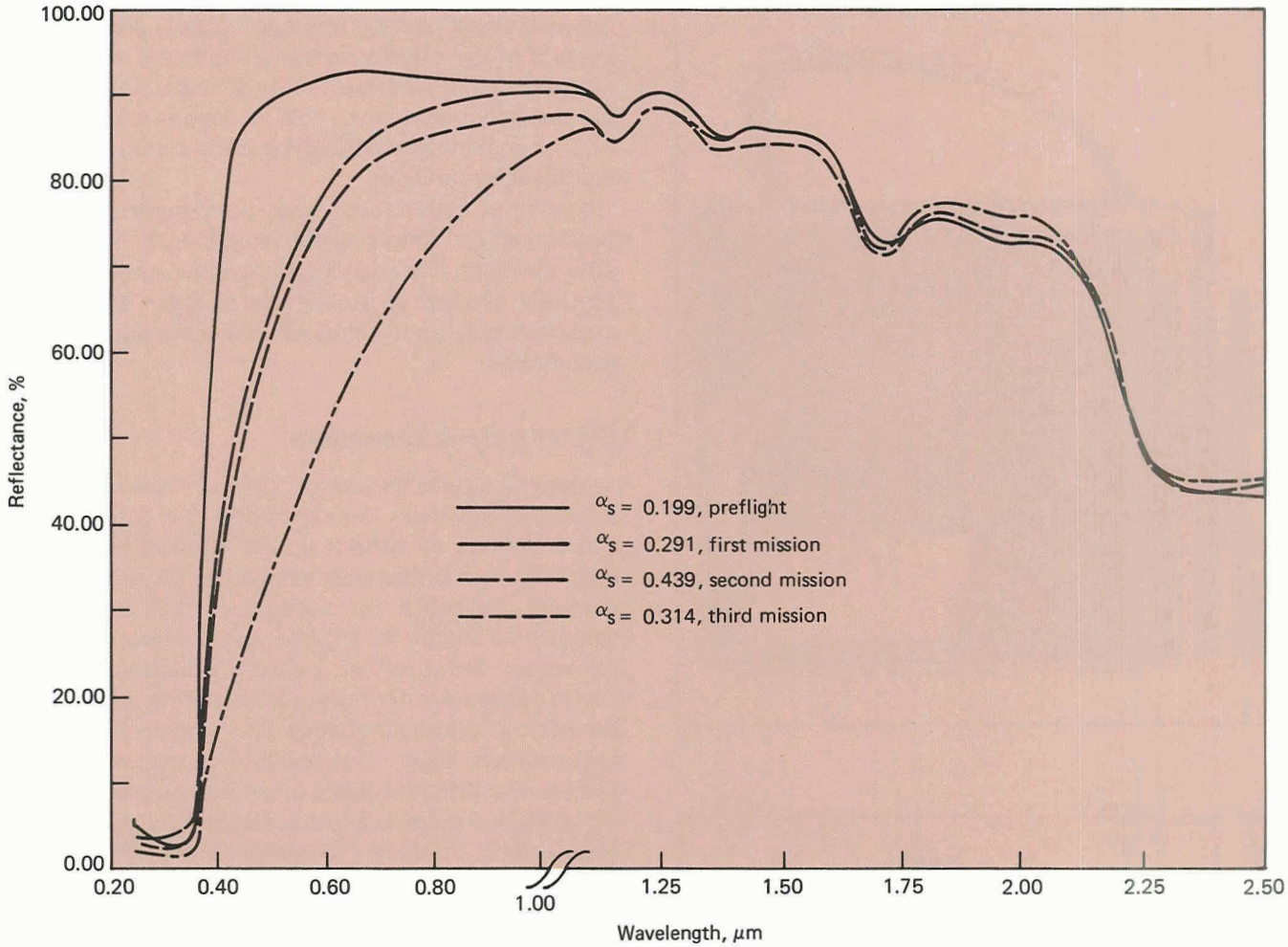

Figure 7-15.—Reflectance-versus-wavelength curves for a thermal control coating (S-13G white paint).

The results of this experiment were unfortunately compromised by the initial launch problem. The experiment had originally been planned for operation through the solar airlock of the orbital workshop within the first 4 days after the unmanned Skylab launch. The first manned launch was delayed approximately 10 days, which caused the experiment to be performed later than desired, so that no observations were obtained during the early phase of outgassing. The parasol was deployed through the solar airlock, preventing the airlock's use for experiments. The experiment was therefore deployed on the other, "cleaner," side of the space station.

Effects on Metallic Foils

The surfaces of equipment for other experiments mounted outside the spacecraft were examined for con-

Figure 7-16.—Sample holder for optical surfaces experiment.

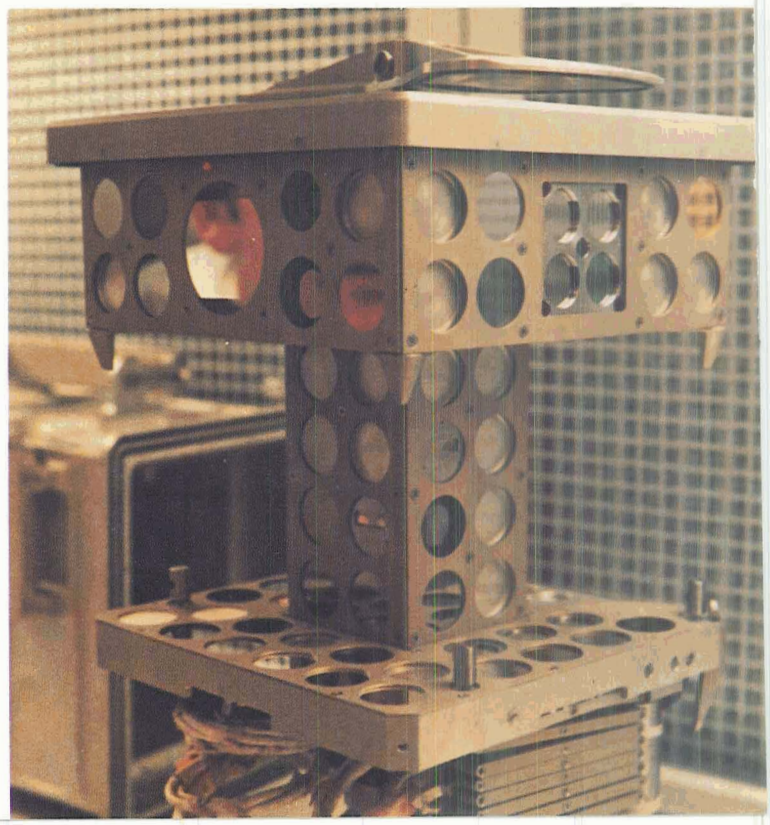

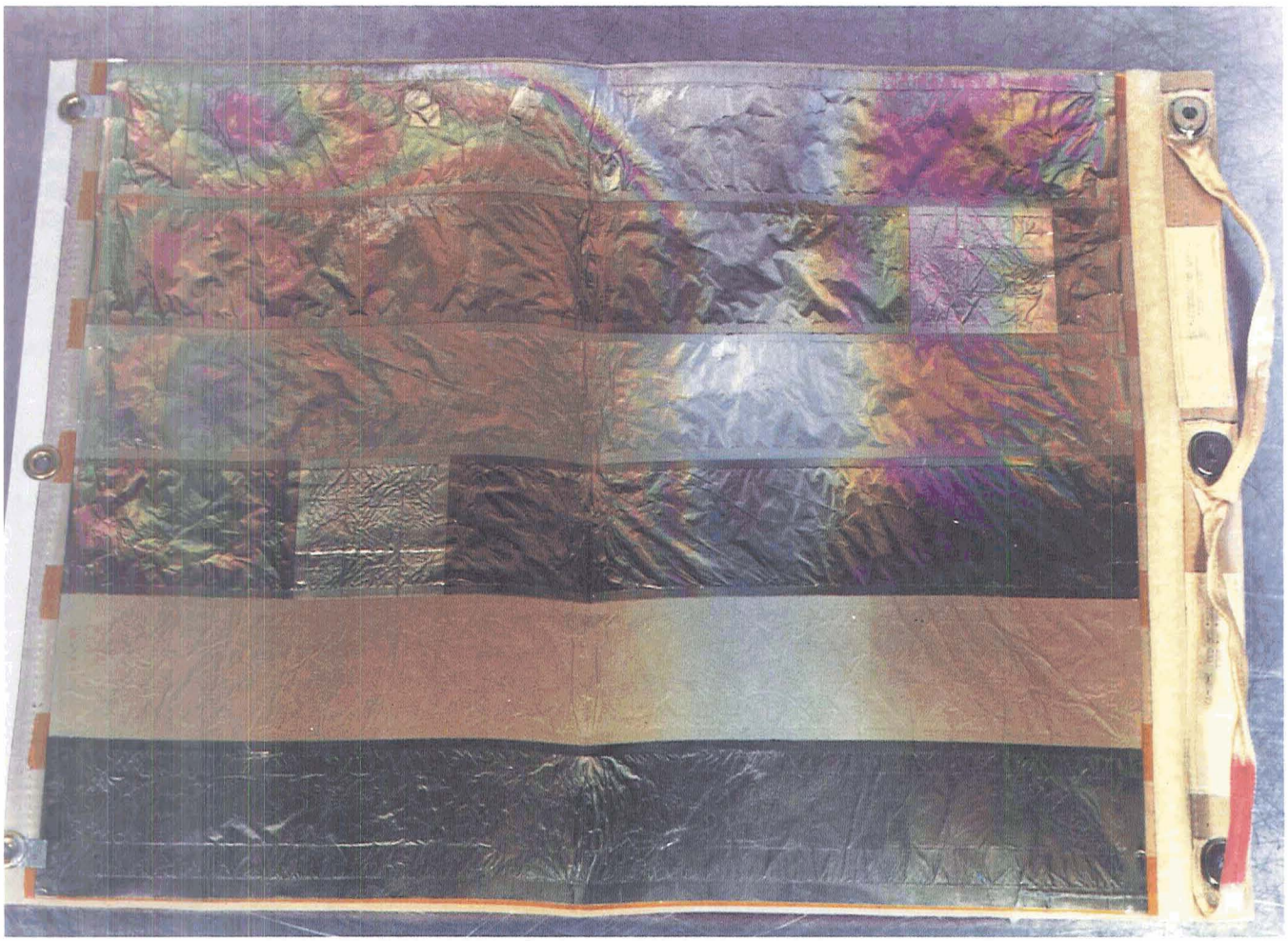

Figure 7-17.—Contaminated metallic foils.

tamination and yielded valuable supplementary data. An experiment by Don Lind to monitor magnetospheric particle composition is described in Chapter 5. The various foils were visibly contaminated with a film of various colors, indicating different contaminant thickness (fig. 7-17). As a consequence of the visible contamination, eleven of these small foil strips were measured for total reflectance at wavelengths from 0.25 to 2.5 μm and for directional reflection with hemispherical incident radiation at wavelengths from 1.2 to 20.5 μm. The reflectance (fig. 7-18) was significantly lower than that of control foils that had remained on the ground.

The reflectance measurements were used to calculate the absorption of solar radiation by the foils. This value was used to determine the effectiveness of surfaces as thermal shields or radiators. Increases in absorption of up to 5 percent per day were measured, which would greatly decrease thermal shield effectiveness in a short time.

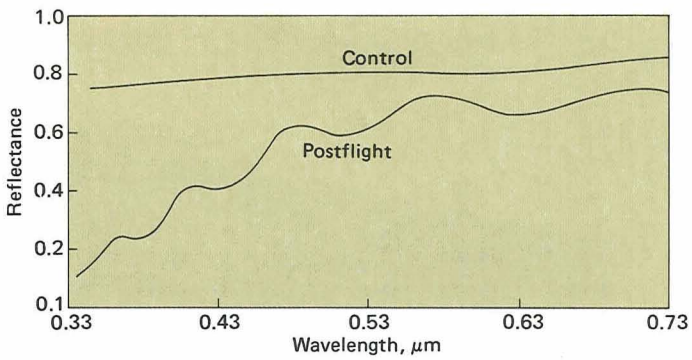

Figure 7-18.—Reflectance-versus-wavelength curves for control and contaminated foils.

Lind prepared cross sections of contaminated foils in order to measure contaminant thickness with an electron microscope. Measurements of suitable cross sections on one specimen showed thicknesses of 30 to 150 nm and on another thicknesses from 70 to 800 nm. The latter specimen was exposed to the space environment for 200 days, a period significantly longer than the exposure of the former.

Other Experimental Contamination Measurements

Richard Tousey of the Naval Research Laboratory, Washington, D.C., was the principal investigator for a camera (S020) with grazing-incidence mirrors and used to photograph the Sun in the extreme ultraviolet and soft X-ray regions. The camera was mounted externally during a spacewalk on the third mission. It showed a decrease in transmission in its indium and beryllium thin-film filters and lost some of its data at far-ultraviolet and X-ray wavelengths. The data loss was probably caused by contamination deposited on the filters. Laboratory tests, which attempted to identify the contaminant composition, were unable to determine the species, although its characteristics were similar to those of silicone-type materials.

Skylab's Optical Environment

Another experiment (T027) designed by Joseph A. Muscari used a photometer system to determine the spatial distribution and temporal variation of the cloud of particles around Skylab (fig. 7-19). This instrument, the same photometer that was used to measure zodiacal light and Gegenschein, also measured the brightness and polarization of sunlight scattered from the contaminant cloud around the space station.

Various areas around Skylab were scanned in daylight and in darkness to separate the natural sky background from the contaminant-scattered light. A significant amount of contaminant scattering of a transitory nature was found on one observation. This may have resulted from a single bright particle moving through the field of view.

Jerry L. Weinberg, the investigator for the zodiacal light experiment, was also concerned about the effects of contaminant material from around the space station. To determine amount of optical contamination early in the mission, measurements of sky brightness in a fixed direction (95° from the Sun) were taken on June 12, 1973, using the instrument described in Chapter 3. Observations were made of 10 wavelengths and were repeated every 2 min, starting in the Earth's shadow and ending in daylight. The plot of relative intensities shows that there were levels of sky brightness in daylight only 5 percent above those at night (fig. 7-20).

Photographs of the Gegenschein were taken with a 35-mm camera, through the airlock of the orbital workshop on the third mission. Photometric analysis of the film was made by K. S. Clifton of the Marshall Space Flight Center. Considerable amounts of scattered light were observed at the edge of the frame. The phenomenon is believed to be the result of light reflected from a Skylab discone antenna into the airlock. However, at the center of the photograph the difference in light intensity between sunlight and shadow conditions was only 5 percent above the Gegenschein brightness. The results indicate that the amount of sunlight reflected by contaminant material was small. Observations of faint

Figure 7-19.—Photometer used to determine the spatial distribution and temporal variation of the cloud of particles around Skylab.

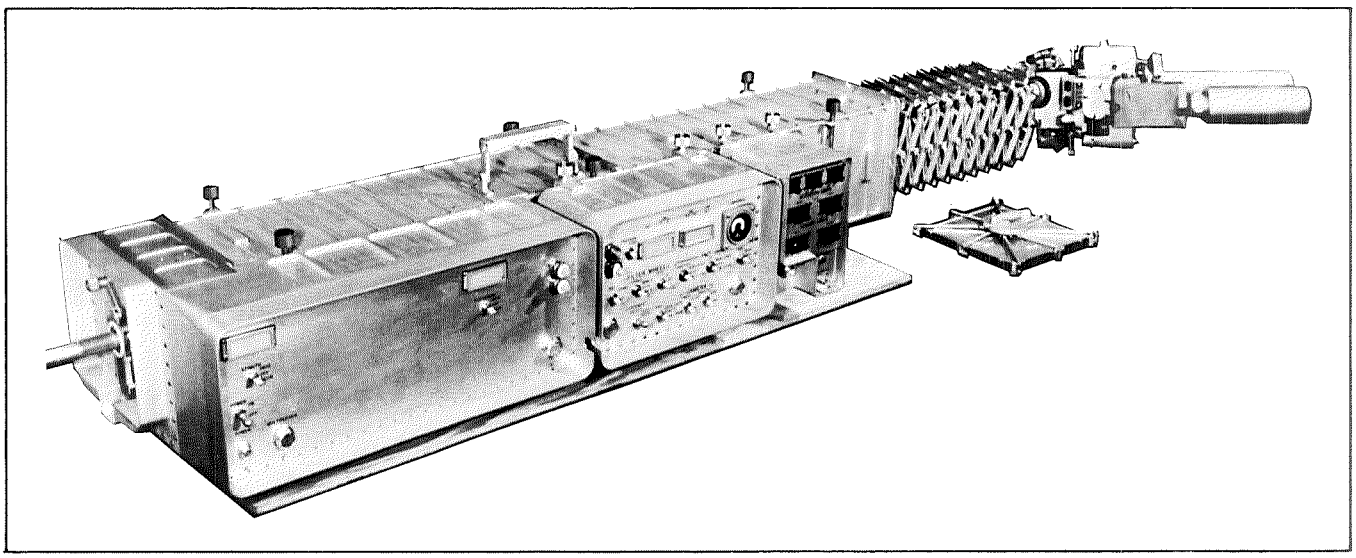

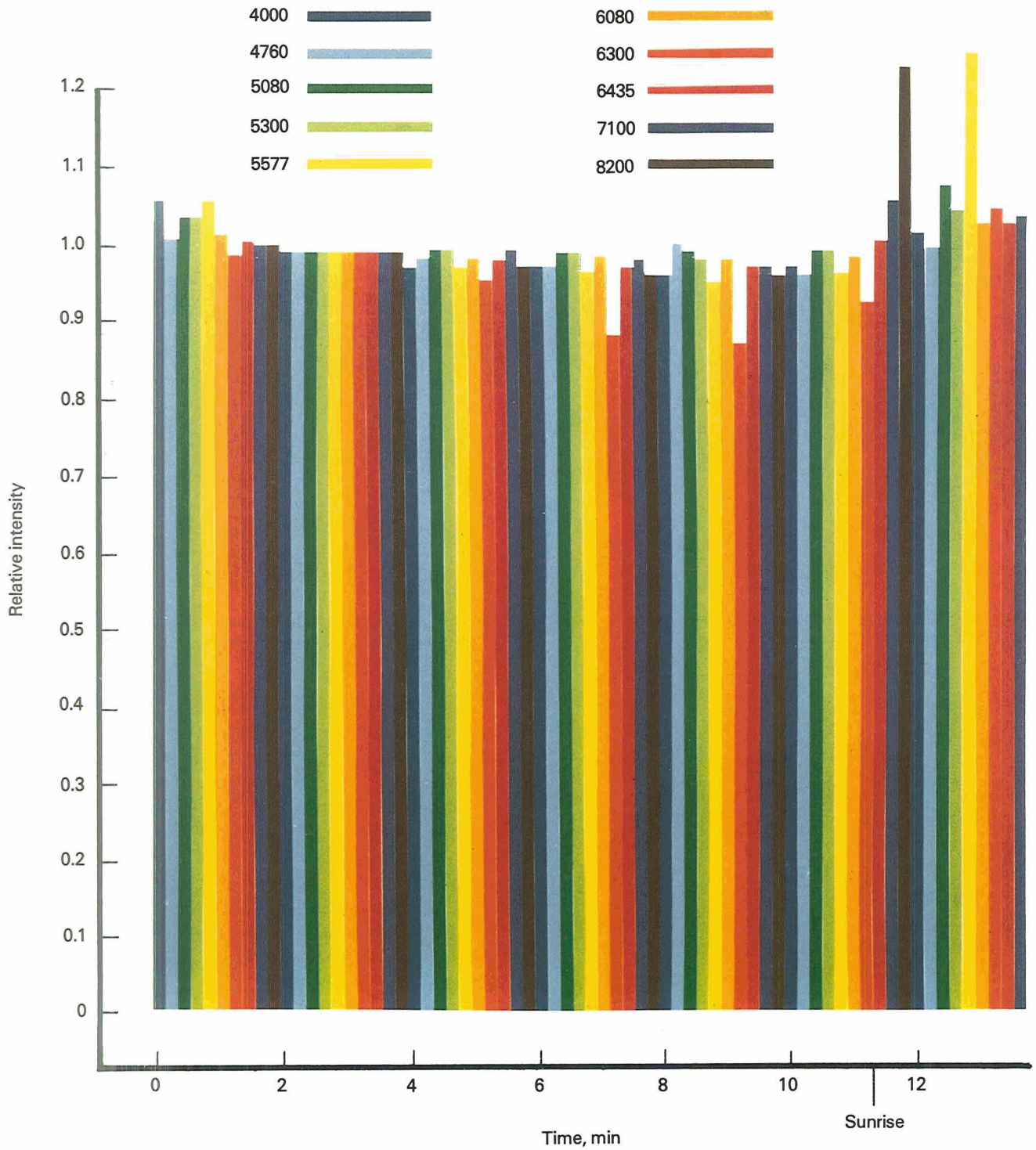

Figure 7-20.—Photometric analysis of film showing levels of sky brightness in darkness and in daylight.

astronomical phenomena could therefore be made from Skylab in daylight.

Figures 7-21, 7-22, and 7-23 are photographs taken through the white-light coronagraph (S052) of Skylab's solar observatory. They show dramatic effects caused by inadvertent venting from Skylab. The photograph in figure 7-21, taken at 1027 GMT on January 21, 1974, shows a typical image of the solar corona, except that the coronal transient in the lower right side of the field is unusual. The picture is free of particulate contamination.

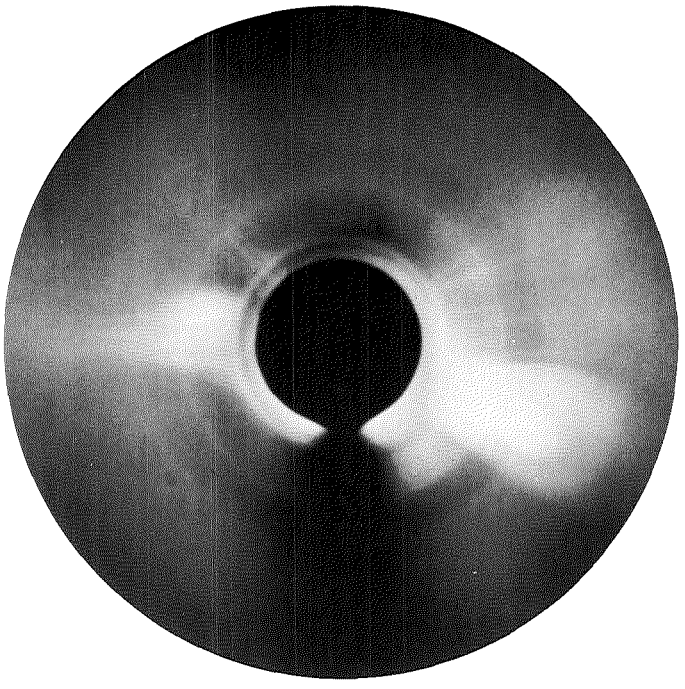

Figure 7-21.—Typical image produced by the white-light coronagraph (9-sec exposure, 1027 GMT, January 21, 1974).

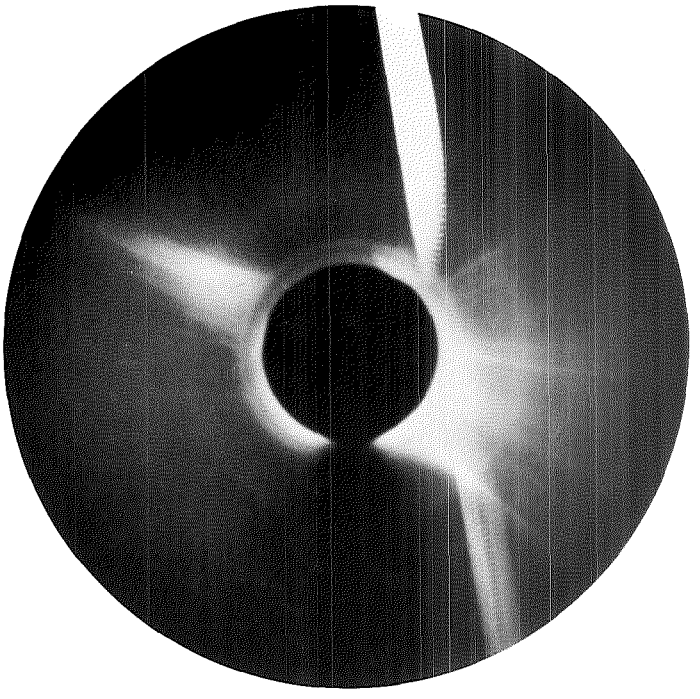

Figure 7-22.—Track of Sun-illuminated spinning particle on coronagraph image (9-sec exposure, 0440 GMT, June 9, 1973).

Figure 7-23.—Random motion of ice particles photographed in the coronagraph's field of view (9-sec exposure, 1408 GMT, August 2, 1973).

The next photograph, figure 7-22, taken at 0440 GMT on June 9, 1973, shows the track of a particle illuminated by sunlight as it passed across the field of the coronagraph. The particle apparently was spinning, and the brighter portions described perfect spirals on the photograph. Such uniform motion was possible because the vacuum outside Skylab offered no appreciable atmospheric drag. Instrumental vignetting caused the track's brightness to be reduced near the center of the picture. The solar coronal background is typical, with a single feature in the northeast and several streamers along the western limb.

The photograph in figure 7-23 was taken at 1408 GMT on August 2, 1973. A few minutes before this exposure, inadvertent venting of the water-condensate system occurred, producing a cloud of particles around Skylab. The photograph shows random motion of many condensed ice particles that passed through the coronagraph's 3.2° field of view. It demonstrates why contamination is of such concern to sensitive instruments. Venting was usually scheduled during space-station night, when the solar experiments were not operating and instrument covers were closed to protect the lenses. This scheduling allowed the contaminant cloud to disperse before observations were resumed. Fortunately, the lens did not suffer contamination from the inadvertent ventings.

S-149 silver samples

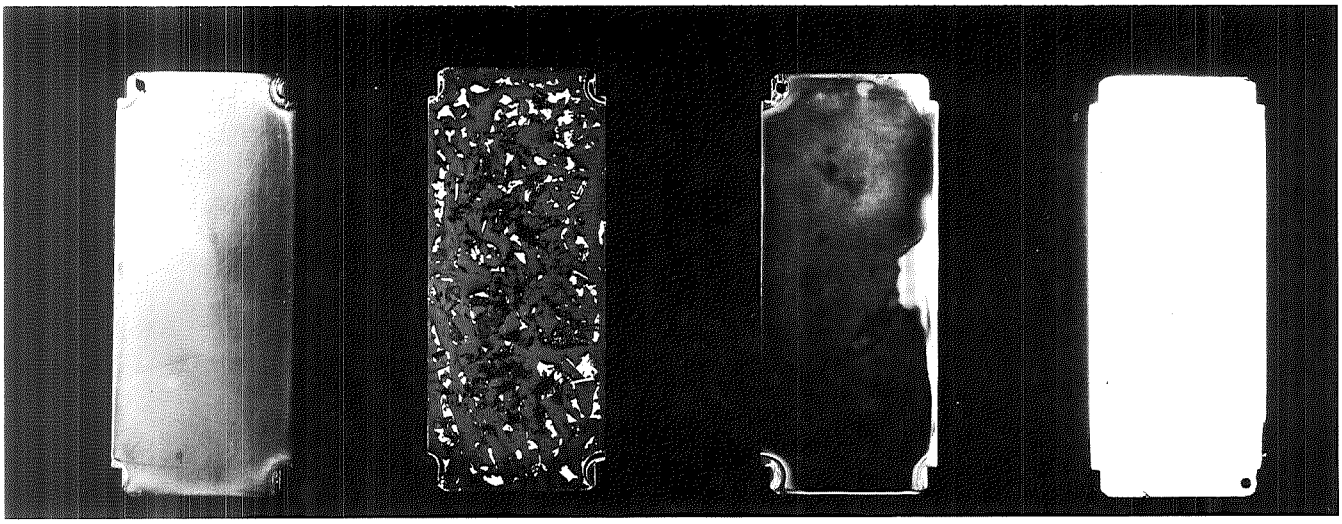

Exposure 1 antisolar | Exposure 2 solar | Exposure 3 solar | Control

Figure 7-24.—Oxidation of silver slides exposed in the antisolar direction (exposure 1) and the solar direction (exposures 2 and 3).

Oxidation

An experiment that recorded micrometeoroid impacts is described in Chapter 3. Among other specimens, this experiment, designed by C. L. Hemenway, exposed silver samples in the space environment. Figure 7-24 shows three exposed silver slides and an unexposed silver slide used as a control. A thick black corrosion layer developed on the silver slides during exposure in the solar direction; a thinner layer, resembling tarnish, developed during exposure in the antisolar direction. Analysis by X-ray diffraction showed the black material to be silver oxide. The silver oxide layer on the solar facing sample was approximately 2 μm thick. The corrosion was so thick that it was impossible to measure micrometeoroid impact craters in the silver samples. Copper slides showed a smaller, but noticeable, amount of oxidation. The oxidation is thought to be the result of a chemical reaction with atomic oxygen in the extremely thin atmosphere at Skylab's orbital altitude. The thermal control coatings experiment, discussed earlier, exposed a thin silver coating, which also tarnished. The oxidation of bare silver and copper in the orbital environment was unexpected, but it provided valuable information on the behavior of materials.

Other Deposits on Optical Surfaces

Contamination also occurred on window surfaces and the mirror that was used for photography through the antisolar airlock of the orbital workshop.

Windows are important for both photography and visual observations. Windows for photography must be of extremely high quality; lower quality windows are adequate for visual observation. A single-pane window on Skylab was designed solely for photographing the Earth. It had a heater that maintained the surface temperature above the cabin dewpoint temperature, and no condensation formed on it. The window was kept covered when not needed for experiments. It remained clean throughout the entire mission. In contrast, the double-paned wardroom window of the orbital workshop was designed primarily for astronaut viewing. It had a heater, which was not on all the time. When the heater was off, a crazed ice condensed on the inner surface of the outer pane (fig. 7-25). It had no external cover, and critical inspection by the astronauts revealed a streaky and oil-like film on its outer surface.

A window in the command module of the last Skylab mission (fig. 7-26) turned brown and was found to have acquired a coating. After return to Earth, material was

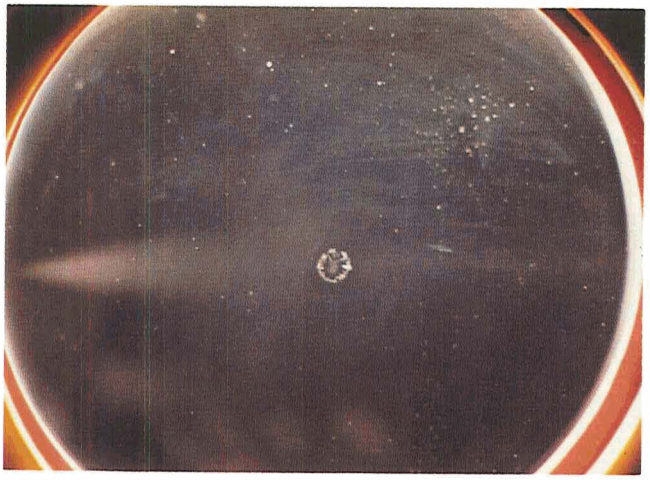

Figure 7-25.—Ice condensed on the inner surface of the outer pane in the double-paned wardroom window of the orbital workshop.

scraped off for analysis. The coating, approximately 1.7 μm thick, proved to be a methyl silicone. Infrared spectroscopy revealed chemical differences from the methyl silicones used on the vehicle, such as the presence of hydroxyl and carbonyl groups, which probably resulted from photochemical processes during the 80-day exposure. The effect was noticed by the third Skylab crew after 38 days in orbit but was not observed on the earlier manned missions.

Inside Atmosphere of Skylab (T003)

The inside atmosphere of Skylab was monitored for aerosol particles with an instrument (fig. 7-27) supplied by W. Z. Leavitt of the U.S. Department of Transportation, Cambridge, Massachusetts. A thorough survey was conducted on each mission. Readings were obtained

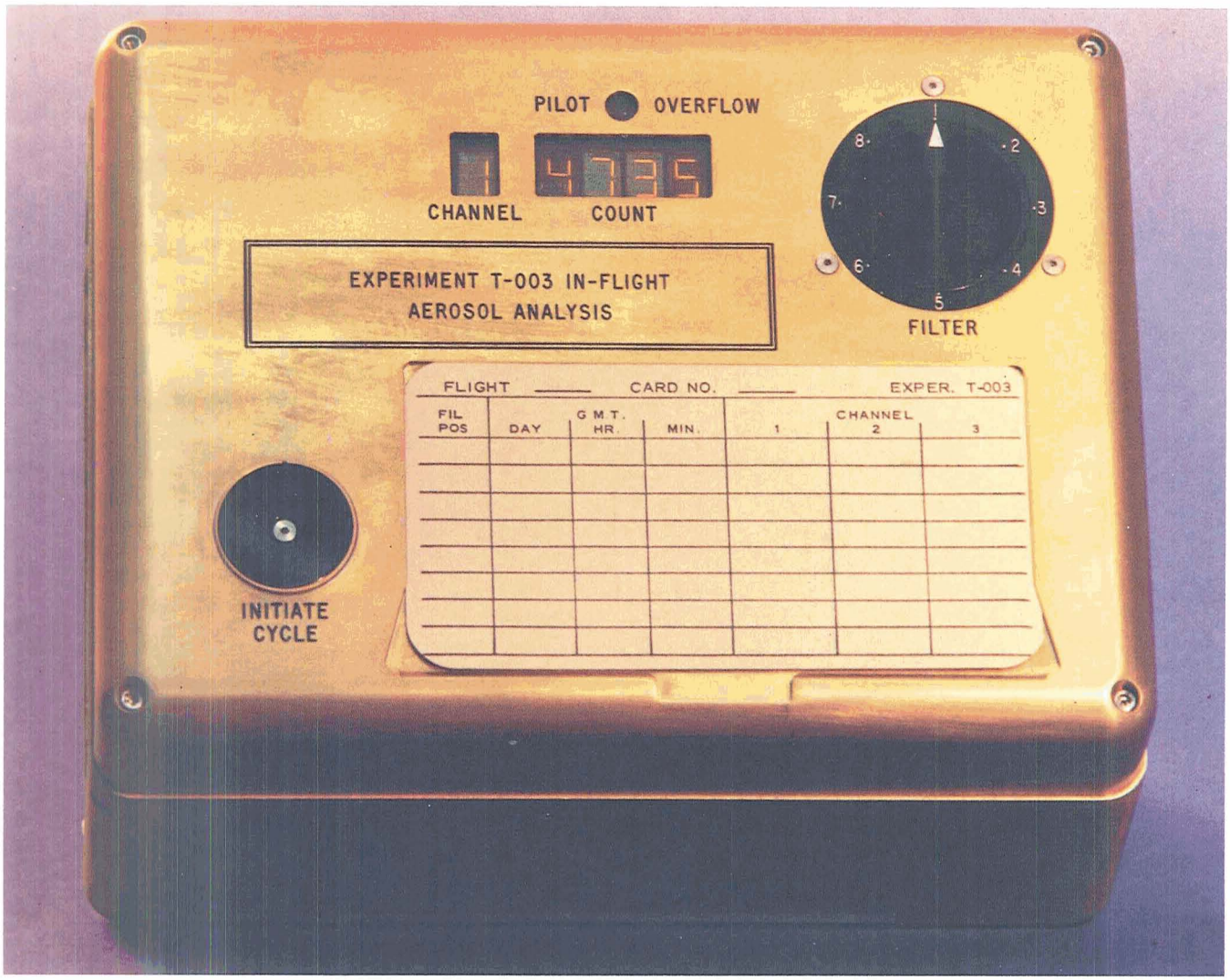

Figure 7-27.—Instrument for in-flight aerosol analysis (T003).

at many locations to assess sources of airborne particles and to evaluate the capability of the space station's environmental control system to maintain a clean atmosphere. Particle sizes from 1 to 100 μm and counts from 0 to 20 000 particles per liter were measurable. Filters were returned to Earth for analysis.

In general, the number of larger particles remained constant throughout, but the number of smaller particles decreased with time. For the three manned missions, the particle loading in the air averaged 187 particles per liter, which indicates that the environmental control system operated efficiently. Such an atmosphere was judged to be extremely clean and comparable to that of a hospital operating room. Particles such as skin flakes, food, and fragmented and abraded materials from the space station were collected by two aerosol analyzers.

Figure 7-28 shows the filter of the ventilation mixing chamber being vacuum cleaned. Objects that were misplaced or "dropped" drifted to these inlets along with debris. The astronauts vacuumed the inlet screens as part of their regular housekeeping tasks every other day.

Figure 7-29 shows an inlet filter from the environmental control system's ventilation fan, before vacuum cleaning. Fans operated continuously and circulated the

Figure 7-26.—Methyl silicone residue on window in the command module of the third manned Skylab mission.

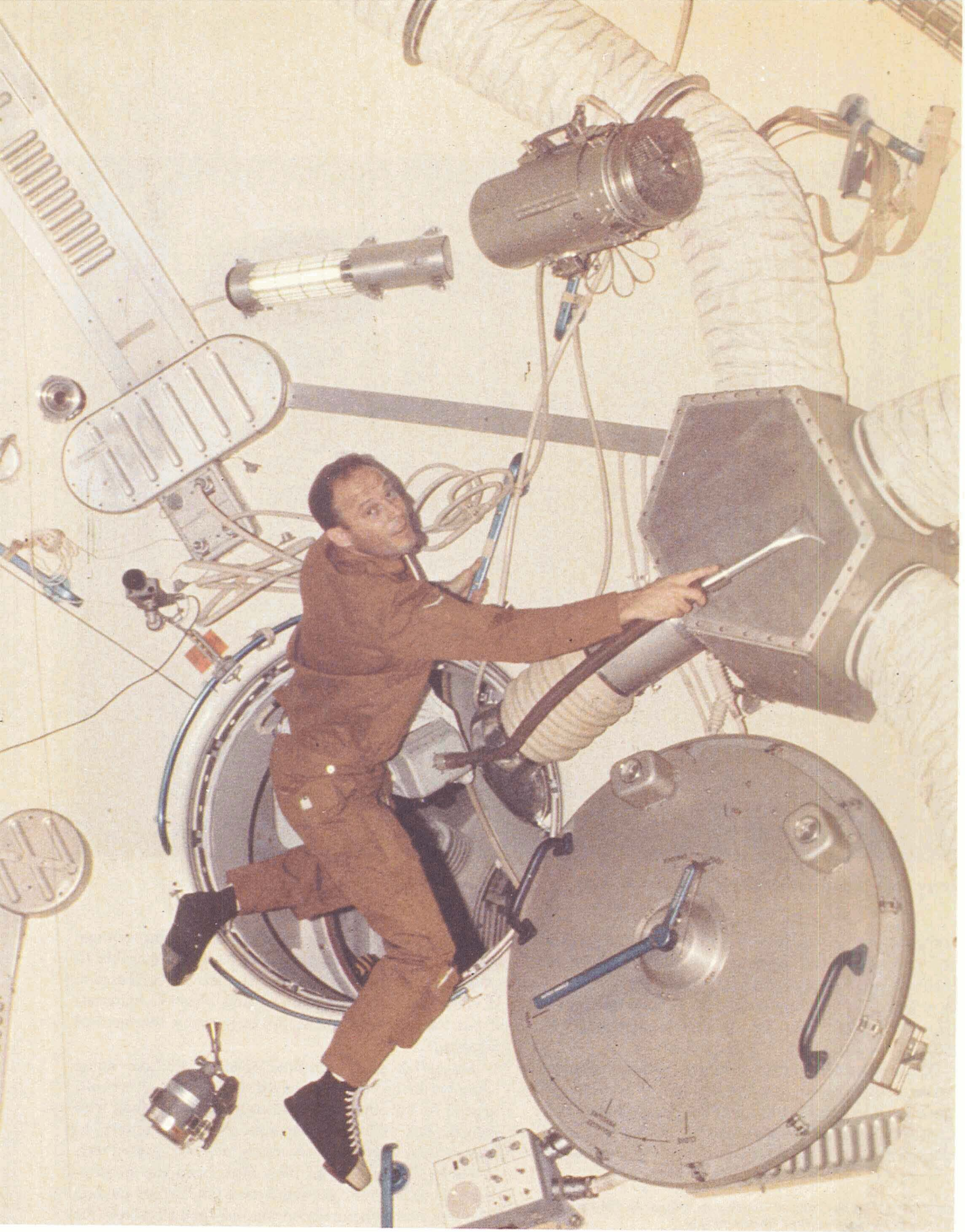

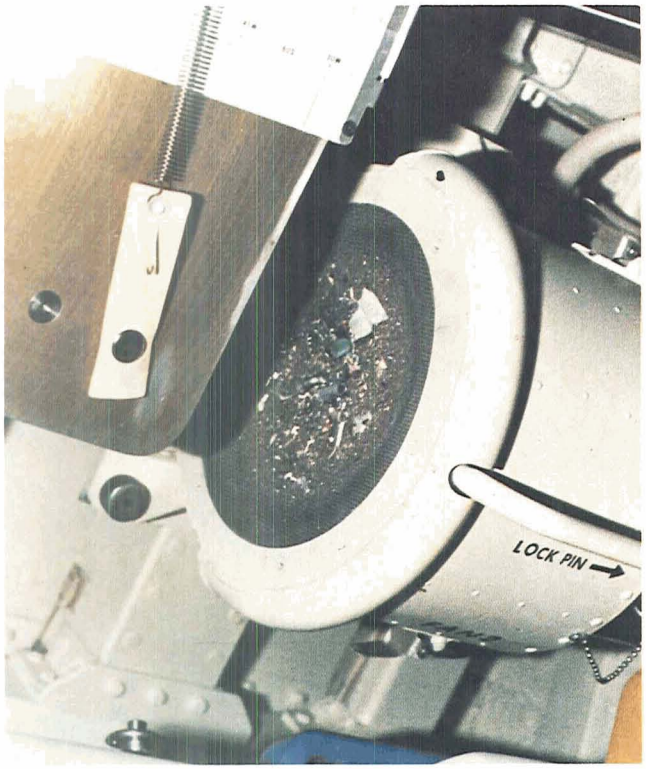

Figure 7-29.—Contamination of inlet filter on the environmental control system's ventilation fan.

cabin air to provide a habitable environment for the astronauts.

Radiation

Since the discovery of the Van Allen belt, much has been learned about orbital radiation environments from a number of Earth satellites. The long-duration Skylab provided a unique opportunity to study radiation and its effects on man and photographic films.

Before Skylab was launched, an elaborate mathematical model was constructed to describe the radiation environment inside the spacecraft. This model was needed to design the space station for astronaut safety and to determine the required film-vault wall thickness for protection against film fogging (fig. 7-30). Radiation doses from trapped protons, trapped electrons, and galactic cosmic rays were calculated. These curves show the total radiation dose rates and their contributors as a function of shielding. They are based on an idealized mathematical model of the radiation devised before the Skylab mission.

Figure 7-28.—Astronaut Jack R. Lousma vacuum cleaning the filter of the ventilation mixing chamber.

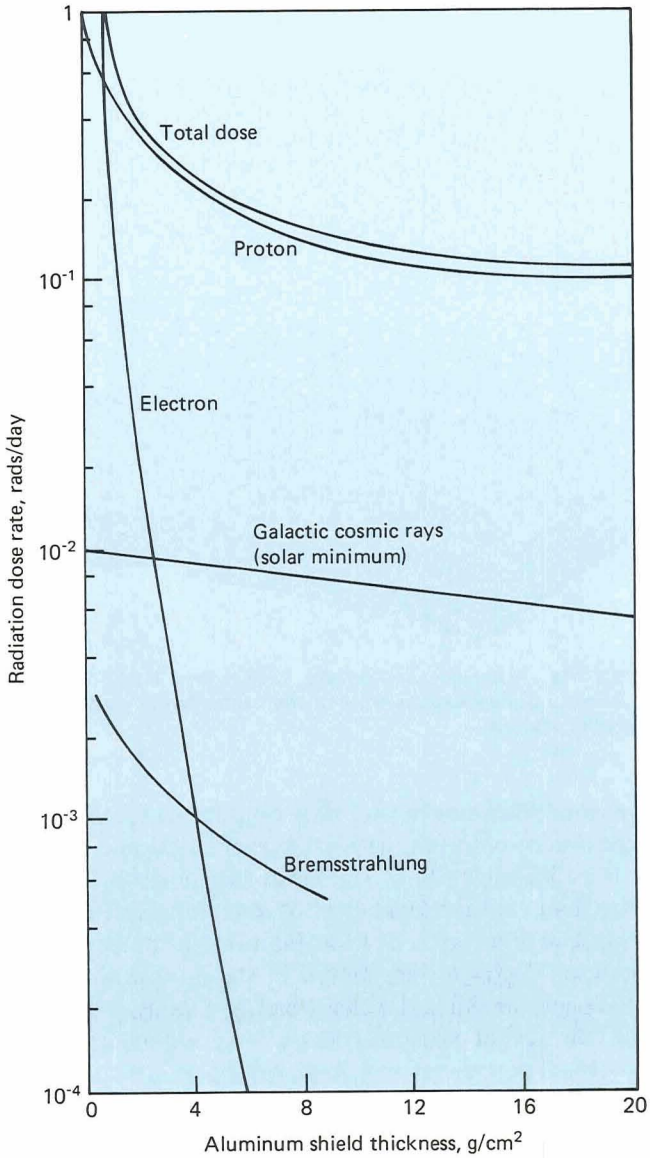

Figure 7-30.—Required shield thickness for film vault as a function of radiation dose rate: mathematical model calculations for a 50° circular orbit, 435-km altitude.

The measured flux of protons with energies higher than 50 MeV was approximately 80 percent of the predicted values, and its spectrum was more energetic than predicted; that is, there were more high-energy protons than expected.

Studies predicted the amount of fogging on all types of film, both in the film vault and in operational locations. Operational procedures, such as returning film to

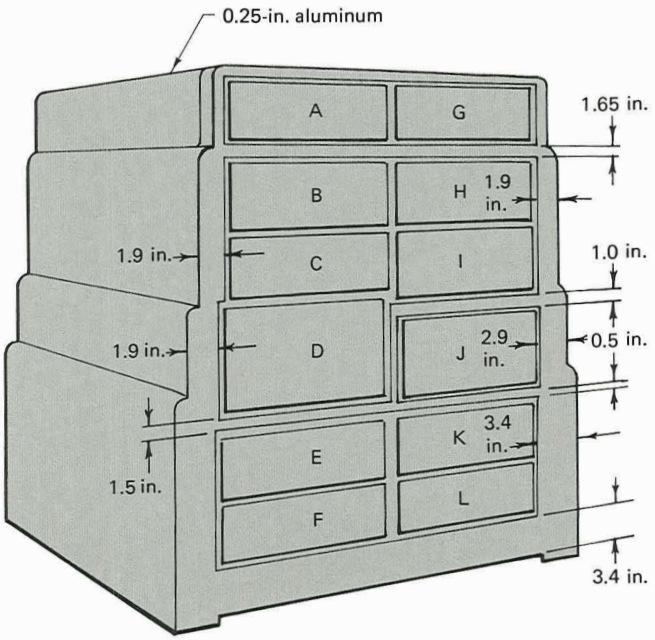

Figure 7-31.—Aluminum-shielded film vault in the orbital workshop, designed to protect various types of film with varying sensitivity to radiation damage.

the vault when not in use, were established to minimize exposure to radiation within the space station.

The film vault (fig. 7-31), located in the orbital workshop, had various thicknesses of aluminum shielding to protect various types of film. Films most susceptible to radiation damage were stored in the bottom drawers, which had the thickest walls. Postflight analysis showed that the actual radiation levels were within approximately 20 percent of the predicted levels, a value considered extremely accurate for a vehicle with such a complex geometry and radiation environment as Skylab.

Van Allen Belt Dosimeters

Van Allen belt dosimeters (fig. 7-32) were used to monitor radiation levels inside the orbital workshop. The device consisted of two ion chambers. The first was covered with an aluminum shield to simulate a layer of skin and tissue 2 in. thick; the second, unshielded, chamber provided information on the amount of radiation impinging on skin. In addition to this dosimeter, the astronauts had personal radiation dosimeters, which they carried whenever they were wearing spacesuits. A radiation survey meter was also on board for measurements throughout the space station, and passive radiation dosimeters were placed in specific locations, such as

Figure 7-32.—Van Allen belt dosimeter.

the film vault. These passive devices were returned to Earth to aid in updating the localized radiation-level models to be used in the future design of large space stations. The Van Allen belt dosimeter and the radiation survey meter read approximately three-fourths of the conservatively predicted radiation dose rates, and the readings were in extremely good agreement with each other.

Effects on Film

The many experiments of Skylab recorded data on several miles of photographic film, covering spectral ranges from the X-ray to the infrared. Film degradation occurred from two distinct causes, high temperatures and radiation.

The high temperatures occurred early in the Skylab mission, before the installation of the parasol. The effect

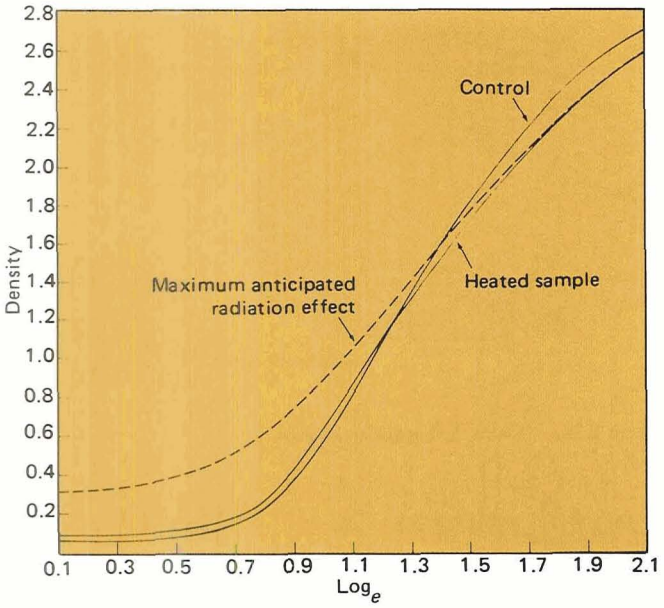

Figure 7-33.—Plot of density versus log exposure for a typical film (S022), showing the effects of heating and maximum anticipated radiation.

of increased temperature (although dependent on film type) is to cause a loss of contrast. Radiation effects were anticipated, and vaults were designed to minimize film fogging. For most films, the ratio of actual to predicted fog ranged from 0.6 to 1.0 in spite of radiation levels sometimes being higher than anticipated.

Figure 7-33 is a plot of density versus log exposure for a typical film, showing control sample, heating effects, and radiation effects.

Radiation Dosimetry (D008)

An experiment that measured radiation in the command module on the first manned mission used active and passive radiation dosimeters. The dosimeters (fig. 7-34) were designed to give a time history of radiation exposure to the astronauts and to define radiation doses behind various wall thicknesses. In figure 7-34, the spherical object is the active dosimeter, and the red and white striped cylinder below it is the passive instrument. The investigators for this experiment were Andrew D. Grimm, Joseph F. Janni, and Glenn C. Ainsworth of the Kirtland Air Force Base, New Mexico.

Comparison of the results of this ionization chamber with those recorded by the orbital workshop's Van Allen belt dosimeter yielded predictable agreement. Any differences in the measured levels can be explained by differences in metallic shielding for each instrument; the command module provided more shielding than did the thin-walled orbital workshop.

Five passive-dosimeter units were located at different shielding locations (fig. 7-35); their readings over the first 28-day mission ranged from 0.96 to 1.67 rads. Such doses were routinely experienced on earlier manned

Figure 7-34.—Radiation dosimeter.

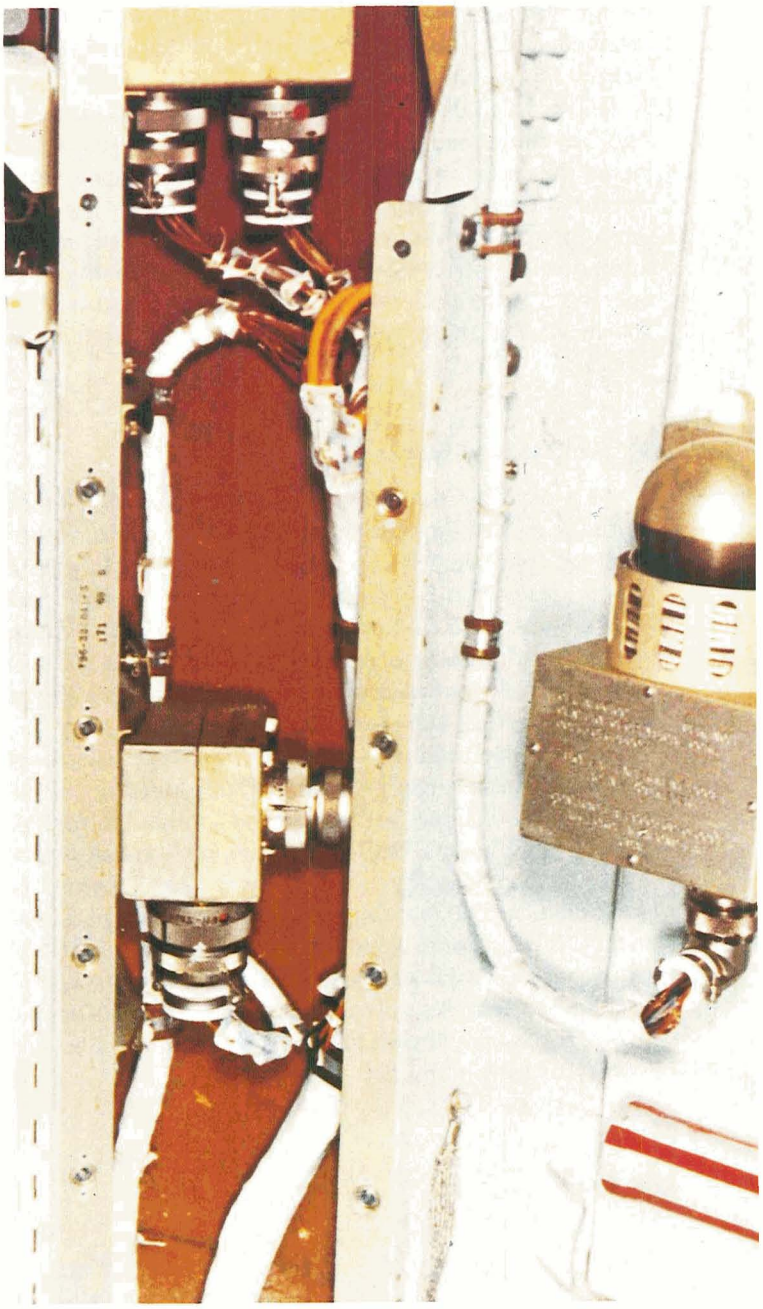

spaceflights and did not produce any measurable biological effects in the astronauts.

Dose-rate curves are shown in figure 7-36 for two typical orbital revolutions passing through the South Atlantic anomaly. Figure 7-37 shows the ground trace of these orbits on a map that also shows the regions in which Skylab encountered the Van Allen belts. Radiation dose rates encountered by Gemini 4, in 1965, were lower than the Skylab measurements, as expected. The former were taken at a lower altitude (325 km) and a 30° inclination and were 0.02 rad/day. The Skylab measurements were made at 435 km and a 50° inclination and were 0.05 rad/day.

On the third day of the first manned Skylab mission, the fire alarm sounded. The astronauts quickly investigated the entire space station to ascertain the cause and found nothing. Analysis showed that this was the first occasion that the vehicle had passed through the highest radiation region of the South Atlantic anomaly. The increased radiation level had triggered the detector. The alarm was disabled before later passages through the region.

A Step Into the Future

As a result of the knowledge gained from Skylab in both the contamination and radiation disciplines, future manned space vehicles such as the Space Shuttle will be better designed to protect their crews, supplies, and instruments. The first orbital flight test of the Shuttle will carry a package of instruments, the Induced Environment and Contamination Monitor, which is a direct outgrowth of Skylab instrumentation.

In a similar manner, of course, the experience and knowledge generated by Skylab and portrayed in part in the previous chapters will be a broad foundation for the coming Shuttle era. The first Shuttle mission carrying a Spacelab produced by the European Space Agency is scheduled, in fact, to emphasize atmospheric measurements. The second Spacelab mission will emphasize astrophysical observations, for which the Skylab experience surveyed in this volume again provides an informative predecessor. Skylab has thus earned a place in the history of astronomy and space sciences.

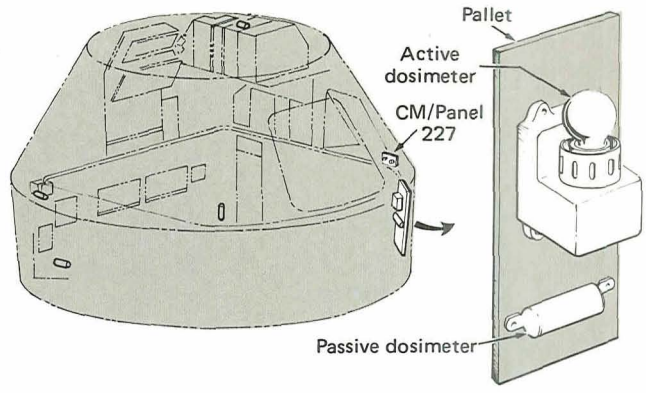

Figure 7-35.—Dosimeter locations in Skylab.

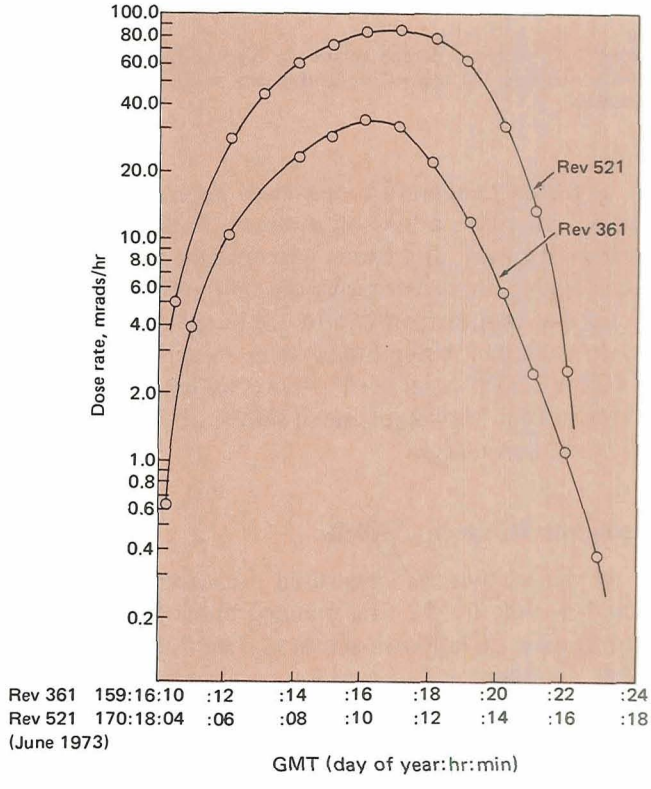

Figure 7-36.—Dose-rate curves for two Skylab orbits.

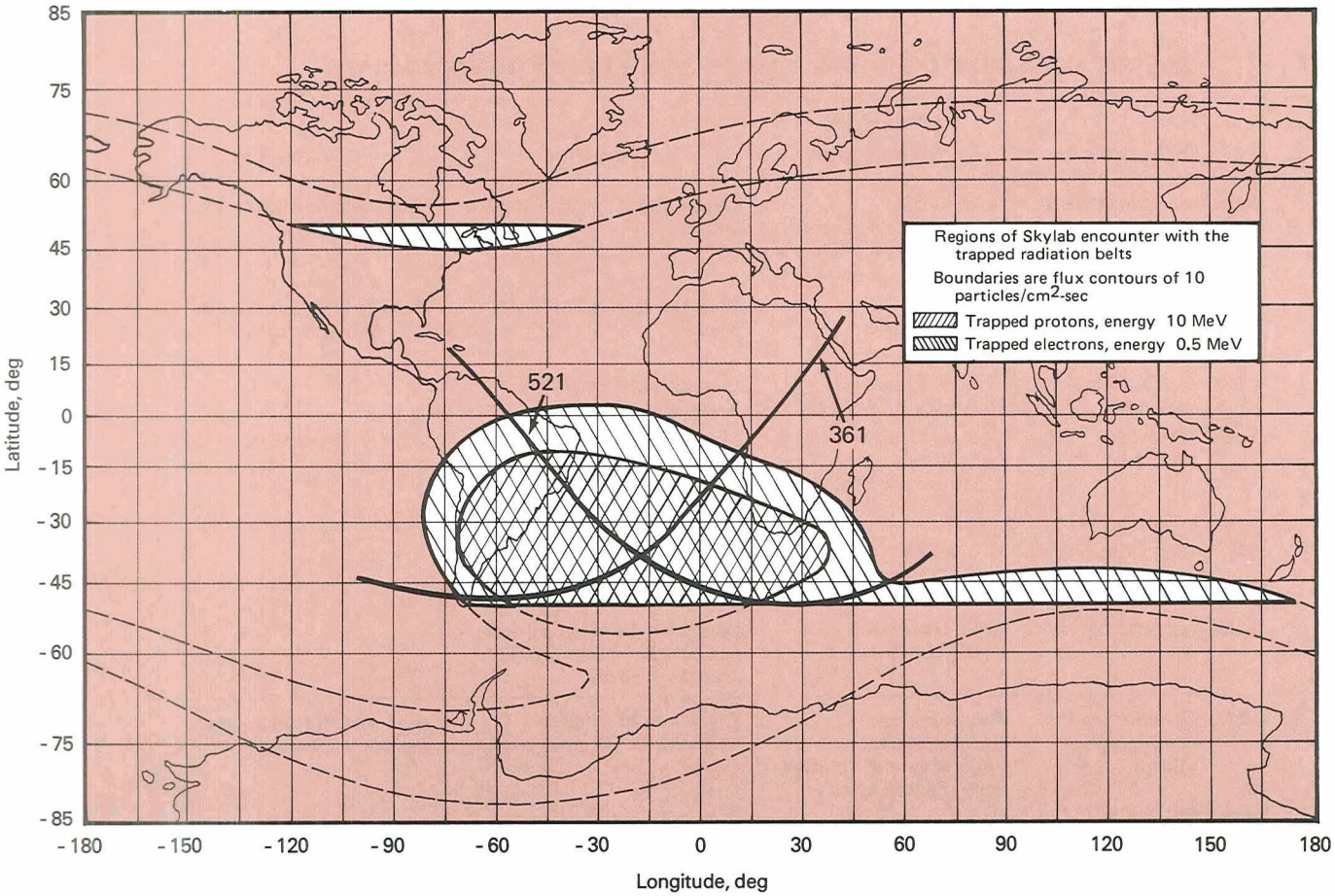

Figure 7-37.—Boundaries of trapped-radiation environments encountered by Skylab.

APPENDIX

Skylab's Astronomy and Space Science Experiments

Topic	*Experiment*	*Principal Investigator*	*Objective*	*Remarks*
Stellar and galactic astronomy	S019—Ultraviolet stellar astronomy	K. S. Henize Northwestern University, Johnson Space Flight Center	Obtain stellar spectra down to 1400 Å	Also used in studies of Comet Kohoutek
	S020—Grazing-incidence camera	R. Tousey Naval Research Laboratory	Solar imaging in EUV-soft X-ray	Also yielded data used in contamination studies
	S150—Galactic X-ray mapping	William Kraushaar University of Wisconsin	Investigate origin of diffuse X-ray background	
	S183—Ultraviolet panorama	Georges Courtes Laboratoire d'Astronomie Spatiale, France	Measure ultraviolet brightness of star fields	Also used in studies of Comet Kohoutek
Interplanetary dust	S073—Gegenschein-zodiacal light	J. L. Weinberg Dudley Observatory	Measure the brightness and polarization of the visible background of the sky	
	S149—Micrometeoroid collection	L. C. Hemenway Dudley Observatory	Determine the mass distribution of micrometeoroids in near-Earth space	
Comet Kohoutek	S201—Far-ultraviolet electrographic camera	Thornton Page Naval Research Laboratory and Johnson Space Flight Center	Study halo of Comet Kohoutek in far ultraviolet	Also used for stellar and galactic astronomy
	S233—Photometric studies	C. A. Lundquist Marshall Space Flight Center	Deduce changes in comet's coma from a brightness history	
	S052—White-light coronagraph	Robert MacQueen High Altitude Observatory, Boulder, Colorado	Observe comet during perihelion passage	Solar instrument also used in studies of Comet Kohoutek
	S055—Ultraviolet scanning polychromator spectroheliometer	Edmond Reeves Harvard College Observatory	Detect hydrogen emissions in comet's coma in the 296- to 1350-Å spectral range	Solar instrument also used in studies of Comet Kohoutek and the Earth's atmosphere
	S082A—Extreme-ultraviolet spectrograph	Richard Tousey Naval Research Laboratory	Measure comet's spectral emission in the 970- to 3040-Å range	Solar instrument also used in studies of Comet Kohoutek and the Earth's atmosphere
	S082B—Extreme-ultraviolet spectroheliograph	Richard Tousey Naval Research Laboratory	Search for comet helium halo in 304- and 584-Å wavelengths	Solar instrument also used in studies of Comet Kohoutek
Energetic particles	S009—Nuclear emulsion	M. M. Shapiro Naval Research Laboratory	Study charge spectrum of primary cosmic rays with emphasis on heavy nuclei	
	S228—Transuranic cosmic rays	P. B. Price University of California, Berkeley	Determine relative abundance of cosmic ray nuclei with atomic mass greater than 65	
	S230—Magnetospheric particle composition	Don Lind Johnson Space Center Johannes Geiss Physics Institute, University of Bern, Switzerland	Measure isotopic abundance of atomic species in magnetosphere	

Skylab's Astronomy and Space Science Experiments (Continued)

Topic	*Experiment*	*Principal Investigator*	*Objective*	*Remarks*
Energetic particles (Continued)	ED-76—Neutron analysis	Terry Quist San Antonio, Texas	Measure ambient neutron flux in orbital workshop	
	TV-108—Neutron environment	Gerald Fishman Marshall Space Flight Center	Measure neutron flux aboard Skylab	
	Visual light-flash observations	R. A. Hoffman Johnson Space Center	Investigate frequency and character of visual light flashes in near-Earth orbit	
Earth's atmosphere	S063—Ultraviolet airglow horizon photography	Donald Packer Naval Research Laboratory	Photograph the twilight airglow and Earth's ozone layer simultaneously in the visible and ultraviolet wavelengths	Also used in Comet Kohoutek investigations
Orbital environment	D008—Radiation in space	A. D. Grimm J. F. Janni G. Ainsworth Johnson Space Center—Kirtland Air Force Base	Provide experimental correlation of radiation levels with theoretical data and identify radiation-induced biological effects on man	
	D024—Thermal control coatings	W. L. Lehn Wright Patterson Air Force Base	Determine effects of near-Earth space environment on selected thermal control coatings	
	T003—In-flight aerosol analysis	W. Z. Leavitt Department of Transportation	Measure and analyze aerosol particle concentration and size distribution inside Skylab	
	T025—Coronagraph contamination measurements	M. Greenberg Dudley Observatory	Determine presence of particulate matter surrounding orbital workshop	Also used for study of particulate matter in the Earth's atmosphere
	T027—Contamination measurements	J. A. Muscari Martin Marietta Corp.	Determine change in properties of optical samples due to deposition of contaminants and measure sky brightness background due to solar illumination of contaminants	

EDITOR'S NOTE

The astronomy and space science of Skylab are primarily the product of the principal investigators, the instruments they built, and the results they derived. Their willing cooperation with the editorial participants in this volume was essential to its completion.

In an enterprise like Skylab, the analysis and interpretation of scientific data are typically the activities that continue beyond all others. In most cases, the investigators can begin a serious attack on the data only after the flight operations have ended and the tapes, film, and specimens have reached a home laboratory. The results of the Skylab astronomy and space science investigations reach the scientific community in diverse ways: through papers presented at summary conferences on Skylab findings (e.g., those sponsored by the American Institute of Aeronautics and Astronautics and the American Geophysical Union jointly, and sponsored by the American Astronautical Society); through specific symposia such as that held in 1974 on Comet Kohoutek; and, most importantly, through refereed papers in various scientific journals. This normal course of prolonged analysis and publication influenced the preparation of this volume. Efforts were made to incorporate new material as it became available, but this was accomplished incompletely at best.

The preparation of this volume was guided by an editorial board composed of the following members: Karl G. Henize and Robert A. Parker of the Lyndon B. Johnson Space Center; Curtis Hemenway of the Dudley Observatory; Jerry L. Weinberg of State University of New York at Albany; and Robert J. Naumann, Martin O. Burrell, William C. Snoddy, and Robert E. Lake of the George C. Marshall Space Flight Center. Jack Waite of the Marshall Center served as the Managing Editor. In the course of coordinating the set of Skylab volumes, Rein Ise also provided valuable advice and comments for this particular volume.

The material for the text was assembled by John W. Kierein, Richard J. Barry, John G. Meeker, and Jorgen Jensen. The manuscript draft was further edited by John C. Goodrum, Mitchell R. Sharpe, and Harry R. Melson, who also helped in preparing the illustrations. Final revisions of the manuscript draft were made by Annette Tingle, by Bob Richards and Aušra Richards, and by Karen Simon.

As editor of *Astronomy and Space Sciences,* I extend my thanks to all who helped. The preparation of this volume was appropriately a collective effort, as was Skylab itself.

CHARLES A. LUNDQUIST
Marshall Space Flight Center

INDEX

Aerobee rocket, 50
Aerosol analysis, 109
Ainsworth, Glenn C., 113
Airlocks, 4, 5
Aldrin, Edwin, 76
Apollo 11, 76
Apollo 16, 6, 15, 22
Argon
    Atmospheric, 79
    Measurement, 66
Articulated mirror system, 8
Asteroid belt, 39, 40
Asteroid system, Sun-Jupiter, Trojan, 41
Astronomy, stellar and galactic, 7
Astronauts
    Aldrin, Edwin, 76
    Bean, Alan, 7, 8
    Garriott, Owen, K., 4, 27, 86
    Gibson, Edward G., 51, 54, 55
    Glenn, John, 93
    Lousma, Jack R., 111
Atmosphere, of Earth, 79–91
Atmospheric extinction profiles, 85
Aurorae, studies, 86–91

Bean, Alan, 7, 8
Bohlin, David, 58
Bolometric magnitude, 12
Bright Star Catalog, 10
Brownlee, Donald, 33
Bunner, Alan, 23
Burnett, Donald, 69

Calcium fluoride
    In electrographic camera, 13
    In objective-prism spectrograph, 8
Cameras
    Earth-terrain, 4
    Extreme ultraviolet and soft X-ray, 104
    Far-ultraviolet electrographic, 13–16, 48, 51
    Ultraviolet panorama, 6
Carbon emission, 7, 10
Carina, 9, 10, 19, 20, 21
Carr, Gerald P., 75
Carruthers, George, 13
Chiu, Hong-Yee, 43
Clifton, K. S., 104
Collimators, in X-ray instrument, 23, 24
Coma, of comet, 44
Comet Kohoutek, 3, 5, 13, 43–63
    Antitail, 46, 58–59
    Helium, 58
    Hydrogen halo, 43, 46, 49–51
    Isophote plot, 53, 54
    Nucleus, 51
    Orbit, 48
    Passing the Sun, 53–54
    Path, 47
    Perihelion, 44, 48
    Photometric studies, 59–60
    Postperihelion, 49
    Preperihelion, 48
    Seen from Earth, 44–47
    Skylab's instruments for, 46, 47–48, 58
    Skylab's location, 48–49
    Solar observatory results, 54, 58
    Syndynes, 58
    Tail, 44, 46, 47
    Ultraviolet images, 53
    Ultraviolet spectra, 51
    Visual magnitude, 60–61

Visually observed, 51, 53, 54, 55
X-rays, 58
Comet orbits, 48
Comet spectrum, 46
Contamination-measuring instruments, 93–95
Contamination studies, 93–114
Coronagraph, 41, 83
Comet Kohoutek, 53–54
White-light, 105, 106
Cosmic rays, 71–72, 74
Flux, 77
Transuranic, 74–76
Ultraheavy, 75
Courtes, Georges, 16
Crab Nebula, 25, 72
Craters, impact 28–33

Deutschman, William A., 60, 61
Dosimeter, radiation, 113
Dosimeter, Van Allen Belt, 112
Dudley Observatory, 28, 83

Earth
Curvature, 80
Environment in space, 64
Limb in ultraviolet, 83–84
Earth-terrain camera, 4
Electrographic data, 14–15
Energetic particles, 65–77
"Evil eyes," 32–33
Experiments
Galactic X-ray mapping, 23
Gegenschein-zodiacal light, 36–38
Magnetospheric particle composition, 65–67
Micrometeoroid collection, 28–31
Neutron analysis, 69–70
Nuclear emulsion, 72–74
Optical surfaces, 101–102
Radiation dosimetry, 113–114
Skylab, inside atmosphere, 108–110
Thermal control and polymeric film, 97–101, 102
Transuranic cosmic ray, 74–76
Ultraviolet, 7–22
Ultraviolet panorama, 16–21
Ultraviolet stellar astronomy, 5–9, 20
Explorer I, 77
Extreme-ultraviolet radiation, 84–85
Extreme-ultraviolet spectroheliograph, 58
Extreme-ultraviolet spectroheliometer, 84

Far-ultraviolet electrographic camera, 13–16, 48, 51
Far-ultraviolet spectra, 11
Film, aboard Skylab, 112–113
Film vault, 112
Fishman, Gerald, 70

Galactic X-ray emissions, 23–25
Galactic X-ray mapping experiment, 23
Gamma Velae, 10
Gamma-ray spectrometer, 71
Garriott, Owen K., 4, 27, 86
Gary, G. A., 59
Gegenschein, 36–38, 40, 104
Geiss, Johannes, 65
Gibson, Edward G., 51, 54, 55
Glenn, John, 93
Goddard Space Flight Center, 43, 44
Gould's belt, 8
Greenberg, Mayo, 83
Grimm, Andrew D., 113
Gum Nebula, 14, 15

Hamburg Observatory, 43
Harvard College Observatory, 58, 60, 85
Helium
Emission, 7
Comet Kohoutek, 58
Measurement, 66
Hemenway, C. L., 28, 107
Henize, Karl S., 8, 21
Henry Draper Catalog, 10
High Altitude Observatory, 53
Hobbs, Robert W., 44
Hoffman, R. A., 77
Hopfield, Alison, 41
Horizon observations, 80–81
Hutchinson, P., 35
Hydrogen
Emission, 7
Lyman-alpha line, 13
Hydrogen halo, Comet Kohoutek, 43, 46, 49–51

Image Data Processing Facility, 20
Instruments
Aerosol analysis, 109
Contamination-measuring, 93–95
Extreme-ultraviolet spectroheliograph, 58
Micrometeoroid collection, 27, 28
Solar Ultraviolet spectrograph, 85
Transuranic cosmic ray detector, 68, 69
Ultraviolet photoelectric scanning, 58
Ultraviolet stellar astronomy, 5
X-ray, 23–25
Instellar dust (micrometeoroids), 10, 12
Integrating vidicon system, 43
Interplanetary dust, 27–41
Ionosphere, 80
Ions, defined, 7
Iron, ionized, 9
Iron peak, 72–74

Isophote plot, 15, 16
Color, 20–21
Comet Kohoutek, 53, 54

Janni, Joseph F., 113
Johnson Space Center, 65, 77
Joint Observatory for Cometary Research, 44, 45, 46

Keller, H. Uwe, 58
Kitt Peak National Observatory, 43
Kohoutek, Lubos, 43
Kraushaar, William, 23

Leavitt, W. Z., 108
Lehn, William L., 97
Lexan, 75
Libration, lunar, 41
Light flashes, observed from Skylab, 76–77
Lind, Don, 65, 103
Lithium fluoride, use in electrographic camera, 13
Lousma, Jack R., 111
Lundquist, Charles A., 59
Lyman-alpha light, 43
Lyman-alpha line, 13, 58

MacQueen, Robert, 41, 53
Magellanic clouds
Large, 6, 7, 15, 21, 22
Small, 15
Magnesium absorption, 9
Magnesium fluoride, use in photometer, 17
Magnetospheric particle composition experiment, 65–67
Map, color-coded
Brightness, 40
Contour, 51
Polarization, 40
Maran, Stephen P., 43
Marshall Space Flight Center, 59, 71, 104
Metallic foils, 102–104
Meteors, 27–28
Methyl silicone, on Skylab windows, 108
Microbalance, quartz-crystal, 93–95
Microdensitometer, 10, 11, 12, 15, 18, 51
Micrometeoroid and heat shield, 1, 5
Micrometeoroids
Collection experiment, 28–31
Collection instrument, 27, 28
Residue, 31, 33–35
Milky Way, 10, 15, 16, 21, 23, 24, 25, 40, 72
Mirror, ultraviolet reflecting, 5, 17
Moon, studies of, 81–83
Moonrise, seen from Skylab, 81
Mt. Haleakala, Hawaii, 35, 36
Muscari, Joseph A., 101, 104
Muscovite mica, in detector foil, 69

NASA, 23
Neon measurement, 66
Neutron analysis experiment, 69–70
Neutron detector, 70
Neutron environment demonstration, 70–71
Neutron radiation, 67–68
Nitrogen
Absorption of solar radiation, 85
Atmospheric, 79
Emission, 7
Noble gases, trapped, 66
Nuclear emulsion experiment, 72–74

Objective-prism spectrograph, 8, 9, 51, 53
O'Dell, C. R., 59
"Operation Kohoutek," 43
Optical surfaces
Deposits on, 107–108
Experiment, 101–102
Orbiting Astronomical Observatories, 8, 10
Orionids, 27
Oxidation experiment, 107
Oxygen
Absorption of solar radiation, 7, 85, 86, 87
Atmospheric, 79
Emission, 7, 10

Packer, Donald, 83, 86
Page, Thornton, 13, 50, 51
Parasol, 1, 5
Photographs
Blue-light, 21
False-color, 43
Far-ultraviolet, 15, 22, 43
Red-light, 22
Ultraviolet, 19, 22
Photometer, 17–19, 39, 40, 104
Pioneer 10 and 11, 39
Pogue, William, 77
Polymeric film experiment, 97–101
Potassium bromide, photocathode, 14
Poynting-Robertson effect, 38–40
Price, P. Buford, 33, 75

Quartz-crystal microbalance, 93–95
Quist, Terry, 69

Radiation dosimetry experiment, 113–114
Radiation studies, 111–114
Extreme ultraviolet, 84–85
Radioactivity measurement, 71
Reeves, Edmond, 58

Saturn IB rocket, 1, 24
Saturn V rocket, 1

Schmidt-Cassegrain camera system, 18, 19, 21
Sekanina, Z., 59
Shapiro, Maurice M., 72
Shirk, E. K., 75
Silicon absorption, 9
Skyglow studies, 40
Skylab
    Altitude, 80
    Crews, 1
    Collector cuff, 65, 66
    Collector foils, 67
    Discoloration, 95-97
    Film, 112-113
    Inside atmosphere, 108-111
    Location, 48
    Mission sequence, 2
    Moonrise, 81
    Optical environment, 104-106
    Orbit, 2
    Special accommodations, 4-5
    Sunrise, 79, 82, 83
    Temperature control, 95
    Tracking network, 2, 3
    Windows, 4, 107, 108, 109
Smithsonian Astrophysical Observatory, 59, 60
Smithsonian Catalog, 14
Solar flare, 86
South Atlantic anomaly, 3, 74, 76, 77
Spectra
    Far-ultraviolet, 11
    Ultraviolet, 8, 9, 10, 13
        Comet Kohoutek, 51
        Hot stars, 11-12
    Widened, 9-11
Spectral line absorption, 85-86, 87
Spectrograph
    Objective-prism, 8, 9, 51, 53
    Solar ultraviolet, 85
Spectroheliograph, extreme ultraviolet, 58
Spectroheliometer, extreme ultraviolet, 84
Spectrometer, gamma-ray, 71
Star field studies, 8
Stars
    Classification, 7, 8, 10, 14
    Hot, 11-12
    Wolf Rayet, 10, 11
Sun, observations, 3, 47, 80
Sunrise, seen from Skylab, 79, 82, 83

Tail, comet, 44, 46, 47
Telescope
    Converted, 8
    Earth-based, 14
Thermal control experiment, 96-101, 102
Theta Muscae, 10
Tousey, Richard, 58, 104
Transuranic cosmic ray detector, 68, 69
Transuranic cosmic ray experiment, 74-76

Ultraviolet experiments, 7-22
Ultraviolet images, Comet Kohoutek, 53
Ultraviolet light, 10, 12
Ultraviolet panorama camera, 6
Ultraviolet panorama experiment, 16-21
Ultraviolet photoelectric scanning instrument, 58
Ultraviolet photographs, 19, 22
Ultraviolet region, 7-8
Ultraviolet spectra, 8, 9, 10, 13
    Comet Kohoutek, 51
    Hot stars, 11-12
Ultraviolet stellar astronomy experiment, 5-9, 20
Ultraviolet stellar astronomy instrument, 5
United States Naval Research Laboratory, 72, 83, 86, 104
University of Michigan Observatory, 21

Van Allen, James, 77
Van Allen Belt, 3, 70, 74, 77, 111

Weinberg, Jerry, 36, 40, 104
Wolf Rayet stars, 10, 11

X-ray emissions, galactic, 23-25
X-ray instrument, 23-25
X-rays
    Comet Kohoutek, 58
    Wavelength band, 2

Zodiacal light, 2, 28, 35-38, 39, 40

☆ U.S. GOVERNMENT PRINTING OFFICE 1979 O—293-841

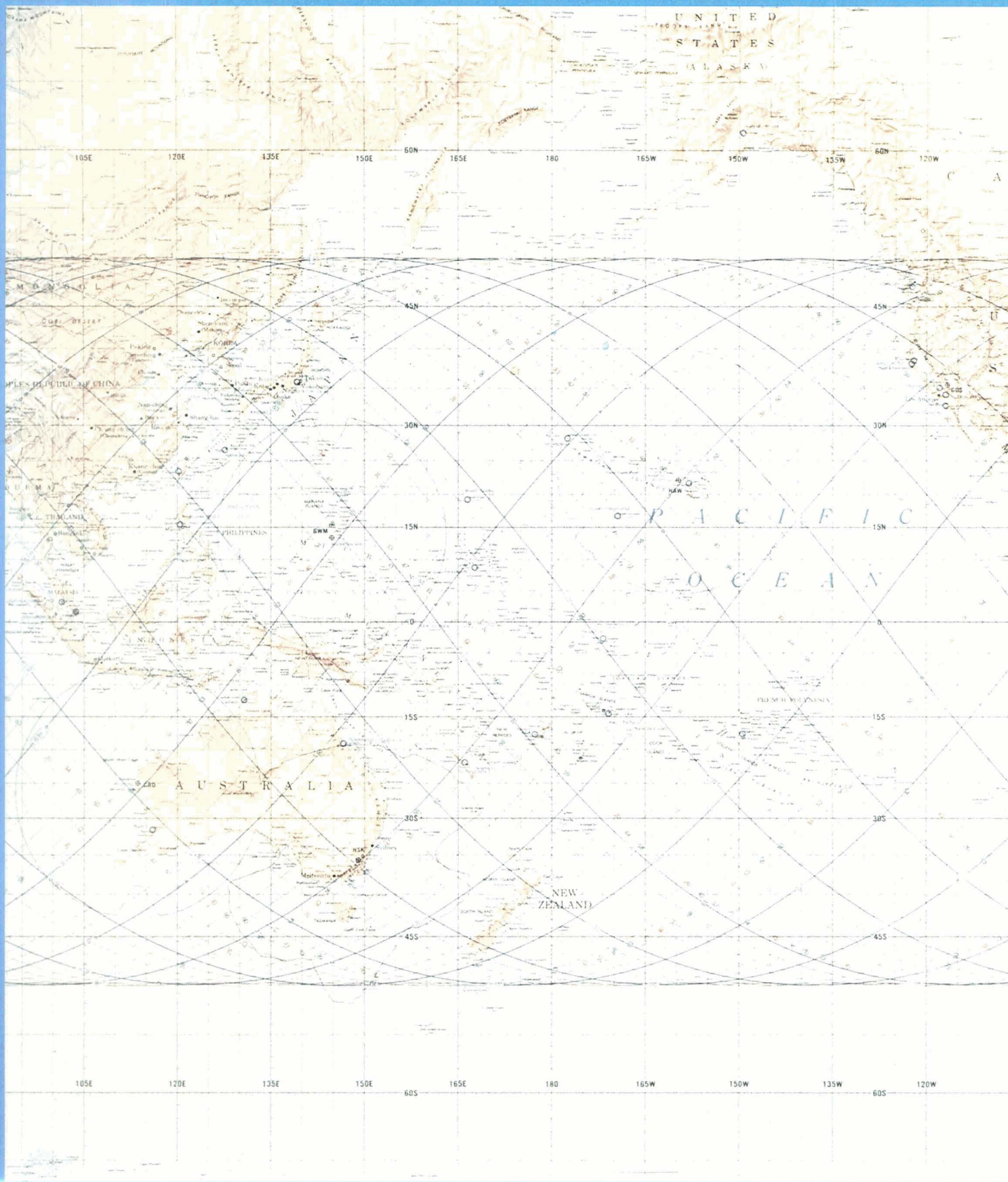
UNITED
STATES
ALASKA
MONGOLIA
KOREA
PHILIPPINES
HAW
GWM
PACIFIC
OCEAN
AUSTRALIA
NSK
NEW
ZEALAND
105E
120E
135E
150E
165E
180
165W
150W
135W
120W
60N
45N
30N
15N
0
15S
30S
45S
60S

UNION OF SOVIET SOCIALIST REPUB
ATLANTIC
OCEAN
BRAZIL
INDIA
OCEA
GREENLAND
ICELAND
UNITED
KINGDOM
ALGERIA
LIBYA
EGYPT
SAUDI
ARABIA
ZAIRE
TANZANIA
SOUTH AFRICA
COLOMBIA
WEST INDIES
MAD
CYI
ACN
VAN SA
BDA
MIL
75W
60W
45W
30W
15W
0
15E
30E
45E
60E
75E
60N
45N
30N
15N
15S
30S
45S
60S